Production of charm jets tagged with D^0 mesons in pp collisions at $\sqrt{s}$ = 13 TeV with ALICE

By

Jakub Kvapil

A thesis submitted to
the University of Birmingham
for the degree of
DOCTOR OF PHILOSOPHY

Nuclear Physics Group
School of Physics and Astronomy
College of Engineering and Physical Sciences
University of Birmingham
March 2022

CERN-THESIS-2022-058
21/04/2022

© Copyright by JAKUB KVAPIL, 2022

All Rights Reserved

SYNOPSIS

The production of charm jets tagged with fully reconstructed D^0 mesons measured at $\sqrt{s} = 13$ TeV by the ALICE detector at the CERN LHC, is presented in this thesis. The D^0 mesons are reconstructed through the hadronic decay channel $D^0 \rightarrow K^- \pi^+$ and its charge conjugate. Jets are reconstructed from charged-particle tracks and the D^0 candidate using the anti-k_T algorithm. Results are given for the jet resolution parameters $R = 0.2$, 0.4, and 0.6 in the pseudorapidity range $\eta_{\text{ch.jet}} < (0.9 - R)$ and charged-particle jet transverse momentum $5 < p_{T,\text{ch jet}} < 50$ GeV/c. The $p_{T,\text{ch jet}}$-differential cross-section and the parallel momentum fraction carried by the D^0, $z_{||}^{\text{ch}}$, is presented in this thesis. The measurement of in-jet fragmentation can provide valuable information for constraining gluon-to-hadron fragmentation functions, and this measurement provides a unique insight into intermediate transverse momentum. The measurement is compared to several Monte Carlo generators with both leading-order and next-to-leading-order accuracy. The models describe the main features of the $p_{T,\text{ch jet}}$ spectra well and provide a good description of the $z_{||}^{\text{ch}}$ distributions for $p_{T,\text{ch jet}} > 10$ GeV/c. A discrepancy in $z_{||}^{\text{ch}}$ between data and models is observed for lower $p_{T,\text{ch jet}}$.

Declaration of author's contribution

A pre-requisite for this analysis was the work of vast number of people, especially detector experts and engineers for construction, operation and calibration of detectors, the ALICE data preparation and Monte Carlo generator groups for creation of the data sets, and the Heavy Flavour working group for pre-selecting the D^0 candidates.

The author contributed to the Quality Assurance checks for the 2017 and 2018 data by developing a framework and evaluating the data sets with respect to inclusive and charm jet variables. The author developed a framework to analyse the charm jet candidates and to study the cross-section and parallel jet momentum, $z_{||}^{\mathrm{ch}}$. His work includes the signal extraction, correction of the signal and studies of systematic uncertainties. Moreover, the author produced MC data for comparison with results of this analysis and to determine the beauty feed-down contribution. An extensive development was done in multidimensional folding and unfolding procedures. The Author is a member of the paper committee for publishing the results.

In addition, the author implemented a transmitter for Trigger-Timing-Control (TTC) protocol based on TTCex-TTCrx and an interface to the new Run 3 triggering protocol for the ALICE Central Trigger System (CTS) at the Local Unit Board (LTU). The design was inspired by previous implementations used by ALICE during Run 1 and 2 and the NA62 experiment, and was re-implemented and fitted on the Xilinx UltraScale FPGA used by the new ALICE CTS. The author also contributed to creating a testing setup in the CTS

laboratory, with installation for detectors, namely the EMC, TRD, CPV, PHS and HMP detectors, and installation in the ALICE cavern. Further support was provided usually related to timing and latency issues. Finally, the author contributed to development of the Central Trigger Processor that controls the LTUs.

DEDICATION

I would like to dedicate this thesis to my parents and grandparents who were supporting me on the whole journey of becoming a PhD.

ACKNOWLEDGMENTS

During the duration of my PhD, I have sought advice from many people. On this page I would like to show my gratitude to those people, and also apologise if I forgot to explicitly mention someone.

First, I would like to thank my supervisors David Evans and Roman Lietava. They were always at hand for discussing the physics and progress of the analysis by sharing their deep knowledge. Moreover, Roman learned me everything about triggering at collider experiments and supported me while creating trigger firmware for the Birmingham group. He was always open for a chat regardless if it was physics, trigger, or life problems. I am especially grateful that they allowed my long stay at CERN, which was especially helpful for the research and developing the trigger. My thanks go to Peter Jones, who has supervised me during my first year as he was the one who made me interested in the jet area. My gratitude goes towards Orlando Villalobos Baillie and to Oliver Jevons who provided me advice in the mysteries of English grammar. Finally, I am especially grateful to Gron Tudor Jones and his family for a hearty welcome in the UK, and long discussions over a cup of Earl Grey.

I would like to thank the University of Birmingham and STFC who provided me with the funding to perform my research, for supporting my stay at CERN, and to CERN UKLO who were helpful while finding the apartments in the area.

I also need to mention colleagues at ALICE, especially Barbara Trzeciak, Auro Mohanty, Nima Zardoshti, Vit Kucera, and Fabio Collamaria for their support and discussion in physics analysis, and to Birmingham's engineers at CERN, Anton Jusko, Marian Krivda,

and Luis Alberto Perez Moreno for their support while working with them, the time we were sharing an office at CERN, and also for the coffees at 2 pm, during which they introduced me to almost every Slovak at CERN.

I need to mention my friends and fellow PhD students and postdocs at Birmingham: Beckie, Chris, Ellie, Emily, Hakan, Harry, Jack, Marianna, Neil, Nima, Pedro, Sammy, Simone, Stuart, Tony, and Yi Ming for the best office atmosphere, enjoyable lunches, and Mondays board game nights, which I truly miss. I would like to thank my friends in Geneva: David, Jan, Jana, Lucie, Marta, Mito, Peter, and Tereza who made me feel like home there. For the pancakes on Sunday, dinners on Wednesday, games and trips during the weekends, and dance classes. Finally, my thanks goes to my friends all over the world Alca, Andrej, Filip, Miro, Renata, Tonda, and Zuzana.

My biggest gratitude goes to my parents who were fully supporting me with my choices and decision of going for a PhD, of which I am the first one in a wide family. Even though my grandparents are not here anymore I think they would be proud.

Four Boards for the Track-kings in the Lodestone,

Four for the Calo-lords in their halls of steel,

Eight for thees absent field doomed to live,

One for the Trigger in his dark crate

In the Land of Cavern where the Shadows lie.

One Board to rule them all, One Board to find them,

One Board to bring them all and in the darkness bind them

In the Land of Cavern where the Shadows lie.

paraphrased J. R. R. Tolkien

In theory, there is no difference between theory and practice,

but in practice, there is.

unknown origin, credited to various sources

Contents

List of Figures

List of Tables

Acronyms

C-RORC Common Readout Receiver Card. 42

EvtGen Monte Carlo Generator for B-Physics. 14, 15, 72, 92, 111, 112

ALICE A Large Ion Collider Experiment. 9, 21, 30, 34, 49, 57, 58, 61, 63–65, 72, 91, 93, 116, 137, 138, 143

ATLAS A Toroidal LHC Apparatus. 24, 26, 30, 57, 61

BC Bunch Crossing. 47, 52, 54–56

CERN The European Organization for Nuclear Research. 27–29, 137

CMS Compact Muon Solenoid. 21, 30, 57, 60

CPV Charged Particle Veto. 46, 52, 54

CRU Common Readout Unit. 46

CTP Central Trigger Processor. 34, 38, 42, 45–47, 50–52, 54–56

CTS Central Trigger System. 45, 46

CUDA Compute Unified Device Architecture. 43

D-RORC DAQ Readout Receiver Card. 42

DAQ Data AcQuisition. 42, 44

DDL Detector Data Links. 42

EDM Event-Destination Manager. 43

EMC Electromagnetic Calorimeter. 46, 52, 54

FERO Front-End Read-Out. 42

FF Flip-Flop. 56

FIFO First In First Out. 54

FONLL Fixed-Order-Next-to-Leading-Logarithm. 57

FPGA Field-Programmable Gate Array. 43, 50, 56

FSR Final State Radiation. 9, 10, 12, 15

GBT GigaBit Transceiver. 45, 46, 52

GM-VFNS General Mass Variable-Flavor-Number Scheme. 57

HB HeartBeat. 46, 47

HEP High Energy Physics. 29

HERWIG Hadron Emission Reactions With Interfering Gluons. 10, 11, 13, 14, 62

HLT High Lever Trigger. 43

HMP High Momentum Particle Identification. 46, 52, 54

ISR Initial State Radiation. 9–12, 15

ITS Inner Tracking System. 34, 37, 38, 67, 91, 103–106, 138

LHAPDF Les Houches Accord Parton Distribution Function. 11, 72, 92, 127

LHC Large Hadron Collider. 7, 21, 22, 27–32, 42, 46–49, 56, 137, 141, 142

LHCb Large Hadron Collider Beauty. 30, 57

LHEF Les Houches Event File. 12, 13

LTU Local Trigger Unit. 42, 45, 47, 48, 50–52, 54, 56

LVDS low-voltage differential signaling. 47, 52, 56

MC Monte Carlo. 9–15, 57, 59, 61, 71–74, 77, 80–82, 84, 98, 103–106, 108, 114–116, 118, 128, 138, 145

MPI Multiple Parton Interaction. 15

PDF Parton Distribution Function. 5, 9, 11, 72, 92, 127

PHS Photon Spectrometer. 46, 52, 54

POWHEG POsitive Weight Hardest Emission Generator. 12, 13, 62, 72, 73, 92, 95, 111, 118–121, 127, 135–137

PP Pre-Pulse. 48, 49, 52–54

pQCD perturbative Quantum Chromodynamics. 2, 5, 18, 57, 58, 61, 64, 111, 137

QCD Quantum Chromodynamics. 2–4, 6, 16, 19, 25, 57, 58, 120

QED Quantum Electrodynamics. 3, 4

QGP Quark–Gluon Plasma. 16, 18, 19, 22–25, 34, 59, 138

RHIC Relativistic Heavy Ion Collider. 16, 21

SDD Silicon Drift Detectors. 37, 38

Sherpa Simulation for High Energy Reactions of PArticle. 10, 11, 13, 14, 59

SPD Silicon Pixel Detectors. 37, 67, 71

SSD Silicon Strip Detectors. 37, 38

TF Time Frame. 47

TOF Time-Of-Flight. 34, 39–41, 70

TPC Time Projection Chamber. 34–40, 43, 46, 67, 70, 76, 77, 103–106

TRD Transition Radiation Detector. 39, 42, 46, 48, 52, 54, 56

TTC Trigger Timing Control. 42, 46, 50–52, 54, 56

TTC-PON Trigger Timing Control Passive Optical Network. 45, 46, 52, 56

TTCex TTC Encoder and Transmitter. 47, 48, 56

TTCrx TTC Receiver. 47–51, 55

UE Underlying Event. 15, 64, 121, 137, 138

VHDL Very High Speed Integrated Circuit Hardware Description Language. 50

ZM-VFNS Zero Mass Variable-Flavor-Number Scheme. 63

Chapter One

Introduction to High Energy Physics

1.1 The Standard Model of Particle Physics

The Standard Model is a theory developed in the second half of the 20th century describing the interaction of elementary particles and fundamental forces [1]. The elementary particles can be divided into two groups – fermions and bosons.

Fermions (quarks and leptons) are spin-$\frac{1}{2}$ particles obeying Fermi-Dirac statistics while bosons obey Bose-Einstein statistics, thus can have spin 0 or 1. The fermions are sorted into three generations (u, d, e^-, ν_e), (s, c, μ^-, ν_μ) and (b, t, τ^-, ν_τ), analogous to the periodic table where elements with similar properties are grouped in different periods. Particles across generations share the same quantum numbers - e.g. electric charge, spin, isospin and hypercharge, but differ in mass. M. Gell-Mann [2] and G. Zweig [3] placed the foundations of the quark model in 1964, by postulating an $SU(3)$ group symmetry known as the Eightfold Way. It played an essential role in predicting at that time unknown hadron, Ω^-, which was later discovered [4]. However, quark spin became troublesome. As quarks are fermions, they must obey Pauli's exclusion principle – it should be impossible to have a particle that contains three quarks in the same quantum state - e.g. Δ^{++} (uuu). Shortly

after, Oscar W. Greenberg proposed the concept of a new hidden quantum number, the colour charge (red (r), green (g), blue (b)) postulating the colour group $SU(3)$ [5]. This additional degree of freedom allows the existence of Δ^{++} and other particles without violating the exclusion principle.

Bosons have either spin 1 (photon, gluons, $W^{\pm}$ and Z^0), which are the force mediators, or spin 0 (Higgs). A photon (γ) is a massless boson mediating the electromagnetic interaction. The γ does not carry any electrical charge, thus interaction with other γs is not allowed. Gluons are the mediators of the strong force responsible for binding quarks together. There are eight gluon colours (superposition of colour–anti-colour) which are well-defined by group theory. As gluons are not colour charge neutral they can undergo a self-interaction of gluons allowing "g $\rightarrow$ gg" processes. This can be observed as 3-jet events, a phenomenon which also proved the existence of the gluons themselves [6]. $W^{\pm}$ [7, 8] and Z^0 [9, 10] bosons are responsible for the weak interaction, which is the only flavour changing force. The scalar Higgs boson [11, 12] is responsible for particle masses. In particular, it allows for the introduction of mass to the $W^{\pm}$ and Z^0 gauge bosons. The strong, weak and electromagnetic forces are described as a gauge theory with $SU(3) \times SU(2) \times U(1)$ symmetry group - this is what is known as the Standard Model.

1.2 Introduction to Quantum Chromodynamics

Quantum Chromodynamics (QCD) is a $SU(3)$ gauge theory describing the interaction between quarks. The strong force coupling constant, α_s, is known as a “running" coupling constant [13] due to its dependency on the energy scale of the interaction Q^2. In perturbative Quantum Chromodynamics (pQCD) the coupling constant [14, 15] can be expressed in a term of renormalisation scale, μ_R. To leading order accuracy, the coupling constant as a

function of Q^2 can be written as

$$\begin{aligned} \alpha_s(Q^2) &= \frac{\alpha_s(\mu_R^2)}{1+\alpha_s(\mu_R^2)\beta_0 \ln(Q^2/\mu_R^2)} = \frac{1}{\beta_0 \ln(Q^2/\Lambda_{QCD}^2)}, \\ \beta_0 &= \frac{11N_c - 2n_f}{12\pi}, \end{aligned} \tag{1.1}$$

where $N_c = 3$ is the number of colours, $n_f = 6$ number of quark flavours, and Λ_{QCD} is the QCD scale parameter. It has to be determined by experiment and has values between $\Lambda_{QCD} \approx 100 - 300$ MeV [16]. For the values of $Q^2 >> \Lambda_{QCD}^2$, the coupling is weak enough for quarks and gluons to become quasi-free, allowing for a perturbative description of the system. The β_0 parameter describes loop corrections to gluon interactions. The n_f term corresponds to the introduction of a $g - q\bar{q} - g$ loop and the N_c term corresponds to the introduction of a $g-gg-g$ self-interaction loop. Unlike in Quantum Electrodynamics (QED), where the β_0 is negative, in QCD it is positive due to the gluon self-interaction term. This phenomenon leads to the anti-screening of the colour charges at large energy scales, which is known as asymptotic freedom [17, 18]. While screening in QED means that a large charge will generate a cancelling cloud around it which reduces its effective charge at long distances. The anti-screening in QCD catalyses the generation of new charges enhancing its power as is shown in Figure 1.1. This would inevitably lead to an infinitely large field which would require infinite energy and is not accessible. This is resolved by binding the quarks inside hadrons where these fields cancel out, resulting in finite field energy. This phenomenon is called the confinement of quarks which results in colour-less states. A three-quark (qqq) state is known as baryon and a quark-antiquark ($q\bar{q}$) state is known as meson. Baryons and mesons are commonly called hadrons.

With the discovery of a J/ψ quarkonium, a $c\bar{c}$ state [19, 20], the heavy-flavour (HF) inter-quark potential, or Cornell potential [21], has been introduced as

$$V(r) = -\frac{4}{3}\frac{\alpha_s}{r} + kr, \tag{1.2}$$

which combines a Coulomb repulsion from gluon exchange at a short distance, going as

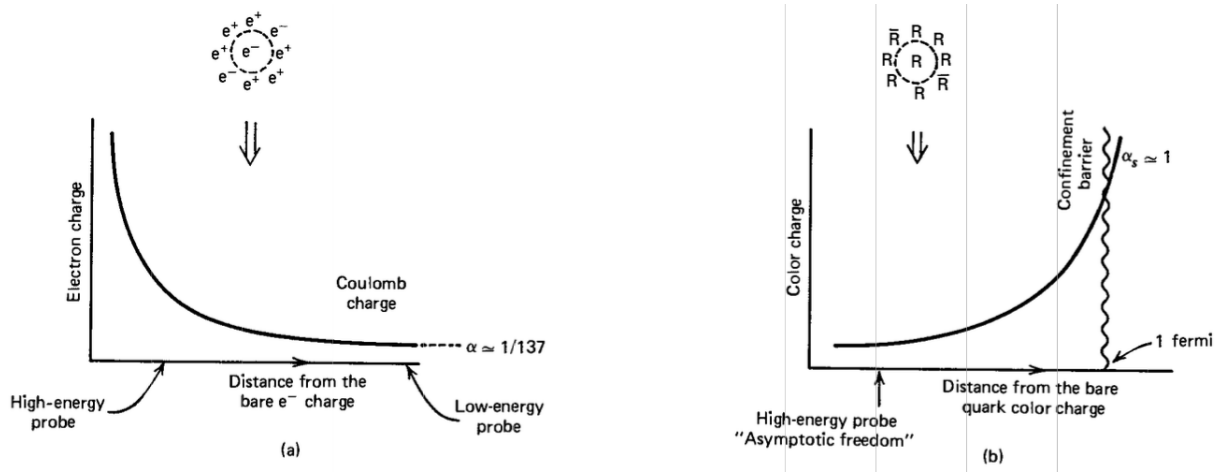

Figure 1.1: (a) The QED coupling constant (electric charge) with screening effect decreasing in amplitude with distance. (b) The QCD coupling constant (colour charge) increases infinitely reaching $\alpha_s = 1$ in a distance of 1 fm due to colour charge anti-screening leading to hadron confinement [13].

$1/r$, with a linearly rising string (see section 1.5.3 below) potential with string tension $k \sim 0.85$ GeVfm^{-1} [21] at large distances r. In contrast to QED, where the field is spread in space, the QCD colour flux remains focused in a narrow tube. When the distance between the quarks increases and the string potential term rises to the energy threshold for quark-antiquark pair production, the string breaks up to shorten itself by creating a new $q\bar{q}$ pair. This is the realisation of confinement explaining what will happen when we try to separate quarks.

1.3 Factorisation theorem of hard processes in QCD

Hard probes are objects created with a large energy transfer (hard process) in the beginning of a collision, like heavy-flavour hadrons (H) or collimated sprays of particles (jets). The production cross-section of hard probes can be reasonably well described by a factorisation

theorem [22]

$$\sigma_{A+B\to H/jet+X} = \sum_{ab} f_A(x_a,\mu_F) f_B(x_b,\mu_F) \cdot \sigma_{a+b\to c+X}(x_a, x_b, p_c, Q, \alpha_s(\mu_R), \frac{Q}{\mu_R}, \frac{Q}{\mu_F}) \cdot D(z,Q), \tag{1.3}$$

where $f_X(x_x,\mu_F)$ is the Parton Distribution Function (PDF), $\sigma_{a+b\to c+X}$ is the parton-to-parton cross-section and $D(z)$ is the fragmentation function. The PDF $f_A(x_a,\mu_F)$ describes the probability that a parton with momentum fraction $x_a = \frac{p_a}{p_A}$ is found inside proton A (similarly for $f_B(x_b,\mu_F)$). These PDFs are measured in lepton deep inelastic scattering experiments and one can directly use them in hadron colliders as long as a same renormalisation scheme is used in both instances. They are measured at a certain energy scale Q, extrapolation to a different energy (for example at LHC) is done using Dokshitzer-Gribov-Lipatov-Altarelli-Parisi (DGLAP) evolution [23–26]. The factorisation scale, μ_F, defines the crossing between long-range (non-perturbative) and short-range (perturbative) effects. This scale treats the infrared (IR) divergences caused by a collinear emission of massless particles. Any emissions below the μ_F momenta are included in the PDF, while emissions above are part of the pQCD calculation.

The parton-to-parton cross-section $\sigma_{a+b\to c+X}$ is calculated using pQCD. The assumption is that partons in a nucleon do not interact during the crossing time and only one parton from each nucleon interacts. A renormalisation scale, μ_R, is needed to govern the renormalisation, which treats the infinities arising from beyond the leading order processes, also known as ultraviolet (UV) divergencies.

$D(z)$ is the fragmentation function, which is the probability that the hadron H, or jet, carries a momentum fraction $z = p_{H/jet}/p_c$ from the hard scattering outgoing parton c. The parton energy must be known in order to describe the fragmentation functions precisely. Thus e^+e^- scattering is often used to extract fragmentation functions since the momentum can be easier calculated from the incident leptons. The process of fragmentation can be split

into three parts. First, the hard parton radiates energy, which evolves into a parton shower. Following this, colourless final state hadrons (hadronisation) are formed from the shower, and finally, the hadrons decay into final state particles, which are measured by the detector. These final state particles will be collimated in the direction of the original parton and are called jets. The fragmentation functions are provided by fitting equation (1.3) to various measured cross-sections.

1.4 Jets

Jets are collimated sprays of hadrons resulting from the fragmentation of a high-p_{T} parton created during hard scattering. They are widely used, and are essential for the study and verification of the QCD. Their production can be described by the QCD factorisation theorem. For the purposes of experimental studies the standard rules defining how the jets are identified, known as jet algorithms, are all collected together in the FASTJET framework [27], used by the majority of experiments. Two steps are required to define a jet using FASTJET. Firstly, the clustering algorithms identify tracks that will be clustered into a jet. Secondly, the tracks four-momenta will be added together using a recombination scheme.

1.4.1 Clustering algorithms

The ideal clustering algorithm must fulfil several criteria [28]:

1. collinear safe – invariant against collinear splitting of a track,
2. infrared safe – invariant against the emission of low p_T gluons,
3. detector and luminosity independent.

The first group of clustering algorithms are the cone algorithms. They put together tracks in specific conical angular regions and were mainly used at the TEVATRON due to lower computing power [27, 29]. As the early cone algorithms are not infrared and collinear safe, they are usually not used for Large Hadron Collider (LHC) analyses. For this reason they will not be discussed in this work. The second group of algorithms, fulfilling the criteria, are the sequential recombination algorithms. In these algorithms, the clustering is performed on a track-by-track basis, given some key criteria. They are quite computing intensive since the clustering difficulty strongly scales with the number of tracks in an event. Thus FASTJET [27] is used because it is optimised to lower the computational difficulty from $\mathcal{O}(N^3)$ to $\mathcal{O}(N \ln N)$.

Sequential algorithms can be generally described as follows: for each track i, the beam distance d_{iB}, and distances to all other tracks j, d_{ij}, are calculated as

$$\begin{aligned} d_{iB} &= p_{T,i}^{2p}, \\ d_{ij} &= \min\left(p_{T,i}^{2p}, p_{T,j}^{2p}\right) \frac{\Delta R_{i,j}^2}{R^2}, \end{aligned} \tag{1.4}$$

where $p_{\mathrm{T},i}$ and $p_{T,j}$ are the transverse momenta of the tracks or pseudojets. Pseudojets are combined tracks, which are not yet completed jets. The rapidity (for definition of rapidity see appendix A.1.1) of tracks or pseudojets is calculated as $y_i = \frac{1}{2} \ln \frac{E_i + p_{\mathrm{z},i}}{E_i - p_{\mathrm{z},i}}$. The distance between two tracks in the rapidity-azimuth plane is then $\Delta R_{i,j}^2 = (y_i - y_j)^2 + (\varphi_i - \varphi_j)^2$, where R is the jet radius is a maximum defined distance between jet center and tracks in the rapidity-azimuth plane. A sequential algorithm finds the minimum of all d_{ij} and d_{iB}; if the smallest quantity is d_{ij}, then the tracks i and j are combined into a pseudojet, with their 4-momenta combined using a given recombination scheme. Details on such schemes will be discussed in section 1.4.2. When d_{iB} is the minimum, the pseudojet i is declared as a jet and is removed from the clustering procedure. This is repeated until every track in an event is clustered into a jet. The parameter p in equation (1.4) defines the type of the algorithm: for the anti-k_{T} [28] algorithm, $p = -1$, for the Cambridge/Aachen algorithm [30, 31], $p = 0$, and

for the k_{T} algorithm [32], $p = 1$. The anti-k_{T} algorithm starts the clustering from the most energetic track, while the $\mathrm{k_t}$ algorithm starts from the least energetic one. A simulated event of these two algorithms is shown in Figure 1.2. The appealing feature of anti-k_{T} algorithm is the creation of circular jets. Moreover, this algorithm is less sensitive to underlying event and pile-up in an event. The Cambridge/Aachen algorithm does not use tracks p_{T} in order to determine which tracks are combined, and only uses the angular distances. This algorithm is mainly used in jet substructure studies [33].

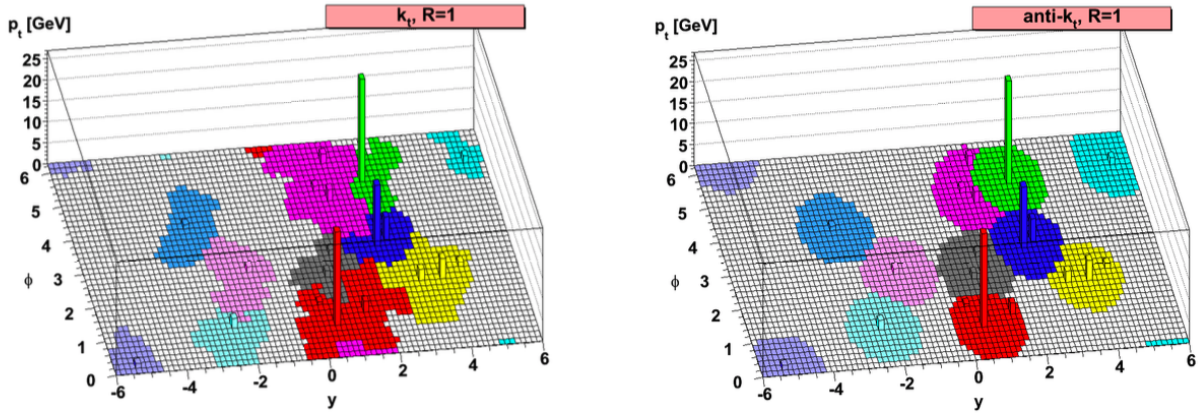

Figure 1.2: Jets generated using HERWIG [34, 35] Monte Carlo generator (see section 1.5)) and clustered with k_{T} and anti-k_{T} clustering algorithms [28].

1.4.2 Recombination schemes

When merging tracks into a jet with the clustering algorithms, one needs to specify how their 4-momenta will be added together. These algorithms are known as recombination schemes [27]. There are several of them; three examples will be described in this section. The most complete scheme is the E-scheme, which simply adds the four-momenta together. The p_{T}-scheme (E_{T}-scheme) is similar, but it first re-scales the energy (momentum) of the tracks to be equal to their momenta (energy), making the tracks effectively massless. The

rapidity, y, and the azimuthal angle, φ, of the tracks is then added as a p_{T}-weighted average

$$\begin{aligned} y_{ij} &= \frac{p_{\mathrm{T},i} y_i + p_{\mathrm{T},j} y_j}{p_{\mathrm{T},i} + p_{\mathrm{T},j}}, \\ \varphi_{ij} &= \frac{p_{\mathrm{T},i} \varphi_i + p_{\mathrm{T},j} \varphi_j}{p_{\mathrm{T},i} + p_{\mathrm{T},j}}. \end{aligned} \tag{1.5}$$

Whilst it is true that the E-scheme is the most complete recombination scheme, there are situations in which it is better to use other schemes. For example, while measuring the charged-particle jets at A Large Ion Collider Experiment (ALICE), neither the mass nor the track's energy is known during the jet finding stage. Assuming that jet mass or energy is not required during the analysis, a p_{T}-scheme offers a good approximation of the true jets.

1.5 Monte Carlo generators

Monte Carlo (MC) generators [1] are used to simulate the collision between particles at every stage of their evolution, which can be decomposed in the following way

- Initial State Radiation (ISR),
- hard processes,
- Final State Radiation (FSR),
- hadronisation,
- decay,
- underlying event.

The important part in dictating the types of events to simulate is the hard process, which defines the interaction between partons found in a hadron. The partons in the protons are described by a PDF and can collinearly radiate, creating a parton shower (ISR) before

entering the hard process. MC generators must connect these parton showers to both, the PDFs and the hard process. Similar radiation also happens after the hard process (FSR). Commonly used MC generators are PYTHIA [36, 37], Hadron Emission Reactions With Interfering Gluons (HERWIG) [34, 35] and Simulation for High Energy Reactions of PArticle (Sherpa) [38]. In the following sections, the main aspects of the MC generators will be described. In addition, a small selection of plugins and improvements relevant to the analysis described in this thesis will be discussed.

1.5.1 Parton showers

The ISR is defined as collinear radiation before the hard scattering and the FSR is defined as being after the hard scattering. They can be defined as $1 \to 2$ processes resulting in a tree-like structure. The FSR showers are treated as time-like interactions (where the invariant mass of the process, $m^2 = E^2 - \vec{p}^{\,2} \geq 0$), while the ISR are classified as being space-like interactions (where $m^2 = E^2 - \vec{p}^{\,2} \leq 0$). These generators are at leading-order (LO) and leading-log (LL) precision [36].

For example in the MC generators parton showers, a process where a quark and a gluon are emitted can be factorised [1] as

$$|\mathcal{M}_{qg}|^2 \mathrm{d}\Phi_{qg} \approx |\mathcal{M}_q|^2 \mathrm{d}\Phi_q \frac{\alpha_s}{2\pi} P_{q,qg}(z) \mathrm{d}z \frac{\mathrm{d}\phi}{2\pi} \frac{\mathrm{d}\theta^2}{\theta^2}, \tag{1.6}$$

where $|\mathcal{M}_{qg}|^2 \mathrm{d}\Phi_{qg}$ and $|\mathcal{M}_q|^2 \mathrm{d}\Phi_q$ are the amplitude and phase space where a quark and a gluon and only a quark are emitted, respectively, $z = \frac{E_q}{E_q + E_g}$ is the energy fraction carried by the quark, and ϕ is the azimuthal of the splitting plane, $P_{q,qg}(z) = \frac{4}{3}\frac{1+z^2}{1-z}$ is one of the Altarelli-Parisi splitting kernel [25], which describes the probability to create a quark and a gluon. Another example of a splitting kernel is production of two gluons, $P_{g,gg}(z) = 3\frac{(1-z(1-z))^2}{z(1-z)}$. The probabilities are divergent for collinear ($\theta \to 0$) or soft ($z \to 0, 1$)

emission which is specific for parton showers. To govern these regions the Sudakov form factors [39], which are the probabilities of no gluon radiation, are used to make the final probability finite.

PYTHIA and Sherpa use p_T ordered showers, while HERWIG uses angular ordered showers. In the latest versions, the MC generators use dipole showers, which treats the splitting as parton pairs rather than a single parton emitting soft parton.

LHAPDF In addition, the ISR probability must be connected to a PDF as defined in Sec. 1.3. The main library where these PDFs can be found is the Les Houches Accord Parton Distribution Function (LHAPDF) [40] with an interpolator used to generalise PDFs taken from discreet measurements. An example of a general purpose PDF set is CT10 NLO [41], which is shown in Figure 1.3.

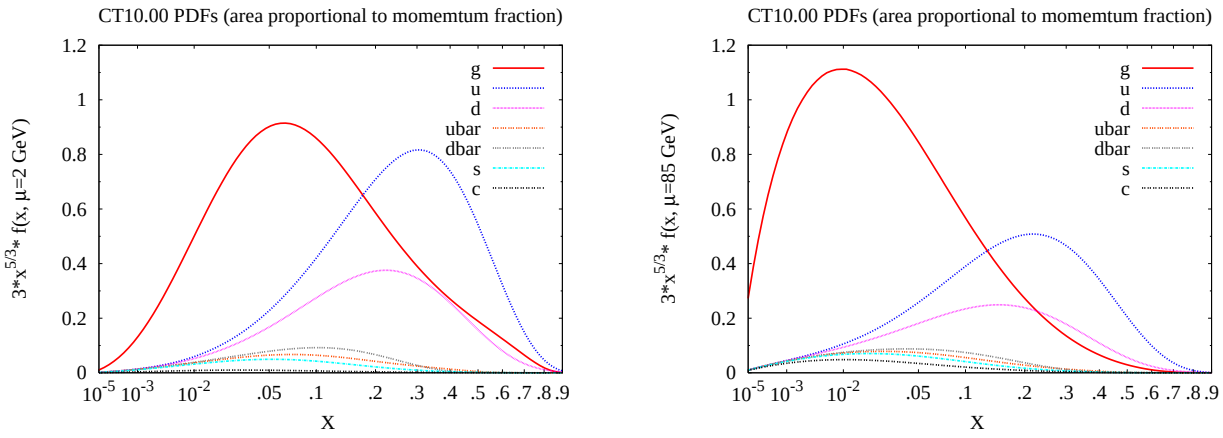

Figure 1.3: The CT10 NLO parton distribution functions as a function of parton momentum fraction x for different quark flavours and gluon with factorisation scale cut $\mu_F = 2$ GeV (left) and $\mu_F = 85$ GeV (right) [41, 42].

1.5.2 Hard processes

The MC generators are used to describe hard (HF production, jets, etc.) and soft processes (ISR and FSR), with a factorisation scale, μ_F, used to define energy scale to separate them. PYTHIA contains a large number of hard processes, mainly $2 \to 1$, $2 \to 2$ and some $2 \to 3$. In order to give parton shower calculations similar precision to the matrix element calculation, a Matrix Element Corrections (MEC) are implemented to correct the difference. This will allow a better description of high angle production, bringing the description of jet emission to LO accuracy [1, 37]. To achieve higher than LO precision, one must use external programs to evaluate the matrix elements at NLO precision, and then connect these tools to the MC generators via an interface.

1.5.2.1 NLO matching

The NLO matching combines the matrix elements precision at large momentum scales (hard processes) and parton showers at low momentum scales (soft emission). Pure usage of matrix elements will not describe jet structure reasonably, so it is desired to combine them with the parton showers. The MC generators contain an interface, for example the Les Houches Event File (LHEF), to connect the external hard scattering event. While connecting, one must treat the double-counting between the hard process and shower emission, otherwise it would leading to an overestimation of the cross-section. The two main external NLO generators are the POsitive Weight Hardest Emission Generator (POWHEG) [43, 44] and MC@NLO [45]. The choice between them is process dependent as each one provides a better description than the other in particular cases, for this analysis POWHEG is used.

POWHEG Several POWHEG methods are implemented in the POWHEG-BOX [46] tool. Since it contains its own set of Sudakov form factors, it can run entirely independently from

the MC generators. POWHEG is then connected to the MC generators using LHEF [47] interface. As POWHEG and PYTHIA define number of parameters differently, PYTHIA contains number of vetoes which prevents addition double-counting.

There are two POWHEG processes of interest to the analyses in this thesis. First, the Heavy-Flavour Hadroproduction (POWHEG-hvq) [48], which implements the NLO calculation for heavy-flavour pair production ($c\bar{c}$, $b\bar{b}$, and $t\bar{t}$) to describe processes such as flavour excitation and gluon splitting. Second, the (POWHEG-dijet) [49] for jet pair production, as dijet production is the most frequent process in hadronic collisions.

MC@NLO tool uses a different approach to match with parton showers, which allows for some events to have negative weight; this does not mean the total cross-section is negative. Due to its construction, MC@NLO must be incorporated within the MC generator.

1.5.3 Hadronisation

Hadronisation is a process during which coloured partons are transformed into colour-less hadrons [1]. Hadronisation is a non-perturbative process at a scale of $Q_{had} \sim \Lambda_{QCD}$, which should follow the perturbative region of showering algorithms. The two main models are the Lund String model [37] implemented in PYTHIA, and the cluster model [34] implemented in HERWIG and Sherpa.

Lund string model String models use a linear potential between two quarks as $V = kx$, where the $k \sim 1$ GeV/fm is the string tension, similar to equation (1.2). When the quarks move apart, the potential rises, the string breaks up and creates a new $q\bar{q}$ pair. In the PYTHIA Lund string model, the flavour composition after breakup is assumed as $u : d : s : c \approx 1 : 1 : 0.3 : 10^{-11}$. The gluons are treated as "kinks" on the string carrying en-

ergy and momentum. In a string model, the gluons are represented by two strings as they carry colour-anticolour, which results in gluon-to-quark colour end-points ratio equal to two. This is an approximation of the ratio of Casimir colour factors $C_A/C_F = \frac{9}{4}$ [37], which are connected to the probability of gluon emission from a gluon over the probability of gluon emission from a quark. Baryon formation is implemented by allowing the string to break into diquark pairs. An alternative approach for baryon production is also implemented by allowing more complex string topologies known as "junctions".

Cluster model Another method of hadronisation is implemented in HERWIG and Sherpa. At the end of the parton shower, any remaining gluons are forced to split into $q\bar{q}$ pairs. Next, the $q\bar{q}$ pairs form colour singlets that are called clusters. Some extremely heavy clusters are then split by creating additional quark pairs (u,d,s) from the vacuum. Each of the two new clusters contains one quark from the original cluster. Finally, clusters decay into two hadrons conserving the flavour and spin structure [34].

1.5.4 Decay

Many of the so-called “primary" hadrons created during the hadronisation process are unstable and so decay further. The MC generators contain a large sets of decay probabilities called branching ratios. The branching ratios for particles containing u,d and s quarks are very well known, and particles with c and b are reasonably well known and are collected in [1].

Dedicated decay packages In some cases, it is convenient to use an external decay packages. An example case where this is true is for B-meson decays. The Monte Carlo Generator for B-Physics (EvtGen) [50] is a main dedicated MC Generator for B Physics.

It includes effects such as oscillation of $B - \bar{B}$ mesons before decay, CP-violation effect, and angular correlations of decay products. The standard MC generators do not include all of these features, and so EvtGen can be connected in order to improve the descriptions of B meson decays. Its effect on the beauty cross-section is around 10% in the analysis described in this thesis.

1.5.5 Underlying event

An Underlying Event (UE) [1] is the contribution from processes beyond the original hard scattering and parton showers. These processes can either be another hard parton scatterings known as Multiple Parton Interaction (MPI), that produce other back-to-back jets within the event, or soft interactions, which are created by the flow of colours arising from hadron breakup. The hard processes are fairly rare in comparison to the soft processes. The MPI are then interleaved with the ISR and FSR showers of the original hard scattering within the MC generators.

Beam remnants and colour reconnection As the interacting partons are not colour neutral, it can be expected that there will be a colour flow between different MPI via the beam remnants [1]. The effect is more dominant at hadron colliders than at lepton colliders. Each of the MC generators contain models to describe such behaviour in the leading colour approximation which allows simple topologies of how the quarks and gluons are connected. There is ongoing effort to include higher order colour parton topologies (Y-junction shaped) in so-called beyond the leading colour approximation. An example of simple and Y-junction colour space topologies are shown in Figure 1.4. The implementation of beyond the leading colour approximation in Pythia is discussed further in [51].

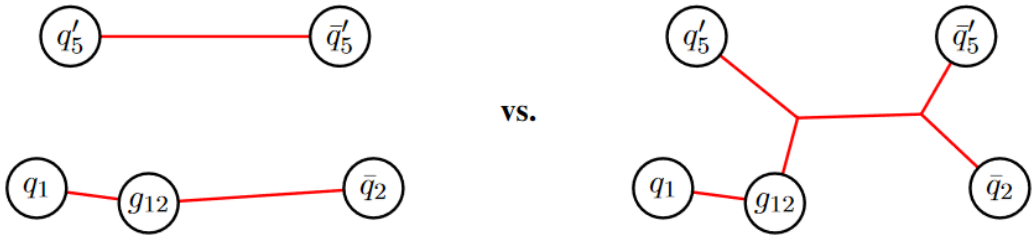

Figure 1.4: Different topologies in colour space in connecting multi-parton states. On the left the leading colour string topology, on the right a beyond the leading colour Y-junction topology [51].

1.6 Nuclear matter phase diagram

Since hadrons have a composite structure, it is speculated that there could be a deconfined state under certain conditions [52]. The nuclear matter phase diagram, as a function of temperature T and baryo-chemical potential μ_B (related to density), is shown in Figure 1.5. For systems in equilibrium, the μ_B denotes an energy change when the baryon number $B = N_B - N_{\bar{B}}$ changes by one. The baryonic matter (nucleus) is degenerate at $T = 0$ resulting in a nuclear density corresponding to $\mu_0 = 922$ MeV. Nuclear matter undergoes a phase transition under extreme temperature and/or baryo-chemical potential (density) into a new state of matter, composed of deconfined quarks and gluons, the Quark–Gluon Plasma (QGP). At larger values of μ_B , there is a first-order phase transition between hadronic matter and QGP. However, at a low baryo-chemical potential, there is a crossover between these two states that happens around a critical temperature T_c, which is estimated by lattice QCD to be around 175 ± 10 MeV [53]. This indicates a critical point where the first-order transition changes to a crossover. This critical point is still yet to be experimentally found, and is one of the main interests of the STAR experiment at the Relativistic Heavy Ion Collider (RHIC) [54].

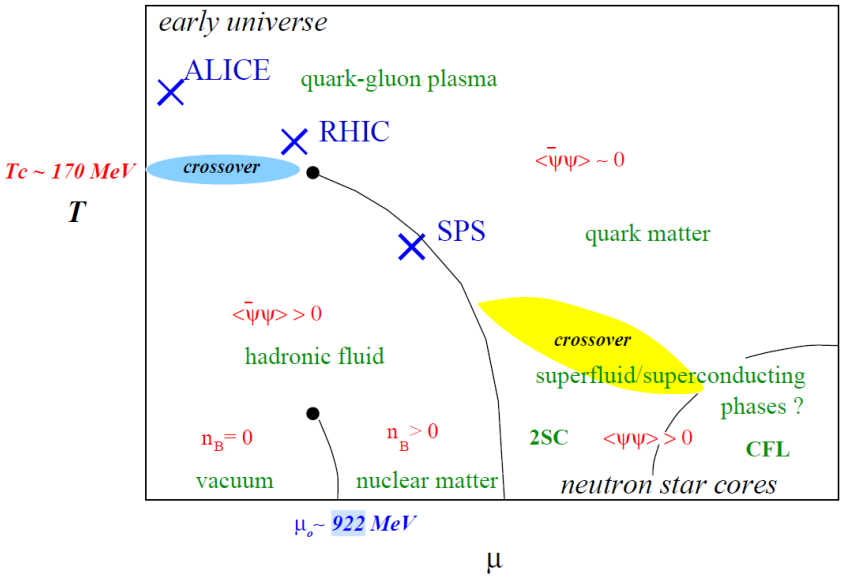

Figure 1.5: The nuclear matter phase diagram as a function of temperature T and baryo-chemical potential μ_B [52].

1.6.1 Evolution of heavy ion collision

In heavy-ion collisions, the system undergoes dynamical evolution which can be divided into several phases [55] as shown in Figure 1.6. Hard probes (jets, heavy-flavour hadrons, high

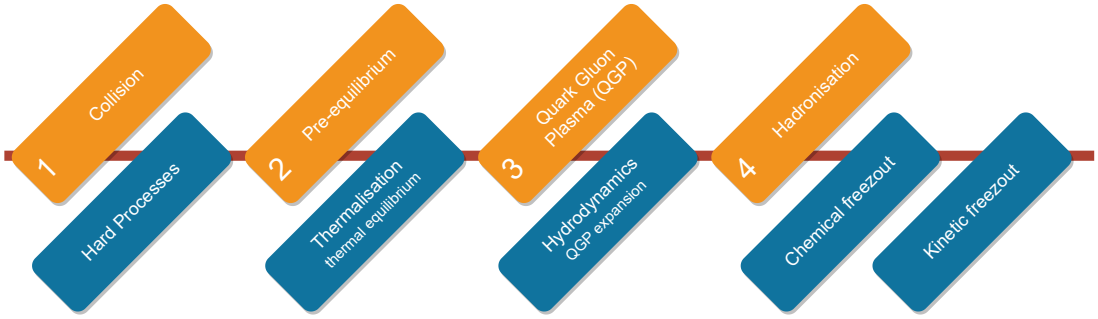

Figure 1.6: Evolution of a heavy ion collision, including the key stages in orange, and the processes which occur at each step, in blue.

p_{T} hadrons, $\mathrm{W}^{\pm}$, Z^{0}) are created during hard scattering in the initial stage of the collision. Their production can be described by pQCD as discussed in section 1.3. The QGP is formed at around a time of 1 fm/c [56] after the initial collision and the later evolution can be described by a hydrodynamical approach. This suggests that the system is already in a thermal equilibrium (the thermalisation in Figure 1.6). The QGP further expands, behaving as a low viscosity fluid until the temperature drops to around $T_c \simeq 170$ MeV where a phase transition into hadrons occurs - the hadronisation. The hadrons can still inelastically interact to create different hadrons until the chemical freeze-out, which occurs at a temperature T_{ch}. After this point, the particle abundance is conserved. Lastly, kinematic freeze-out occurs at temperature T_{fo} where hadrons stop interacting elastically, and particle momenta are conserved until they reach the detector. As the hard probes were formed before the QGP formation, they are the ideal probe of this medium. A space-time evolution of a nuclear collision with depicted phases is shown in Figure 1.7.

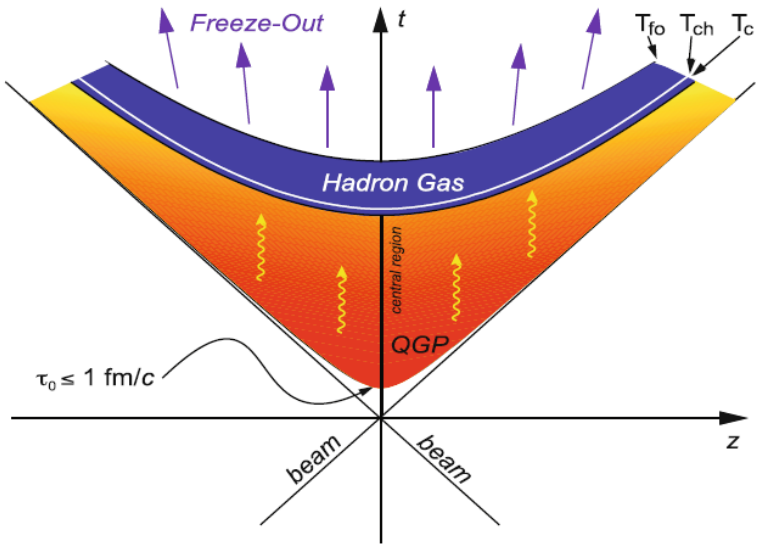

Figure 1.7: The space(z)–time(t) evolution of nuclear collision. The QGP is formed around $\tau_0 \simeq 1$ fm/c, hadronisation occurs around $T_c \simeq 170$ MeV, chemical freeze-out at temperature T_{ch} and kinetic freeze-out at T_{fo} [56].

One can ask a question how can experimentalists quantify the baryo-chemical potential and temperature of the collisions. The higher the collision energy, the lower the effect from the baryonic number of the original collided particles in the central rapidity. The smaller baryon–anti-baryon difference results in probing lower values of μ_B. Moreover, performing a heavy-ion collision will produce a fireball, where the mid-rapidity region will have net baryon density $n_B \approx 0$, while forward rapidities will be baryon rich corresponding to the original direction of the colliding baryons. Changing the collision energy and exploring different rapidity regions allows for probing the QCD phase diagram at different values of baryo-chemical potential [52]. To measure a temperature, one can use different hard probe bound states as an internal thermometer to measure the QGP temperature, as different hadrons dissolve at different temperatures because of their different binding energy (or size). The important variable for such studies is the Debye radius r_D [57], an inverse value of the Debye mass m_D, to leading order thermal pQCD precision defined as

$$r_D \equiv \frac{1}{m_D} = \frac{1}{\sqrt{4\pi\alpha_s}T}, \tag{1.7}$$

where α_s is the strong coupling constant and T is the medium temperature. This radius is an essential variable since when r_D is smaller than the physical size of a bound state, the colour charge is screened, resulting in deconfinement [58]. That means every bound state larger than r_D will be dissolved. This phenomenon is called the Debye screening of colour charge.

1.7 Parton energy loss in QGP matter

A coloured parton traversing through the coloured QGP interacts with it and looses energy. The total parton energy loss [59, 60] in a medium is defined as the sum of the collisional and radiative energy loss $\Delta E = \Delta E_{coll} + \Delta E_{rad}$. The average collisional energy loss per medium

length L for light (q) and heavy (Q) quarks and gluons (g) is estimated [59, 60] as

$$\begin{aligned} \Delta E_{coll}|_{q,g} &= \frac{1}{4} C_R \alpha_s m_D^2 L \ln\left(\frac{ET}{m_D^2}\right), \\ \Delta E_{coll}|_{Q} &= \Delta E_{coll}|_{q} + \frac{2}{9} C_R \pi \alpha_s^2 T^2 L \ln\left(\frac{ET}{M^2}\right), \end{aligned} \tag{1.8}$$

where $C_R = 4/3(3)$ is the quark (gluon) colour factor, α_s is the strong coupling constant, m_D is the Debye mass, E is the energy of incident parton, M is the heavy-quark mass, and T is the medium temperature. The radiative energy loss occurs via emission of gluons. For a medium larger than the mean free path of a particle in it, $L >> \lambda$ (Landau-Pomeranchuk-Migdal regime), the radiative energy loss can be expressed as

$$\Delta E_{rad} \approx C_R \alpha_s \frac{m_D^2 L^2}{\lambda} \begin{cases} 1 & (\omega < \omega_c) \\ \ln\left(\frac{E\lambda}{m_D^2 L^2}\right) & (\omega > \omega_c) \end{cases}, \tag{1.9}$$

where $\lambda = \frac{1}{\rho\sigma}$ is the mean free path defined as an inverse product of medium density ρ and integrated cross-section of the particle-medium interaction σ, ω is the emitted gluon energy, and $\omega_c = \frac{1}{2}\frac{m_D^2 L^2}{\lambda}$ is the characteristic gluonstrahlung energy, which distinguishes between hard and soft gluon radiation. The main difference from the collisional loss is the L^2 dependence, so the radiative energy loss will be dominant in large mediums.

However, due to kinematic restraints, the radiative loss changes for heavy quarks. The probability of a gluon emission in small angles, $\theta << 1$, can be approximated [61] as

$$\mathrm{d}\sigma \sim \frac{\theta^2 \mathrm{d}\theta^2}{(\theta^2 + \frac{M^2}{E^2})^2} \frac{\mathrm{d}\omega}{\omega}, \tag{1.10}$$

where θ is the angle between the quark and radiated gluon, M is the quark mass, E is the quark energy, and ω is the emitted gluon energy. For light quarks, the probability is logarithmic, whereas for heavy quarks the probability is no longer logarithmic. This leads to a suppression in angles smaller than $\theta < \frac{M}{E}$ known as the dead-cone effect [61, 62]. The energy loss of partons will be then ordered as

$$\Delta E_{rad}(g) > E_{rad}(u, d, s) > E_{rad}(c) > E_{rad}(b) >> E_{coll}. \tag{1.11}$$

1.7.1 Experimental observation of parton energy loss

In this section, several observables which hint at the existence of in-medium parton energy loss will be shown. Namely, the nuclear modification factor of charged hadrons, the nuclear modification factor of the J/ψ, the c quark quarkonium state, the jet quenching and the medium modified fragmentation function will be discussed.

Nuclear Modification Factor Parton energy loss in a medium can be quantified by comparing particle momentum spectra in heavy ion collisions to a vacuum case corresponding to pp collisions. The nuclear modification factor, R_{AA}, [63] is defined as

$$R_{AA}\left(p_T\right) = \frac{1}{\langle N_{coll}\rangle} \frac{\frac{\mathrm{d}N_{AA}}{\mathrm{d}y}\left(p_T\right)}{\frac{\mathrm{d}N_{pp}}{\mathrm{d}y}\left(p_T\right)}, \tag{1.12}$$

where $\frac{\mathrm{d}N_{AA}}{\mathrm{d}y}$ is the particle invariant yield in AA collisions, $\frac{\mathrm{d}N_{pp}}{\mathrm{d}y}$ in pp collisions, and $\langle N_{coll}\rangle$ is the mean number of binary nucleon-nucleon collisions within heavy ion collisions at given centrality (for definition of centrality see appendix A.1.5). If a strongly-interacting medium is created, it would be expected that the measured R_{AA} will be less than unity. The nuclear modification factor R_{AA} in most central collisions measured by ALICE, STAR and PHENIX is shown in Figure 1.8 (left). Measurements suggest a large suppression in different collision systems and collision energies. The peak around $p_{\mathrm{T}} = 2 - 3$ GeV/c is created by the interplay between the nuclear shadowing, Cronin effect, and the partonic energy loss [64]. The suppression seems to be larger at LHC energies in comparison to RHIC energies which would suggest a denser medium and thus higher energy loss of partons in the medium. Moreover, the suppression is becoming smaller with increased hadron's momentum. A nuclear modification factor of D^0 mesons, which contain a single c quark, compared to values obtained from all charged particles, as measured by the Compact Muon Solenoid (CMS) experiment, is shown in Figure 1.8 (right). Both measurements of R_{AA} are consistent above $p_{\mathrm{T}} > 4$ GeV/c with a hint of smaller suppression of D^0 with respect to charged hadrons in a region $p_{\mathrm{T}} < 4$ GeV/c.

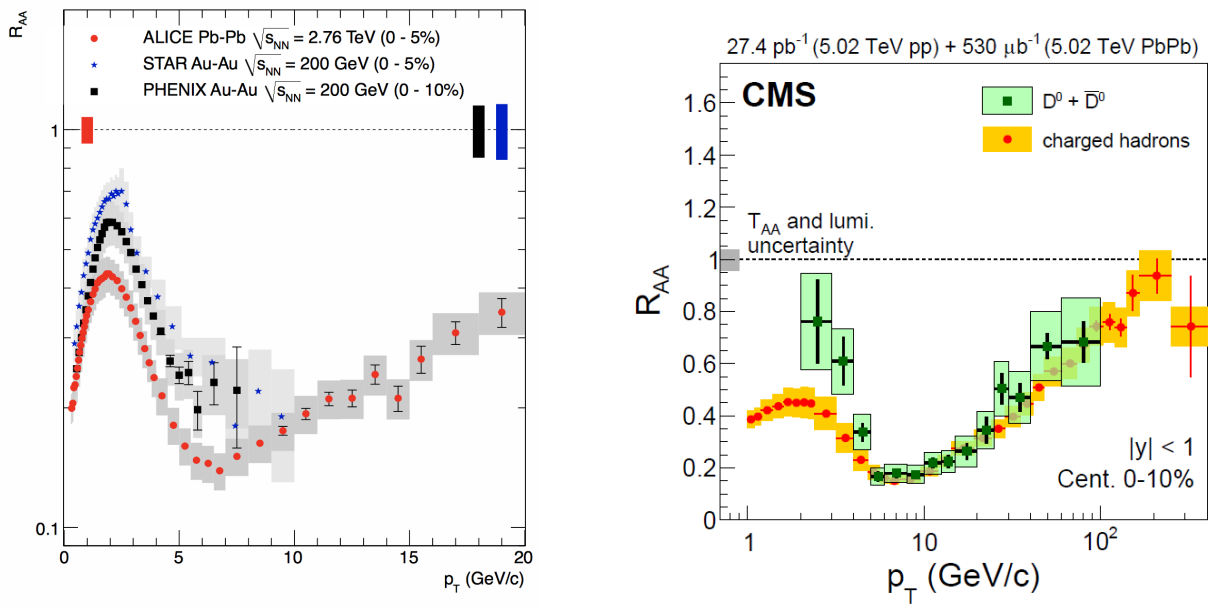

Figure 1.8: Left: Nuclear modification factor of charged hadrons measured by ALICE in Pb–Pb collisions at $\sqrt{s_{\mathrm{NN}}}$ = 2.76 TeV and by STAR and PHENIX in Au+Au collisions at $\sqrt{s_{\mathrm{NN}}}$ = 200 GeV. Global errors are the uncertainty of a number of binary collisions for their respective experiments [63]. Right: Nuclear modification factor of D^0 mesons in the 0-10% centrality range compared to the nuclear modification factor of charged hadrons, as measured by the CMS experiment in Pb–Pb collisions at $\sqrt{s_{\mathrm{NN}}}$ = 5.02 TeV [65].

Quarkonia suppression Due to the Debye screening introduced in chapter 1.6, it is expected that the J/ψ particle, which is a $c\bar{c}$ bound state, and $\Upsilon(1\mathrm{S})$ and $\Upsilon(2\mathrm{S})$, which are $b\bar{b}$ bound states, will be particularly sensitive to the QGP medium. The nuclear modification factor of J/ψ measured by the ALICE and PHENIX experiments is shown in Figure 1.9 (left). The suppression of J/ψ production increases as a function of the number of participant nucleons in the collision, which can be related to a higher system temperature. Surprisingly the suppression is more pronounced at the lower collision energy probed by PHENIX than in the ALICE experiment. This can be explained by the increased production of charm quarks at LHC energies resulting in a larger (re)combination effect, in which more J/ψ particles are formed during the chemical freeze-out of the QGP [66]. The nuclear modification factors of

Υ(1S) and Υ(2S) measured by CMS are shown in Figure 1.9 (right). Similarly to the J/ψ, an increase in the suppression for the Υ(1S) as a function of the number of participant nucleons in the collision is observed. The Υ(2S) state shows a larger suppression compared to Υ(1S) which is given by a larger bound state size and thus lower binding energy, as predicted.

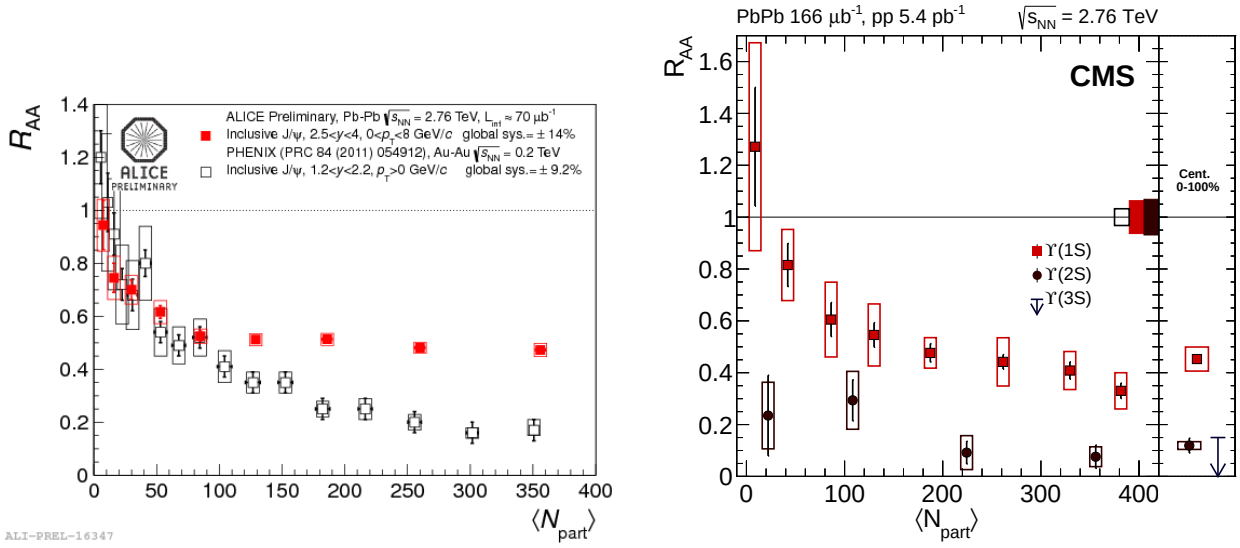

Figure 1.9: Left: Centrality dependence of nuclear modification factor R_{AA} of J/ψ measured by ALICE in Pb–Pb collisions at $\sqrt{s_{\mathrm{NN}}}$ = 2.76 TeV and PHENIX in Au+Au collisions at $\sqrt{s_{\mathrm{NN}}}$ = 200 GeV [67]. Right: Centrality dependence of nuclear modification factor R_{AA} of Υ(1S) and Υ(2S) measured by CMS in in Pb–Pb collisions at $\sqrt{s_{\mathrm{NN}}}$ = 2.76 TeV [68].

Jet quenching Since jets are created back-to-back in dijet events, one can study the effects that the medium has on this phenomenon. If a $q\bar{q}$ pair is created at the edge of the QGP, one jet leaves this medium immediately, almost unmodified, while the other will traverse through the medium, losing energy, and eventually can be completely quenched. A schematic diagram of this effect is shown in Figure 1.10. The effect can be measured by studying the azimuthal dependence on two-hadron correlations [69], as seen in Figure 1.11. The away-side peak in central Pb–Pb collisions is suppressed compared to that observed in pp collisions. On the other hand, the near-side peak exhibits an enhancement in central Pb–Pb collisions. This

can be explained in multiple ways. First, the fragmentation functions in the medium are softened as hadrons carry a smaller momentum fraction from the original parton. Therefore, hadrons at a given p_{T} originate from a larger parton momentum, resulting in enhancement. Secondly, there can be a different fraction of quark jets to gluon jets due to the coupling with the medium. Lastly, there can be a bias in p_{T} due to the trigger particle selection.

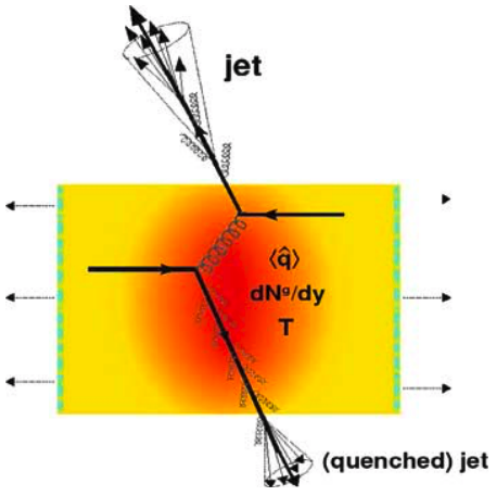

Figure 1.10: Jet quenching in a QGP. One jet leaves the medium almost unmodified while the other needs to traverse through the medium loses energy before leaving [57].

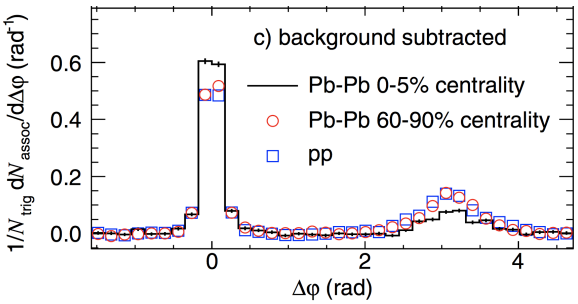

Figure 1.11: Corrected per-trigger two-hadron correlated yield in Pb-Pb and pp collisions measured by ALICE experiment [69].

Another observable to look at is the jet energy imbalance [70], defined as

$$A_J = \frac{E_{\mathrm{T},1} - E_{\mathrm{T},2}}{E_{\mathrm{T},1} + E_{\mathrm{T},2}}, \tag{1.13}$$

where $E_{\mathrm{T},X}$ is the transverse energy of the two most energetic jets in an event. In order to reduce the contribution from multi-jet events it is required that the jets are separated by more than $\Delta\phi = \frac{\pi}{2}$ in azimuthal angle. It is expected that dijet events have A_J around zero, and energy loss in the QGP can create an imbalance. The jet energy imbalance A_J and azimuthal separation $\Delta\phi$ in different centrality bins measured by the A Toroidal LHC Apparatus (ATLAS) collaboration in pp and Pb–Pb collisions [70] are shown in Figure 1.12. The

figure also shows PYTHIA events superimposed to HIJING events which are in agreement with the pp measurement as expected. The measurements from pp collisions are consistent with those from peripheral Pb-Pb collisions, within uncertainties. Increasing the centrality indicates a higher asymmetry in dijet production. For most central collisions there is a visible peak in the imbalance around $A_J = 0.5$ showing a large modification of the Pb–Pb jet energy distribution. The azimuthal separation $\Delta\phi$ show that the jets are primarily created back-to-back. In larger centrality intervals there is an increase in a rate in larger angles of the recoil jets. The difference in imbalance and azimuthal separation in Pb–Pb can be explained by QGP-induced jet QCD energy loss.

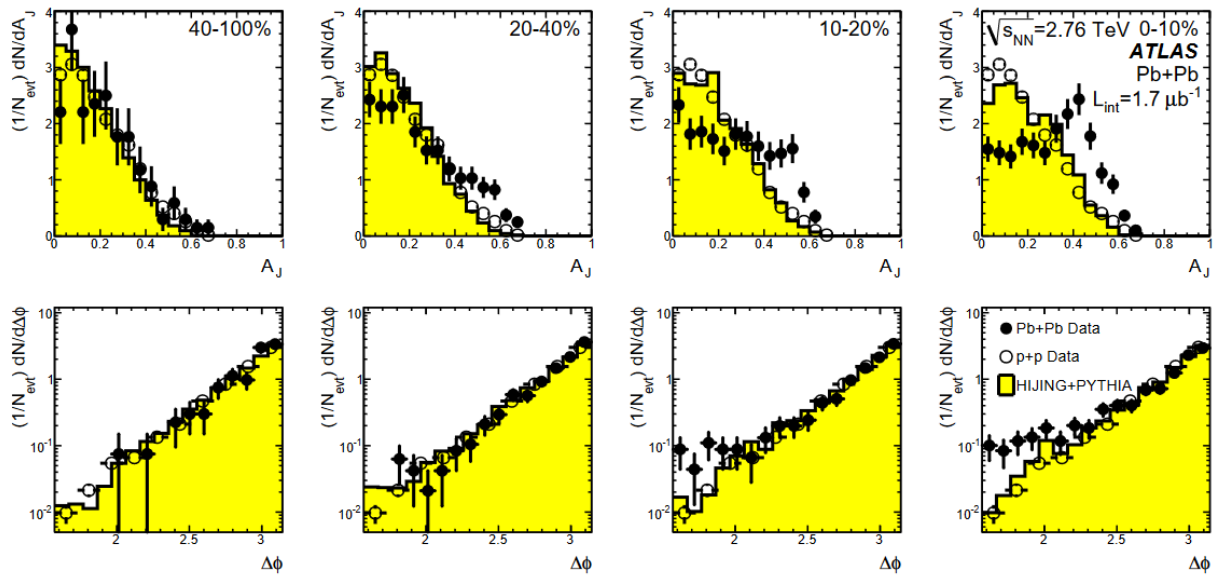

Figure 1.12: The dijet energy imbalance A_J and azimuthal separation $\Delta\phi$ for different centrality bins in pp and Pb–Pb collisions at $\sqrt{s_{\mathrm{NN}}} = 2.76$ TeV measured by the ATLAS experiment [70] and compared to PYTHIA + HIJING.

Jet fragmentation The fragmentation function is defined [71] as the charged-track distribution

$$D = \frac{1}{N^{\text{jet}}} \frac{\mathrm{d}n_{\text{ch}}}{\mathrm{d}z}, \tag{1.14}$$

where $z = p_{\text{T}} \cos(\Delta R)/p_{\text{T,jet}}$ is the charged-track (n_{ch}) longitudinal momentum fraction and ΔR is the track-jet distance in pseudorapidity-azimuth plane. The ratio $R_{D(z)}$ of fragmentation functions in Pb–Pb and pp collisions for different $p_{\text{T,jet}}$ and centrality bins measured by the ATLAS experiment are shown in Figure 1.13. In the most central collisions $(0-10\%)$, the modification of fragmentation functions is as high as 70%. There is an enhancement of particles in low and high z regions, and a depletion in intermediate z of 20%. The deviation from unity is smaller as the centrality bin of the measurement increases. In semi-central collisions $(30-40\%)$, the modification is less than 30 %. This supports the statement that medium effects are expected to be smaller in this region.

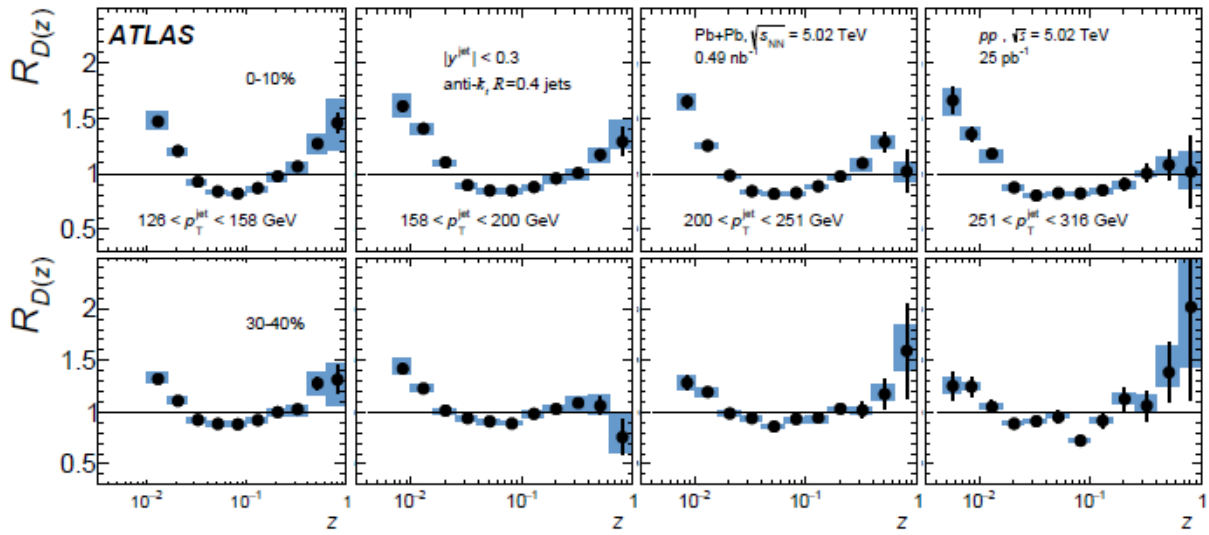

Figure 1.13: The ratio R of fragmentation functions in Pb–Pb and pp collisions at $\sqrt{s_{\text{NN}}} = 5.02$ TeV for different $p_{\text{T,jet}}$ and centrality bins measured by the ATLAS experiment [71].

Chapter Two

Introduction to the Large Hadron Collider and the ALICE experiment

2.1 European Organisation for Nuclear Research

The first meeting of the The European Organization for Nuclear Research (CERN) council took place at UNESCO in 1952 and was fully ratified by the 12 founding members in 1954. The construction of the Meyrin site on the border of France and Switzerland began in 1954. The first synchrocyclotron went into operation in 1957, reaching an energy of 600 MeV and remained in operation for 33 years. For decades CERN has pioneered new physics. Today, it accommodates the most powerful accelerator, the LHC, providing a collisional energy $\sqrt{s}$ = 13 TeV for pp and $\sqrt{s_{\mathrm{NN}}}$ = 5.02 TeV for Pb–Pb collisions [72].

2.2 The accelerator complex

A schematic diagram of the CERN accelerator complex is shown in Figure 2.1. The latest

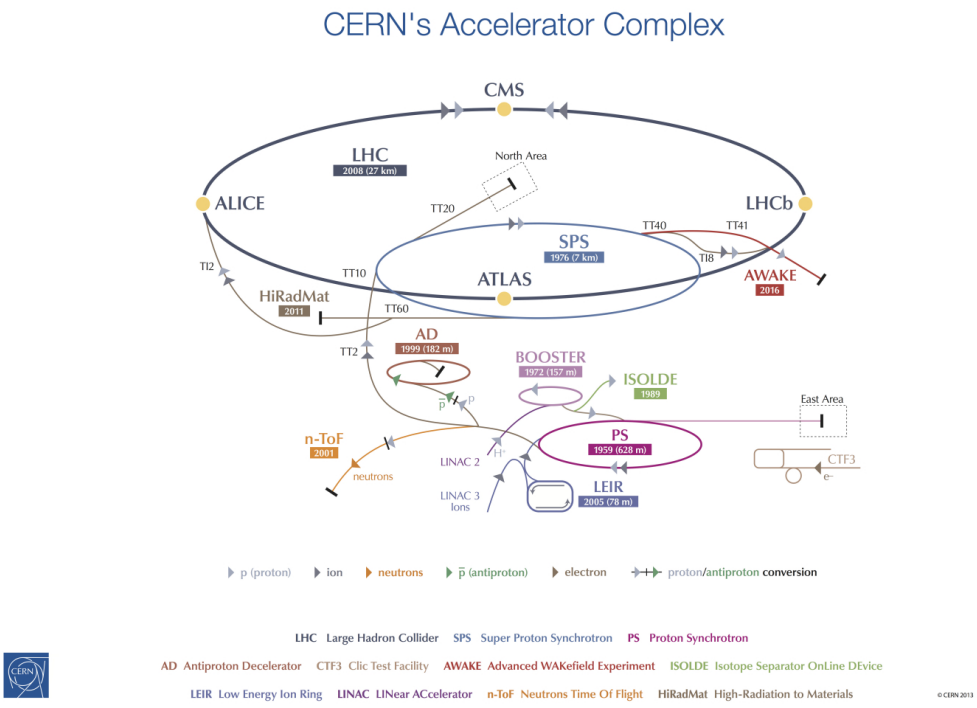

Figure 2.1: A schematic diagram of CERN accelerator complex [73].

collider, the LHC (2008), is the largest human-built machine in the world. The older accelerators became pre-stages for the newer ones. A hydrogen bottle as a source of protons is used. The hydrogen is stripped of an electron in the duoplasmatron, creating a plasma of protons that feeds the linear accelerator LINAC 2. Protons are accelerated to 50 MeV before being injected into the Proton Synchrotron Booster (PSB), where they reach an energy of 1.4 GeV before the injection into the Proton Synchrotron (PS). The PS was built in 1959 and it was the first accelerator to use strong focusing for beam stabilisation, reaching a beam energy of 28 GeV, surpassing three times the energy of accelerators at that time. Ions are generated using an electron-cyclotron-resonance ion source which partially strips lead ions to around Pb^{29+}. Only the Pb^{29+} ions enter the LINAC 3, which accelerate them up to 4.2 MeV. They are stripped of additional electrons creating Pb^{54+} ions and enter Low Energy Ion Ring (LEIR) accelerator, reaching an energy of 72.2 MeV before feeding the PS. A PS

accelerates protons to 25 GeV and lead ions to 5.9 GeV, removes the remaining electrons in the lead, and injects them into the Super Synchrotron (SPS). The SPS accelerates protons up to 450 GeV and lead up to 177 GeV. Finally, the beam is injected into the LHC, which accelerates protons up to 6.5 TeV and lead ion up to 2.51 TeV. Just a tiny fraction of accelerated protons (less than 0.1 %) is used by the LHC, as shown in Figure 2.2. Once the LHC is filled, it stores the beam and performs collisions for a few hours before the beam deteriorates and require a new injection. While not being used by the LHC, the accelerated beams are used by other experiments placed around several CERN sites in the area. The usage includes other High Energy Physics (HEP) experiment and the generation of medical-use isotopes, neutron beams, neutrino beams and antimatter.

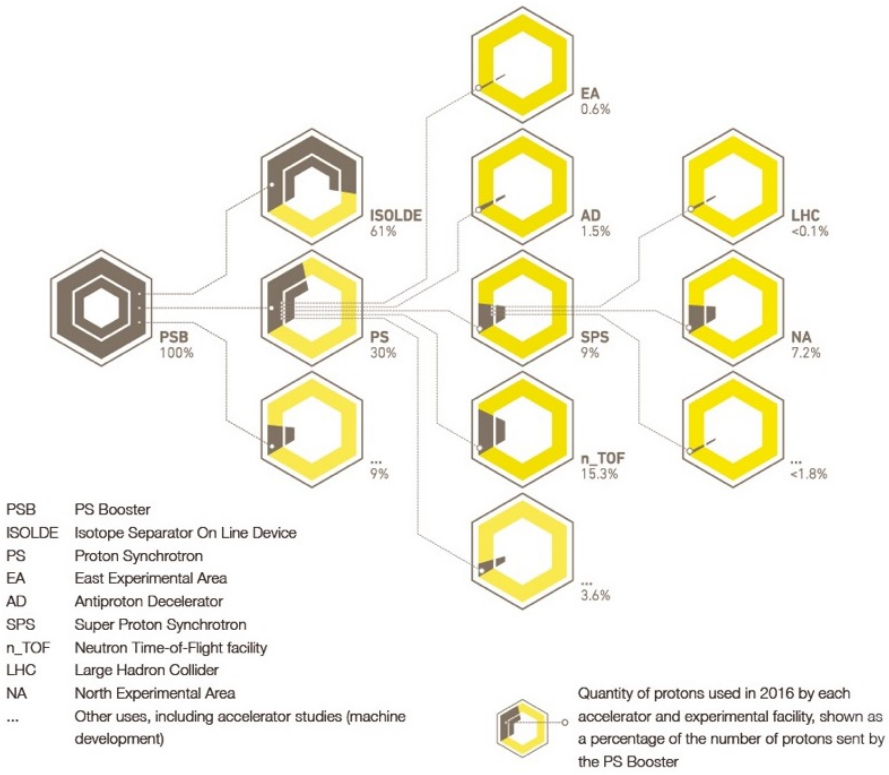

Figure 2.2: The distribution of accelerated protons between CERN facilities [74].

2.3 The Large Hadron Collider

The LHC is a 27 km ring in circumference, symmetrically divided into eight access shaft - points. Point 1, which is next to the Meyrin site, houses the ATLAS experiment. Moving clockwise in point 2 is ALICE, point 5 CMS, and point 8 Large Hadron Collider Beauty (LHCb). The beam crossings are only in these points. SPS injection is in point 2 for clockwise and point 8 for anticlockwise beam. Point 4 contains accelerating cavities, point 6 a beam-dump, points 3 and 7 focusing elements.

2.3.1 Acceleration and power

The LHC has two separate pipes - one for the clockwise and one for the anticlockwise beam. The acceleration (see chapters 4 and 6 in [75]) is done using radio-frequency cavities in point 4. There are eight cavities per beam, each operating at 2 MV with 400 MHz frequency, and protons gain 485 keV per turn. Multiple orbits are required to accelerate the proton beam from the SPS collisional energy of $\sqrt{s}$ = 450 GeV ($\sqrt{s_{\mathrm{NN}}}$ = 177 GeV for Pb–Pb ions) to $\sqrt{s}$ = 13 TeV ($\sqrt{s_{\mathrm{NN}}}$ = 5.02 TeV). The beam is divided into 35640 buckets based on the 400 MHz frequency, which can be occupied by protons/ions. Less than a tenth of buckets are occupied creating 2808 filled buckets (bunches) with a 25 ns spacing. Feedback from the accelerated particles is processed, and it serves as the LHC central 40 MHz clock for the experiments. As the velocity of particles changes during acceleration also the main distributed clock changes. Multiple high-power klystrons, one per cavity, generate microwave power to feed the cavities. A relatively small power of 275 kW is needed per beam acceleration. However, a much larger power is needed to drive this field. Each klystron delivers 300 kW of microwave power per cavity, with a total power of 4.8 MW for 16 klystrons [76]. The LHC klystron is shown in Figure 2.3 (left) and cavities in Figure 2.3 (right).

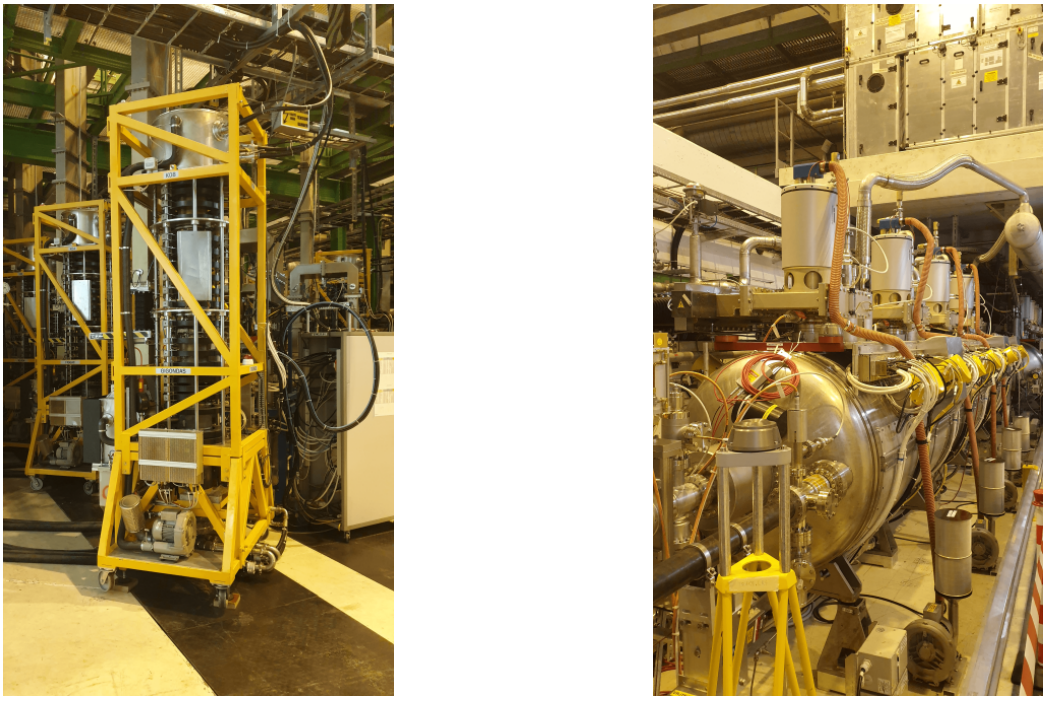

Figure 2.3: Left: One of the LHC klystrons generating microwave power for cavity. Right: One segment containing four LHC radio-frequency cavities.

2.3.2 Magnets

The LHC is not a perfect circle; around each interaction point, approximately 100 m long straight sections are used to prepare the beam for interaction at experiment points. They contain collimators and inner triplets for the beam focusing and septa and kickers if there is an injection/ejection point. Moreover, there are also powering supplies for the dipoles section. The ring is a "sandwich" of dipoles for bending and higher multipoles for focusing (see chapter 3 in [75]).

Dipoles Dipole magnets are used in guiding the beam between accelerators and keeping the beam on a circular trajectory of storage-ring type accelerators. 1232 dipoles are needed to create a circular guide for the LHC beam. Each dipole is 15 metres long, weighs 27 tonnes, and the nominal magnetic field is 8.33 T by a current of 11.85 A, and curves the beam by

5.1 mrad. The magnets are superconducting, cooled by supra-fluid helium at a temperature of 1.9 K. A beam loses approximately 6.9 keV (at 7 TeV) via the synchrotron radiation per proton per orbit which is equivalent to 3.7 kW per beam. This heats up the magnets and hence the cooling is particularly challenging as there is only a small margin within which the superconductivity is maintained.

Multipoles Multipole magnets (quadrupole, sextupole, octupole etc.) are used for beam correction to increase the beam's lifetime. One magnet focuses the beam on one axis and defocuses on the other. Thus they alternate to keep the beam focused around a central point. This principle is called strong focusing. An LHC quadrupole between two dipoles is shown in Figure 2.4 (left). As high luminosity is demanded by the experiments, it is advantageous to focus the beam before the collision as much as possible. The "inner triplet" is a composition of multipoles to squeeze the beam 100 times for the interaction point. An inner triplet on anticlockwise side of point 2 is shown on Figure 2.4 (right).

Kickers and septa Kicker magnets (see chapter 11 in [75]) are used to inject (eject) beam into (from) the LHC orbit. As they must not influence the beam already present, they must switch fast (< 1 μs). A kicker magnet for beam ejection at point 6 is shown on Figure 2.5 (left). As the kicker magnets have relatively small power, Lambertson-type septa magnets bend the beam more. The septum is a special type of magnet that is divided into two field regions. One region contains a maximum field for bending the kicked beam, and the second region contains a zero field where the circulating beam is placed. Since the septa are usually constantly powered and long, they provide high power for beam bending. An LHC septum magnet (green) with beam-pipes for orbiting and ejected beam at point 6 is shown on Figure 2.5 (right).

Figure 2.4: Left: An LHC quadrupole (chromium) between two dipoles (blue). Right: Inner triplet magnet (red) at A-side of the ALICE experiment for lowering the beam cross-section.

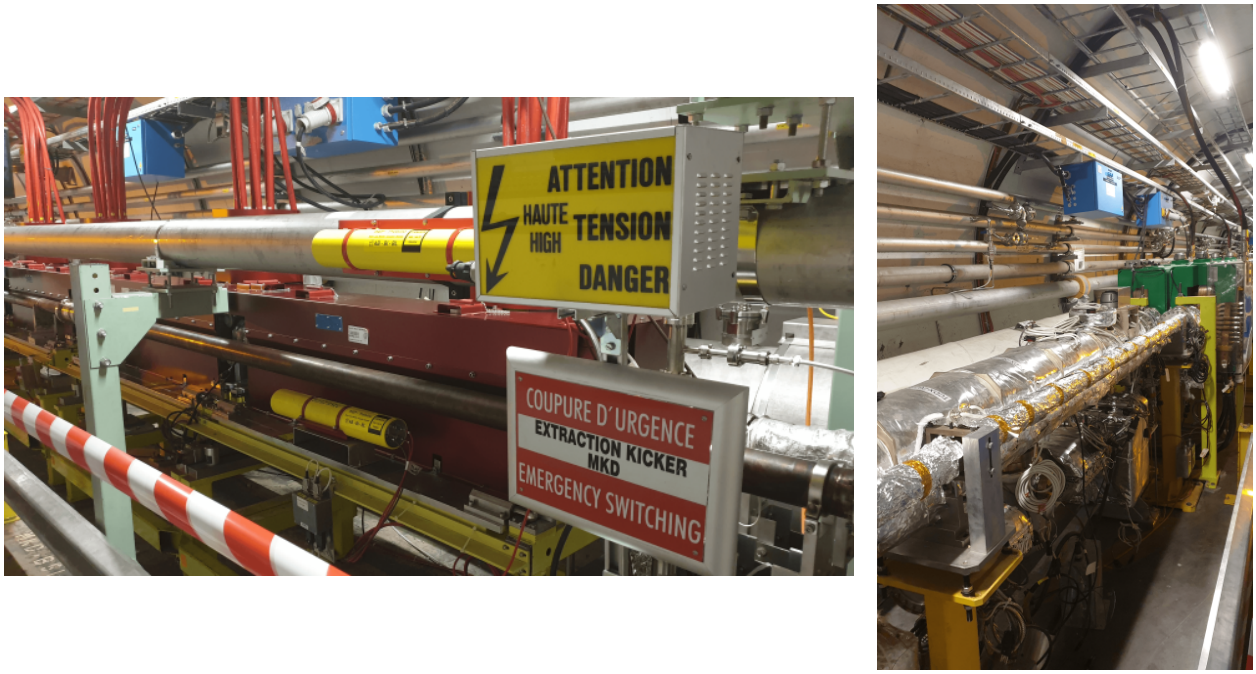

Figure 2.5: Left: An LHC kicker magnet for beam ejection at point 6. Right: An LHC septum magnet (green) with beampipes for orbiting and ejected beam.

2.4 ALICE

The main focus of ALICE is to probe the strong force and to study the properties of QGP. ALICE was designed to excel in heavy-ion collisions, which is characteristic of a high density of tracks. The detector is placed 56 m underground at the LHC point 2 in the Ain department of France. It is 26 m long, 16 m wide and high and weighs around 10,000 tonnes. The ALICE collaboration consists of almost 2000 physicists, technicians and engineers from 39 countries worldwide [77]. In this section, the main component of ALICE will be described, namely, the tracking detectors - Time Projection Chamber (TPC) and Inner Tracking System (ITS), the particle identification with TPC and Time-Of-Flight (TOF) and triggering system using V0, as well as the Central Trigger Processor (CTP) [78]. An overview of ALICE sub-detectors can be seen in Figure 2.6.

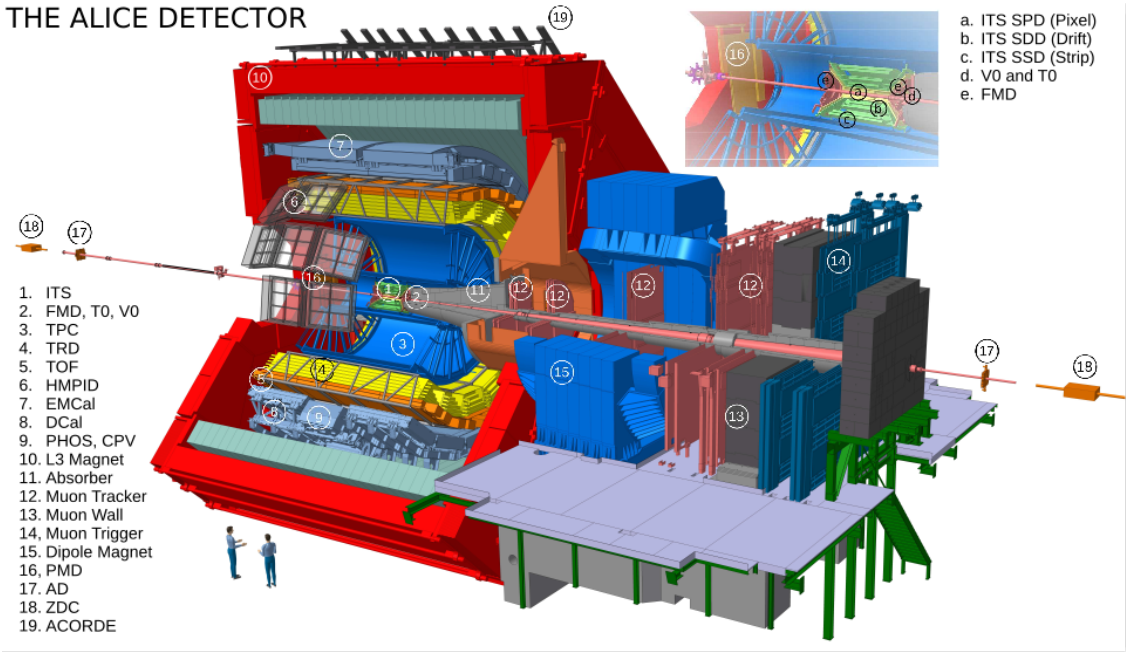

Figure 2.6: ALICE with every sub-detector depicted [79].

2.4.1 Tracking detectors

2.4.1.1 TPC

The TPC (see section 3.2 in [78]) is the primary mid-rapidity tracking detector highlighted in Figure 2.7, optimised to provide momentum and particle identification of charged particles and to determine the vertex position. The pseudorapidity coverage of the TPC is $|\eta| < 0.9$, it covers full azimuth and can measure tracks with transverse momentum of $p_{\mathrm{T}} = 0.1 - 100$ GeV/c. Ionising particles created during collisions create electron-ion pairs in the volume which drift toward the cylinder top and bottom. Electrons are detected at the end caps by multi-wire proportional chambers, which provide 2D track information. The third component for 3D imaging is given by the drift time, so a precise characterisation of the drift time is needed. The space resolution is 400-800 μm and the p_{T} resolution 1% for low p_{T} tracks up to 20% for tracks at 100 GeV/c from heavy-ion collisions. Moreover, the TPC can provide particle identification by measuring track energy loss in the gas.

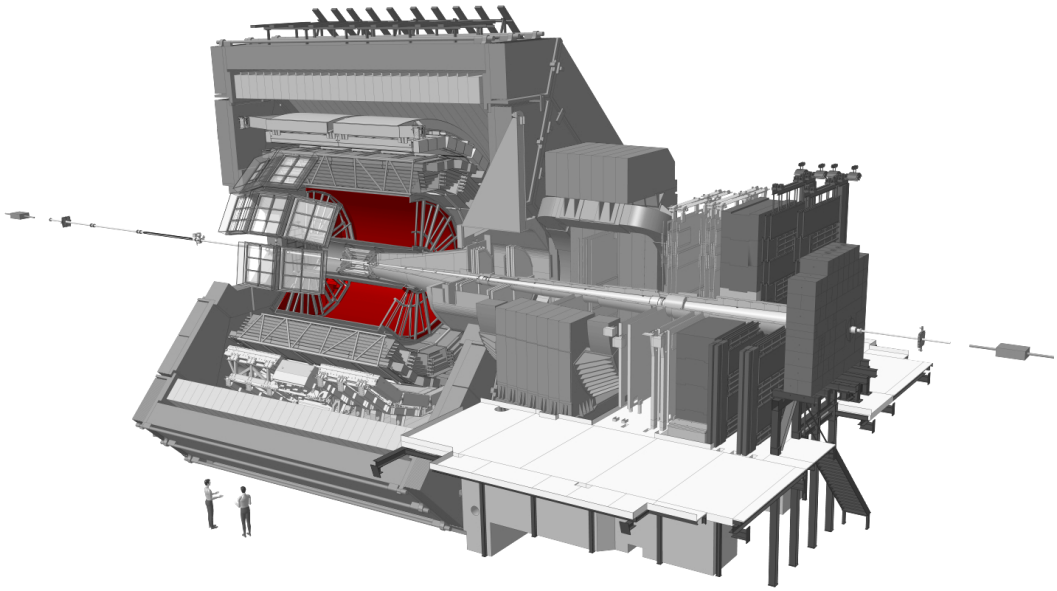

Figure 2.7: Location of the TPC within ALICE [79].

The TPC schematic diagram is shown in Figure 2.8, it is cylindrical with an inner radius of 85 cm, an outer radius of 250 cm and a length of 5 m. The electric field cage is divided in half by the central -100 kV electrode providing a uniform electric field of 400 V/cm. It is flushed by CO_2 to isolate it from the grounded containment cage. The main gas can be either argon or neon. Neon is mainly used due to its higher mobility and smaller space charge building in the chamber; argon was only used in 2017. To prevent the creation of excited states of the ions, CO_2 was used as a quenching gas. Moreover, the addition of N_2 can be used to gain more stable operation at the cost of lower drift velocity, which also eliminated a problem of atmospheric leak into the containment cage. The admixture of $Ne - CO_2 - N_2$ in a fraction of $90 - 10 - 5$ was used as nominal. The maximum drift time is 90 μs which is approximately the time of one LHC orbit.

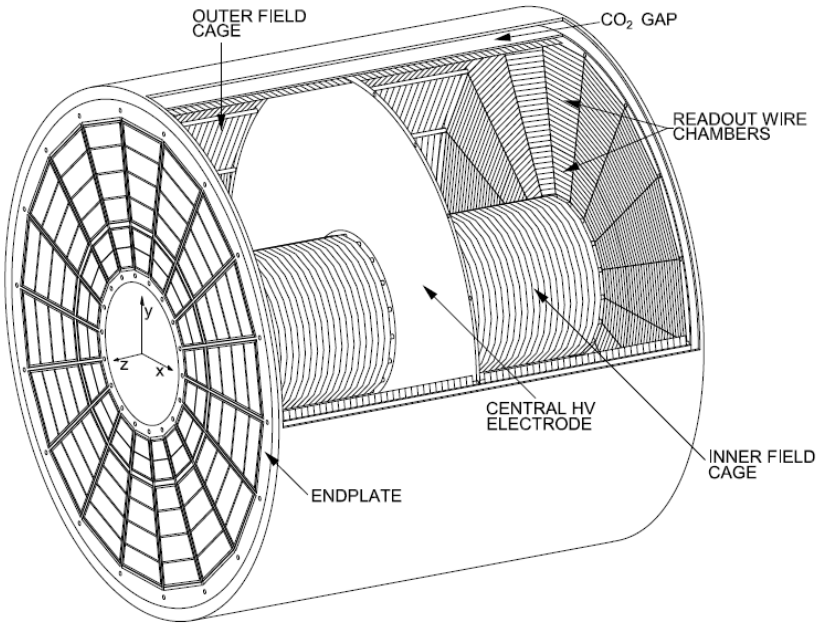

Figure 2.8: Main components of ALICE TPC [80].

2.4.1.2 Inner tracking system

The main task of the ITS (see section 3.1 in [78]) is to localise the primary interaction vertex with a high resolution and to identify tracks with momentum below 200 MeV/c, thus extending the acceptance of TPC. It covers $|\eta| < 0.9$, full azimuth and is located inside the TPC as seen in Figure 2.9 (left). The ITS consists of six layers of three different types of silicon-based detectors. The outermost two layers are Silicon Strip Detectors (SSD), the two middle one Silicon Drift Detectors (SDD) and the two innermost Silicon Pixel Detectors (SPD). The tracking resolution of the impact parameter is around 30 μm for $p_{\mathrm{T}} > 3$ GeV/c in Pb–Pb events as seen in Figure 2.9 (right).

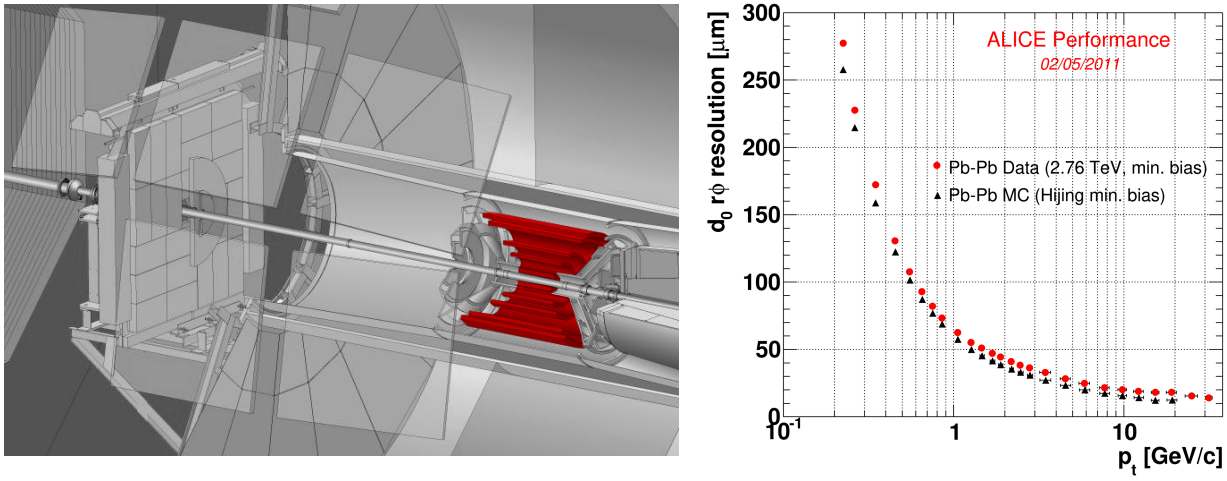

Figure 2.9: Left: Location of ITS within ALICE [79]. Right: Transverse impact parameter resolution for tracks reconstructed by ITS in Pb–Pb at $\sqrt{s_{\mathrm{NN}}} = 2.76$ TeV [81].

Silicon Pixel Detector The SPD (see section 3.1.1 in [78]) consists of two hybrid pixel detector layers, and it equips the innermost part of the ITS. Each sensor is a reverse-biased diode detector bonded to a readout chip with a total number of 9.8 M pixels. Both layers are 14.1 cm long and are located at a radial distance $r = 3.9$ cm and $r = 7.6$ cm from the nominal beamline. Each chip can provide a fast-OR signal with a frequency of 10 MHz

(4 integrated bunch-crossings), contributing to the L0 trigger level of the CTP (see Section 2.4.3.2). SPD's main purpose is to identify the primary vertex position and measure the secondary vertices impact parameter of weak decays.

Silicon Drift Detector The SDD (see section 3.1.2 in [78]) comprises of two intermediate layers of the ITS located at radial distances $r = 15$ cm and $r = 23.9$ cm and of length 22.2 cm and 29.7 cm, respectively. Each sensor's sensitive area is divided into two drift regions by a high-voltage cathode at a nominal voltage of -2.4 kV. A passing particle creates electron-hole pairs in the sensitive area, which then drift to collecting electrodes. The drift time serves as a second component in measuring track position, giving a 2D projection. The SDD has a good multi-track identification capability and can provide energy loss signal for particle identification done by the ITS system.

Silicon Strip Detector The two outer layers, SSD (see section 3.1.3 in [78]), are used to match tracks from TPC to the inner layers of the ITS. It consists of two layers of double-sided silicon strip detectors located at radial distances $r = 38$ cm and $r = 43$ cm and of length 43.1 cm and 48.9 cm, respectively. It can provide track energy loss for additional particle identification in the low momentum region.

2.4.2 Particle Identification

Charged particles can be identified via the characteristic ionising energy loss in matter using the Bethe-Bloch formula [1]

$$-\left\langle \frac{dE}{dx} \right\rangle = K \frac{Z}{A} \frac{z^2}{\beta^2} \left[\frac{1}{2} \ln \frac{2 m_e c^2 \beta^2 \gamma^2 W_{max}}{I^2} - \beta^2 - \frac{\delta(\beta\gamma)}{2} \right], \tag{2.1}$$

where the coefficient $K = 0.307075$ MeVmol^{-1}cm^2, Z is the medium atomic number, A is the medium mass number, z is charge of the interacting particle, $\beta = v/c$, where v is the

velocity of the interacting particle and c is the speed of light, m_e is the electron mass, γ is the Lorentz factor, W_{max} is the maximum possible energy transfer to an electron in a single collision, I is the mean medium excitation energy, and δ is the density correction of ionisation energy loss due to medium polarisation.

Time Projection Chamber The primary particle identification detector for the central barrel is the TPC (see section 3.2 and 8.2 in [78]). The TPC ionisation signal for different incident particle species as a function of momentum is shown in Figure 2.10 (left). The aforementioned Bethe-Bloch formula is used to fit each particle signal. In a given momentum slice, the values are compared to a theoretical value of an energy loss as seen in Figure 2.10 (right) and are fitted by a multiple-Gaussian. The standard deviation σ of each Gaussian is then used to determine the probability of identifying a given particle.

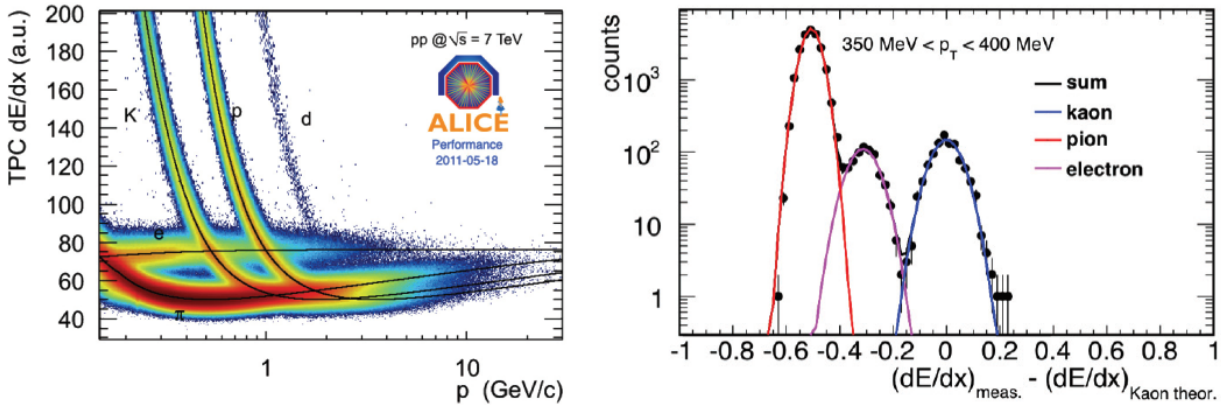

Figure 2.10: The ionisation signal of tracks, from pp interactions, measured by the TPC (left) and multi-Gaussian fit of energy loss difference from theoretical values (right) [82].

Time Of Flight The second mid-rapidity particle identification detector is the TOF (see section 3.4 in [78]). It is based on Multi-gap Resistive Plate Chamber technology, and it is placed on top of the Transition Radiation Detector (TRD), which wraps around the

TPC as seen in Figure 2.11. The TOF covers $|\eta| < 0.9$ and full azimuth. Due to the track curvature in the ALICE magnetic field, the minimum track momentum to reach the TOF is $p_{\mathrm{T}} > 500$ MeV/c for protons, pions and kaons. Identification of high p_{T} particles is determined by the detector velocity measurement and thus is dependent on the time resolution. The maximum p_{T} is 3 GeV/c for pions and kaons, and 6 GeV/c for protons [83]. The measured β for different particle species is shown in Figure 2.12 (left) and β for particles with momentum 3 GeV/c in Pb–Pb at $\sqrt{s_{\mathrm{NN}}} = 5.02$ TeV is shown in Figure 2.12 (right). Kaon/pion separation can be achieved up to 3 GeV/c and proton/kaon separation up to 5 GeV/c [84].

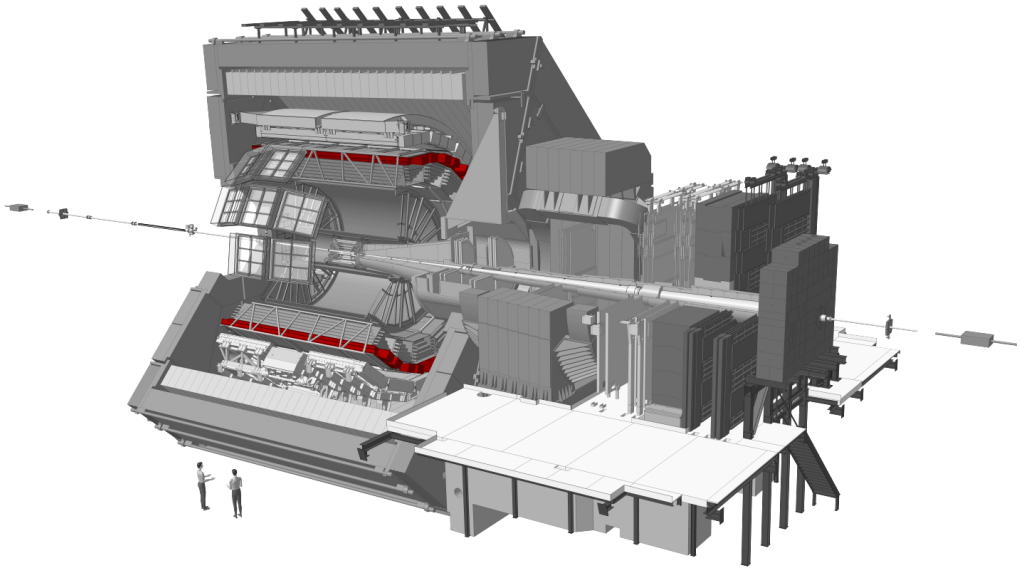

Figure 2.11: Location of the TOF within ALICE [79].

The quality of identification is characterised by a standard deviation and can be expressed as

$$n_{\sigma} = \frac{t_{\mathrm{TOF}} - t_{ev} - t_{exp}(m_i, p, L)}{\sigma_{tot}(m_i, p, t_{ev})}, \tag{2.2}$$

where t_{TOF} is the arrival time to detector, t_{ev} is the collision time and t_{exp} is the expected time for a particle of mass m, momentum p and track length L. The total time resolution σ_{tot} contains TOF and collision time resolution and uncertainty imposed due to tracking

and reconstruction. The collision time can be determined using two approaches. The first approach uses a forward T0 detector which can directly estimate the collision time. However, due to the T0 acceptance, a fraction of events in pp collisions have no signal and therefore the identification was not possible. Thus an alternative approach was developed where the TOF determines the t_{ev} by minimising the χ^2 while comparing t_{TOF} and t_{exp} for each track at a fixed t_{ev}. The more tracks are in an event, the better the estimation will be. For physics analysis, a combined event time by both methods is used [83].

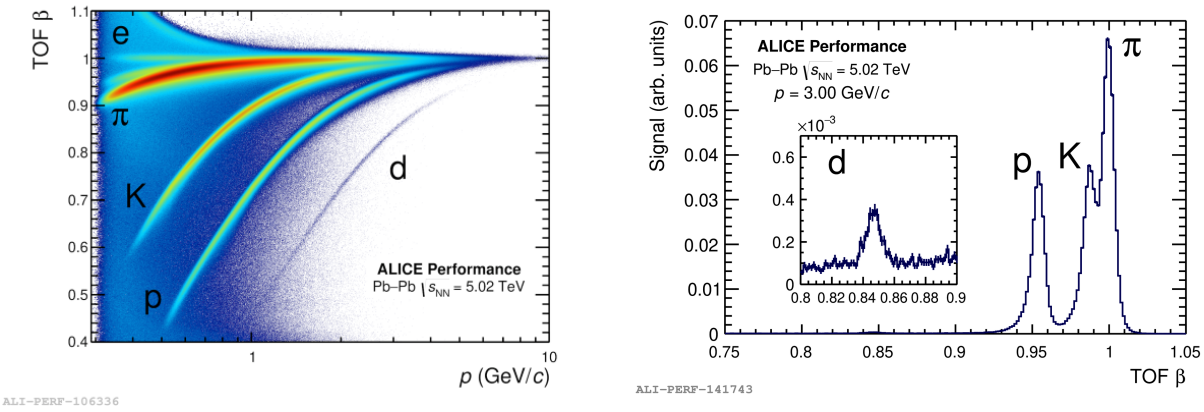

Figure 2.12: Left: TOF β velocity vs momentum p performance plot in Pb–Pb collisions at $\sqrt{s_{\mathrm{NN}}}$ = 5.02 TeV [84]. Right: TOF β velocity for particles with momentum 3.0 GeV/c in Pb–Pb collisions at $\sqrt{s_{\mathrm{NN}}}$ = 5.02 TeV [84].

2.4.3 Triggering and Data Acquisition

2.4.3.1 V0 detector

One of the main triggering detectors is the V0 detector (see section 5.4 in [78]) which consists of two arrays of scintillator counters, V0A (3.4 m from the vertex) and V0C (90 cm from the vertex), on either side of the interaction point as seen in Figure 2.13 (left). They measure particles originating from the initial collision and those scattered in the beam-pipe.

A coincidence in both arrays serves as the main minimum bias (MB) trigger, which is in main interest of this thesis. It also serves as an indicator of collision centrality, as the relation of the integrated pulse heights in the detector scales to the number of registered particles and is monotonic.

2.4.3.2 Central Trigger system

The CTP (see section 6.1 in [78]) handles trigger inputs from multiple detectors on multiple latencies, decides whenever interaction is of physics interest and initiates detector readouts and Data AcQuisition (DAQ). There are three hierarchical levels of the hardware triggers with different latencies: L0 (1.2 μs), L1 (8.2 μs) and L2 (106.4 μs). A latency is defined as a time between the interaction at LHC and the trigger arrival to detectors. Furthermore, an LM (825 ns) level, which serves as a pre-trigger for the TRD, was added at the beginning of Run 2. The current system involves a CTP, Local Trigger Unit (LTU) for each detector, and Trigger Timing Control (TTC) for each detector (total 19), a schematic diagram of the installation in P2 is shown in Figure 2.13 (right). Moreover, the CTP distributes the LHC clock to each detector and protects them from receiving another trigger when they are in busy state.

2.4.3.3 Data Acquisition

The architecture of the ALICE DAQ system (see section 6.2 in [78]) is shown in Figure 2.14. The TTC signal sent by the LTU is received by the Front-End Read-Out (FERO) electronics, which then sends detector data via Detector Data Links (DDL) to the DAQ Readout Receiver Card (D-RORC). The D-RORC was replaced by a new Common Readout Receiver Card (C-RORC) for Run 2, which increased the bandwidth available for data transfer. The data from the RORC cards are collected in Local Data Concentrators (LDCs) computing clusters;

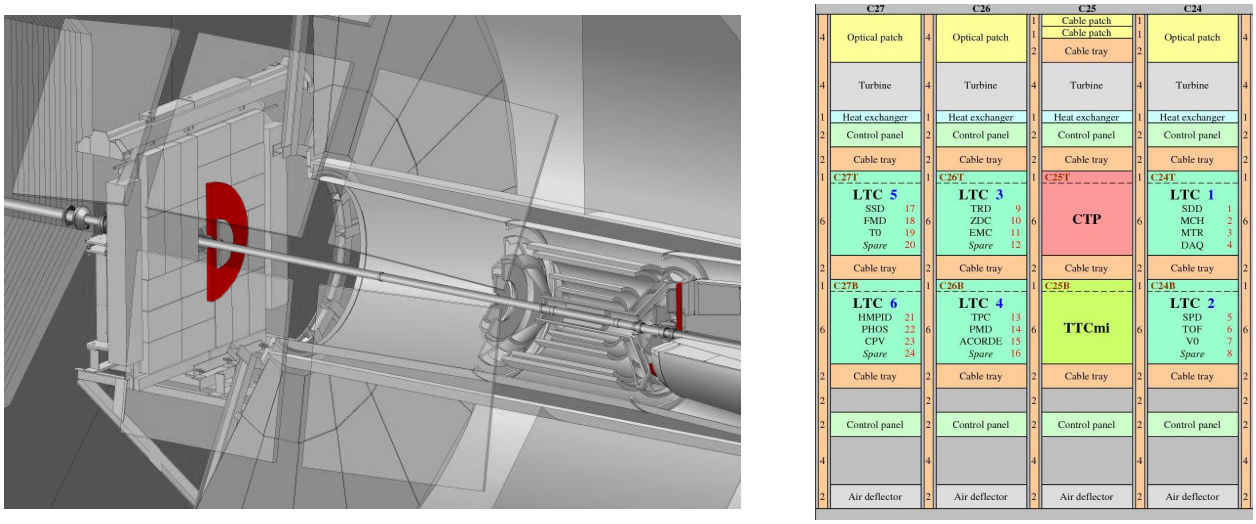

Figure 2.13: Left: Location of the V0 within ALICE [79]. Right: The installation of the Central Trigger Processor at point 2.

every detector has one or more LDCs. The received data are built into sub-events in the LDCs and sent to the Global Data Collectors (GDCs) where a full event is built. The load between GDCs is data-driven and managed by an Event-Destination Manager (EDM). The fully built events from GDCs are then shipped to computing centres for permanent storage and registered in the ALICE Grid software (AliEn). The ALICE High Lever Trigger (HLT) [85] is based on a unique combination of Field-Programmable Gate Array (FPGA) and graphics processing units, which use Compute Unified Device Architecture (CUDA) technology. The CUDA technology provides a significant boost in computing capabilities especially in the clustering of the TPC data and performing online calibrations.

The data are stored in Tier-0 computing centres [86, 87] at CERN and the Wigner Institute in Hungary. In addition, the data are copied to regional Tier-1 computing centers for redundancy. There are in total 13 Tier-1 centres around the globe and organised data processing usually takes place on them. Finally, there are around 155 Tier-2 centers which are dedicated to end-user analysis and simulations, which usually use the closest Tier-1 centre as data storage.

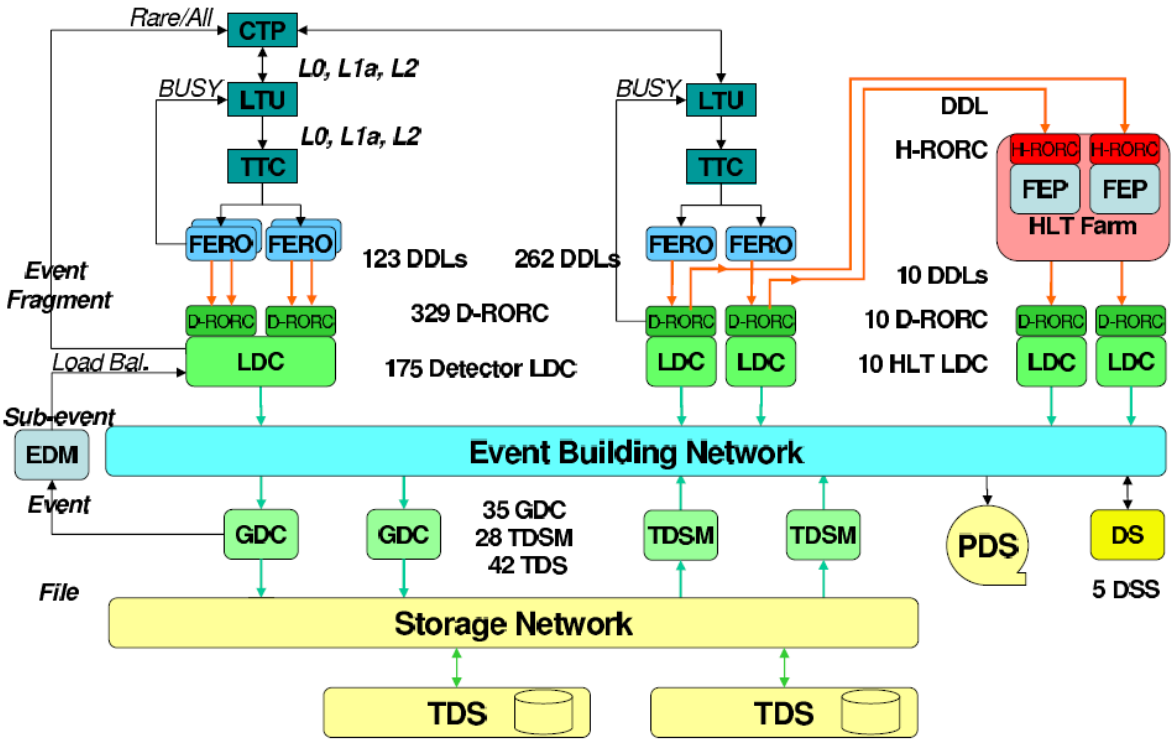

Figure 2.14: The architecture of the ALICE DAQ system, the D-RORC cards have been replaced by C-RORC card for Run 2 [78].

Chapter Three

ALICE Central Trigger System Upgrade

3.1 Overview

The ALICE experiment is undergoing a major upgrade in the years 2018-2022 with an aim to increase the read-out capabilities of its detectors. The front-end electronics and data processing system is being upgraded to new technology, based on GigaBit Transceiver (GBT) and Trigger Timing Control Passive Optical Network (TTC-PON) network, called the Online-Offline (O^2) system. The upgraded readout will allow for the continuous readout of the detectors, with a rate of 1 MHz in pp collisions and 50 kHz for Pb–Pb collisions. In order to support the O^2 system, a new Central Trigger System (CTS) has been designed, produced, assembled, and programmed. There is one CTP and LTU for each detector, this two-stage system will allow for the decoupling of a single detector from the CTP, without influencing the remaining detectors. The connection between the CTP and LTU is done using the TTC-PON network. An overview of the CTS upgrade, written by the author of this thesis, is summarised in [88]. It is included in appendix C, and can act as an introduction to the hardware and software of the CTS and the logic of CTP.

Instead of relying on an external trigger unit, the upgraded detectors will be self-triggered, and will continuously push data towards the ALICE data processing system. The CTS provides timing, synchronises the detector's read-out streams, and every bunch-crossing sends downstream 200 bits of information describing what happened in a given bunch-crossing. In the case that some Common Readout Unit (CRU) is unable to process the data, a signal is sent upstream to the CTS which then stops the data taking for a given set of detectors, that are supposed to be read together. This minimum busy window is one HeartBeat (HB), which is approximately the time needed to read out the TPC and is equal to one LHC orbit - 88 μs. Moreover, CTP collects information from the detectors to built a record for O^2, summarising the beam and trigger conditions. This record can be then used while later reconstructing the data.

Some of the detectors are not fully upgraded, namely the Electromagnetic Calorimeter (EMC), Photon Spectrometer (PHS), High Momentum Particle Identification (HMP), Charged Particle Veto (CPV), and TRD. These detectors still require a trigger distribution over the Run 2 RD12 TTC system as described in section 3.2. These detectors require a physical trigger signal from the CTS to initiate the readout. After each trigger, the CTS must protect those detectors against a new trigger until the data is successfully read-out and transferred. The trigger signal can be sent with three latencies – LM (825 ns), L0 (1.2 μs), and L1 (8.2 μs). Detectors usually require a combination of two latencies, this is referred to as the multi-level trigger distribution system. The trigger decision at the CTP depends on the current beam conditions, which detectors are to be read out together, and the list of trigger inputs for a given latency. As the bandwidth is limited, only a selection of given trigger information is transmitted for these detectors. The author's main contribution was to design and implement such a system under the new CTS, and to create an interface between the GBT/TTC-PON [89, 90] and RD12 TTC [91] system.

3.1.1 Trigger message

A trigger message is 76 bits long, and consists of the trigger Type (32 bits) and event identification information: Orbit ID (32 bits) and Bunch Crossing (BC) ID (12 bits). The length of the Orbit ID message allows 106.3 hours of continuous data taking, which is longer than the LHC fill duration before refilling. The BC ID defines a collision slot within a given Orbit, and goes up to 3564. The trigger message contains information for a given event identification, e.g. physics trigger, calibration trigger, HB, and Time Frame (TF). It also contains information on the start and end of the current continuous and triggered runs, which together are known as XOX software triggers.

3.2 RD12 Trigger-Timing-Control distribution in ALICE

The trigger distribution used in Run 1 and 2 was designed by the RD12 collaboration in the late 90s [91]. The hardware used for the distribution of trigger signals is comprised of the LTU, TTC Encoder and Transmitter (TTCex) [92], and TTC Receiver (TTCrx) [92] systems. The TTCex takes two electrical low-voltage differential signaling (LVDS) 3.3 V signal, called *channel A* and *channel B*, and the LHC clock. The two channels are alternately read (time-division multiplexing) and an exclusive or with the clock (biphase mark or Manchester encoded) [93] is made into a 160.32 MHz laser and transmitted into the readout electronics. The LTU must guarantee that the correct phase of the incoming signals is passed to the TTCex board. The connections between the CTP, LTU, TTCex, and TTCrx electronics are shown in Figure 3.1.

The channel A (TTC-A) is dedicated to the synchronous transmission of triggers with respect to the LHC bunch-crossing. The default value is 0 V and the TTCex strobes the signal with the falling edge of the LHC clock; one bit can be transmitted per LHC bunch-

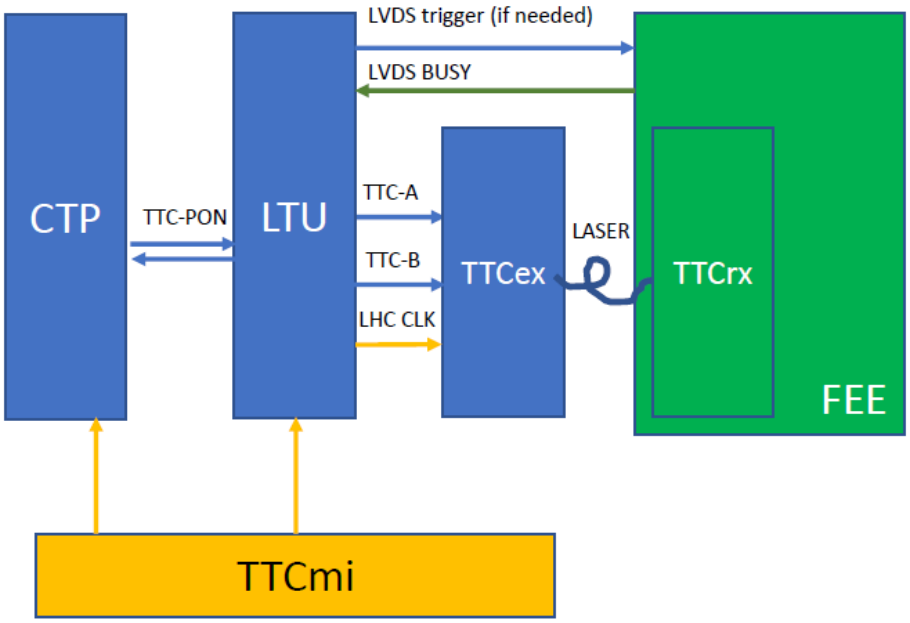

Figure 3.1: The connection between the CTP, LTU, TTCex, and detectors front-end electronics (FEE) via the TTCrx. The LHC clock is provided via the TTC machine interface (TTCmi).

crossing. In ALICE Run 3, different pulses will be used for different signals. The LM and L0 trigger messages will be 1 clock-wide pulses, the L1 trigger will take a 2 clock-wide pulse, and the TRD calibration will use a 3 clock-wide pulse.

The channel B (TTC-B) is dedicated to the asynchronous transmission of serialised trigger messages and the TTCrx control signals, and the synchronous transmission of the LHC orbit message and the detector pre-calibration trigger, known as the Pre-Pulse (PP). The TTCex board strobes this signal with the rising edge of the LHC clock; in this way one bit of data can be transmitted per bunch-crossing. The signal in this channel must be properly formatted as shown in Figure 3.2 in order for the TTCrx chip to correctly reconstruct the data. There are two types of messages, broadcast (short) and individually-addressed (long) commands. Within ALICE, every detector has its own LTU and TTCex board. As such,

every long message can be transmitted to every receiver chip on a particular network, without having to select a specific TTCrx address (`TTCrx ADDR = 0x0`) for the message. To avoid confusion, "short message" and "long message" notation will be used in this work. The short message is 16 bits long with 8 bits of user payload, and the long message is 42 bits long with 16 bits of user payload.

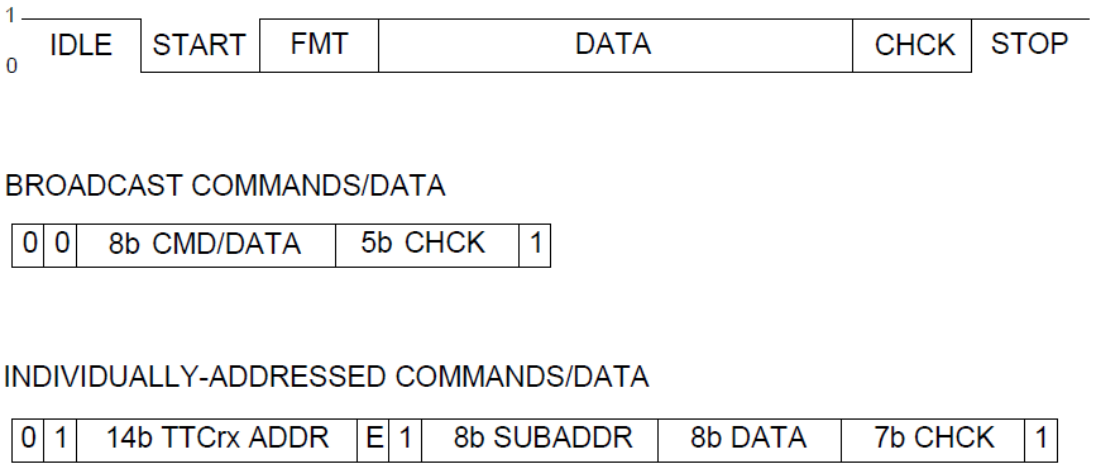

Figure 3.2: The broadcast (short) and individually-addressed (long) messages transmitted via the TTC-B channel [94].

At ALICE, the short messages are utilised to be synchronous with the bunch-crossing, which means that the TTCrx will receive and decode the commands with fixed latency, with respect to the bunch-crossing of an event. They are dedicated to transmission of the LHC orbit and PP signals. The long messages are used to transmit trigger messages at the L1 latency, which contains trigger information of a given L0 latency. At ALICE, both `SUBADDR` and `DATA` are used for a payload, which results in 16 bits of information within one long message. The messages are Hamming encoded in order to correct single-bit errors. Since double-bit errors would be undetected and the message will be false-correctly accepted, an additional parity bit is added to extend the algorithm into SECDED, single-bit error corrections, with double-bit error detection. The short message is encoded with

the Hamming(16,11) algorithm, and the long message by the Hamming(64,57) algorithm. The first number in the algorithm notation denotes the maximum number of total bits used in each message, and the second number refers to the maximum number of data bits. The TTCrx chip decodes these messages and corrects for potential bit errors and/or reject double-bit erroneous data.

3.3 Design of RD12 TTC module for Run 3 LTU

The TTC module for Run 3 was designed in a such way that it is fully separated from the rest of the LTU logic, with a well defined interface. This has a major advantage that, not only can the module be used on a standalone board, but it can also be removed from LTU boards which do not need the RD12 TTC interface, providing more FPGA resources for additional logic. The implementation was done on Xilinx Kintex Ultrascale FPGA using Very High Speed Integrated Circuit Hardware Description Language (VHDL). There are several important blocks in the logic:

- TTC processor,
- TTC-B encoder,
- CTP interface,
- LTU interface,
- Busy handler,
- IPbus interface,
- Monitoring unit,
- TTC-A state machine.

The main unit in the logic is comprised of the TTC processor and TTC-B encoder, which builds the trigger messages, buffers the triggers, handle the transmission priorities and encodes the messages in the required format for the TTCrx chips. These treat the information from the CTP and the LTU in the same way. The CTP and LTU interfaces are there to translate between the Run 3 triggering scheme and RD12 triggering protocol. The busy handler processes the busy signals from the detectors and TTC-B encoder, and correctly throttles the triggers. The control and monitoring of the LTU is accomplished via Ethernet links, using the IPbus firmware and software packages. The monitoring block reports the status of each unit and the TTC-A state machine checks the correct pulse widths and latencies on the TTC-A channel. In order for the LTU logic to be fully operational, it also requires TTC-PON/GBT links, and flash memory and DDR4 interfaces. The LTU logic is shown schematically in Figure 3.3. The rest of this section will describe the main features of the TTC design.

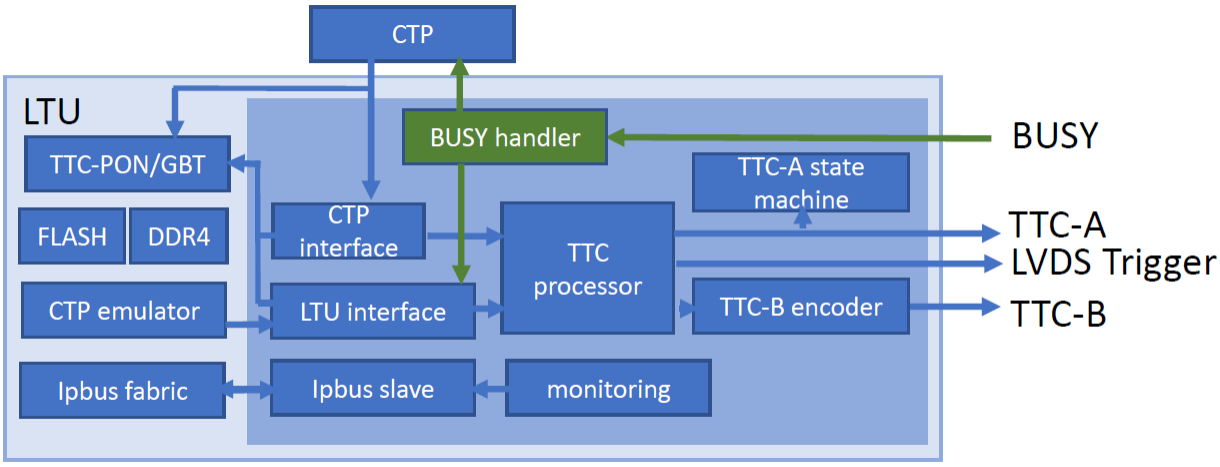

Figure 3.3: The design of the TTC logic on the LTU.

3.3.1 TTC processor

The TTC processor receives the CTP or LTU trigger messages and transmits synchronous triggers to the TTC-A channel, according to which detector is connected to a given LTU. In the case of the TTC detectors (EMC, PHS, HMP), a one-wide pulse is sent to TTC-A at L0 latency and the trigger message is buffered. If an L1 trigger is rejected at L1 latency or no trigger is received, the buffer is cleared. If there is an L1 accept trigger, a two-wide pulse is sent into the TTC-A channel. Moreover, the buffered trigger message from L0 time is chopped into seven 16-bit long payloads for the long message and is pushed to the buffers of the TTC-B encoder for transmission. The trigger message formatting for the TTC detector is shown in Table 3.1. The first 4 bits specify a header (`0x1` for the first word and `0x2` for consecutive words), the remaining bits contain Orbit ID, BC ID and trigger type. This is called a "full trigger sequence" - L0 trigger, L1 trigger, L1 message. As there is a limited bandwidth, only messages related to physics trigger, calibration trigger, and XOX software triggers are sent.

When an Orbit or PP trigger is received, a payload for a short message is prepared; `0x1` for orbit and `0xFC` for PP, and sent into the encoder. Both messages must be transmitted synchronously, thus they must be received by the LTU 60 BC in advance, in order to guarantee a clear transmission channel and proper arrival time to the detectors.

In the case of the TRD detector, a one-wide pulse is sent into TTC-A at LM and L0 latency. For each Nth accepted L0 trigger (programmable), a three-wide calibration pulse is sent 9 BC after the L0. For the CPV detector, a one-wise pulse is sent over LVDS at L0 latency. Both the TRD and CPV detectors do not use the trigger distribution over the TTC-B, but instead use the TTC-PON or GBT.

Table 3.1: TTC data format Trigger Message (EMC,HMP,PHS)

TTC word	Payload	Content	Payload
0	<15:12>	LL1 header	<3:0>
0	<11:8>	Spare	<0:0>
0	<7:0>	TType	<31:24>
1	<15:12>	LL1 data	<3:0>
1	<11:0>	TType	<23:12>
2	<15:12>	LL1 data	<3:0>
2	<11:0>	<11:0>	TType
3	<15:12>	LL1 data	<3:0>
3	<11:0>	BC ID	<11:0>
4	<15:12>	LL1 data	<3:0>
4	<11:8>	Spare	<0:0>
4	<7:0>	Orbit ID	<31:24>
5	<15:12>	LL1 data	<3:0>
5	<11:0>	Orbit ID	<23:12>
6	<15:12>	LL1 data	<3:0>
6	<11:0>	Orbit ID	<11:0>

3.3.2 TTC-B encoder

This unit encodes the short and long messages and handles the priorities of transmission. The short message is encoded by Hamming(16,11) and the long message by Hamming(64,57), and transmitted via shift-register with a rate of one bit per bunch-crossing. The priority of transmission is the following, from highest to lowest priority: orbit short message, PP short message, L1 trigger long message, and user-defined long message. Both short messages

are required to be transmitted synchronously with LHC collisions, thus when the request is received from the TTC processor, the transmission of new long messages is stopped, and any ongoing transmission is finished. The higher priority of orbit messages over the PP messages means that, if the PP is requested around the Orbit window, it will be suppressed. The reason is that the Orbit is the main time-synchronisation message which must always be received by the detectors at the correct time. Setting the correct time for the PP transmission is on the operator to do. The L1 trigger message, which is chopped into 7 long words, takes 308 bunch-crossing to transmit. Both long messages have their buffers, a 512 words deep First In First Out (FIFO), which is processed whenever the transmission channel is ready. This means that the L1 trigger message can be received up to seven orbits later after the collision happened.

3.3.3 CTP/LTU interpreter

The TTC processor can be driven either by a CTP emulator on the LTU or by the CTP itself. Even though the CTP emulator on the LTU is the same as its equivalent Local Trigger Generator (LTG) on the CTP, it is missing some features. In particular, on the CTP there is a class logic, which generates triggers on different latencies, protects against new triggers between the two latencies, and handles the incoming busy. The LTU emulator of the CTP has simplified logic, and some of the above features are added in an LTU interpreter.

The LTU interpreter emulates a class logic creating a two-level trigger distribution with programmable latencies and L1 trigger reject by modifying the trigger message. For the EMC, CPV, HMP and PHS, a new trigger generation is protected for the L0-L1 duration in order to account for the signal propagation until the detector busy take over. The two-level trigger is generated also for XOX and calibration signals. The TRD detector has a special protocol: triggers are generated at LM and L0 latencies, which are 15 BC apart.

The protection between two LM triggers is 64 BC, in order to give time for the receipt of a “detector busy" signal. In addition, a calibration trigger is required after each Nth successful L0 trigger, with a latency of L0 + 9 BC.

When receiving data from the CTP, all these features are generated by the CTP class logic. The CTP interpreter adds a two-level scheme to software triggers which are generated level-less inside the LTG.

3.3.4 Control and monitoring

The control and monitoring of the TTC module are done via the IPbus suite [95]. Some signals are also connected to the DDR4 memory and recorded as a snap-shot for debugging. In addition, users can transmit a user-defined long message in order to program the TTCrx chip. Control can be generated via the IPbus software. An example of a user-defined command is the TTCinit sequence, which programs the TTCrx chip to receive TTC-B messages. This message is needed to correctly configure receiver chips in the beginning of data taking. If not received, the detectors would not accept any of the trigger messages sent to them. At ALICE the sequence is:

1. `0x800006FF` – TTCrx reset
2. `0x80000000` – setting TTCrx fine delay 1 to 3126 ps
3. `0x80000180` – setting TTCrx fine delay 2 to 16459 ps
4. `0x80000200` – setting TTCrx course delay to 0 ps
5. `0x800003F9` – activate channel TTC-B
6. `0x80018000` – reset TTCrx BC counter

The TRD detector requires very low latency, as such a direct electrical LVDS connection has been made between the CTP and the TRD LTU, which saves around 55 ns. The caveat is that the CTP must properly format the TTC-A stream. In order to have monitoring of the LVDS connection, a state machine is created which checks the pulse widths and latencies. This is to detect any instabilities potentially caused by a bad timing between the CTP and the LTU.

3.3.5 Timing and latency

The TTCex requires that both the TTC-A and the TTC-B signals arrive in their correct phases. Every compilation of the FPGA can have a different timing between the last Flip-Flop (FF) and the TTCex. In order to assure the same timing between compilations, an ODDRE1 in the FPGA's IO bank, which is physically burnt into the silicon, is used for both channels. Furthermore, a delay logic is inserted between the TTC processor and TTC-B encoder to fine-tune the phase by 4.16-24.96 ns (4.16 ns step).

As already described, the TRD requires very low trigger latency. As such, special attention was paid to optimise the firmware for minimal latency. The CTP/LTU interpreter increases the latency by 1/6 BC which is directly connected to the TTC processor. The TTC processor adds 2/6 BC to the latency, the ODDRE1 adds another 1/6 BC and the delay logic adds between 1/6 and 7/6 BC to the final latency. This adds to a total 5/6 to 11/6 BC (or 21 to 46 ns) latency of the RD12 TTC logic. As the TTC-PON stream is required to be in parallel with the messages in the TTC, the LTU/CTP messages are resynchronised using the LHC clock, adding one BC in latency onto the TTC-PON data.

Chapter Four

D^0-meson tagged jets

4.1 Overview of past measurements

Heavy-flavour quarks The heavy-flavour quarks are dominantly produced during hard partonic scattering. As their masses are larger than the QCD scale, Λ_{QCD}, their production cross-section can be calculated down to $p_{\mathrm{T}} = 0$ GeV/c using pQCD based methods as discussed in [96–98]. The production cross-section measured by CDF [99], STAR [100], ATLAS [101], LHCb [102], ALICE [103], and CMS [65] are very well described by pQCD based models, for example using the Fixed-Order-Next-to-Leading-Logarithm (FONLL) [104, 105] or General Mass Variable-Flavor-Number Scheme (GM-VFNS) [97] calculations. The p_{T}-differential production cross-section for D^0 meson in pp collisions measured by CMS and ALICE compared to FONLL and GM-VFNS calculations is shown in Figure 4.1.

Heavy-flavour jets Studying heavy-flavour-tagged jets provides additional information to test pQCD and to tune the MC generators. The $p_{\mathrm{T,jet}}$-differential production cross-section of charm jets and charm jets fraction in pp collisions at $\sqrt{s} = 5.02$ TeV measured by CMS is shown in Figure 4.2 (left). The $p_{\mathrm{T,ch\,jet}}$-differential production cross-section for charm jets

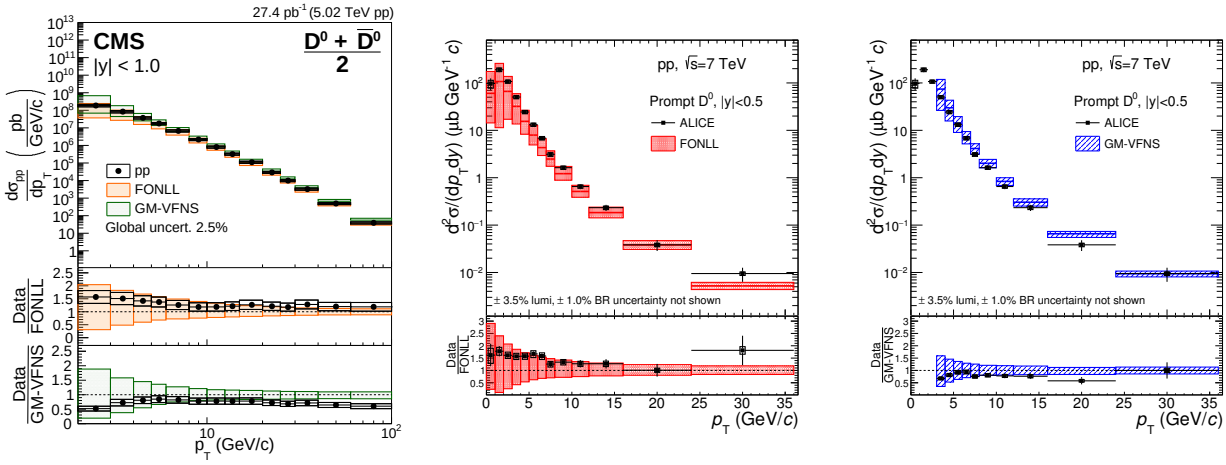

Figure 4.1: The p_{T}-differential cross-section for D^0 meson in pp collisions at $\sqrt{s}$ = 5.02 TeV measured by CMS (left) [65] with comparisons to FONLL [104, 105] and GM-VFNS [97] calculations. The p_{T}-differential cross-section for D^0 meson production in pp collisions at $\sqrt{s}$ = 7 TeV measured by ALICE [103] with comparisons to FONLL [104, 105] (middle) and GM-VFNS [97] (right) calculations.

tagged with D^0 and charm jet fraction in pp collisions at $\sqrt{s}$ = 7 TeV measured by ALICE is shown in Figure 4.2 (middle and right). Both measurements are consistent with NLO pQCD calculations within uncertainties.

Dead-cone effect The dead-cone is a QCD effect first introduced in section 1.7. A first direct measurement of the dead-cone effect, as measured by the ALICE experiment is shown in Figure 4.3. The ratio $R(\theta)$ of the splitting angle probability distribution for jets tagged with D^0 meson and inclusive jets as a function of splitting angle θ is defined as

$$R(\theta) = \frac{1}{N^{\mathrm{D}^0}} \frac{\mathrm{d}n^{\mathrm{D}^0}}{\mathrm{d}\ln(1/\theta)} \Big/ \frac{1}{N^{\mathrm{inclusive}}} \frac{\mathrm{d}n^{\mathrm{inclusive}}}{\mathrm{d}\ln(1/\theta)}, \tag{4.1}$$

where $\frac{1}{N^{\mathrm{D}^0}} \frac{\mathrm{d}n^{\mathrm{D}^0}}{\mathrm{d}\ln(1/\theta)}$ is N^{D^0} per jet normalised number of parton splittings n, given an initial energy E_{Radiator} of the parton radiator. One can clearly see a suppression for smaller angles in Figure 4.3. The suppression is smaller when increasing the radiator energy, as expected

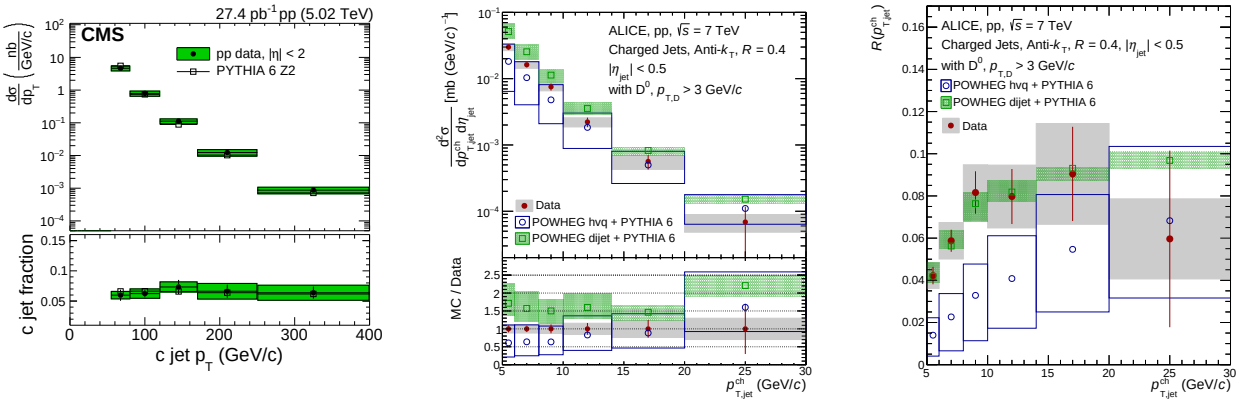

Figure 4.2: The $p_{\mathrm{T,ch\,jet}}$-differential production cross-section of charm jets and charm jet fraction in pp collisions at $\sqrt{s}$ = 5.02 TeV measured by CMS (left) [106] with comparison to PYTHIA [36] Z2 [107] tune. The $p_{\mathrm{T,ch\,jet}}$-differential production cross-section (middle) for charm jets tagged with D^0 and charm jet fraction (right) in pp collisions at $\sqrt{s}$ = 7 TeV measured by ALICE [108] with comparison to POWHEG hvq + PYTHIA 8 [37, 48] and POWHEG dijet + PYTHIA 8 [37, 49] predictions.

from the theoretical expectation $\theta < \frac{M}{E}$, which is marked by the pink shaded area. The ratio $R(\theta)$ is compared to PYTHIA and Sherpa MC calculations, where Sherpa provides a slightly better description of the data. Both MC calculations are also prepared in the "no dead-cone limit" where light quark mass is assumed. The difference from the data directly shows the suppression of charm-quark emission for small angles.

Studying the heavy-ion collisions Understanding heavy-flavour production in pp collisions is crucial for interpretation of heavy-ion collisions and QGP related observables. As heavy-flavour quarks are created before the QGP is formed, they will endure its whole evolution; thus they act as an ideal, self-generated, inner probe. They allow extraction of medium transport properties, related to the radiative and collisional interactions and energy loss [109, 110]. Jets provide additional insight on how the lost energy was radiated and dissipated into the medium. The collisional energy loss of heavy quarks might not be as small as

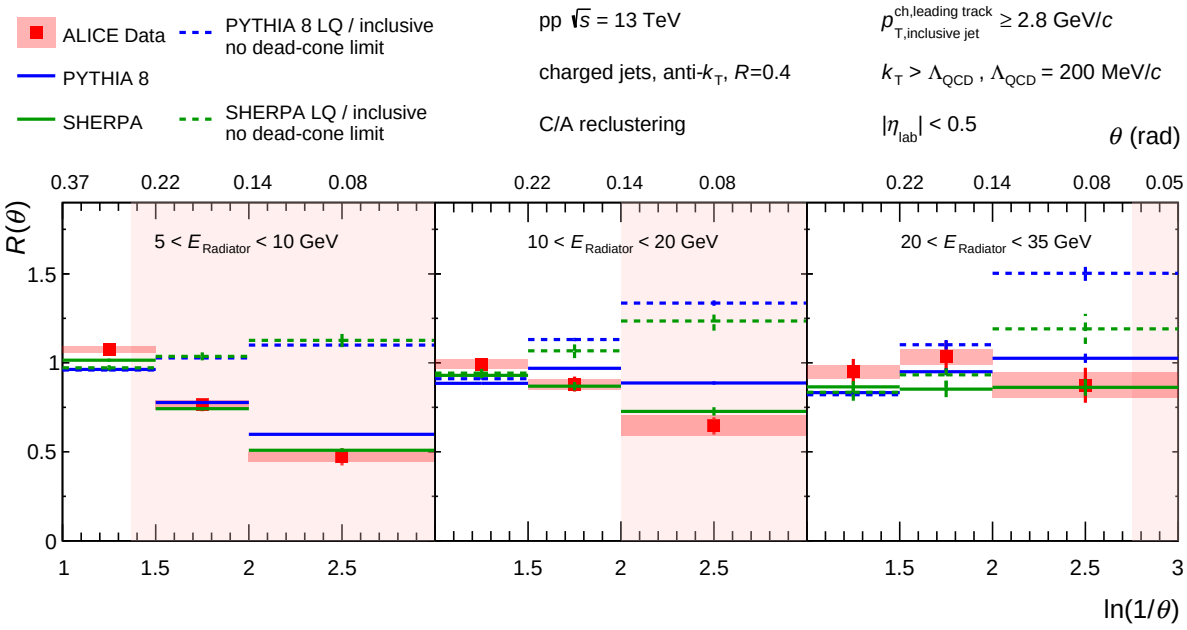

Figure 4.3: The ratio $R(\theta)$ of the splitting angle probability distribution for D^0-tagged and inclusive jets for different energies of the radiator E_{Radiator} with comparison to PYTHIA and Sherpa [62].

has been proposed by theoretical calculation in [111]. The difference in nuclear modification factors by considering the radiative, collisional, cold nuclear matter and isospin effects is shown in Figure 4.4 (left). A prediction of this model for b-jet nuclear modification factor in different centrality bins and compared to CMS data is shown in Figure 4.4 (right). In addition, jets allow studying a possible flavour dependence of parton energy loss and modifications of the fragmentation functions. The CMS experiment performed the first study of charm quark diffusion with respect to the jet axis, which can provide input for the medium diffusion coefficients [112].

Heavy-flavour fragmentation Further insight into heavy-flavour fragmentation can be provided by observing the fully reconstructed heavy-flavour particles in a jet, i.e. by measuring the momentum fraction $z_{||}^{\text{ch}}$ carried by the heavy-flavour hadron along the jet axis. There

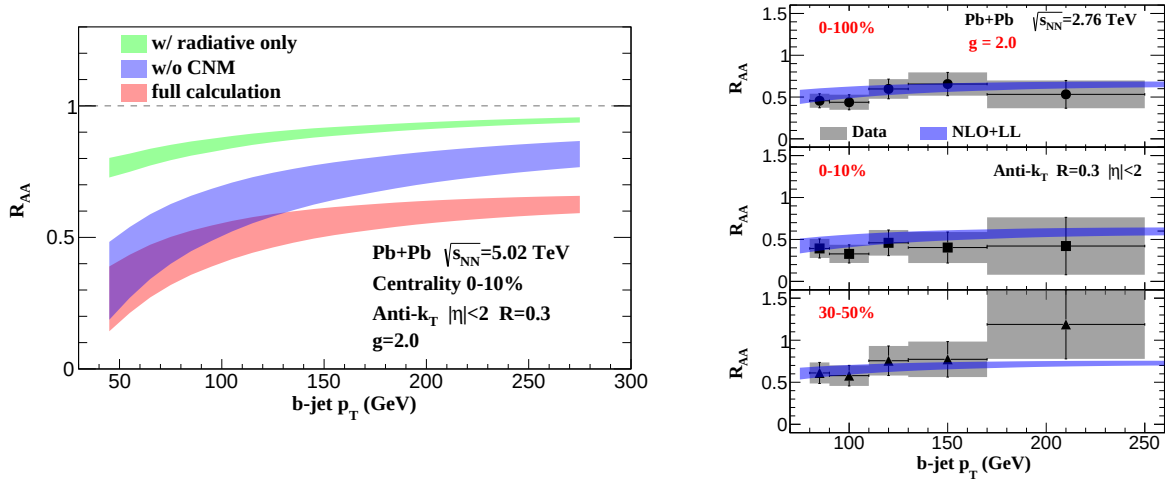

Figure 4.4: Left: The b-jet nuclear modification factor model for central Pb–Pb collisions at $\sqrt{s_{\mathrm{NN}}} = 5.02$ TeV. The suppression by including only radiative processes can be seen with the green band, with collisional and radiative processes by the blue band and including cold nuclear matter (CNM) effects and isospin effects by the red band [111]. Right: The prediction of b-jet nuclear modification factor in different centrality bins compared to CMS data [111].

are several studies of the $D^{*\pm}$ momentum fraction measured in pp collisions by STAR at 200 GeV [113] and ATLAS at 7 TeV [114], in $p\overline{p}$ collisions measured by CDF at 1.8 TeV [115] and at the UA1 at 630 GeV [116], and the $z_{||}^{\mathrm{ch}}$ of D^0-tagged jets in pp collisions measured by ALICE at 7 TeV [108]. The momentum fraction z carried by the $D^{*\pm}$ in jets in pp collisions at $\sqrt{s} = 7$ TeV measured by the ATLAS collaboration is shown in Figure 4.5. The momentum fraction $z_{||}^{\mathrm{ch}}$ carried by the D^0 in charged-particle jets in pp collisions at $\sqrt{s} = 7$ TeV measured by the ALICE collaboration is shown in Figure 4.6. The distributions of low z measurements by ATLAS and STAR disagree with MC generators. On the contrary, the ALICE measurement is in good agreement with NLO pQCD calculations within uncertainties.

These measurements hinted at the importance of contribution from higher-order charm production mechanisms, like gluon splitting and flavour excitation. The ATLAS mea-

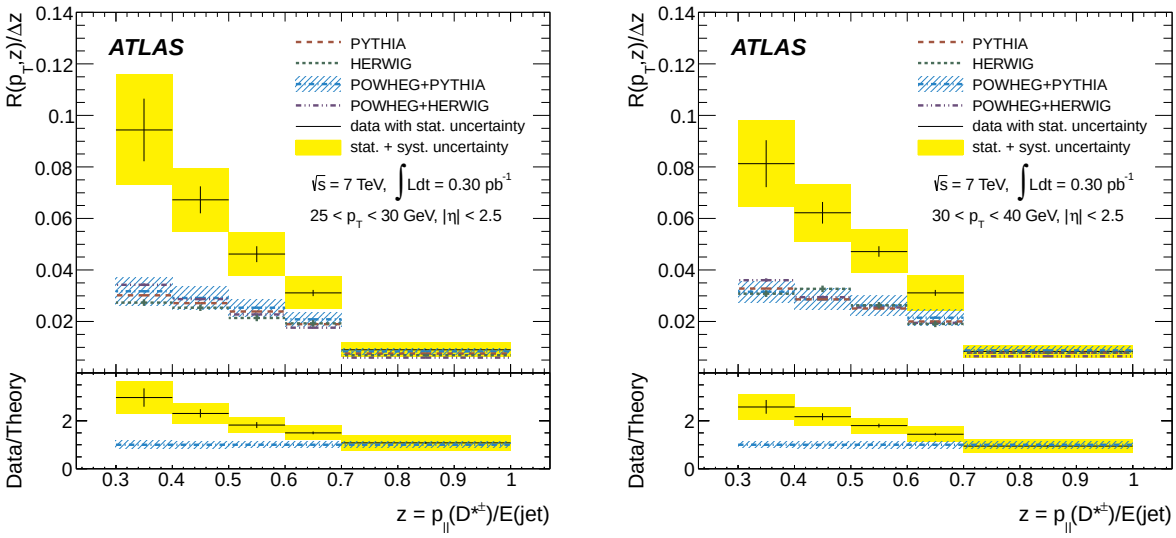

Figure 4.5: The momentum fraction z carried by the D$^{*\pm}$ in jets measured for two $p_{\mathrm{T,ch\,jet}}$ intervals in pp collisions at $\sqrt{s}$ = 7 TeV by the ATLAS collaboration [114], compared to PYTHIA, HERWIG, and POWHEG predictions.

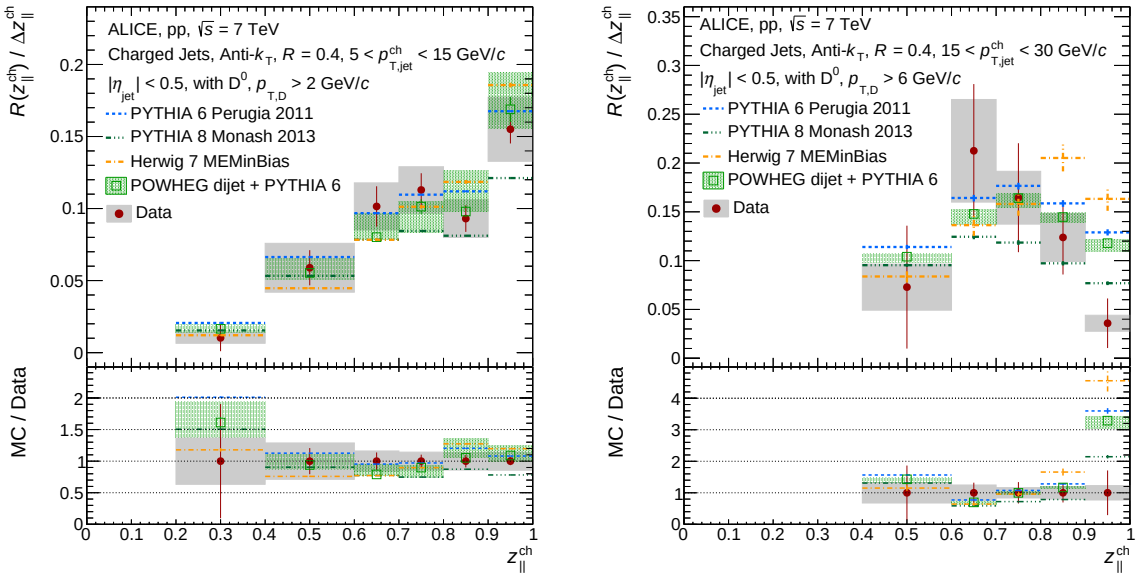

Figure 4.6: The momentum fraction $z_{||}^{\mathrm{ch}}$ carried by the D^0 in charged-particle jets measured for two $p_{\mathrm{T,ch\,jet}}$ intervals in pp collisions at $\sqrt{s}$ = 7 TeV by the ALICE collaboration [108], compared to PYTHIA, HERWIG and POWHEG predictions.

surement can be reasonably well described by enhancing the gluon-to-hadron fragmentation functions as seen in [117]. The fragmentation functions are usually estimated from electron-positron annihilation data [118, 119], which are extended using DGLAP evolution towards the hadron collider energies. However, by including the gluon-to-hadron fragmentation functions from hadronic colliders, the model description of the ATLAS measurement improved significantly [120]. The momentum fraction z carried by the $D^{*\pm}$ in jets in pp collisions at $\sqrt{s} = 7$ TeV measured by ATLAS compared with a Zero Mass Variable-Flavor-Number Scheme (ZM-VFNS) based model with electron-positron annihilation fragmentation functions and with fragmentation functions with added gluon-to-hadron contribution is shown in Figure 4.7. The measurement of the in-jet fragmentation can provide valuable information in constraining these gluon-to-hadron fragmentation functions. The ALICE experiment can provide a unique insight into intermediate transverse momentum.

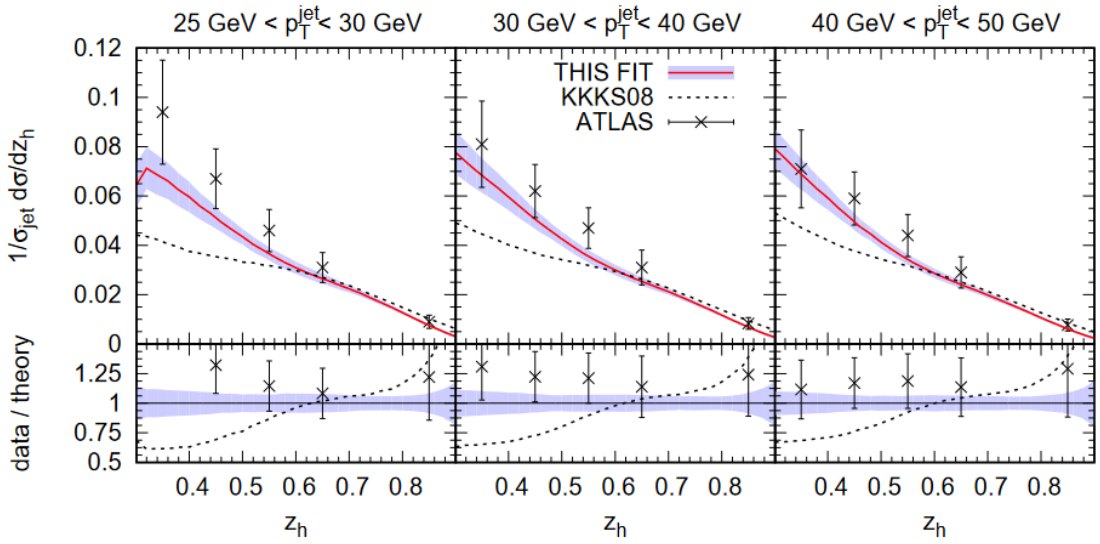

Figure 4.7: The momentum fraction z carried by the $D^{*\pm}$ in jets measured for two $p_{\mathrm{T,ch\,jet}}$ intervals in pp collisions at $\sqrt{s} = 7$ TeV by the ATLAS collaboration [114] with a ZM-VFNS based model with electron-positron annihilation fragmentation functions (KKKS08) and added gluon-to-hadron fragmentation functions (THIS FIT) [120].

A challenging aspect at hadron colliders is matching the simulated jets at a partonic level to the reconstructed jets at the detector. The matching is usually done geometrically; however, due to background fluctuations in pp collisions, and especially in ion-ion collisions, it is quite challenging. Consequently, jets are measured in large transverse momentum regions, bringing larger matching uncertainties at lower momentum. A big advantage of tagging jets with a hard probe (gamma, heavy-flavour) is a perfect matching of partonic and detector found jets. The heavy-flavour particle can be described by pQCD down to low momentum and its dominant production is during the hard partonic collisions. This allows probing low $p_{\mathrm{T,jet}}$ which is based on the minimum momentum of the hard probe. For example, the ALICE experiment is able to reconstruct D^0 mesons to almost $p_{\mathrm{T,D}} \approx 0$ GeV/c.

With respect to the previous measurements, this analysis provides in-hadron fragmentation in the intermediate transverse momentum region of $2 < p_{\mathrm{T,ch\,jet}} < 50$ GeV/c. In addition, different jet resolutions (radii) have been studied in order to determine the influence of hadronisation (low R) and UE (large R) effects. In order to have access to larger statistics, only charged-particle jets (jets containing only charged tracks) have been reconstructed. Measurements of full-jets (jets containing both charged and neutral tracks) would require the addition of calorimeters which in ALICE unfortunately have smaller acceptance and would significantly limit the measurement. The $p_{\mathrm{T,ch\,jet}}$-differential production cross-section and momentum fraction $z_{||}^{\mathrm{ch}}$ of charm jets with jet radii $R = 0.2$, $R = 0.4$, and $R = 0.6$ tagged with D^0 meson measured by ALICE in pp collisions at $\sqrt{s} = 13$ TeV will be presented in this thesis.

4.2 Data Sample

For this analysis, a pp $\sqrt{s}$ = 13 TeV minimum-bias data collected in 2016, 2017 and 2018 by the ALICE experiment has been used. The ALICE raw data are first processed into the Event Summary Data (ESD) object and then further processed into Analysis Object Data (AOD) files intended for users. The AOD files contain a filtered selection of objects (tracks and vertices) marked by a version number, which can have several iterations marked as passes. The collected data are grouped into several periods, defining data taking runs with similar beam and detector conditions. The following periods of minimum-bias data were considered for the analysis: year 2016: `LHC16d`, `LHC16e`, `LHC16g`, `LHC16h`, `LHC16j`, `LHC16k`, `LHC16l`, `LHC16o`, `LHC16p`; year 2017: `LHC17e`, `LHC17f`, `LHC17h`, `LHC17i`, `LHC17j`, `LHC17k`, `LHC17l`, `LHC17m`, `LHC17o`, `LHC17r`; year 2018: `LHC18b`, `LHC18d`, `LHC18e`, `LHC18f`, `LHC18g`, `LHC18h`, `LHC18i`, `LHC18j`, `LHC18k`, `LHC18l`, `LHC18m`, `LHC18n`, `LHC18o`, `LHC18p`. Moreover, additional information related to D-meson analysis with pre-reconstructed candidates is stored in special files (`AOD.vertexingHF`) accompanying the general AOD. The total number of analysed events is 1.49×10^9.

4.2.1 Trigger and luminosity determination

A minimum bias trigger, which requires a coincidence of signal in both V0 arrays (described in section 2.4.3.1), has been used. Internally it corresponds to an offline trigger type `kINT7`. The instantaneous interaction rate fulfil

$$\frac{\mathrm{d}N}{\mathrm{d}t} = \epsilon_{\mathrm{V0AND}} \cdot \sigma_{\mathrm{pp-inelastic}} \cdot \mathscr{L} = \sigma_{\mathrm{V0AND}} \cdot \mathscr{L}, \tag{4.2}$$

where $\epsilon_{\mathrm{V0AND}}$ is the trigger efficiency, $\sigma_{\mathrm{pp-inelastic}}$ is the pp inelastic cross-section and $\mathscr{L}$ is an instantaneous luminosity. The luminosity is a measure of the beam intensity product in the collision region for a colliding beam accelerator (for details see appendix A.1.4). The

cross-section measured by V0 arrays, σ_{V0AND}, is determined by reference runs, so-called Van der Meer scans [121]. The cross-section of 2016, 2017, and 2018 data was determined as $\sigma_{\mathrm{V0AND}} = (57.89 \pm 0.96)$ mb [122]. The Run 2 *integrated* luminosity can be estimated from the total number of analysed events by integrating (4.2) as

$$\mathscr{L}_{\mathrm{int}} = \frac{N}{\sigma_{\mathrm{V0AND}}} = (25.81 \pm 0.43)\ \mathrm{nb}^{-1}. \tag{4.3}$$

4.2.2 Event selection

An event selection has been made to assure a good detector coverage of the particle collision and to reject background from beam–beampipe and beam–gas interactions. First, only events with the primary vertex $|z| < 10$ cm (z is a coordinate in the beam direction) from the centre of the inner barrel were accepted. Secondly, an event was rejected as a pile-up if another vertex (pile-up vertex) fulfilling the following criteria was found:

- pile-up vertex contains more than 5 tracks,
- the χ^2/nDF of the tracks and the pile-up vertex < 5,
- the primary and pile-up vertex can be separated with a good resolution in the z-direction.

When another vertex was found, but the above-mentioned criteria were not fulfilled, the event was kept as it would be impossible to distinguish between real and pile-up collisions. This selection effectively reduced the impact of in-bunch pile-up events.

4.2.3 Track selection

The track selection can be distinguished into two categories. First, the D^0 daughter tracks selection is based on the `AOD.vertexingHF` which contains pre-reconstructed candidates.

Second, the selection of remaining tracks in an event is based on the `AOD`.

The common selection on both sets is as follows:

- track's distance of the closest approach to primary vertex in transverse plane < 2.4 cm,
- track's distance of the closest approach to primary vertex in z plane < 3.2 cm,
- track has at least 70 (out of 159) TPC crossed readout rows,
- ratio of crossed rows over findable clusters in the TPC is larger then 0.8,
- track has at least two hits in ITS (out of six), where at least one is in any layer of SPD.

4.2.3.1 D^0 candidate selection

The D^0 were reconstructed at central rapidity using the charged hadronic decay channel $D^0 \rightarrow K^-\pi^+$ with branching ratio $f_{BR} = (3.950 \pm 0.031)\%$ [1] and mean decay length $c\tau \approx 123$ μm. In addition to standard selection described above, the D^0 decay tracks are required to fulfill following:

- $|\eta| < 0.8$,
- $p_T > 0.3$ GeV/c,
- $\chi^2/nDF < 2$ of TPC track fit,
- tracks with $p_T < 3$ GeV/c must have a hit in first layer of SPD.

This track selection reduces the D^0 rapidity acceptance, which grows from $y_{lab,D} = 0.5$ at $p_{T,D} = 0$ GeV/c to $y_{lab,D} = 0.8$ at $p_{T,D} = 5$ GeV/c. Thus an additional selection on the fiducial rapidity acceptance $|y_{lab,D}| < y_{fid}(p_{T,D})$ has been implemented as

$$y_{fid}(p_{T,D}) = \begin{cases} -\frac{0.2}{15}p_{T,D}^2 + \frac{1.9}{15}p_{T,D} + 0.5 & 0 \leq p_{T,D} \leq 5 \text{ GeV}/c \\ 0.8 & p_{T,D} > 5 \text{ GeV}/c \end{cases} \tag{4.4}$$

This analysis uses a selection procedure for secondary vertex topologies that provides a reasonable separation from a primary vertex and suppress the background. A graphical depiction of the chosen D^0 decay topology is shown in Figure 4.8 with impact parameters and pointing angles indicated.

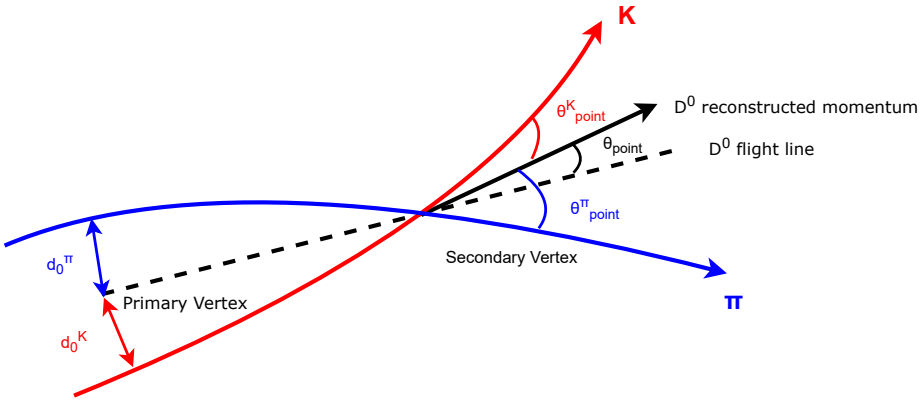

Figure 4.8: The D^0 decay topology into K–π pairs with depicted impact parameters and pointing angles.

The candidate selection, optimised to provide high signal-over-background ratio, is described in [123] and was adopted in this analysis. A $p_{\mathrm{T,D}}$ dependent topological selection is summarised in Table 4.1 and it consists of the following variables:

- $\Delta M_{\mathrm{D^0}}$ - the difference between the PDG [1] and reconstructed D^0 mass.
- $p_{\mathrm{T}}^{K(\pi)}$ - transverse momentum of $K^{\mp}$ and $\pi^{\pm}$.
- $d_0^{K(\pi)}$ - $K^{\mp}$ and $\pi^{\pm}$ signed impact parameter. Impact parameter is a distance of closest approach between track and primary vertex, for D^0 it is of order of 100 μm. A sign represents a direction from the vertex.
- $d_0^K \cdot d_0^\pi$ - product of $K^{\mp}$ and $\pi^{\pm}$ impact parameters. The daughter trajectories of a D^0 are always on opposite sides of the primary vertex. Thus, imposing a negative cut is a powerful selection tool.

- $DCA_{K^{\mp}\pi^{\pm}}$ - the distance of closest approach between the decay tracks, for tracks originating from the same vertex, this should be as close to zero as the resolution allows.

- $\cos(\theta^*)$ - θ^* is the angle between the K and D^0 flight line in the D^0 rest frame. The distribution for a D^0 produces a uniform distribution, while the background will produce peaks at -1 and 1.

- $\cos(\theta_{\text{point}})$ - θ_{point} angle between D^0 flight line and the reconstructed D^0 momentum. For a real D^0 this value is close to one, while the combinatorial background produces uniform distribution.

- $L_{xy}/\sigma_{L_{xy}}$ - normalised D^0 decay length in a transverse plane to the beam direction. The decay length is the distance between the primary and secondary vertex. The transverse plane is chosen as detectors provide better resolution in it.

- $n\sigma_{res}$ - the difference between reconstructed and expected impact parameters for candidate tracks, internally called “the topomatic", was created to exploit the tracks impact parameters employing the topology and kinematics. It is defined as

$$n\sigma_{res}^{K(\pi)} \approx \frac{d_{0,exp}^{K(\pi)} - d_{0,reco}^{K(\pi)}}{\sqrt{\sigma_{L_{xy}}^2 \cdot \sin^2(\theta_{\text{point}}^{K(\pi)}) + \sigma_{d_{0,reco}^{K(\pi)}}^2}}, \tag{4.5}$$

  where $d_{0,reco}^{K(\pi)}$ is the daughter track impact parameter and $\sigma_{d_{0,reco}^{K(\pi)}}^2$ its uncertainty. The expected impact parameter is approximated as $d_{0,exp}^{K(\pi)} \approx L_{xy} \cdot \sin(\theta_{\text{point}}^{K(\pi)})$, where L_{xy} is the measured D^0 decay length and $\theta_{\text{point}}^{K(\pi)}$ angle between the daughter track flight line and the reconstructed D^0 momentum. The topomatic helps in reducing the background and feed-down contribution of the D^0 mesons while cutting out a negligible amount of signal.

Table 4.1: D^0 cuts for pp collisions at $\sqrt{s} = 13$ TeV.

p_{T,D^0}	(GeV/c)	$2-4$	$4-5$	$5-6$	$6-8$	$8-12$	$12-16$	$16-36$
$\lvert\Delta M_{D^0}\rvert$	(GeV/c^2)	< 0.4	< 0.4	< 0.4	< 0.4	< 0.4	< 0.4	< 0.4
$\lvert p_T^{K(\pi)}\rvert$	(GeV/c)	> 0.7	> 0.7	> 0.7	> 0.7	> 0.7	> 0.7	> 0.7
$\lvert d_0^{K(\pi)}\rvert$	(cm)	< 0.1	< 0.1	< 0.1	< 0.1	< 0.1	< 0.1	< 0.1
$d_0^K \cdot d_0^\pi$	(10^{-4} cm^2)	< -3	< -1.5	< -1	< -0.8	< -0.5	< 1	< 1
$\mathrm{DCA}_{K^\mp\pi^\pm}$	(cm)	< 0.03	< 0.03	< 0.03	< 0.03	< 0.03	< 0.03	< 0.03
$\lvert\cos(\theta^*)\rvert$		< 0.8	< 0.8	< 0.8	< 0.8	< 0.9	< 1.0	< 1.0
$\cos(\theta_{\mathrm{point}})$		> 0.95	> 0.95	> 0.95	> 0.95	> 0.95	> 0.95	> 0.90
$L_{xy}/\sigma_{L_{xy}}$		> 5	> 5	> 4	> 4	> 3	> 3	> 3
$n\sigma_{res}$		< 2	< 2	< 2	< 2	< 2	< 2	< 2

Particle identification The tracks were identified via the TPC and TOF as described in section 2.4.2. The significance cut on both $K^\mp$ and $\pi^\pm$ are $n_{\sigma,\mathrm{TPC}} < 3$ and $n_{\sigma,\mathrm{TOF}} < 3$. For tracks where no TOF information was available, identification only via the TPC has been used. When PID is inconclusive, and neither the pion nor the kaon mass hypothesis can be excluded, tracks compatible with both hypotheses were retained for analysis. As a result, the decay pairs are counted twice with two possible mass assignments. If the pair does not correspond to a real D^0, it would add two background entries, while if it corresponds to a real D^0, it would add one signal and one background entry. Cases where a wrong mass hypothesis is accepted while the correct one is rejected are negligible. A correction on track double counting is done and will be explained in section 4.6.1.1.

4.2.3.2 Jet track selection

Tracks are required to have $p_{\mathrm{T}} > 0.150$ GeV/c and be in a fiducial acceptance of $|\eta| < 0.9 - R$, where R is the jet radius. Unfortunately, the common track selection described in section 4.2.3 causes a drop in φ acceptance due to disabled or malfunctioning sensors in the SPD in different periods. This will result in biased jet composition, thus a global constrained hybrid track selection has been used to reduce this effect. The complementary tracks have the same selection, except they do not require to contain SPD hits. Further constraints to the track-primary vertex are required to reach a good momentum resolution despite missing SPD information. Including these complementary tracks results in a smooth φ distribution.

4.3 Monte Carlo sample

The MC production can be divided into two groups. In the first group, a general heavy flavour production MC is anchored to $\sqrt{s} = 13$ TeV pp data, to address different detector conditions for each period. This MC production is used to compute the D-meson efficiency in tagged jets, acceptance corrections and a response matrix of D-tagged jets with prompt and non-prompt D^0: c,b $\rightarrow$ D^0. The second group is a dedicated custom production generated for this analysis and used for the feed-down contribution of D^0-jets from beauty decays and a prompt D^0-jets used as model comparisons. The custom productions were generated only on a particle(generator)-level, which means a propagation through the detector (GEANT) has not been used in order to save computing resources. In this case, reconstructed data were calculated using a response matrix from the general production.

4.3.1 General heavy-flavour period-anchored production

This production is heavy-flavour enriched by producing a $c\bar{c}$ or $b\bar{b}$ pair in every event. Furthermore, all D mesons are forced to decay hadronically only. The MC simulation was generated using PYTHIA 6.4.25 [36] with the Perugia-2011 tune [124] and particles were propagated through the ALICE detectors using GEANT 3.21.11 [125] transport model to address detector layout and conditions during each period. MC productions marked as `LHC17c3a1`, `LHC17c3a2`, `LHC17h8a`, `LHC18l4a` and `LHC18l4b` are anchored to the `LHC16k`, `LHC16l`, rest of `LHC16*`, `LHC17*`, and `LHC18*` periods, respectively. A total number of 3.3×10^8 events has been generated.

4.3.2 Custom production for feed-down estimation

This production was generated using PYTHIA 6.4.25 matched with POWHEG-hvq NLO generator and EVTGEN for beauty decays. A CT10 NLO PDF set with LHAPDF 6 interpolator has been used. Events with $b\bar{b}$ pairs were produced exclusively. The central set contains default values of renormalisation, factorisation scales, and quark mass. The variations consist of halving/doubling the scales (6 different scales), beauty quark mass variation (±250 MeV/c^2), and excluding EVTGEN. The total number of generated events is 25×10^6 per set.

4.3.3 Custom production for model comparison

This production consisted of several configuration listed below:

- CT10NLO + PYTHIA 8.21 HardQCD Monash tune,

- CT10NLO + Pythia 8.21 SoftQCD Mode 2 tune,
- CT10NLO + Pythia 8.21 HardQCD Monash tune + POWHEG-hvq.

The $c\bar{c}$ process was required in each event. The POWHEG variations consisted of halving or doubling the scales (6) and a variation of charm mass (2). 20×10^6 events have been generated per configuration and set.

4.4 Data and Monte Carlo Quality Assurance

The track quality and heavy-flavour specific Quality Assurance (QA) have been done by Data Preparation Group (DPG) and Hadronic Decays of Heavy Flavour groups (D2H), respectively. The D2H group verified the primary vertex position, the multiplicity, number of good tracks per event, and the daughter tracks' impact parameter. The other part related to an inclusive and D-meson tagged jets observable for the 2017 and 2018 periods was verified by the author. The 2016 periods were QA'ed by other groups in the past. The following observables were extracted for each period in 2017 and 2018, inclusive and D-tagged jets, data and MC:

- jet φ, η and p_{T},
- jet constituents (tracks) φ, η and p_{T},
- jet area in $\eta - \varphi$ space,
- number of constituents (tracks) in a jet.

The verification was composed of the following steps for both inclusive and D^0-tagged jets:

1. consistency check between data and MC on particle and detector level for each individual period
   (a) for each observable as a function of $p_{T,ch\,jet}$ and self-normalised (see example Figure B.1)
   (b) for each observable integrated over $p_{T,ch\,jet}$ and self-normalised (see example Figure B.2)
2. comparison between each individual periods for data and MC on particle and detector level:
   (a) for each observable as a function of $p_{T,ch\,jet}$ normalised per number of events (see example Figure B.3)
   (b) for each observable integrated over $p_{T,ch\,jet}$ normalised per number of events (see example Figure B.4)
3. comparison of efficiency corrected D^0-tagged $p_{T,ch\,jet}$ spectra between individual periods

The quality assurance graphs have been created and cross-checked in search of irregularities. Typical QA distributions having the correct appearance are shown in appendix B. The following text will be focused on data periods that were rejected from the analysis.

Three issues have been identified. Firstly, the period `LHC17c` has a spike in φ and η jet and constituents distribution for both inclusive and D-tagged jets. They were not described by the MC as seen in Figure 4.9. The D2H group also found similar irregularities in D^0 related observables, so this period was excluded from the analysis.

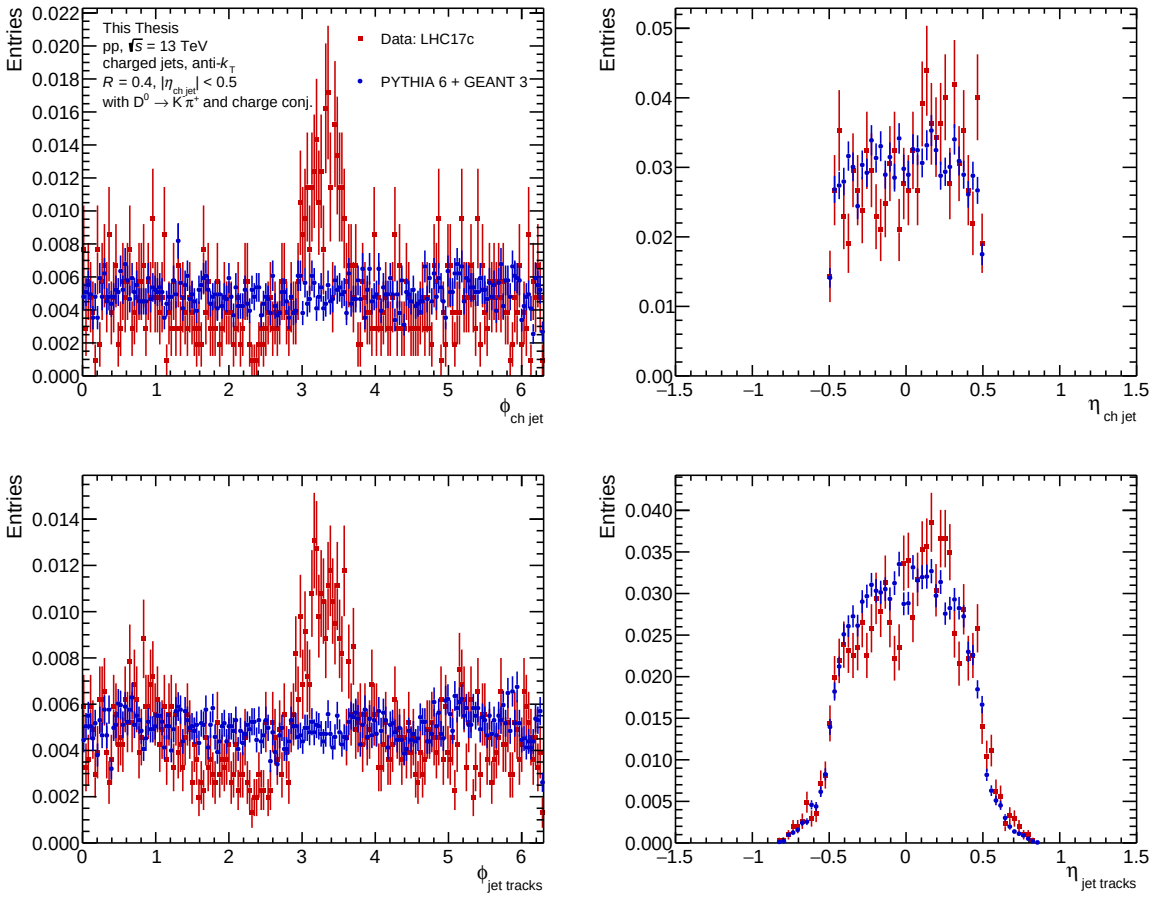

Figure 4.9: The φ and η distributions for D-jets and its constituents for data (green) from period `LHC17c` and the respective anchored PYTHIA 6 + GEANT 3 MC (red) production.

Secondly, irregularity has been found with `LHC18b` period with an example selected in Figure 4.10. The distributions are normalised by the number of selected events for every period. All periods are consistent except the `LHC18b`, which exhibited a wrong normalisation scaling, as seen in Figure 4.10. It was first excluded from the analysis until the problem has been identified and solved by the Data Preparation Group. The problem was related to the inconsistency between online and offline primary vertex selection which resulted in a large number of events being wrongly rejected. After addressing the problem, this period was reintroduced in the analysis.

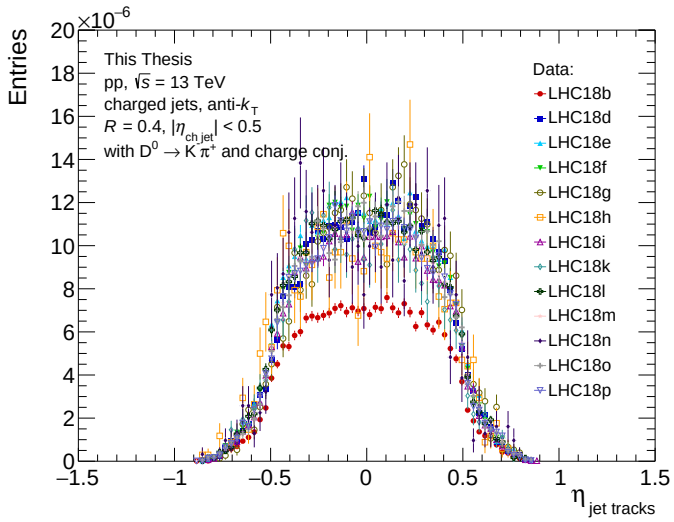

Figure 4.10: The η distributions for D-jets normalised per event from every 2018 period.

Finally, some run numbers in each period were marked by DPG as having an incomplete TPC readout. For example, the φ distribution for D-jets and its tracks for `LHC16o` with incomplete TPC is shown in Figure 4.11. The analysed jets would depend on how many malfunctioning pads there were during the run and the size of the jets that were studied. Even though the φ distribution for jets is smooth, it is not true for its constituents. The missing pads result in a worse quality of tracks, which are rejected afterwards, resulting in a dip in the track distribution. As an observable of this work, $z_{||}^{\mathrm{ch}}$, relies on the jet composition, all run numbers with incomplete TPC readout were rejected from the analysis so as not to bias the results.

The last verification was related to the question of which periods can be merged and processed together. Ideally, each period would be analysed and corrected before merging in the final result. Unfortunately, this is impossible for some periods as they have small statistics, and mass fit extraction will not be possible. Data taking within one year can be treated as stable since no major changes in detector configuration are expected. The periods have been merged within a year, except for `LHC16k` and `LHC16l` that were checked separately

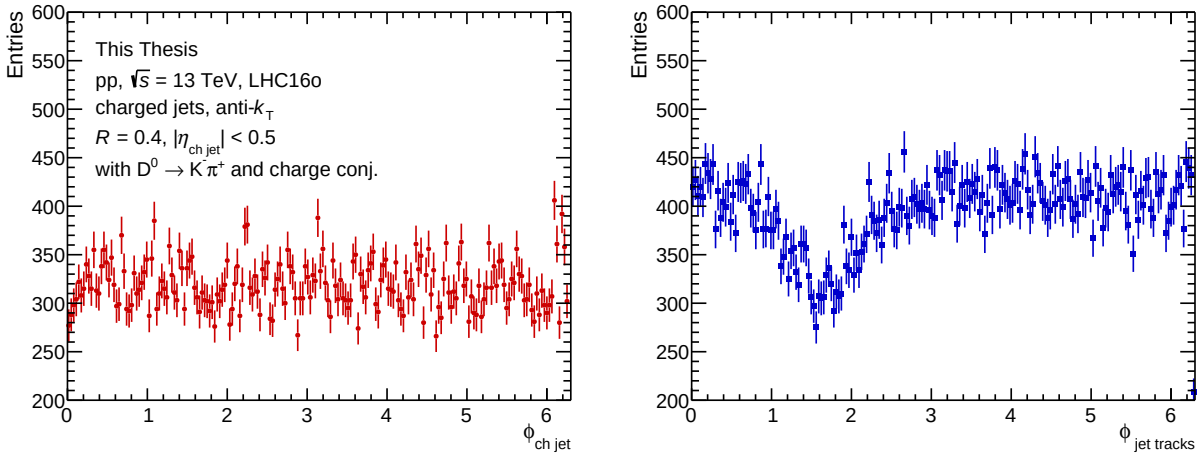

Figure 4.11: The φ distributions for D-jets and its constituents for data from the period `LHC16o` with incomplete TPC readout.

and `LHC18b` that exhibited issues discussed above. One caveat of merging periods could be a problem in the MC description, as the TPC gas changed between years. Another caveat is that the spectra would be corrected by weighted averaged efficiency. This would rely on a correct relative abundance for each period contained in the MC sample.

The luminosity normalised and efficiency corrected $p_{\mathrm{T,ch\,jet}}$ spectra have been compared for different years as shown in Figure 4.12 (left). The $p_{\mathrm{T,ch\,jet}}$ spectra extraction procedure is described in section 4.6. As can be seen, the corrected spectra are consistent with each other except for `LHC18b` due to the problems discussed above. Finally, fully corrected $p_{\mathrm{T,ch\,jet}}$ spectra have been compared and are seen in Figure 4.12 (right). The first sample had all periods (separate `LHC16k+l`, `LHC16*`, `LHC17*`, and `LHC18*`, excluding `LHC18b`) merged at the beginning before signal extraction, the second sample contained same division but were merged at D^0 $p_{\mathrm{T,ch\,jet}}$ cross-section level. As all these tests showed consistency between the periods, it was decided to merge the data at the beginning of the analysis process, simplifying the analysis procedure. The `LHC18b` period was merged with the rest of the sample after its issues had been resolved.

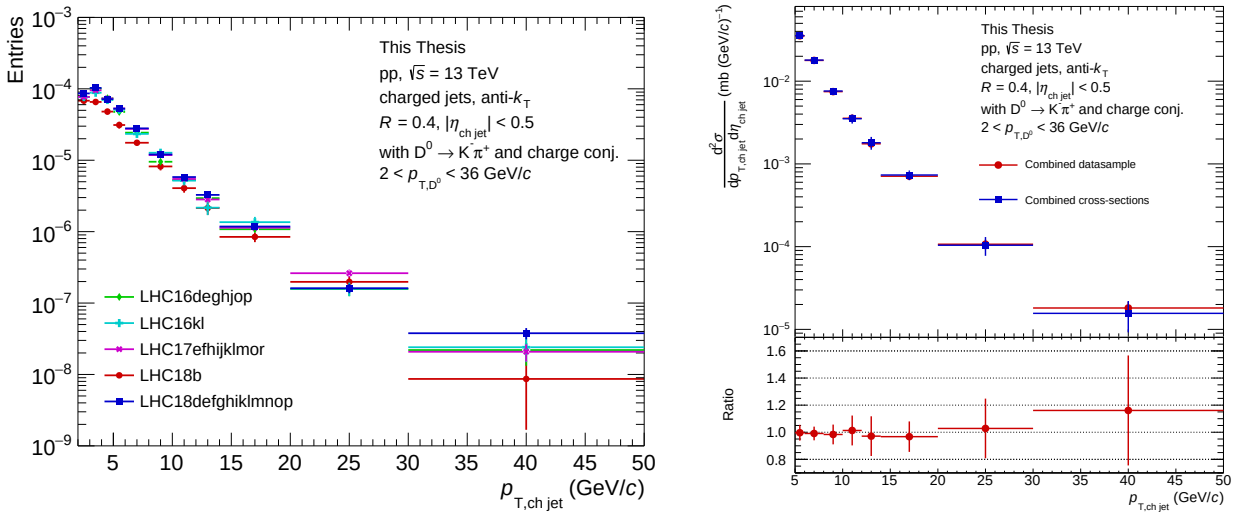

Figure 4.12: Left: Efficiency and number of events corrected $p_{\mathrm{T,ch\,jet}}$ spectra for each year, `LHC16k`, `LHC16l`, and `LHC18b`. Right: Fully corrected $p_{\mathrm{T,ch\,jet}}$ spectra, first sample was fully merged before signal extraction, second, cross-section for each `LHC16k+l`, `LHC16*`, `LHC17*`, `LHC18*`, excluding `LHC18b` periods was extracted and merged.

4.5 Analysis procedure

The D^0s were studied by combining oppositely charged kaons and pions. The D^0 meson and its antiparticle $\bar{D}^0$ were analysed in the same way, thus by referring to D^0 a mixed sample is considered unless otherwise specified. Considered jet resolution parameters (radii) are $R = \{0.2, 0.4, 0.6\}$. To ensure that the whole jet is contained within detector acceptance, the jet axis $\eta_{\mathrm{ch.jet}} < (0.9 - R)$ is required. At lower momenta, the D^0 daughter tracks can be emitted at angles larger than is the jet cone. In order to ensure both kaon and pion are clustered in the same jet, the daughter track four-momenta are removed from the event and replaced by the D^0 candidate four-momentum. In the rare cases where multiple candidates are identified within an event, the procedure is repeated for each candidate separately. The probability to have $1:2:3:4$ candidates in a same event is of order of $1:10^{-2}:10^{-4}:10^{-5}$. For this analysis, only charged-particle tracks are used to reconstruct the jets (charged-

particle jets). The modified events are provided to the FASTJET package to build jets, and only those with D^0 candidates are kept. The jets are clustered using the anti-k_T algorithm with p_T-recombination scheme.

The observables of interest are the $p_{T,jet}$ differential cross-section ($p_{T,ch\,jet}$– as only charged tracks are used to reconstruct jets) and the parallel jet momentum fraction carried by the D^0 ($z_{||}^{ch}$), defined as

$$z_{||}^{ch} = \frac{\vec{p}_{ch.jet} \cdot \vec{p}_{D^0}}{\vec{p}_{ch.jet} \cdot \vec{p}_{ch.jet}}, \tag{4.6}$$

where $\vec{p}_{ch.jet}$ and $\vec{p}_{D^0}$ are the jet and D^0 momentum, respectively. The analysed bins of $p_{T,ch\,jet}$ are defined via bin edges as $\{2, 3, 4, 5, 6, 7, 8, 10, 12, 14, 20, 30, 50\}$ GeV/c with a momentum $p_{T,D} = 2 - 36$ GeV/c for each jet radius R. The analysed $z_{||}^{ch}$ bins are defined via following bin edges $\{0.4, 0.6, 0.7, 0.8, 0.9, 1.0\}$ with $p_{T,ch\,jet}$ and $p_{T,D}$ specified in Table 4.2. The range $p_{T,ch\,jet} = 2 - 5$ GeV/c is kept only for the purpose of unfolding and are not reported as final results. The binning was tuned together with the $\sqrt{s} = 5.02$ TeV analysis[1] so a comparison between different collision energies can be made. Moreover, the D^0 signal in $p_{T,D}$ intervals were optimised for maximal signal-over-background yield.

The analysis workflow can be written as follows:

1. selection of minimum-bias events,
2. selection of D^0 candidates based on kinematic, topological and PID selection,
3. selection of jet tracks based on kinematics and replacement of D^0 daughter tracks by the D^0 four-momentum,
4. reconstruction of jets for each D^0 candidate in an event,
5. extraction of the raw yield in bins of variable of interest ($p_{T,ch\,jet}$, $z_{||}^{ch}$) based on D^0 invariant mass extraction with correction on the reflected mass hypothesis,

[1] paper in preparation

6. D^0 tagging efficiency correction,

7. subtraction of beauty feed-down estimated from MC,

8. $p_{T,ch\,jet}$ resolution correction via the unfolding procedure,

9. normalisation of the distribution,

10. study of systematic uncertainties.

Points 1.-3. were described in section 4.2 and point 4. above. The remaining points will be described in detail in subsequent sections.

Table 4.2: $p_{T,ch\,jet}$ and $p_{T,D}$ intervals for different jet radii R along with a note whether the values were considered for the final results.

R	$p_{T,ch\,jet}$ (GeV/c)	$p_{T,D}$ (GeV/c)	reported
0.2	$2-5$	$2-5$	no
0.2	$5-7$	$2-7$	yes
0.2	$7-10$	$4-10$	yes
0.2	$10-15$	$5-15$	yes
0.2	$15-50$	$10-36$	yes
0.4, 0.6	$2-5$	$2-5$	no
0.4, 0.6	$5-7$	$2-7$	yes
0.4, 0.6	$7-10$	$3-10$	yes
0.4, 0.6	$10-15$	$5-15$	yes
0.4, 0.6	$15-50$	$5-36$	yes

4.6 $p_{\mathrm{T,ch\,jet}}$ cross-section

The goal is to extract the $p_{\mathrm{T,ch\,jet}}$ distribution of a D^0-tagged jet. The analysis is performed differentially in transverse momentum of D^0, $p_{\mathrm{T,D}}$, transverse momentum of D^0-tagged jet, $p_{\mathrm{T,ch\,jet}}$ and jet radius, R. The D^0 signal is extracted in every $p_{\mathrm{T,D}}$ and $p_{\mathrm{T,ch\,jet}}$ bin and corrected by the tagging efficiency as a function of $p_{\mathrm{T,D}}$, which is the product of D^0 reconstruction efficiency and acceptance.

4.6.1 D^0 yields extraction

Invariant mass histograms of correct-sign $K - \pi$ pairs are produced. The measured yields are a mixture of prompt D^0, originating charm quark hard scattering and from decays of excited states of D^0, and non-prompt D^0, originating from beauty decays. The topological selection is not enough to distinguish them and a correction for beauty feed-down is applied and described in section 4.6.2.2. Mass peak signal extraction is performed in order to distinguish the signal from the combinatorial background statistically. The mass distributions are divided in $p_{\mathrm{T,D}}$ intervals defined via bin edges as $\{2,\ 3,\ 4,\ 5,\ 6,\ 7,\ 8,\ 10,\ 12,\ 14,\ 16,\ 24,\ 36\}$ GeV/c. It is assumed that the mass distribution depends on the $p_{\mathrm{T,D}}$ and negligibly on the $p_{\mathrm{T,ch\,jet}}$, thus the considered $p_{\mathrm{T,ch\,jet}}$ interval is $2 - 50$ GeV/c. The invariant mass fits are extracted for each $p_{\mathrm{T,D}}$ bin separately. The fitting is done using an exponential function for the background, a Gaussian function for the signal and a MC reflection function to take into account the reflected mass

$$\frac{\mathrm{d}N}{\mathrm{d}M} = A_{\mathrm{B}} e^{B_{\mathrm{B}} M} + \frac{A_{\mathrm{S}}}{\sqrt{2\pi}\sigma_{\mathrm{S}}} e^{-\frac{(M-B_{\mathrm{S}})^2}{2\sigma_{\mathrm{S}}^2}} + S f(M) f_{\mathrm{R}}, \tag{4.7}$$

- A_{B}, B_{B} – free parameters of the exponential background fit,
- A_{S}, B_{S}, σ_{S} – free parameters of the Gaussian signal fit,

- S – parameter of the signal above the background in the signal peak region obtained iteratively assuming $f_R = 0$ for the first iteration,
- $f(M)$ – fixed normalised reflection template function estimated from the MC,
- f_R – fixed parameter of reflection-over-signal fraction estimated from the MC in a range of $1.7 - 2.1$ GeV/c^2.

One can see that the fitting function (4.7) requires a signal above the background S in the peak region, thus the fitting procedure is done in stages (iterations). First, the distribution is fitted using only the exponential background function with masked signal peak region. Second, the signal above the exponential background fit is estimated. Lastly, the full fit (4.7) is performed. The reflection function shape $f(M)$ and the reflection fraction f_R is extracted from MC and is described in the Section 4.6.1.1. Fitted invariant mass distributions for each $p_{T,D}$ interval of D^0-tagged jets with $R = 0.4$ in pp collisions at $\sqrt{s} = 13$ TeV are shown in Figure 4.13. The background fit contains both the exponential background and the reflection function. The signal region is defined in the interval $(-2\sigma_S, 2\sigma_S)$ and the side-band regions as $(-9\sigma_S, -4\sigma_S)$ and $(4\sigma_S, 9\sigma_S)$, where σ_S is the width of the Gaussian signal peak fit.

4.6.1.1 Reflected mass correction

In cases where PID in data is inconclusive for both K and π, both mass combinations are retained for the candidate construction, which results in double-counting. The daughter track pair of a real D^0 with inconclusive PID corresponds to one signal and one background entry. These two pairs are added in the invariant mass distributions. Two background entries are added for D^0 candidate pair, which does not correspond to a real D^0. To estimate the rate and invariant mass shape introduced by this reflected mass procedure, a MC must be used. The same PID selection as in data is applied on the MC sample with the difference

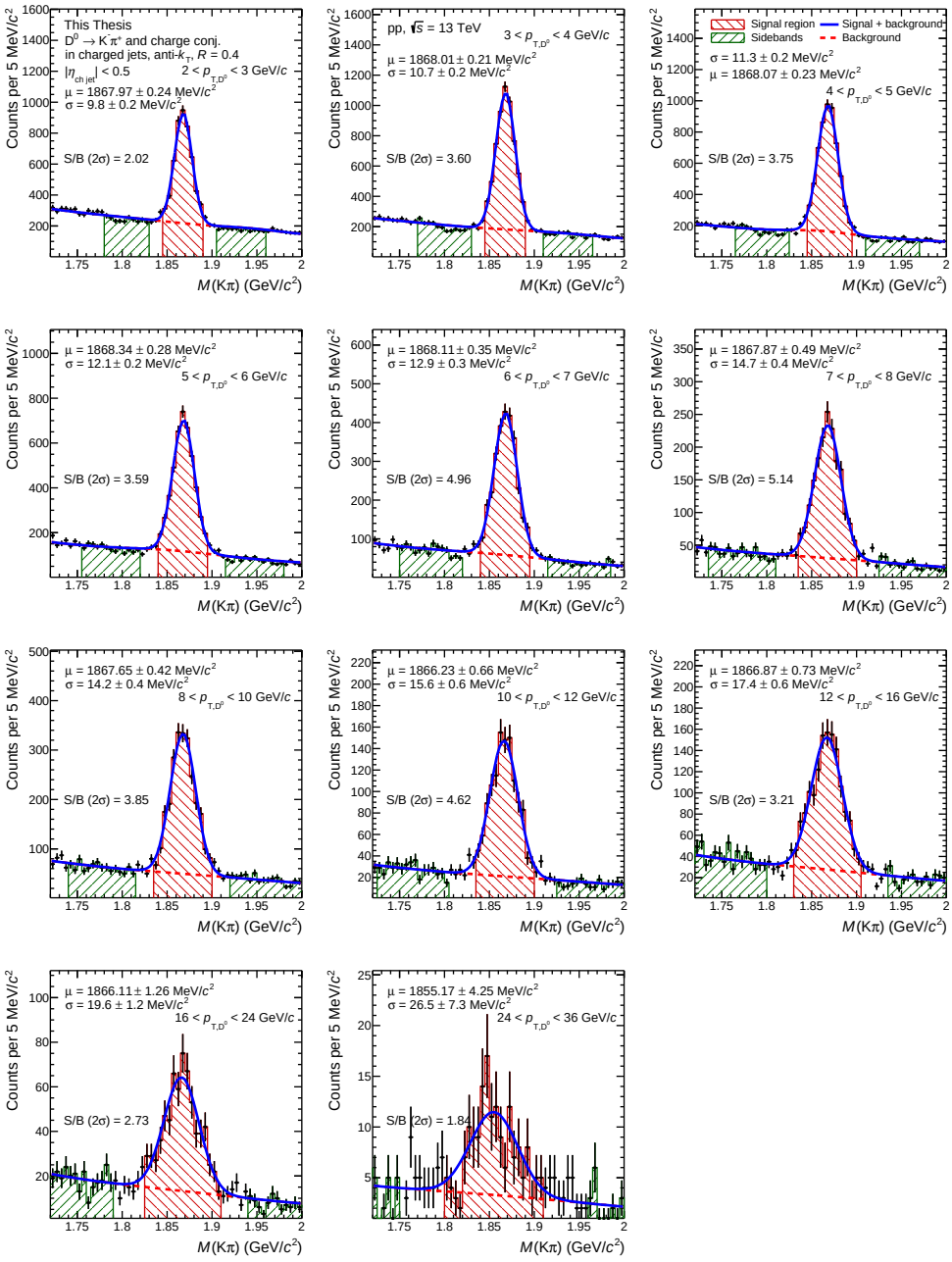

Figure 4.13: The invariant mass fits for each of the $p_{\mathrm{T,D}}$ interval of D^0-tagged jets with $R = 0.4$ in pp collisions at $\sqrt{s} = 13$ TeV. The background fit contains both exponential combinatorial background and double-Gaussian reflection function. The signal region is defined as $(-2\sigma_{\mathrm{S}}, 2\sigma_{\mathrm{S}})$ (red) and the side-band regions as $(-9\sigma_{\mathrm{S}}, -4\sigma_{\mathrm{S}})$ and $(4\sigma_{\mathrm{S}}, 9\sigma_{\mathrm{S}})$ (green).

that the candidate D^0s true nature is known. For the candidate pairs in MC, both mass hypotheses m_1 and m_2 corresponding to D^0 and $\overline{D^0}$ are calculated by assuming the PDG masses for daughter tracks. Then the masses are distributed between signal and reflected mass distributions as follows:

1. if the D^0 ($\overline{D^0}$) can be correctly identified $m_1(m_2)$ fills the signal distribution
2. if the PID is inconclusive, but the combination belongs to D^0, m_1 fills the signal distribution, while m_2 fills the reflected mass distribution
3. if the PID is inconclusive, but the combination belongs to $\overline{D^0}$, m_2 fills the signal distribution, while m_1 fills the reflected mass distribution

The signal distribution is fitted by a Gaussian function

$$g(M) = \frac{A}{\sqrt{2\pi}\sigma} \mathrm{e}^{-\frac{(M-B)^2}{2\sigma^2}}, \tag{4.8}$$

where A, σ and B are the free fit parameters of Gaussian distribution. The reflected mass distributions is fitted by a double-Gaussian function

$$h(M) = \frac{A_1}{\sqrt{2\pi}\sigma_1} \mathrm{e}^{-\frac{(M-B_1)^2}{2\sigma_1^2}} + \frac{A_2}{\sqrt{2\pi}\sigma_2} \mathrm{e}^{-\frac{(M-B_2)^2}{2\sigma_2^2}}, \tag{4.9}$$

where A_1, σ_1, B_1, A_2, σ_2 and B_2 are the free fit parameters. Fit functions $g(M)$ and $h(M)$ for three $p_{\mathrm{T,D}}$ intervals of D^0 mesons in pp collisions at $\sqrt{s} = 13$ TeV are shown in Figure 4.15. The reflection over background ratio f_{R} is then defined by integrating over the analysed mass range $m = (1.7 - 2.1)$ GeV/c^2 as

$$f_{\mathrm{R}} = \frac{\int_{1.7}^{2.1} h(M)\mathrm{d}M}{\int_{1.7}^{2.1} g(M)\mathrm{d}M}. \tag{4.10}$$

Figure 4.14 shows the ratio f_R as function of $p_{\mathrm{T,D}}$ of D^0 in pp collisions at $\sqrt{s} = 13$ TeV. The reflection function $f(M)$ is a normalised probability density calculated as

$$f(M) = \frac{h(M)}{\int_{1.7}^{2.1} h(M)\mathrm{d}M}. \tag{4.11}$$

The values of f_{R} and $f(M)$ are calculated separately for each $p_{\mathrm{T,D}}$ interval considered for invariant mass extraction.

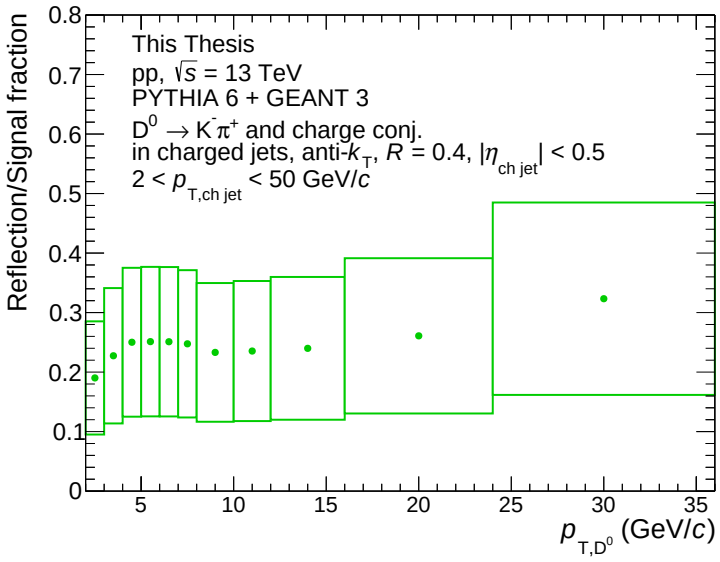

Figure 4.14: The reflection over signal f_{R} fraction as a function of $p_{\mathrm{T,D}}$ of D^0 meson in pp collisions at $\sqrt{s}$ = 13 TeV estimated using PYTHIA 6 + GEANT 3 with a uncertainty given by ±50% variation of a function f_{R}.

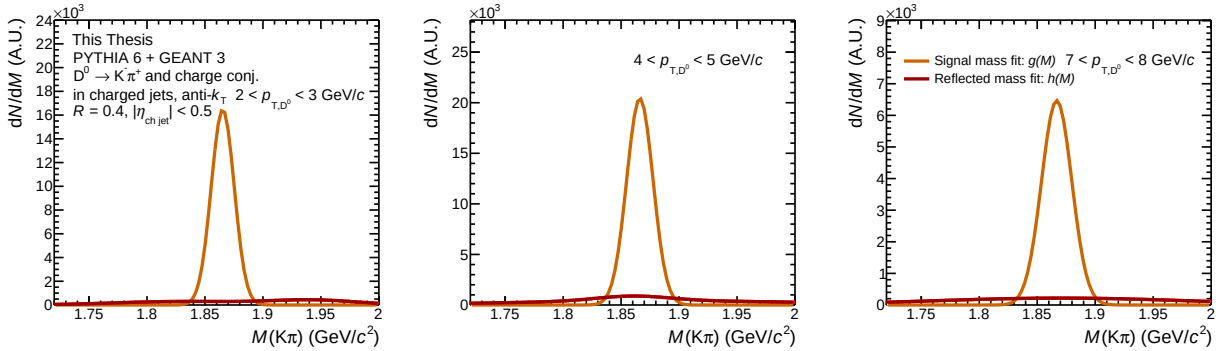

Figure 4.15: The Gaussian signal peak and double-Gaussian reflected mass fits for three $p_{\mathrm{T,D}}$ regions of D^0 meson in pp collisions at $\sqrt{s}$ = 13 TeV simulated by using PYTHIA 6 + GEANT 3.

4.6.1.2 $p_{T,ch\,jet}$ yield extraction

In the previous section, the D^0 mass fits and yield have been performed independently of $p_{T,ch\,jet}$. In this section, a $p_{T,ch\,jet}$-dependent yield will be calculated using those fitting parameters. The signal region of D^0 meson mass distribution for each of the $p_{T,D}$ bins has been identified as $(-2\sigma_S, 2\sigma_S)$ and the side-bands regions as $(-9\sigma_S, -4\sigma_S)$ and $(4\sigma_S, 9\sigma_S)$. The choice of $2\sigma_S$ over the commonly used $3\sigma_S$ for the signal is due to this analysis being sensitive to signal-over-background. Especially in the higher $p_{T,D}$ intervals, where the signal-over-background is low, the three-sigma interval caused unreliable signal extraction due to the background contamination. For the sake of clarity, the following indexation will be used: side-band (SB), peak (P) region, background (B), reflection (R), and signal (S) contribution. The total yield in the side-bands $Y^{SB} = Y^{L,SB} + Y^{R,SB}$ is defined as a sum of respective left and right side-band regions. These contributions to yield are depicted in Figure 4.16.

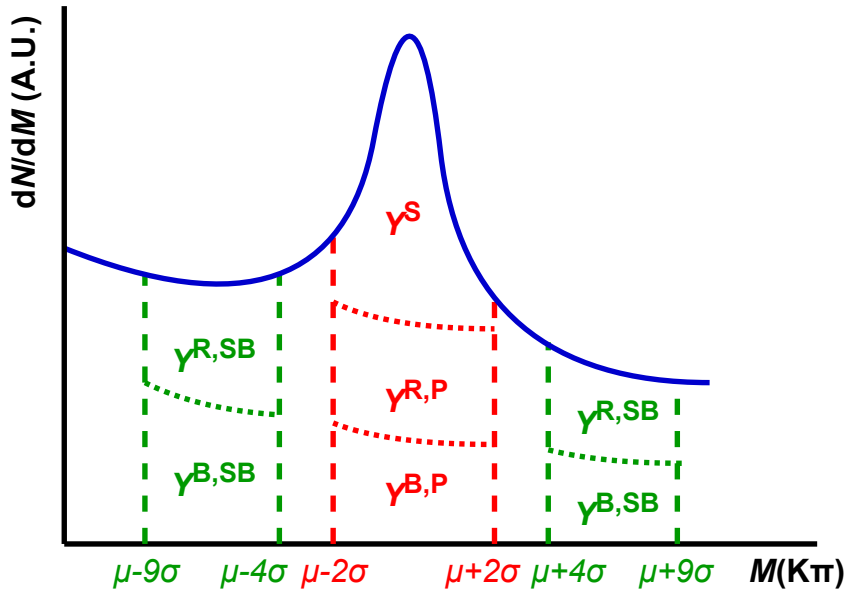

Figure 4.16: The invariant mass histogram with depicted yields Y in side-band (SB), peak (P) region for combinatorial background (B), reflection (R), and signal (S) contribution. Ranges are defined by the mean μ and standard deviation σ of the Gaussian signal peak fit.

The total yield in peak region Y^{P} is defined as a sum of the signal Y^{S}, background $Y^{\mathrm{B,P}}$, and reflection $Y^{\mathrm{R,P}}$ contributions. The letter Y_i is used for the D^0 spectra yields integrated over $p_{\mathrm{T,ch\,jet}}$, obtained from the mass fits described in the previous chapter. The index i denotes the transverse momentum of the D meson $p_{\mathrm{T,D}}$.

The letter $N_{i,j}$ is used for two-dimensional yields where index i denotes $p_{\mathrm{T,D}}$ and index j denotes the transverse momentum of jet $p_{\mathrm{T,ch\,jet}}$. Similarly, the peak region contains contributions from a signal, combinatorial background and reflection. The background and reflection subtracted yield is then

$$N_{i,j}^{\mathrm{S}} = N_{i,j}^{\mathrm{P}} - N_{i,j}^{\mathrm{B,P}} - N_{i,j}^{\mathrm{R,P}}, \tag{4.12}$$

where the background contribution in peak region can be extracted from side-bands as

$$N_{i,j}^{B,P} = (N_{i,j}^{SB} - N_{i,j}^{R,SB})\frac{Y_i^{B,P}}{Y_i^{B,SB}}. \tag{4.13}$$

The peak yield $N_{i,j}^{\mathrm{P}}$ is extracted from the $(-2\sigma_{\mathrm{S}}, 2\sigma_{\mathrm{S}})$ region of D^0 mass and the side-band N_j^{SB} is extracted from the $(-9\sigma_{\mathrm{S}}, -4\sigma_{\mathrm{S}})$ and $(4\sigma_{\mathrm{S}}, 9\sigma_{\mathrm{S}})$ mass regions. The peak width σ_{S} and the scaling ratio $Y_i^{B,P}/Y_i^{B,SB}$ are extracted from $p_{\mathrm{T,ch\,jet}}$ integrated invariant mass distributions. These parameters are expected not to depend on jet momentum and they are used in order to suppress statistical fluctuations. The next step is to properly address the reflections which contribution scales as signal. The reflection contributions are estimated assuming they are independent of $p_{\mathrm{T,ch\,jet}}$ as they are the result of identifying D^0 itself. The reflection in the peak, $N_{i,j}^{R,P}$, and side-band, $N_{i,j}^{R,SB}$, regions can be written as

$$N_{i,j}^{R,P} = N_{i,j}^{S}\frac{Y_i^{R,P}}{Y_i^{S}}, \tag{4.14}$$

and

$$N_{i,j}^{R,SB} = N_{i,j}^{S}\frac{Y_i^{R,SB}}{Y_i^{S}}. \tag{4.15}$$

Putting everything together, the D-tagged $N_{i,j}^{\mathrm{S}}$ signal can be expressed as a function of the

peak $N^{\mathrm{P}}_{i,j}$ and side-band $N^{\mathrm{SB}}_{i,j}$ as:

$$\begin{aligned} N^{\mathrm{S}}_{i,j} &= N^{\mathrm{P}}_{i,j} - \frac{Y_i^{\mathrm{B,P}}}{Y_i^{\mathrm{B,SB}}}\left(N^{\mathrm{SB}}_{i,j} - \frac{Y_i^{\mathrm{R,SB}}}{Y_i^{\mathrm{S}}}N^{\mathrm{S}}_{i,j}\right) - \frac{Y_i^{\mathrm{R,P}}}{Y_i^{\mathrm{S}}}N^{\mathrm{S}}_{i,j} \\ N^{\mathrm{S}}_{i,j} &= \left(N^{\mathrm{P}}_{i,j} - \frac{Y_i^{\mathrm{B,P}}}{Y_i^{\mathrm{B,SB}}}N^{\mathrm{SB}}_{i,j}\right)\left(\frac{Y_i^{\mathrm{S}}}{Y_i^{\mathrm{S}} + Y_i^{\mathrm{R,P}} - \frac{Y_i^{\mathrm{B,P}}}{Y_i^{\mathrm{B,SB}}}Y_i^{\mathrm{R,SB}}}\right) \end{aligned} \tag{4.16}$$

The $p_{\mathrm{T,ch\,jet}}$ yields for D^0-tagged jets with $R = 0.4$ in pp collisions at $\sqrt{s} = 13$ TeV for each $p_{\mathrm{T,D}}$ bin are shown in Figure 4.17, where the signal region $N^{\mathrm{P}}_{i,j}$, normalised side-bands $\frac{Y_i^{\mathrm{B,P}}}{Y_i^{\mathrm{B,SB}}}N^{\mathrm{SB}}_{i,j}$, and the background subtracted, reflection corrected $N^{\mathrm{S}}_{i,j}$ yields are shown. Ideally, a full $p_{\mathrm{T,ch\,jet}}$ spectra correction for each $p_{\mathrm{T,D}}$ bin should be done separately. As is shown in Figure 4.17, the statistics in the large $p_{\mathrm{T,D}}$ bins do not allow it and would cast significant uncertainties in the further steps. Thus, the total $p_{\mathrm{T,ch\,jet}}$ spectra are created by summing over the $p_{\mathrm{T,D}}$ bins as

$$N_j^{\mathrm{raw}} = \frac{1}{0.9545}\sum_{i \in p_{\mathrm{T,D}}} N^{\mathrm{S}}_{i,j}, \tag{4.17}$$

the scaling factor $1/0.9545$ is there as the signal was extracted from the $2\sigma_{\mathrm{S}}$ range only.

4.6.2 Corrections

The correction procedure consists of the following steps

- correct raw yield for the D^0 tag reconstruction efficiency and acceptance as a function of $p_{\mathrm{T,D}}$,
- subtract b-quark decay feed-down from the raw D-tagged jet yields,
- unfold the spectra for detector-related effects on $p_{\mathrm{T,ch\,jet}}$.

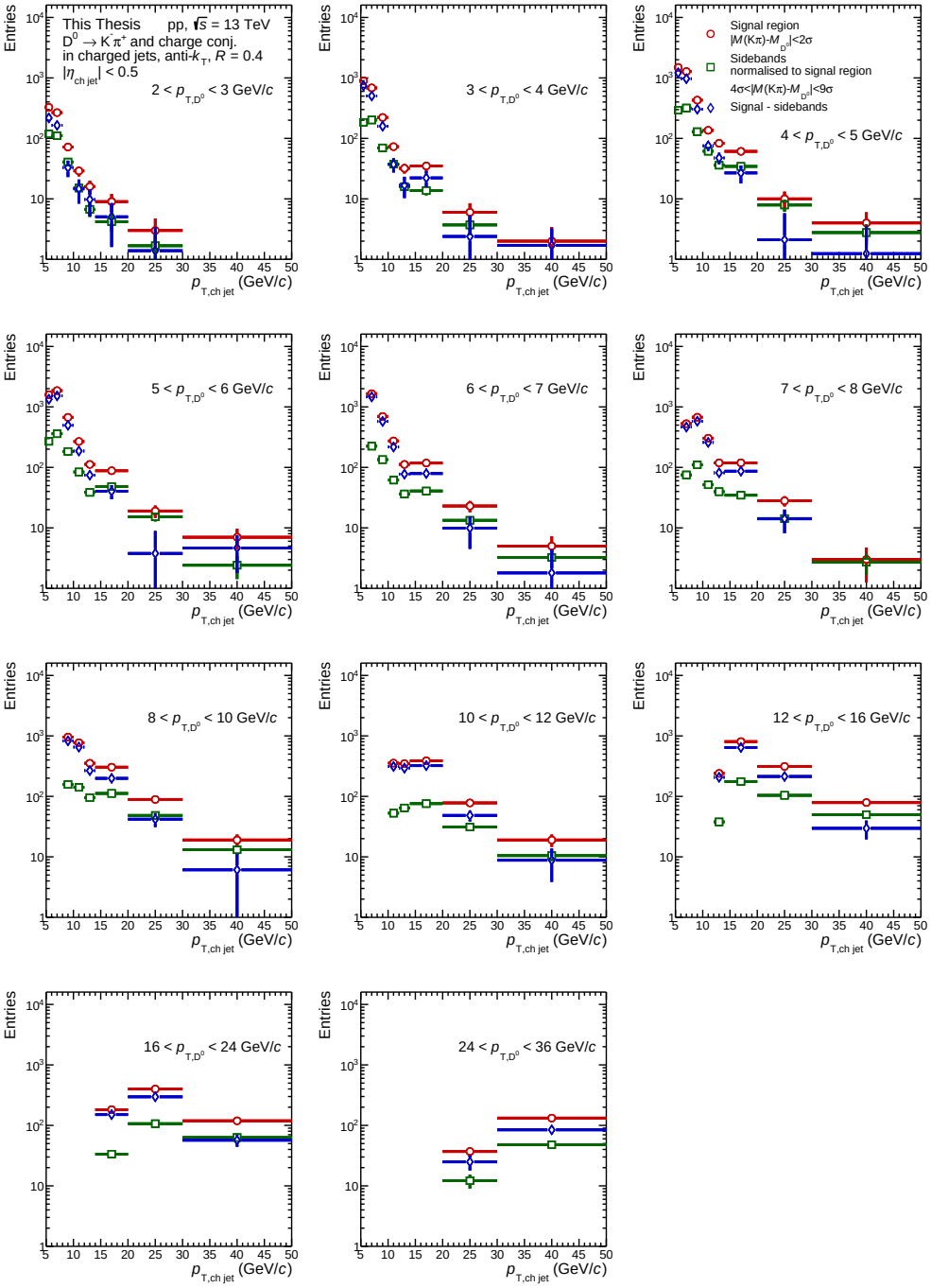

Figure 4.17: The $p_{\mathrm{T,ch\,jet}}$ distribution for D^0-tagged jets with $R = 0.4$ in pp collisions at $\sqrt{s} = 13$ TeV for each $p_{\mathrm{T,D}}$ bin with the signal (red circle), normalised side-bands (green squares), and background subtracted reflection corrected (blue diamond) yields.

4.6.2.1 Reconstruction efficiency

The products of acceptance and reconstruction efficiency are used to address tracking efficiencies, kinematic selection of candidates and the limited acceptance of the detectors. As the jets are identified via a particular D^0 meson, the efficiency correction of the $p_{T,\text{ch jet}}$ spectra is done as a function of $p_{T,D}$. The D^0 detector efficiency is roughly related to a product of the K and π tracking efficiencies. Further reduction is imposed by the topological selection on the D^0 and by kinematics restrictions in pseudorapidity. The efficiency was calculated using PYTHIA 6 + GEANT 3 and is defined as a ratio of number of D^0 found in the detector, d, over the generated number of D^0, g, as a function of D^0 generated momentum, p^{gen}_{T,D^0},

$$\epsilon_i = \frac{d\left(p^{\text{gen}}_{T,D^0}\right)}{g\left(p^{\text{gen}}_{T,D^0}\right)}. \tag{4.18}$$

As the $p_{T,D}$ resolution on D^0 in pp collisions is better than the studied $p_{T,D}$ bin widths, the efficiency was calculated as a function of p^{gen}_{T,D^0}. The $p_{T,D}$ dependent efficiencies are extracted for both prompt D^0 mesons, ϵ^{c}_i, and for non-prompt D^0, ϵ^{b}_i, and an example for $R = 0.4$ D^0-tagged jets with $p_{T,\text{ch jet}} = 5 - 50$ GeV/c in pp collisions at $\sqrt{s} = 13$ TeV is shown in Figure 4.18 (right).

The efficiency is produced as a function $p_{T,D}$ for a fixed $p_{T,\text{ch jet}} > 5$ GeV/c intervals, it has negligible dependence on $p_{T,\text{ch jet}}$ as can be seen in Figure 4.18 (left) where the efficiencies overlap for every selection of $p_{T,\text{ch jet}}$. The region $p_{T,\text{ch jet}} == 2 - 5$ GeV/c, on the other hand, shows up to 10% $p_{T,\text{ch jet}}$ dependence on the efficiency corrected $p_{T,\text{ch jet}}$ spectra. However, as this region is kept for the unfolding purpose described in section 4.6.2.3 and is not reported, a $p_{T,\text{ch jet}} = 5 - 50$ GeV/c was used to generate the efficiency. This means the $p_{T,\text{ch jet}} = 2 - 5$ GeV/c region is corrected by an imprecise efficiency and will impact the reported region $p_{T,\text{ch jet}} = 5 - 50$ GeV/c due to the unfolding smearing. It has been verified that imposing $p_{T,\text{ch jet}} = 5 - 50$ GeV/c efficiency has 1% effect on the $p_{T,\text{ch jet}} = 5 - 6$ GeV/c

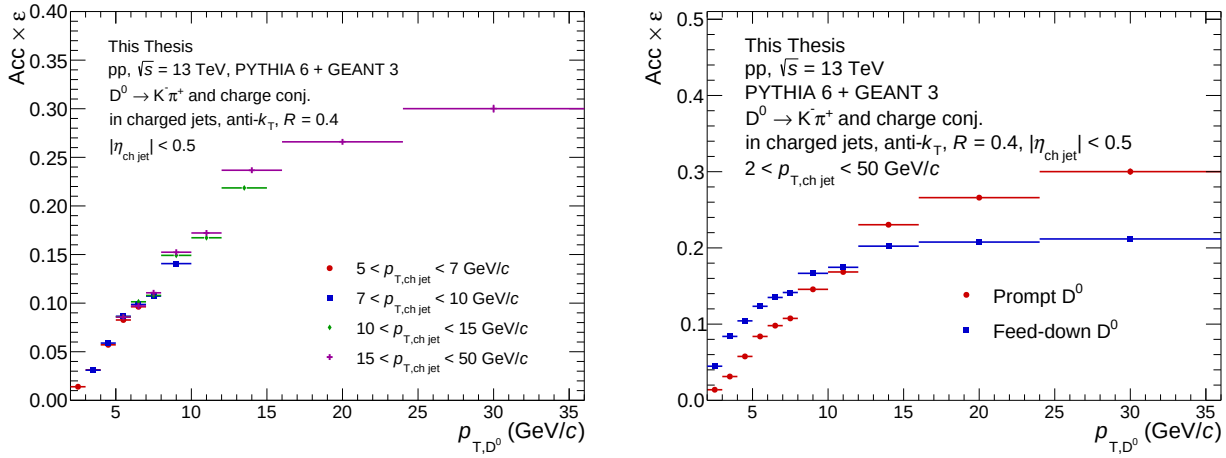

Figure 4.18: Left: The prompt ϵ_i^{c} product of acceptance and reconstruction efficiencies for D^0-tagged jets with $R = 0.4$ in different bins of $p_{\mathrm{T,ch\,jet}}$. Right: The prompt ϵ_i^{c} and non-prompt ϵ_i^{b} efficiencies for D^0-tagged jets with $R = 0.4$ with $p_{\mathrm{T,ch\,jet}} = 5 - 50$ GeV/c in pp collisions at $\sqrt{s} = 13$ TeV.

in comparison to $p_{\mathrm{T,ch\,jet}}$ dependent efficiency.

The prompt efficiency is then applied for jet spectra in each $p_{\mathrm{T,D}}$ bin modifying (4.17) into

$$N_j^{\mathrm{eff.corr.}} = \frac{1}{0.9545} \sum_{i \in p_{\mathrm{T,D}}} N_{i,j}^{\mathrm{raw}} \frac{1}{\epsilon_i^{\mathrm{c}}}. \tag{4.19}$$

The efficiency corrected measured $p_{\mathrm{T,ch\,jet}}$ spectrum $N^{\mathrm{eff.corr.}}$ for D^0-tagged jets with $R = 0.4$ in pp collisions at $\sqrt{s} = 13$ TeV is shown in Figure 4.19.

4.6.2.2 Beauty Feed-Down Subtraction

Currently, the ALICE ITS does not allow to fully separate between prompt and non-prompt D^0 mesons. After the upgrade of the ITS [126], in Run 3 ALICE will be able to distinguish between prompt and non-prompt D^0 experimentally. To calculate the non-prompt fraction, ALICE usually uses the FONLL [104, 105] method, as described in analyses [127, 128]. This

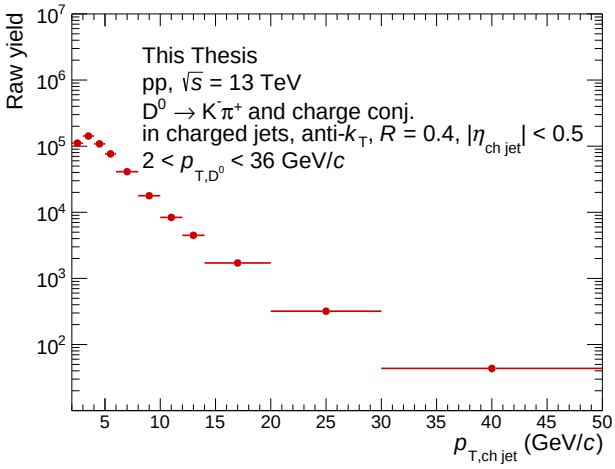

Figure 4.19: The efficiency and bin width corrected $p_{\mathrm{T,ch\,jet}}$ spectrum for D^0-tagged jets with $R = 0.4$ in pp collisions at $\sqrt{s}$ = 13 TeV.

method cannot be adopted in this work as it only provides the fraction as a function of $p_{\mathrm{T,D}}$. The non-prompt fraction as a function of the $p_{\mathrm{T,D}}$, $p_{\mathrm{T,ch\,jet}}$ and $z_{||}^{\mathrm{ch}}$ with given jet resolution parameter R, clustering algorithm and recombination scheme is needed to correct D^0-tagged jets properly. Thus a POWHEG-hvq with $\mathrm{b\bar{b}}$ process coupled with PYTHIA 6 event generator and CT10 NLO PDF with LHAPDF 6 interpolator has been used. In addition, a EVTGEN has been used as a beauty hadron decayer.

The correction on feed-down contribution is to subtract the simulated non-prompt contribution, $N_j^{sim,\mathrm{b}\to\mathrm{D}^0}$, from the measured mixed sample, $N_j^{\mathrm{eff.corr.}}$. First, the simulation must be normalised on the data sample sizes as

$$\frac{\sigma_{\mathrm{pp-inelastic,sim}}}{N_{\mathrm{sim}}} \frac{N_{\mathrm{data}}}{\sigma_{\mathrm{V0AND,data}}} = \frac{\mathscr{L}_{\mathrm{data}}}{\mathscr{L}_{\mathrm{sim}}}, \tag{4.20}$$

where the σ, N, and $\mathscr{L}$ is the cross-section, number of events, and luminosity, respectively, for the measured sample and generated simulation. Second, as only D^0 in a given decay channel are measured, the simulated sample is multiplied by a D^0 branching ratio, $f_{\mathrm{BR}} = (3.950 \pm 0.031)\%$ [1]. Lastly, to reduce the required computing resources, propagation

through the ALICE detector by GEANT package has not been used. Instead, the generated feed-down yield, $N_{km}^{sim,\ b\to D^0}$, is done in a separate $p_{T,D}$ and $p_{T,ch\,jet}$ bins, and is multiplied by the non-prompt efficiency, ϵ_k^b, and folded with the detector response matrix as a form of a "fast" simulation. The feed-down contribution is written as

$$N_m^{\prime sim,\ b\to D^0} = \frac{\mathscr{L}_{data}}{\mathscr{L}_{sim}} f_{BR} \sum_{k\in p_{T,D}^{gen}} (N_{km}^{sim,\ b\to D^0} \frac{\epsilon_k^b}{\epsilon_k^c}). \tag{4.21}$$

The measured, mixed prompt and non-prompt sample $N_j^{eff.corr.}$ is corrected only by the prompt efficiency ϵ_i^c. Thus the $N_{km}^{sim,\ b\to D^0}$ is scaled by ϵ^c to address it. The final step is to fold $N_m^{\prime sim,\ b\to D^0}$ with non-prompt response matrix $\mathcal{R}^b$ in order to impose detector smearing on the $p_{T,ch\,jet}$. As both measured and simulated samples were scaled by prompt efficiency ϵ_i^c, the detector level is weighted by the prompt efficiency to give the $p_{T,ch\,jet}$ smearing proper weights as

$$\mathcal{R}_{j,m}^{+,b} = \sum_{i\in p_{T,D}^{det}} \left(\mathcal{R}_{j,m,i}^{b} \frac{1}{\epsilon_i^c} \right), \tag{4.22}$$

where $\mathcal{R}_{j,m}^{+,b}$ is number of reconstructed objects in j-th measured bin of $p_{T,ch\,jet}^{det}$ originating from m-th generated bin of $p_{T,ch\,jet}^{gen}$, normalised in the total number of generated objects in m-th bin. The non-prompt response matrix $\mathcal{R}^{+,b}$ for $R = 0.4$ jets is shown in Figure 4.20. Finally, the response matrix is normalised as

$$\mathcal{R}_{j,m}^{*,b} = \frac{\mathcal{R}_{j,m}^{+,b}}{\sum_{j\in p_{T,ch\,jet}^{det}} \mathcal{R}_{j,m}^{+,b}}, \tag{4.23}$$

meaning that only smearing is applied. The folded spectrum is then

$$N_j^{b\to D^0} = \sum_{m\in p_{T,ch\,jet}^{gen}} \mathcal{R}_{j,m}^{*,b} N_m^{\prime sim,\ b\to D^0}. \tag{4.24}$$

The response matrix contains only fully matched entries (entries with information on both detector and particle levels). It does not include entries that are inside the generated $p_{T,ch\,jet}^{gen}$ range but outside the detector $p_{T,ch\,jet}^{det}$ range or that are inside the detector range but outside the generated range. These "inefficiencies" and "impurities" are then injected

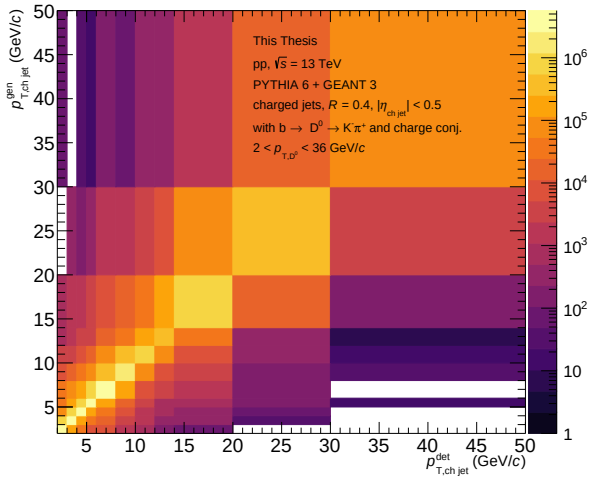

Figure 4.20: The non-prompt response matrix $\mathcal{R}^{+,\mathrm{b}}_{j,m}$ for non-prompt D^0-tagged jets with $R = 0.4$ in pp collisions at $\sqrt{s} = 13$ TeV.

into the simulations as follows. The first contamination described entries that lie inside the detector range d_j^{in} but are outside the generated range g_j^{out}

$$\epsilon_j^{\mathrm{b,\ det}} = \frac{d_j^{\mathrm{in}} \wedge g^{\mathrm{in}}}{(d_j^{\mathrm{in}} \wedge g^{\mathrm{in}}) + (d_j^{\mathrm{in}} \wedge g^{\mathrm{out}})} = \frac{d_j^{\mathrm{in}} \wedge g^{\mathrm{in}}}{d_j^{\mathrm{in}}} \tag{4.25}$$

and it divides folded spectra. The second source of contamination addresses entries of the response matrix that lie outside the detector range d_j^{out} but are inside the generated range g_j^{in}

$$\epsilon_m^{\mathrm{b,\ gen}} = \frac{d^{\mathrm{in}} \wedge g_m^{\mathrm{in}}}{(d^{\mathrm{in}} \wedge g_m^{\mathrm{in}}) + (d^{\mathrm{out}} \wedge g_m^{\mathrm{in}})} = \frac{d^{\mathrm{in}} \wedge g_m^{\mathrm{in}}}{g_m^{\mathrm{in}}}. \tag{4.26}$$

and it multiplies the spectra prior folding. Equation (4.24) then modifies into

$$N_j^{\mathrm{b}\to\mathrm{D}^0} = \frac{1}{\epsilon_j^{\mathrm{b,\ det}}} \sum_{m \in p_{\mathrm{T,ch\,jet}}^{\mathrm{gen}}} \mathcal{R}^{*,\mathrm{b}}_{j,m} \epsilon_m^{\mathrm{b,\ gen}} N_m^{\prime \mathrm{sim,\ b}\to\mathrm{D}^0}. \tag{4.27}$$

Finally, the feed-down contribution is subtracted from the measured sample as

$$N_j^{\mathrm{c}\to\mathrm{D}^0} = N_j^{\mathrm{eff.corr.}} - N_j^{\mathrm{b}\to\mathrm{D}^0} \tag{4.28}$$

The feed-down fraction $N_j^{\mathrm{b}\to\mathrm{D}^0}/N_j^{\mathrm{eff.corr.}}$ for $R = 0.4$ D^0-tagged jets in pp collisions at $\sqrt{s} = 13$ TeV is shown in Figure 4.21 (left). The measured $N_j^{\mathrm{eff.corr.}}$ and feed-down sub-

tracted $N_j^{\mathrm{c}\to\mathrm{D}^0}$ spectra, and a feed-down contribution $N_j^{\mathrm{b}\to\mathrm{D}^0}$ for D^0-tagged jets with $R = 0.4$ in pp collisions at $\sqrt{s}$ = 13 TeV are shown in Figure 4.21 (right).

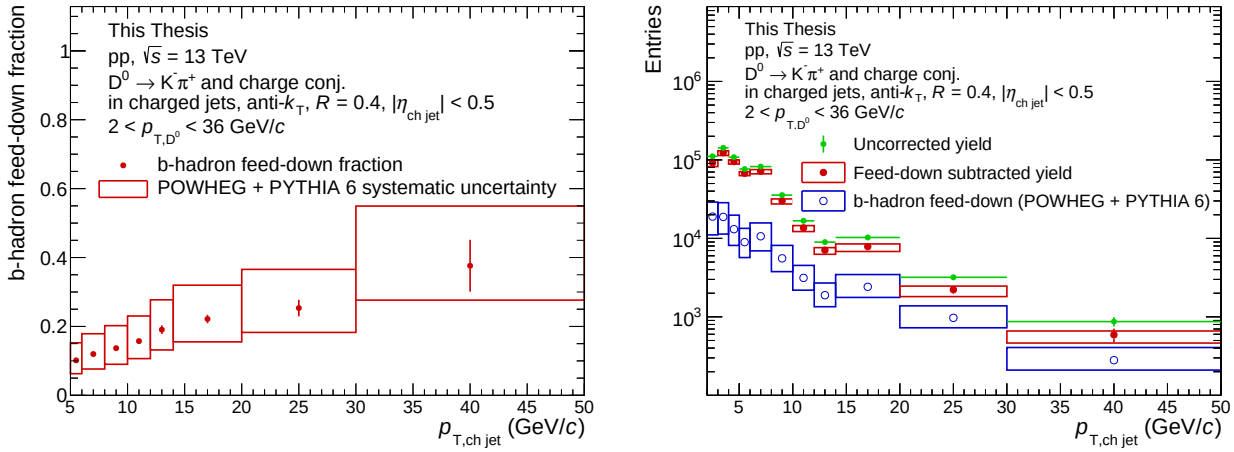

Figure 4.21: Left: The feed-down fraction for D^0-tagged jets with $R = 0.4$ in pp collisions at $\sqrt{s}$ = 13 TeV. Right: The efficiency corrected measured mixed sample of D^0 tagged jets with $R = 0.4$ in pp collisions at $\sqrt{s}$ = 13 TeV (green), beauty feed-down contribution simulated using POWHEG + PYTHIA 6 (blue), and feed-down subtracted jet spectra (red).

4.6.2.3 Unfolding

The last step consists of unfolding the measured prompt distribution, $N_j^{\mathrm{c}\to\mathrm{D}^0}$, by a prompt response matrix to address the finite detector precision and smearing on the sample. As the measured sample has already been corrected by the efficiency, only a fully-matched (generated entries have been found in the detector) response matrix has been used. Similarly to the feed-down matrix, it was re-weighted by the efficiency to correct the weights

$$\mathcal{R}_{j,m}^{+,\mathrm{c}} = \sum_{i \in p_{\mathrm{T,D}}^{\mathrm{det}}} \left(\mathcal{R}_{j,m,i}^{\mathrm{c}} \frac{1}{\epsilon_i^c} \right). \tag{4.29}$$

A response matrix $\mathcal{R}^{+,\mathrm{c}}$ for D^0-tagged jets with prompt D^0 and $R = 0.4$ in pp collisions at $\sqrt{s}$ = 13 TeV is shown in Figure 4.22 (left). A relative $p_{\mathrm{T,ch\,jet}}$ resolution, defined as $\Delta p_{\mathrm{T}} = \left(p_{\mathrm{T,chjet}}^{\mathrm{det}} - p_{\mathrm{T,chjet}}^{\mathrm{gen}}\right) / p_{\mathrm{T,chjet}}^{\mathrm{gen}}$, is shown in Figure 4.22 (right).

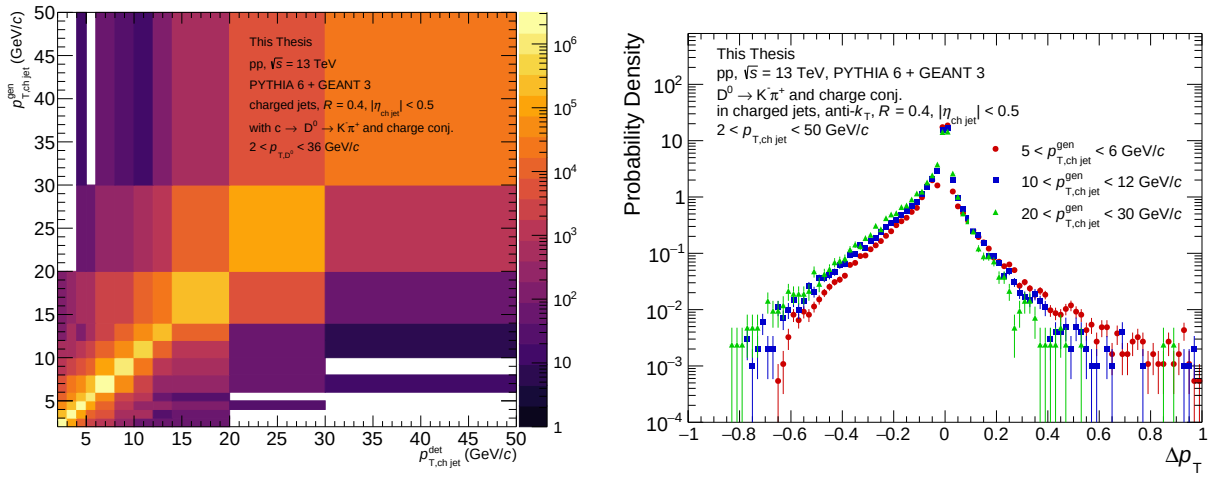

Figure 4.22: Left: A response matrix of fully-matched entries $\mathcal{R}^{+,\mathrm{c}}$ for D^0-tagged jets with $R = 0.4$ in pp collisions at $\sqrt{s} = 13$ TeV. Right: Probability density distributions of $\Delta p_{\mathrm{T}} = \left(p^{\mathrm{det}}_{\mathrm{T,chjet}} - p^{\mathrm{gen}}_{\mathrm{T,chjet}}\right)/p^{\mathrm{gen}}_{\mathrm{T,chjet}}$ for D^0-tagged jets with $R = 0.4$ in pp collisions at $\sqrt{s} = 13$ TeV.

The measured spectra must be corrected for entries that lie outside the generated range but are inside the detector range of the response matrix $\mathcal{R}^{+,\mathrm{c}}_{j,m}$ as defined in (4.25). The measured spectrum is multiplied (as opposed to folding) by a factor $\epsilon^{\mathrm{c,\ det}}_{j}$

$$N^{*}_{j} = N^{\mathrm{c}\to\mathrm{D}^0}_{j}\,\epsilon^{\mathrm{c,\ det}}_{j}. \tag{4.30}$$

The RooUnfold package [129] is used to carry out the unfolding. In a first step, the response matrix $\mathcal{R}^{+,\mathrm{c}}_{j,m}$ is normalised to the total number of generated jets as

$$\mathcal{R}^{*,\mathrm{c}}_{j,m} = \frac{\mathcal{R}^{+,\mathrm{c}}_{j,m}}{n_m}, \tag{4.31}$$

where $\mathcal{R}^{+,\mathrm{c}}_{j,m}$ is number of reconstructed objects in the j-th measured bin originating from the m-th generated bin and n_m is the total number of generated jets in the m-th bin. Since the provided response matrix contains only reconstructed entries $n_m = \sum_{j\in p^{\mathrm{det}}_{\mathrm{T,ch\,jet}}} \mathcal{R}^{+,\mathrm{c}}_{j,m}$. Secondly, a Bayesian unfolding as defined in [129] is performed. The k-th iteration is

$$N^{k}_{m} = \sum_{j\in p^{\mathrm{det}}_{\mathrm{T,ch\,jet}}} \left[\frac{\mathcal{R}^{*,\mathrm{c}}_{j,m} P^{k-1}_{m}}{\epsilon_m \sum_{l\in p^{\mathrm{gen}}_{\mathrm{T,ch\,jet}}} \left(\mathcal{R}^{*,\mathrm{c}}_{jl} P^{k-1}_{l}\right)} N^{*}_{j} \right], \tag{4.32}$$

where the priors are

$$P_m^k \begin{cases} \frac{N_m^k}{\sum_{m\in p_{\mathrm{T,ch\,jet}}^{\mathrm{gen}}} N_m^k} & (k>0) \\ \frac{n_m}{\sum_{m\in p_{\mathrm{T,ch\,jet}}^{\mathrm{gen}}} n_m} & (k=0) \end{cases} \tag{4.33}$$

and the efficiency $\epsilon_m = \sum_{l\in p_{\mathrm{T,ch\,jet}}^{\mathrm{det}}} \mathcal{R}_{lm}^{*,\mathrm{c}}$ is equal to $\vec{1}$ as the response matrix contains only entries that were reconstructed and is self-normalised per measured bins. This is the intended behaviour as the spectra are already corrected by $p_{\mathrm{T,D}}$ efficiency before unfolding. Finally, the $k = 5$ iteration was chosen for the regularisation, and the spectra are corrected on entries that lie inside the generated range but are outside the detector range of the response matrix as defined in (4.26) and the unfolded spectra is divided by it

$$N_m^{\mathrm{unfolded}} = N_m^5 \frac{1}{\epsilon_m^{\mathrm{c,\ gen}}}. \tag{4.34}$$

Another important aspect is how to choose the amount of regularisation (iteration). There are several methods how to determine a proper choice [130], e.g. χ^2 and Pearson correlation. The Pearson correlation method was used in this thesis. A covariance matrix, $(V_{mm})^k$, of the k-th iteration of unfolded spectra describes the statistical uncertainties between bins. In the case of fully statistically independent bins, the matrix is diagonal. A Pearson correlation coefficient is defined as

$$\rho_{xy}^k = \frac{\left((V_{mm})^k\right)_{xy}}{\sqrt{\left((V_{mm})^k\right)_{xx}}\sqrt{\left((V_{mm})^k\right)_{yy}}}. \tag{4.35}$$

A $\rho_{xy} = +1$ corresponds to full correlation between bin x and y, $\rho_{xy} = 0$ to no correlation and $\rho_{xy} = -1$ to full anti-correlation. The Pearson correlation coefficient for $1-6$th iteration of D^0-tagged jets with $R = 0.4$ in pp collisions at $\sqrt{s} = 13$ TeV is shown in Figure 4.23. The unfolded spectra are expected to have a strong correlation between bins close to each other, the 1st iteration is positively correlated because of smearing, and thus more iterations are needed. The best choice of regularisation is when the next-to-diagonal bins exhibit a mild anti-correlation, so $k \geq 3$ is suitable. A strong anti-correlation would mean an oscillation pattern appeared, and the spectra are weakly regularised (too many iterations). A refolding

and closure test have been performed to verify a good choice of the regularisation. The unfolded spectra are folded back using the response matrix and compared to measured values as seen in Figure 4.24. The refolded spectra are closer to the original measured values with increased iterations. The 5-th iteration has been chosen for the regularisation as a more conservative value. The measured $N_j^{c\to D^0}$, unfolded spectra with Bayesian method with 5-th iteration, N_m^{unfolded}, and refolded spectra is shown in Figure 4.25 (left).

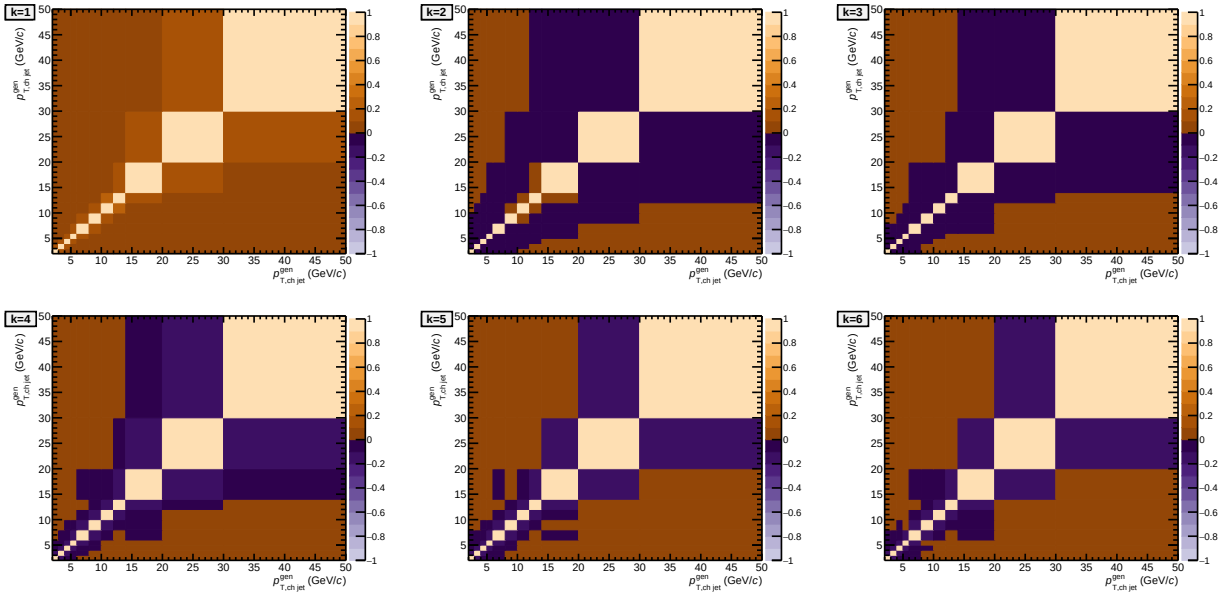

Figure 4.23: Pearson correlation coefficient for k-th iteration of D^0-tagged jets with $R = 0.4$ in pp collisions at $\sqrt{s}$ = 13 TeV.

A closure test for the 5-th iteration is shown in Figure 4.25 (right). The MC sample used to fill the response matrix for unfolding has been randomly split between the closure test response matrix and a test sample in a fraction of 80:20. The large $p_{T,ch\,jet}$ is described within statistical uncertainties, while the lower $p_{T,ch\,jet}$ show a discrepancy larger than 1σ. This will be discussed more in detail in section 4.6.3.7 while studying the systematic uncertainty of the unfolding procedure. In the same section, other tests to verify the stability of the unfolding will be presented.

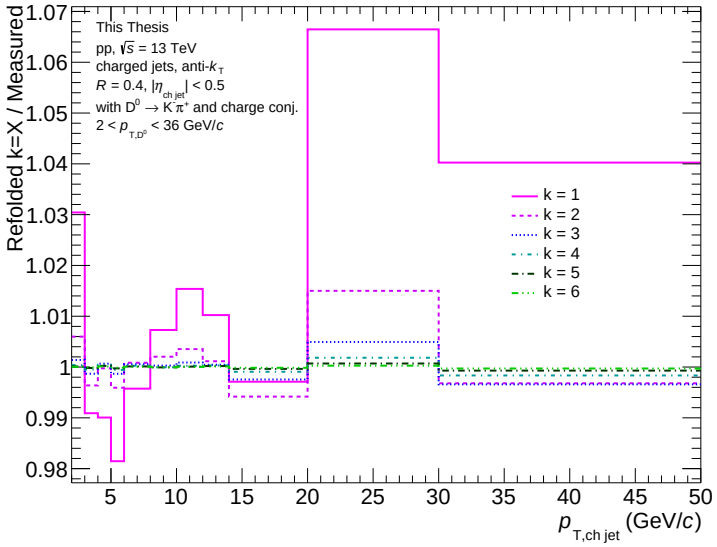

Figure 4.24: Ratio of refolded to measured spectra for k-th iteration of D^0-tagged jets with $R = 0.4$ in pp collisions at $\sqrt{s}$ = 13 TeV.

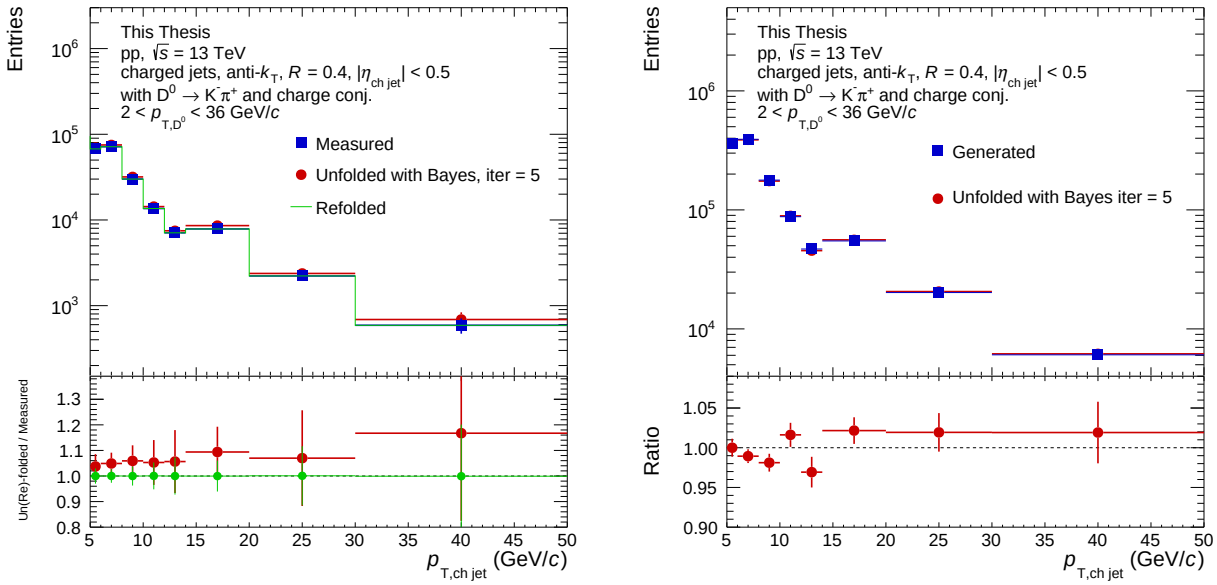

Figure 4.25: Left: Measured, unfolded, and refolded spectra of D^0-tagged jets with $R = 0.4$ in pp collisions at $\sqrt{s}$ = 13 TeV. Right: Closure test for D^0-tagged jets with $R = 0.4$ in pp collisions at $\sqrt{s}$ = 13 TeV. The division of MC is done randomly between response matrix and test sample in a ratio of 80:20.

4.6.3 Systematic uncertainties

The systematic uncertainties are estimated in order to determine a bias given by the selections and choices made in the analysis. They can be divided into several groups: uncertainty of the raw yield extraction, tracking efficiency, topological selection, feed-down contribution, unfolding and cross-section normalisation.

4.6.3.1 Raw yield extraction

Fitting procedure To verify the stability of the mass fitting procedure a several variation (trials) has been performed while extracting the D^0 fitting parameters. The following variations were considered for the D^0 mean and width

- free width σ, free mean m_{D^0},
- fixed width $\sigma = \sigma_{MC}$, free mean m_{D^0},
- fixed width $\sigma = 0.85 \cdot \sigma_{MC}$, free mean m_{D^0},
- fixed width $\sigma = 1.15 \cdot \sigma_{MC}$, free mean m_{D^0},
- free width σ, fixed mean $m_{D^0} = m_{PDG}$,
- fixed width $\sigma = \sigma_{MC}$, fixed mean $m_{D^0} = m_{PDG}$.

and following variations were considered on the fitting procedure

- background functions: exponential, linear,
- lower limit of fit range: 1.72, 1.74 GeV/c^2,
- upper limit of fit range: 2.00, 2.03 GeV/c^2,
- mass bin width: 5 MeV/c^2, 10 MeV/c^2.

This results in a total number of $6 \cdot (2 \cdot 2 \cdot 2 \cdot 2) = 96$ trials. The configuration of the central values is: free width σ, free mean m_{D^0}, exponential background, 1.71 GeV/c^2, 2.1 GeV/c^2 fitting range limits, and 5 MeV/c^2 bin width. This is done for each $p_{\mathrm{T,D}}$ bin, an example for $p_{\mathrm{T,D}} = 2 - 3$ GeV/c is shown in Figure 4.26.

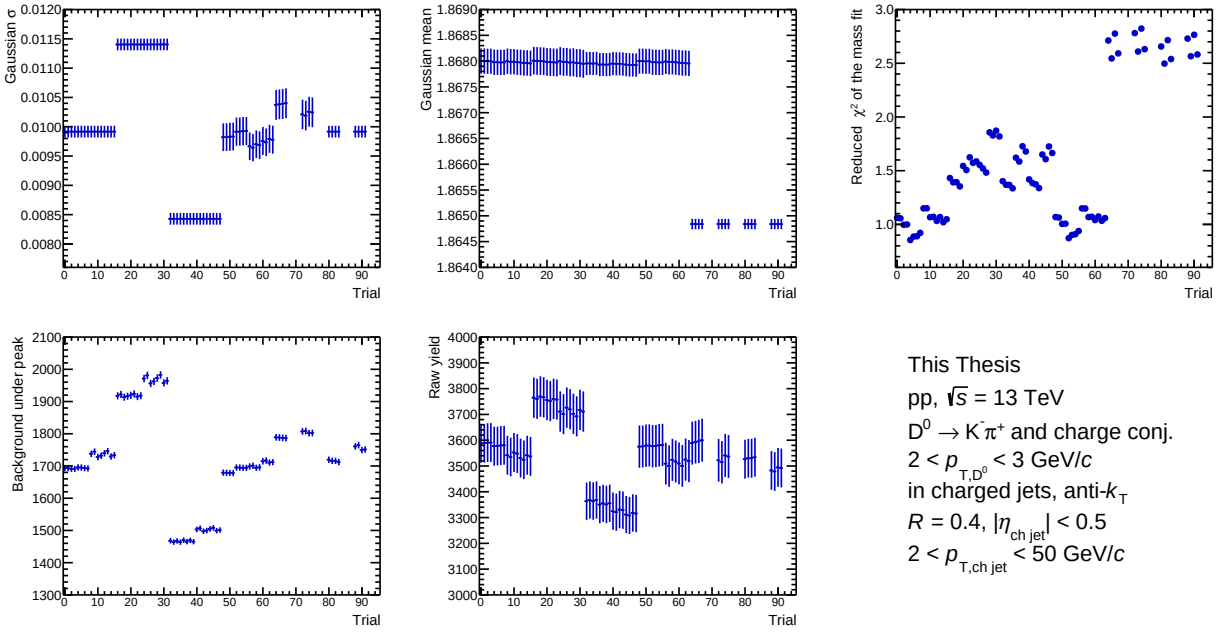

Figure 4.26: Signal peak width σ, mean mass, χ^2 of the fit, background under the signal peak and background subtracted yield for multiple signal extraction trials in $p_{\mathrm{T,D}} = 2 - 3$ GeV/c for D^0 in $R = 0.4$ jets in pp collisions at $\sqrt{s} = 13$ TeV.

As not always all 96 trials are successful in extracting the mass fits, a randomised selection of 40 trials out of the successful trials is made for each $p_{\mathrm{T,D}}$ bin. Using this sub-sample of trials 40 jet spectra are built following the procedure described in section 4.6.1.2. A ratio of each trial to the yield with default settings for D^0-tagged jets with $R = 0.4$ in pp collisions at $\sqrt{s} = 13$ TeV is shown in Figure 4.27 (left). The uncertainty of the mass fit extraction is calculated as the Root Mean Square (RMS) of the deviations from the mean value of the trials and for D^0-tagged jets with $R = 0.4$ in pp collisions at $\sqrt{s} = 13$ TeV is shown in Figure 4.27 (right).

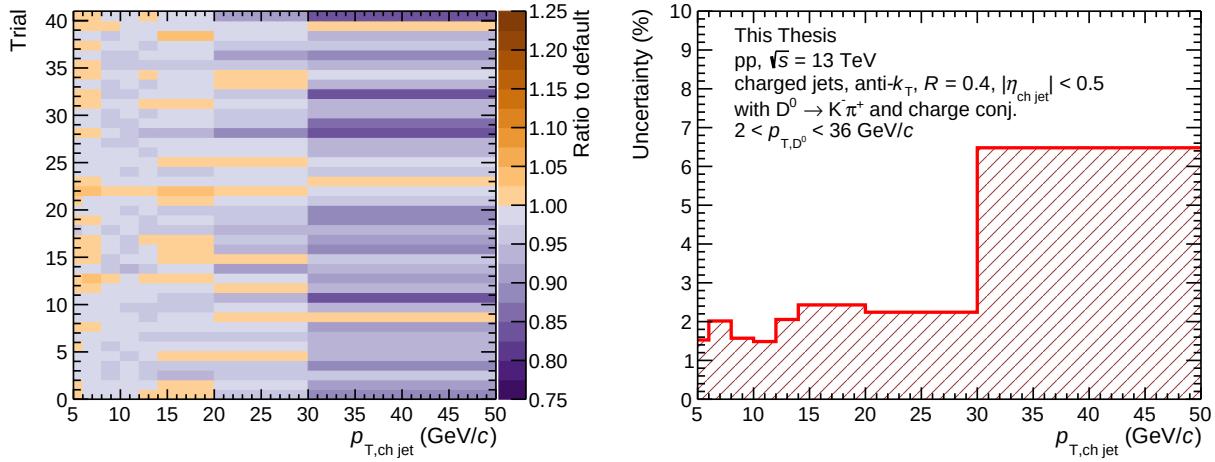

Figure 4.27: Left: Ratio of $p_{\mathrm{T,ch\,jet}}$ yield for each trial to the yield with default settings of D^0-tagged jets with $R = 0.4$ in pp collisions at $\sqrt{s} = 13$ TeV. Right: Uncertainty of the mass fitting procedure calculated as a ratio of RMS and mean of the trials of D^0-tagged jets with $R = 0.4$ in pp collisions at $\sqrt{s} = 13$ TeV.

Signal and background bands definition The signal area is defined as Gaussian 2σ distance from the Gaussian mean on both sides. The central side-band regions are defined as -9σ to -4σ and 4σ to -9σ. A following variations were considered

- signal: 2σ; side-bands: -8σ to -3σ and 3σ to 8σ
- signal: 2σ; side-bands: -10σ to -4σ and 4σ to 10σ
- signal: 2σ; side-bands: -12σ to -4σ and 4σ to 12σ
- signal: 2σ; side-bands: -15σ to -4σ and 4σ to 15σ
- signal: 3σ; side-bands: -9σ to -4σ and 4σ to 9σ
- signal: 3σ; side-bands: -12σ to -4σ and 4σ to 12σ

A ratio of each variation to the central values for D^0-tagged jets with $R = 0.4$ in

pp collisions at $\sqrt{s}$ = 13 TeV is shown in Figure 4.28 (left). A systematic uncertainty is calculated as RMS and is shown in Figure 4.28 (right).

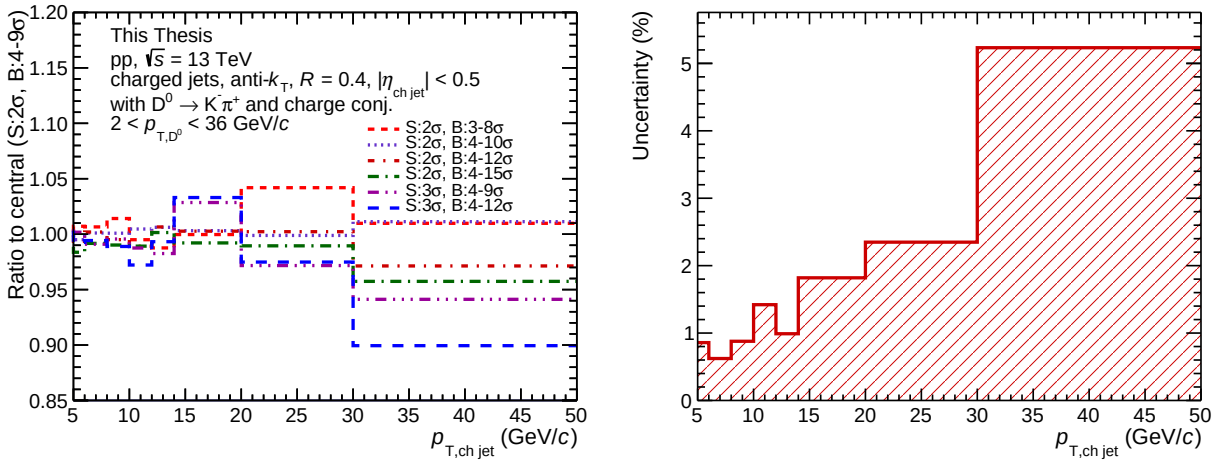

Figure 4.28: Left: Ratio of $p_{\mathrm{T,ch\,jet}}$ yield for signal and background bands region definition to central yield of D^0-tagged jets with $R = 0.4$ in pp collisions at $\sqrt{s}$ = 13 TeV. Right: Uncertainty of the signal and background bands region definition calculated as a ratio of RMS to the central value of D^0-tagged jets with $R = 0.4$ in pp collisions at $\sqrt{s}$ = 13 TeV.

Reflection over signal fraction The last parameter in the fitting procedure is the reflection over signal f_{R} fraction. This fraction relies on a particle identification description between data and MC, the fraction has been conservatively varied by ±50%. A ratio of the variations to the central value for D^0-tagged jets with R = 0.4 in pp collisions at $\sqrt{s}$ = 13 TeV is shown in Figure 4.29 (left). A systematic uncertainty is calculated as a maximum variation and is shown in Figure 4.29 (right).

4.6.3.2 D^0-tracking reconstruction efficiency uncertainty

This uncertainty covers the uncertainty arising from the track quality selection of the daughter tracks, track finding in the TPC and track propagation from the TPC to the ITS. It is

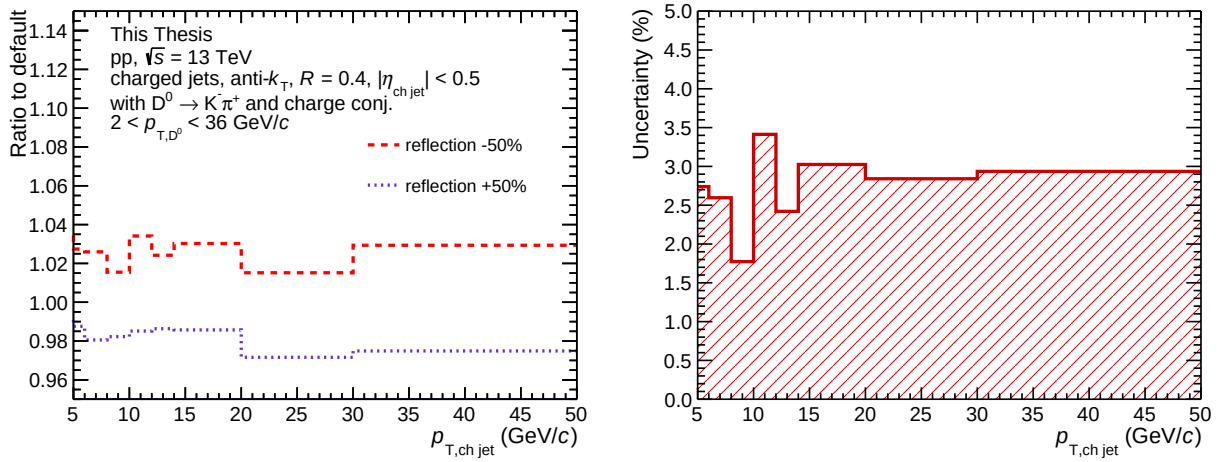

Figure 4.29: Left: Ratio of $p_{\mathrm{T,ch\,jet}}$ yield for both reflection over signal variation of D^0-tagged jets with $R = 0.4$ in pp collisions at $\sqrt{s}$ = 13 TeV. Right: Uncertainty of the reflection over signal variation calculated as a maximum variation for the D^0-tagged jets with $R = 0.4$ in pp collisions at $\sqrt{s}$ = 13 TeV.

important for the cross-section measurement as the D^0 particle has been used as a jet tag. It composes of two main ingredients

- Comparison of efficiency corrected D^0 yields produced with different TPC track selection
- Comparing the TPC-ITS matching efficiency between data and MC

TPC track quality Alongside the default selection described in section 4.2.3 the following variation of TPC track selection criteria were considered

- TPC crossed rows larger then $120 - \frac{5}{p_{\mathrm{T,\ track}}}$
- number of TPC clusters larger than 0.65 number of TPC crossed rows
- ratio of crossed rows over findable cluster in TPC larger than 0.9

The efficiency corrected D^0 yields of the variations are compared to the default yields. The systematic uncertainty of the TPC track quality is then calculated as a spread of this comparison, and for the D^0 in pp collisions at $\sqrt{s}$ = 13 TeV is shown in Figure 4.30 (left).

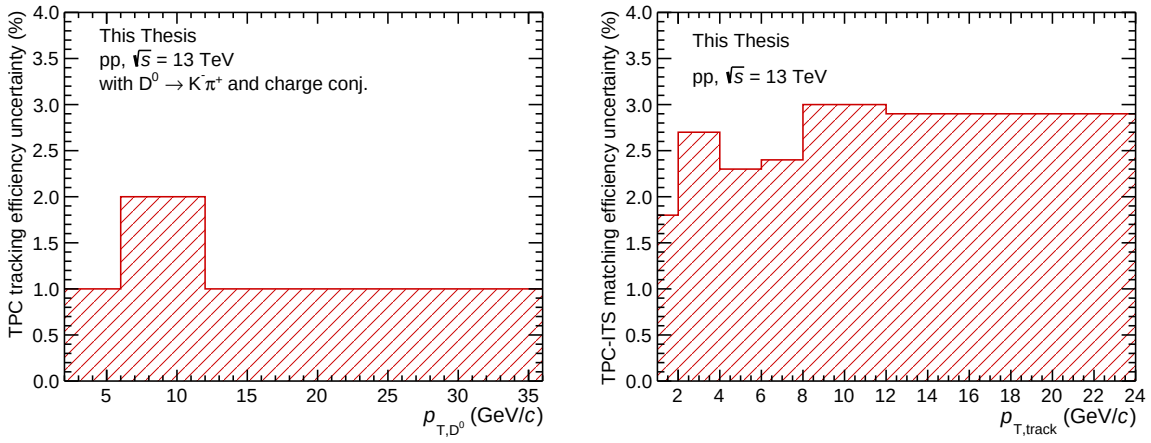

Figure 4.30: Left: The uncertainty on TPC tracking efficiency for D^0 in pp collisions at $\sqrt{s}$ = 13 TeV. Right: The uncertainty of TPC-ITC matching for tracks in pp collisions at $\sqrt{s}$ = 13 TeV.

TPC-ITS matching efficiency uncertainty The matching efficiency is defined as a fraction of tracks that have clusters in both TPC and ITS over tracks that have clusters in the TPC. The efficiency in the MC is calculated separately for primary tracks originating from the primary vertex and secondary tracks originating from decays. The primary tracks have efficiency around 0.9 while the efficiency of the secondary track drops steeply with p_{T} from around 0.8 down to 0.2. This is because the particles decay on the edge of the ITS, and thus, not complete information is available. The discrepancy in the fraction of primary tracks between data and MC would lead to a wrong estimation of the uncertainty. In the first step, an actual fraction of primary tracks in the data $f^{Data}_{\mathrm{primary}}$ is estimated by template fitting. In a second step, a corrected inclusive MC efficiency is calculated as

$$\epsilon^{MC}_{\mathrm{inclusive}} = f^{Data}_{\mathrm{primary}} \epsilon^{MC}_{\mathrm{primary}} + \left(1 - f^{Data}_{\mathrm{primary}}\right) \epsilon^{MC}_{\mathrm{secondary}}, \tag{4.36}$$

where $\epsilon^{MC}_{\text{primary}}$ and $\epsilon^{MC}_{\text{secondary}}$ are the respective TPC-ITS matching efficiencies from MC. The uncertainty is then defined as

$$\delta_{\text{TPC-ITS}} = \frac{\epsilon^{Data}_{\text{inclusive}} - \epsilon^{MC}_{\text{inclusive}}}{\epsilon^{Data}_{\text{inclusive}}}, \tag{4.37}$$

where $\epsilon^{Data}_{\text{inclusive}}$ is the matching efficiency in data. The uncertainty is estimated as p_{T}-dependent for each period by the Data Preparation Group. The systematic uncertainty is averaged between periods and final value for $\sqrt{s} = 13$ TeV pp collisions data sample is shown in Figure 4.30 (right).

The final step consists of propagating the TPC tracking uncertainty and the TPC-ITS matching uncertainty to the D^0 level with given daughter kinematics and PID. The matching uncertainty for the daughter tracks is added together and then added in quadrature with the TPC tracking uncertainty. The $p_{\text{T,D}}$-dependent tracking uncertainty map for D^0 in pp collisions at $\sqrt{s} = 13$ TeV is shown in Figure 4.31 (left) and a final uncertainty calculated as weighted average is shown in Figure 4.31 (right). As the TPC-ITS uncertainty has not been evaluated for every period and a non-weighted average has been used, given that the final tracking uncertainty is only mildly dependent on $p_{\text{T,D}}$, it has been decided to use flat 5% for the jet analysis. This is to avoid the propagation to $p_{\text{T,ch jet}}$ and $z^{\text{ch}}_{||}$, which would not be as trivial.

4.6.3.3 Jet Momentum Resolution

The effect of tracking uncertainty for the D^0 daughters as described in section 4.6.3.2 is also present for other tracks in the jets. This will influence the $p_{\text{T,ch jet}}$ while building the response matrix for both folding and unfolding. As seen in the Section 4.6.3.2, the TPC tracking uncertainty is around 0.5-1% per track and the TPC-ITS matching uncertainty around 2-3%. A second response matrix for both feed-down and prompt D^0 has been created with randomly discarded 4% of tracks. The full analysis procedure has been repeated, and

the cross-section was compared to the default case and is shown in Figure 4.32 (left). The difference is taken as the uncertainty and is shown in Figure 4.32 (right).

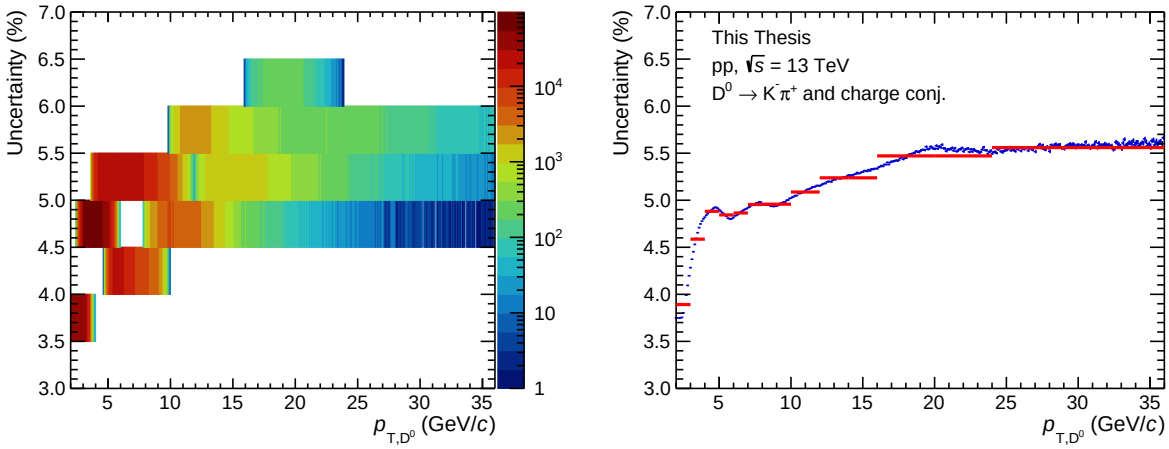

Figure 4.31: Left: The total tracking uncertainty map, containing both TPC tracking and TPC-ITS matching uncertainties, propagated to D^0 level in pp collisions at $\sqrt{s}$ = 13 TeV. Right: The total tracking uncertainty calculated as a weighted average from the map for D^0 in pp collisions at $\sqrt{s}$ = 13 TeV.

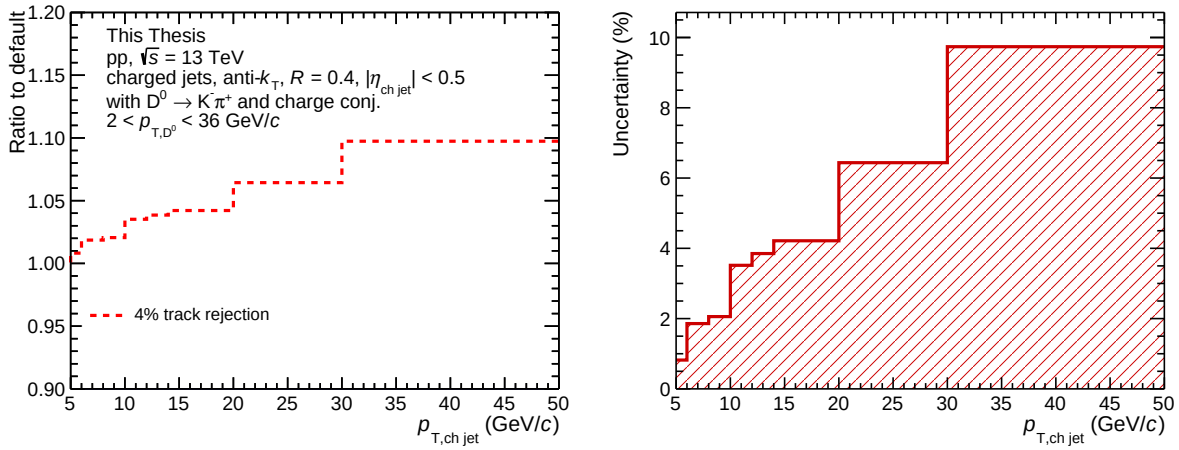

Figure 4.32: Left: The ratios of D^0-tagged jet cross-section for analysis with 4% removed tracks from response matrices of $R = 0.4$ jets in pp collisions at $\sqrt{s}$ = 13 TeV. Right: The jet energy scale uncertainty calculated as a difference for $R = 0.4$ D^0-tagged jets in pp collisions at $\sqrt{s}$ = 13 TeV.

4.6.3.4 Generated D^0 $p_{T,D}$ shape

This systematic covers the uncertainty of efficiency by assuming a different model for generating the shape of $p_{T,D}$ spectra. By default, a GEANT 3 + PYTHIA 6 is used to calculate the efficiency. The second set of efficiency has been prepared in which the p_T spectrum was re-weighted to address the difference in shape between the PYTHIA and FONLL prediction. The uncertainty is defined as a relative difference between efficiencies of these two sets of models, and for D^0 in pp collisions at $\sqrt{s} = 13$ TeV is shown in Figure 4.33. As the uncertainty is negligible in the studied $p_{T,D}$ region, it was rounded down to 0%.

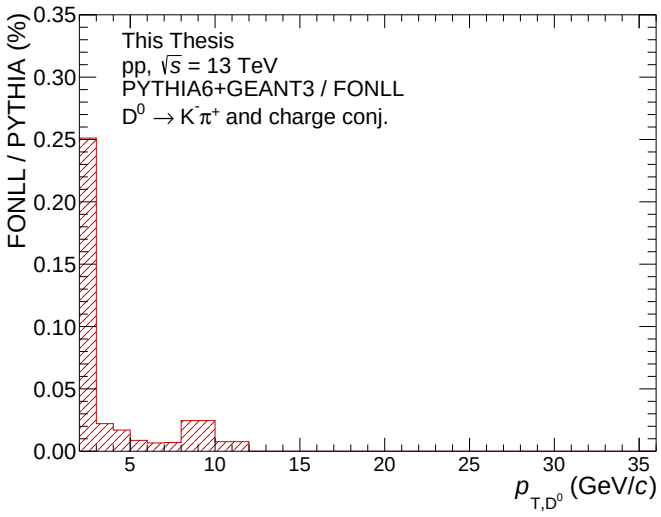

Figure 4.33: The difference in D^0 efficiency in pp collisions at $\sqrt{s} = 13$ TeV between the GEANT 3 + PYTHIA 6 and FONLL weighted sample.

4.6.3.5 Topological Selection Variation

The measured yields are corrected by the detector acceptance and efficiency, determined from Monte Carlo simulations. A possible discrepancy between the data and MC of the topological variables can bias the corrected yields. In order to estimate this effect, two sets of looser and two sets of tighter topological selection, have been prepared, which vary the

efficiency by about 25%. A topological selection variation is shown in Table 4.3. The table only shows variables that are different from the standard selection shown in Table 4.1. The ratio of modified and default efficiencies for both prompt and feed-down D^0 mesons is shown in Figure 4.34. The different topological selection also affects the response matrices for the folding and unfolding part, the spectra were compared after unfolding on the cross-section level. The ratio of cross-sections for modified and default selection is shown in Figure 4.35 (left). The difference on the last $p_{\mathrm{T,ch\,jet}}$ bin from the `Looser variation 2` was quite large, probably due to the combination of small signal over the background in higher $p_{\mathrm{T,D}}$ bins and the 60-80% variation of the efficiencies in lower $p_{\mathrm{T,D}}$. Thus it has been decided to remove `Looser variation 2` from the last bin for the uncertainty evaluation. The final uncertainty is shown in Figure 4.35 (right) and is estimated as RMS from the variations.

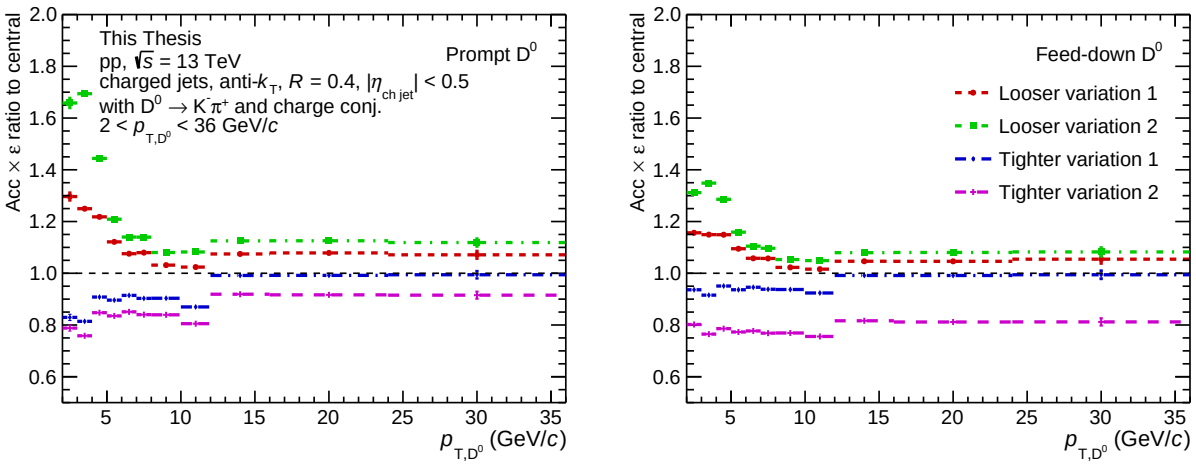

Figure 4.34: The acceptance and efficiency for different D^0 topological selection of prompt (left) and feed-down (right) D^0 mesons in pp collisions at $\sqrt{s}$ = 13 TeV.

Table 4.3: D^0 cuts variation for pp collisions at $\sqrt{s} = 13$ TeV. Table shows only variables that are changed from their defaults as listed in Table 4.1.

Looser variation 1

p_{T,D^0} (GeV/c)	$2-3$	$3-4$	$4-5$	$5-6$	$6-7$	$7-8$	$8-12$	$12-16$	$16-24$	$24-36$
$d_0^K \cdot d_0^\pi$ (10^{-4} cm^2)	< -2.7	< -2.7	< -1.3	< -0.9	< -0.8	< -0.7	< -0.5	< 1	–	–
$\cos(\theta_{\text{point}})$	> 0.93	> 0.93	> 0.93	> 0.93	> 0.93	> 0.93	> 0.93	> 0.93	> 0.87	> 0.87
$L_{xy}/\sigma_{L_{xy}}$	> 4	> 4	> 4	> 3	> 3	> 3	> 2	> 2	> 2	> 2

Looser variation 2

p_{T,D^0} (GeV/c)	$2-3$	$3-4$	$4-5$	$5-6$	$6-7$	$7-8$	$8-12$	$12-16$	$16-24$	$24-36$
$d_0^K \cdot d_0^\pi$ (10^{-4} cm^2)	< -2.2	< -2.0	< -1.0	< -0.8	< -0.7	< -0.6	< -0.4	< 1	–	–
$\cos(\theta_{\text{point}})$	> 0.9	> 0.9	> 0.9	> 0.9	> 0.9	> 0.9	> 0.9	> 0.9	> 0.85	> 0.85
$L_{xy}/\sigma_{L_{xy}}$	> 3	> 3	> 3	> 2	> 2	> 2	> 1	> 1	> 1	> 1

Tighter variation 1

p_{T,D^0} (GeV/c)	$2-3$	$3-4$	$4-5$	$5-6$	$6-7$	$7-8$	$8-12$	$12-16$	$16-24$	$24-36$
$d_0^K \cdot d_0^\pi$ (10^{-4} cm^2)	< -4	< -4	< -2	< -1.5	< -1.2	< -1.2	< -0.8	< 0.5	< 0.5	< 0.5
$\cos(\theta_{\text{point}})$	> 0.95	> 0.95	> 0.95	> 0.95	> 0.95	> 0.95	> 0.95	> 0.95	> 0.95	> 0.9

Tighter variation 2

p_{T,D^0} (GeV/c)	$2-3$	$3-4$	$4-5$	$5-6$	$6-7$	$7-8$	$8-12$	$12-16$	$16-24$	$24-36$
$d_0^K \cdot d_0^\pi$ (10^{-4} cm^2)	< -4	< -4	< -2	< -1.5	< -1.2	< -1.2	< -0.8	< 0.5	< 0.5	< 0.5
$\cos(\theta_{\text{point}})$	> 0.95	> 0.95	> 0.95	> 0.95	> 0.95	> 0.95	> 0.95	> 0.95	> 0.95	> 0.9
$n\sigma_{res}$	< 1.5	< 1.5	< 1.5	< 1.5	< 1.5	< 1.5	< 1.5	< 1.5	< 1.5	< 1.5

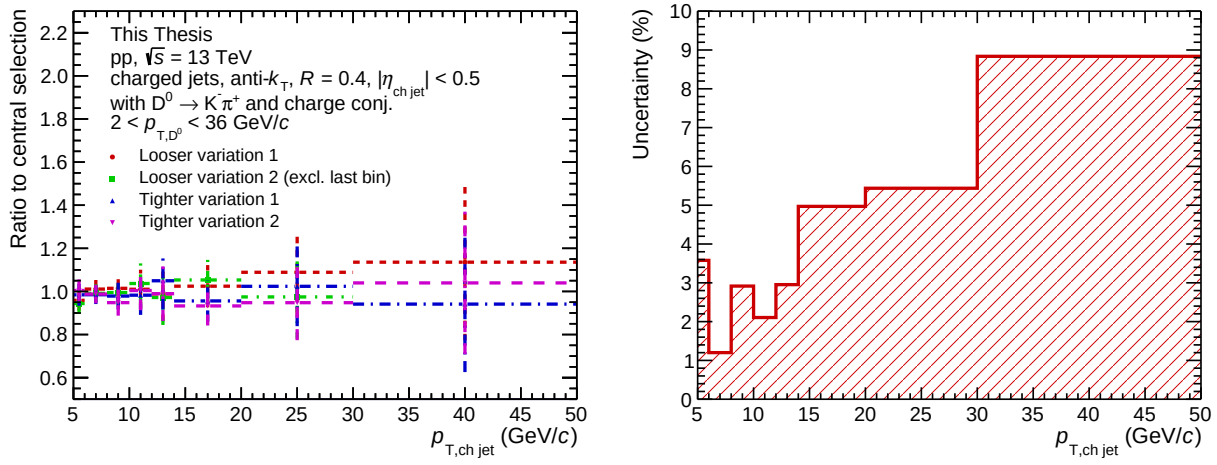

Figure 4.35: Left: The ratios of D^0-tagged jet cross-section for variation and default values for topological selection for $R = 0.4$ jets in pp collisions at $\sqrt{s} = 13$ TeV. Right: The total topological variation uncertainty calculated as a RMS of the variation for $R = 0.4$ D^0-tagged jets in pp collisions at $\sqrt{s} = 13$ TeV. Looser variation 2 has been excluded from the calculation for the last $p_{\mathrm{T,ch\,jet}}$ bin.

4.6.3.6 Beauty Feed Down uncertainty

This analysis adopted a model-dependent approach in determining the feed-down contribution from the beauty decays, and thus the feed-down shape and fraction depend on the model parameters. The POWHEG-hvq+PYTHIA 6+EVTGEN +CT10NLO+LHAPDF6 has been used. The main parameters that can be varied are the pQCD factorisation, μ_F, and renormalisation, μ_R, scales and beauty quark mass, m_b. The central value is defined as $\mu_F = \mu_R = \mu_0 = m_b = 4.75$ GeV/c^2, and the variations are defined using the scaling parameters C_F and C_R as follows

$$\begin{aligned} \mu_F &= C_F \mu_0, \\ \mu_R &= C_R \mu_0. \end{aligned} \tag{4.38}$$

Following variations of scales have been considered $(C_F, C_R) = (0.5, 0.5)$, $(0.5, 1)$, $(1, 0.5)$, $(1, 2)$, $(2, 1)$, and $(2, 2)$. In addition, two beauty quark mass variations $m_b = 4.5$ GeV/c^2

and $m_b = 5.0$ GeV/c^2, and one variation without EvtGen have been produced with central scales $(C_F, C_R) = (1, 1)$. The ratio of each variation and the central configuration for $R = 0.4$ D^0-tagged jets in pp collisions at $\sqrt{s} = 13$ TeV is shown in Figure 4.36. The mass and EvtGen variations have a small effect of the order of 10-20%. As the scale variations are arbitrary and neither can be preferred over the others, an upper and lower band has been taken to evaluate the uncertainty. In the $\sqrt{s} = 7$ TeV measurement [108] the largest variation of either the upper or lower band was taken as the final symmetric uncertainty. However, as the upper and lower band are not symmetrical this method would artificially inflate one side of the uncertainty. Instead in this analysis, the uncertainty was evaluated as asymmetric to reflect the original spread of the yields from the scales variation. The uncertainty on the feed-down fraction can be seen as white rectangles in Figure 4.21 (left). The upper and lower value is then used while subtracting the feed-down from the yields as described in section 4.6.2.2. The feed-down subtracted yield is shown in Figure 4.21 (right). Since the feed-down shape is different in the $p_{\mathrm{T,ch\,jet}}$ between variation and central value, the final uncertainty is evaluated after the unfolding on the cross-section level. The ratio of cross-sections for the upper and lower band of feed-down variation and the default selection for the $R = 0.4$ D^0-tagged jets in pp collisions at $\sqrt{s} = 13$ TeV is shown in Figure 4.37 (left). The final asymmetric uncertainty of the feed-down subtraction is the relative spread of the cross-sections and is shown in Figure 4.37 (right).

4.6.3.7 Unfolding

To determine the stability and the uncertainty of the unfolding procedure two methods have been implemented. The first consisted in varying the unfolding ranges, iterations, initial prior and comparison to a different method of unfolding - Singular Value Decomposition (SVD). The second approach has been built around a closure test.

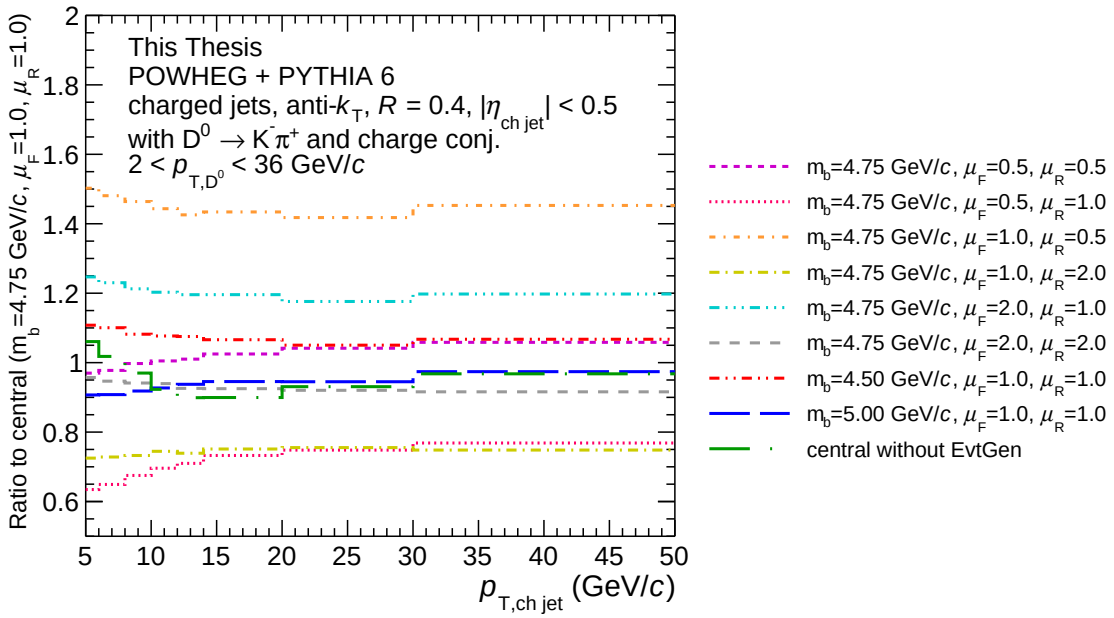

Figure 4.36: The ratio of beauty feed-down POWHEG-hvq variation and the central settings for $R = 0.4$ D^0-tagged jets in pp collisions at $\sqrt{s}$ = 13 TeV.

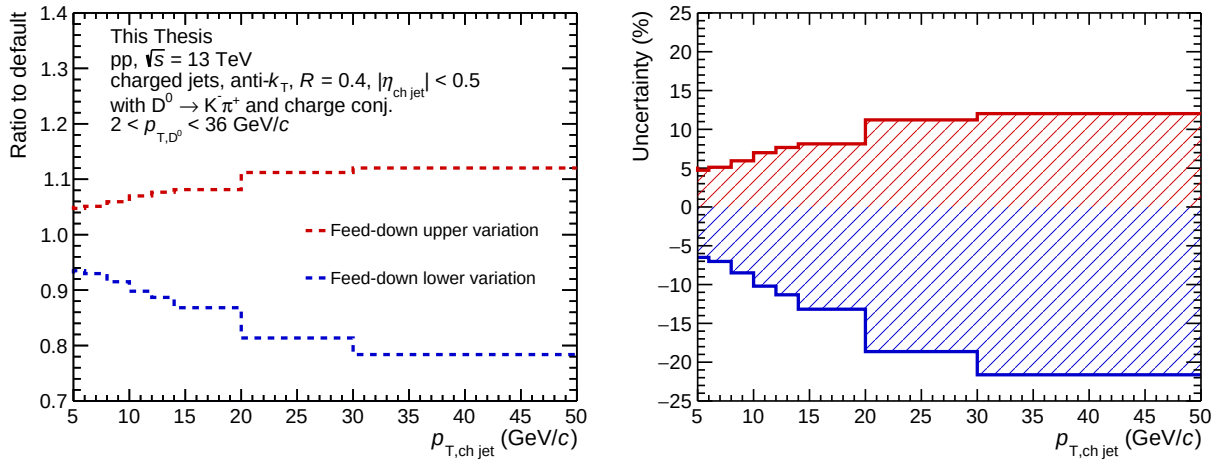

Figure 4.37: Left: The ratios of D^0-tagged jet cross-section for upper and lower band and default feed-down contribution for $R = 0.4$ jets in pp collisions at $\sqrt{s}$ = 13 TeV. Right: The total feed-down uncertainty calculated as a spread of the variation for $R = 0.4$ D^0-tagged jets in pp collisions at $\sqrt{s}$ = 13 TeV.

In the first group of tests, the default choice for Bayesian regularisation, 5-th iteration, is varied by one to the 4-th and 6-th iteration, respectively. The default unfolded ranges, defined via bin edges, are $(p^{\text{gen}}_{\text{T,ch jet}}, p^{\text{det}}_{\text{T,ch jet}}) = (\{2,3,4,5,...\},\{2,3,4,5,...\})$ and the following variations have been considered $(\{3,4,5,...\},\{2,3,4,5,...\})$, $(\{4,5,...\},\{2,3,4,5,...\})$, $(\{5,...\},\{2,3,4,5,...\})$, $(\{3,4,5,...\},\{3,4,5,...\})$, $(\{4,5,...\},\{3,4,5,...\})$, $(\{5,...\},\{3,4,5,...\})$, $(\{4,5,...\},\{4,5,...\})$, $(\{5,...\},\{4,5,...\})$, and $(\{5,...\},\{5,...\})$. An RMS from the iterations and range variation was calculated and is around 1%. The baseline prior used for the unfolding is the generated spectrum from PYTHIA. For the variations the priors were produced using power-law function a

$$P^0 = p^{-a}_{\text{T,ch jet}} e^{-\frac{-ab}{p_{\text{T,ch jet}}}}, \tag{4.39}$$

where a is the power-law index and b is the position of the local maximum. The exponential factor was added to avoid infinities at zero and to receive a more realistic distribution. Following variations have been used for $R = 0.4$ D^0-tagged jets $(a,b) = (4.4,4.4)$, $(3,4.4)$, $(4,4.4)$, $(5,4.4)$, $(6,4.4)$, $(7,4.4)$, $(4.4,3)$, $(4.4,5)$, and the last prior was fit to the measured spectrum. The uncertainty from the prior variation is smaller than 0.5% for lower $p_{\text{T,ch jet}}$ and 2% for the last momentum bin. The last test consisted in a comparison to unfolded spectrum using SVD with regularisation 5, 6, and 7. The mean of the variations with respect to the Bayesian method has been used. Uncertainty from this source is of the order of 1% for low $p_{\text{T,ch jet}}$ and 11% in the last two momentum bins. These methods showed a negligible uncertainty in the lower $p_{\text{T,ch jet}}$ but a larger one in the last bins which can be caused by the statistical fluctuations.

Thus an alternative approach was used to study the uncertainty coming from the unfolding. A closure test that mimics the analysis procedure for the charm-only spectrum has been developed. The generated GEANT 3 +PYTHIA 6 MC sample has been randomly split between the response matrix and test sample in a fraction 80:20. The random division and unfolding have been repeated 10 times, and RMS has been taken as the final unfolding

uncertainty. The cross-section of $R = 0.4$ D^0-tagged jets is shown in Figure 4.38. The spread between trials is most likely due to the statistical fluctuations while performing the random division of the MC, thus the systematic uncertainty is the constant shift of the ratio from the unity. As this uncertainty source gives a slightly larger uncertainty in the lower $p_{\mathrm{T,ch\,jet}}$ in comparison to the previous uncertainty source, it is believed to better address the uncertainty of the unfolding. Moreover, performing the trials and taking RMS absorbs possible statistical fluctuations. This method has a big impact on the large $p_{\mathrm{T,ch\,jet}}$ providing a smaller uncertainty in comparison to the first set of variations, described in previous paragraph.

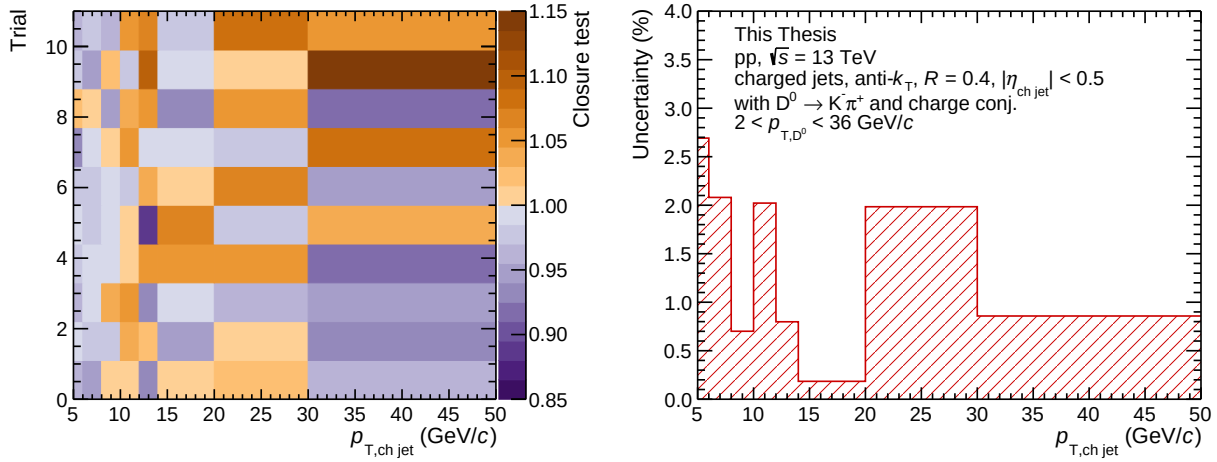

Figure 4.38: Left: The ratios of D^0-tagged jet cross-section for unfolding trials of $R = 0.4$ jets in pp collisions at $\sqrt{s} = 13$ TeV. Right: The total unfolding uncertainty calculated as a RMS of the trials for $R = 0.4$ D^0-tagged jets in pp collisions at $\sqrt{s} = 13$ TeV.

4.6.3.8 Normalisation

The normalisation uncertainty is important while normalising to cross-section and originates from two sources, the luminosity determination and the D^0 branching ratio. The luminosity uncertainty of the sample used in this thesis was calculated as 1.7% as shown in section 4.2.1. The 0.8% uncertainty on of D^0 branching ratio is based on the uncertainty listed in [1].

4.6.3.9 Total systematic uncertainty

The total systematic uncertainty is calculated by adding each uncertainty source in quadrature. The summary of each uncertainty sources, the final systematic uncertainty, and statistical uncertainty as a function of $p_{\mathrm{T,ch\,jet}}$ for $R = 0.2$, 0.4, and 0.6 jets in pp collisions at $\sqrt{s} = 13$ TeV are shown in Table 4.4. The dominant uncertainty source is from estimating the beauty feed-down contribution, which is given by varying the factorisation and renormalisation scales. This uncertainty can be significantly reduced with a new tracking system, as planned at ALICE for Run 3, which will allow topological selection to distinguish primary and secondary vertices, and consequently reduce the beauty feed-down contribution. The second biggest uncertainty originates from the topological selection. The larger uncertainty in high $p_{\mathrm{T,ch\,jet}}$ can be explained by partial influence from statistical fluctuation, which is difficult to determine. These bins usually exhibit the lowest signal-to-background ratio on which analysis is sensitive. The third largest uncertainty source is the jet energy scale uncertainty. Removing the tracks from MC will cause a shift of the spectra towards lower $p_{\mathrm{T,ch\,jet}}$, this will cause worse signal in the high $p_{\mathrm{T,ch\,jet}}$ bins, which might explain the larger uncertainty. Moreover, removing 4% of the tracks is a conservative choice, removing 3-3.5% of the tracks might also be considered in case this would be the dominant uncertainty. Together with D^0 tracking uncertainty, they are given by the detector performance and cannot be improved further. The signal extraction uncertainty relies on how purely the signal can be extracted, thus this uncertainty can be improved by having a better signal-over-background ratio, which is mainly given by the detector performance. The unfolding uncertainty is negligible for most values of $p_{\mathrm{T,ch\,jet}}$.

Table 4.4: Systematic and statistical uncertainties as a function of $p_{\mathrm{T,ch\,jet}}$ for $R = 0.2$, 0.4, and 0.6 in pp collisions at $\sqrt{s} = 13$ TeV.

$p_{\mathrm{T,ch\,jet}}$ (GeV/c)		5 – 6	6 – 8	8 – 10	10 – 12	12 – 14	14 – 20	20 – 30	30 – 50
Source (%)	R								
Raw Yield Extraction	0.2	2.6	2.9	2.0	2.1	2.7	2.7	2.5	9.2
	0.4	3.3	3.3	2.5	4.0	3.3	4.3	4.3	8.8
	0.6	3.0	2.7	2.1	2.6	3.3	3.9	3.1	7.6
Tracking Eff. (D-Meson)		5.0							
$p_{\mathrm{T,D}}$ shape		0.0							
Topological Selection	0.2	1.1	1.8	1.7	4.0	3.0	3.2	6.1	9.6
	0.4	3.6	1.2	2.9	2.1	3.0	5.0	5.4	8.8
	0.6	6.3	2.6	4.8	4.0	4.0	5.3	11.9	25.4
B Feed-Down	0.2	+4.7	+4.8	+4.8	+5.4	+4.6	+5.6	+6.0	9.1
		–6.7	–6.8	–7.3	–8.1	–7.5	–9.7	–9.8	–15.6
	0.4	+4.7	+5.1	+5.9	+7.0	+7.7	+8.1	+11.2	+12.0
		–6.5	–7.0	–8.5	–10.2	–11.3	–13.2	–18.6	–21.6
	0.6	+4.1	+4.9	+5.3	+5.9	+7.2	+8.6	+9.3	+16.7
		–5.4	–6.6	–7.5	–8.4	–10.6	–12.6	–14.7	–29.1
Unfolding	0.2	0.9	0.2	0.1	1.4	1.0	1.1	3.9	4.2
	0.4	2.7	2.1	0.7	2.0	0.8	0.2	2.0	0.9
	0.6	5.7	3.1	2.9	1.9	2.0	2.4	0.3	0.5
Tracking Eff. (Jet Energy Scale)	0.2	0.5	0.9	1.3	1.4	1.7	2.2	3.0	6.6
	0.4	0.8	1.9	2.1	3.5	3.9	4.2	6.4	9.7
	0.6	0.1	0.6	2.9	3.8	5.2	6.4	7.5	15.1
Luminosity		1.7							
D^0 Branching ratio		0.8							
Total	0.2	+7.7	+8.0	+7.7	+9.1	+8.4	+9.1	+11.5	+18.7
		-9.1	-9.3	-9.5	-10.9	-10.3	-12.1	-13.9	-22.6
	0.4	+9.1	+8.7	+9.1	+10.7	+11.1	+12.5	+15.7	+20.6
		-10.1	-9.9	-11.0	-13.0	-13.9	-16.2	-21.7	-27.3
	0.6	+11.3	+8.7	+10.1	+10.2	+11.7	+13.9	+18.0	+35.2
		-11.8	-9.8	-11.3	-11.8	-14.1	-16.7	-21.3	-42.5
Statistical Uncertainty	0.2	2.7	2.4	3.1	5.0	3.1	6.4	8.4	19.7
	0.4	3.6	3.0	4.4	6.5	9.1	6.7	13.1	21.3
	0.6	5.2	4.2	5.5	7.6	10.7	8.1	14.0	35.2

4.6.4 Results

This section contains the final results of the unfolded yield N_m^{unfolded} and a discussion of the comparison with models. The cross-section is calculated using following formula

$$\frac{\mathrm{d}^2\sigma}{\mathrm{d}\eta_{\text{ch.jet}}\mathrm{d}p_{\text{T,ch jet}}} = \frac{1}{\mathscr{L}_{\text{int}} f_{\text{BR}}} \frac{\frac{1}{2}N_m^{\text{unfolded}}}{\Delta p_{\text{T,ch jet}} \Delta\eta_{\text{ch.jet}}}, \tag{4.40}$$

where N_m^{unfolded} is the unfolded measured yield in the m-th bin corresponding to $p_{\text{T,ch jet}}$, the factor $\frac{1}{2}$ represent that the yields were extracted for both D^0 and $\overline{\mathrm{D}^0}$ together, $\Delta p_{\text{T,ch jet}}$ is the bin width in $p_{\text{T,ch jet}}$, $\Delta\eta_{\text{ch.jet}} = 2 \cdot (0.9 - R)$ is the studied pseudorapidity interval defined as fiducial acceptance via the jet radius R, $\mathscr{L}_{\text{int}} = (25.81 \pm 0.43)$ nb^{-1} is the integrated luminosity of $\sqrt{s} = 13$ TeV pp collisions data calculated using equation (4.3) and $f_{\text{BR}} = (3.950 \pm 0.031)\%$ [1] is the branching ratio of the studied decay channel.

The $p_{\text{T,ch jet}}$-differential cross-section of charm jets tagged with D^0 mesons for $R = 0.2$, 0.4, and 0.6 in pp collisions at $\sqrt{s} = 13$ TeV is shown in Figure 4.39 with comparison to Pythia 8 HardQCD Monash tune, Pythia 8 SoftQCD Mode 2 tune, and POWHEG-hvq + Pythia 8 HardQCD Monash tune predictions. The reported jets, in both the measurement and models, are required to have $p_{\text{T,D}}$ between 2 and 36 GeV/c and maximum jet momentum of $p_{\text{T,ch jet}} = 50$ GeV/c. The lower momentum cut is imposed, because the D^0 reconstruction efficiency falls rapidly at low $p_{\text{T,D}}$. This helps to avoid large statistical uncertainties caused by large weights from these regions. It was shown in a previous analysis at $\sqrt{s} = 7$ TeV [108] that introducing $p_{\text{T,D}} > 3$ GeV/c selection has a negligible bias on the fragmentation in the reported $p_{\text{T,ch jet}} > 5$ GeV/c spectra, thus inducing $p_{\text{T,D}} > 2$ GeV/c should have even smaller bias. The upper cut is imposed because the size of the data sample does not allow a reliable mass extraction beyond this value.

The model calculation using Pythia 8.210 Monash tune [37, 131] MC generator overpredicts the data for all three jet resolution parameters R. Incorporating inelastic

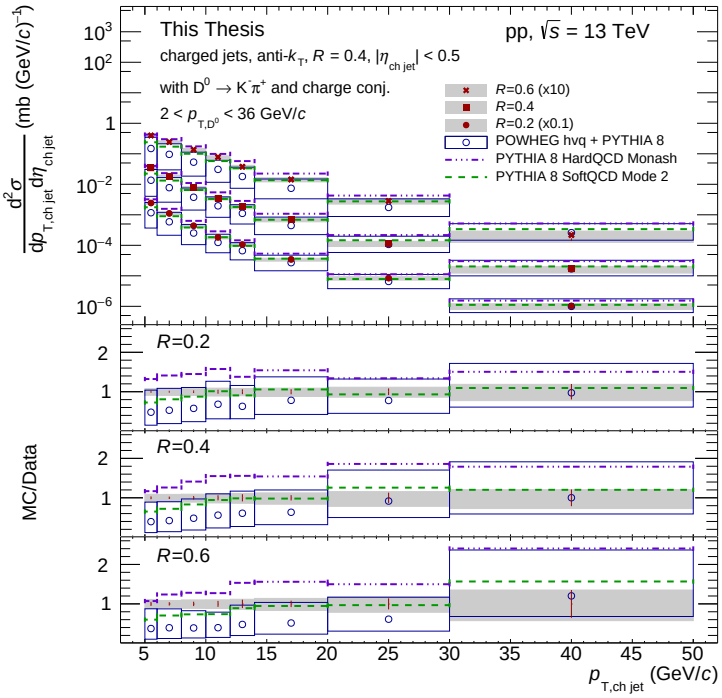

Figure 4.39: The $p_{\mathrm{T,ch\,jet}}$-differential cross-section of charm jets tagged with D^0 mesons for $R = 0.2$, 0.4 and 0.6 in pp collisions at $\sqrt{s} = 13$ TeV compared to PYTHIA 8 HardQCD Monash tune (dash-dotted lines), PYTHIA 8 SoftQCD Mode 2 (dashed line) and POWHEG-hvq + PYTHIA 8 (open circles) predictions. The vertical lines represent the statistical uncertainty and the shaded bands indicate the systematic uncertainty on the measured cross-section. The crosses represent the cross-section for $R = 0.6$ (multiplied by 10), squares represent the cross-section for $R = 0.4$, and circles represent the cross-section for $R = 0.2$ (divided by 10).

non-diffractive processes and beyond the leading colour approximation (Colour reconnection) [51], denoted as PYTHIA 8 SoftQCD Mode 2 tune, improves the agreement with data in the region $p_{\mathrm{T,ch\,jet}} > 10$ GeV/c. On the other hand, this mode underpredicts the regions $p_{\mathrm{T,ch\,jet}} < 10$ GeV/c. The POWHEG-hvq + PYTHIA 8 [37, 48] model describes the data within theoretical and experimental uncertainties. The model uncertainty is calculated by varying the factorisation, renormalisation scales and mass. The same variation as for the

feed-down has been considered $(\mu_F, \mu_R) = (0.5, 0.5)$, $(0.5, 1)$, $(1, 0.5)$, $(1, 2)$, $(2, 1)$ and $(2, 2)$, and the mass was varied from $m_c = 1.5$ GeV/c^2 to $m_c = 1.3$ GeV/c^2 and $m_c = 1.7$ GeV/c^2. The central values of the prediction agree with data in $p_{\mathrm{T,ch\,jet}} > 20$ GeV/c. In the lower $p_{\mathrm{T,ch\,jet}}$, the data lie on the upper edge of the model uncertainty band. In this region, the model provides a slightly better description for lower jet resolution. The low $p_{\mathrm{T,ch\,jet}}$ regions is difficult to describe theoretically due to a large contribution from non-perturbative effects and is expected to be more sensitive on hadronisation model.

The ratios of $p_{\mathrm{T,ch\,jet}}$-differential cross-section of charm jets tagged with D^0 mesons in pp collisions at $\sqrt{s} = 13$ TeV are shown in Figure 4.40, with comparisons to PYTHIA 8 HardQCD Monash tune, PYTHIA 8 SoftQCD Mode 2 tune and POWHEG-hvq + PYTHIA 8 predictions. The ratios considered are $\sigma(R = 0.2)/\sigma(R - 0.4)$ and $\sigma(R = 0.2)/\sigma(R - 0.6)$. Statistical uncertainties are treated as fully uncorrelated and summed in quadrature, thus probably overestimated. The D^0 tracking, luminosity and D^0 branching ratio systematic uncertainties are treated as fully correlated and removed. The jet energy scale uncertainty is calculated as a difference between the reported cross-section ratios and the cross-section ratios extracted with response matrices with discarded tracks. The topological selection uncertainty of the ratio is calculated as an average between the two constituent radii. For the models, the uncertainties from the factorisation and renormalisation scales are varied separately, and minimum and maximum from the ratios are taken.

The ratio of different jet resolution parameters can help explore the parton shower development and provide insight into the interplay between perturbative and non-perturbative effects. The departure from unity is due to the jet QCD radiation. Each of the considered models describes the shape qualitatively. The ratio decrease with increasing $p_{\mathrm{T,ch\,jet}}$ and become flat for $p_{\mathrm{T,ch\,jet}} > 10$ GeV/c within uncertainties. Both PYTHIA 8 tunes describe the data within uncertainties, they are slightly overpredicting the data in $\sigma(R = 0.2)/\sigma(R - 0.6)$ below $p_{\mathrm{T,ch\,jet}} < 12$ GeV/c. The $\sigma(R = 0.2)/\sigma(R - 0.6)$ ratio is expected to be more sensitive

to UE contribution. In comparison to the cross-section measurement seen in Figure 4.39, the difference between these two tunes largely cancels while probing the R ratios. POWHEG-hvq + PYTHIA 8 overestimates the data at lower $p_{\mathrm{T,ch\,jet}}$, with a larger discrepancy seen for $R = 0.6$.

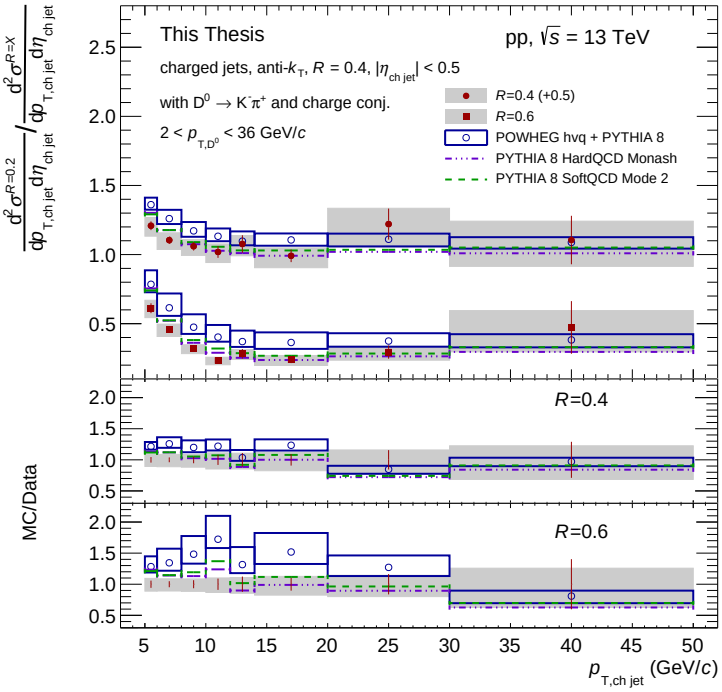

Figure 4.40: The ratios of $p_{\mathrm{T,ch\,jet}}$-differential cross-section of charm jets tagged with D^0 mesons in pp collisions at $\sqrt{s}$ = 13 TeV compared to PYTHIA 8 HardQCD Monash tune (dash-dotted lines), PYTHIA 8 SoftQCD Mode 2 tune (dashed line) and POWHEG-hvq + PYTHIA 8 (open circles) predictions. The ratios considered are $\sigma(R = 0.2)/\sigma(R - 0.4)$ (circles, shifted by +0.5) and $\sigma(R = 0.2)/\sigma(R - 0.6)$ (squares). The vertical lines represent the statistical uncertainty and the shaded bands indicate the systematic uncertainty on the measured cross-section.

4.7 Parallel jet momentum

The extraction of parallel jet momentum $z_{||}^{\mathrm{ch}}$ follows a similar extraction procedure as for the $p_{\mathrm{T,ch\,jet}}$ described in section 4.6. The main difference from the previous section is that the analysis is done differentially both in the $z_{||}^{\mathrm{ch}}$ and $p_{\mathrm{T,ch\,jet}}$ variables. The D^0 tagging efficiency is extracted in the $p_{\mathrm{T,ch\,jet}}$ and $p_{\mathrm{T,D}}$ variables and the folding and unfolding procedure is done in two dimensions ($z_{||}^{\mathrm{ch}}$,$p_{\mathrm{T,ch\,jet}}$). In the following section, the extraction of $z_{||}^{\mathrm{ch}}$ cross-section and probability densities will be briefly described and the comparison to models will be discussed.

4.7.1 $z_{||}^{\mathrm{ch}}$ yield extraction

The extraction intervals considered are described in table 4.2. Even though it was shown there is a negligible bias on the $p_{\mathrm{T,ch\,jet}}$ cross-section while assuming independence of $p_{\mathrm{T,ch\,jet}}$ for the mass extraction, reflection and D^0 tagging efficiency, it might be significant for $z_{||}^{\mathrm{ch}}$. As $z_{||}^{\mathrm{ch}}$ is defined by using the $p_{\mathrm{T,D}}$ and $p_{\mathrm{T,ch\,jet}}$ momenta, studying the efficiency in $p_{\mathrm{T,D}}$ and $p_{\mathrm{T,ch\,jet}}$ variables, should treat any possible bias. The D^0 meson signal mass distribution for each $p_{\mathrm{T,D}}$ and $p_{\mathrm{T,ch\,jet}}$ has been identified as $(-2\sigma_{\mathrm{S}}, 2\sigma_{\mathrm{S}})$ and the side-band regions as $(-9\sigma_{\mathrm{S}}, -4\sigma_{\mathrm{S}})$ and $(4\sigma_{\mathrm{S}}, 9\sigma_{\mathrm{S}})$. The invariant mass fits for selected $p_{\mathrm{T,D}}$ intervals of D^0-tagged jets for every reported $p_{\mathrm{T,ch\,jet}}$ momentum region in $R = 0.4$ jets at in pp collisions $\sqrt{s}$ = 13 TeV is shown in Figure 4.41. The reflection templates have been extracted per given $p_{\mathrm{T,ch\,jet}}$ and $p_{\mathrm{T,D}}$ interval and an example of the reflection over signal f_{R} fraction in $p_{\mathrm{T,ch\,jet}} = 5 - 7$ GeV/c and $p_{\mathrm{T,ch\,jet}} = 15 - 50$ GeV/c as a function of $p_{\mathrm{T,D}}$ in pp collisions at $\sqrt{s}$ = 13 TeV is shown in Figure 4.42.

The letter $N_{i,j,z}$ is used for three-dimensional yields, where index i denotes $p_{\mathrm{T,D}}$, index j denotes the transverse momentum of jet, $p_{\mathrm{T,ch\,jet}}$, and index z denotes the parallel jet momentum, $z_{||}^{\mathrm{ch}}$. The following indexation will be used: side-band (SB), peak (P) region,

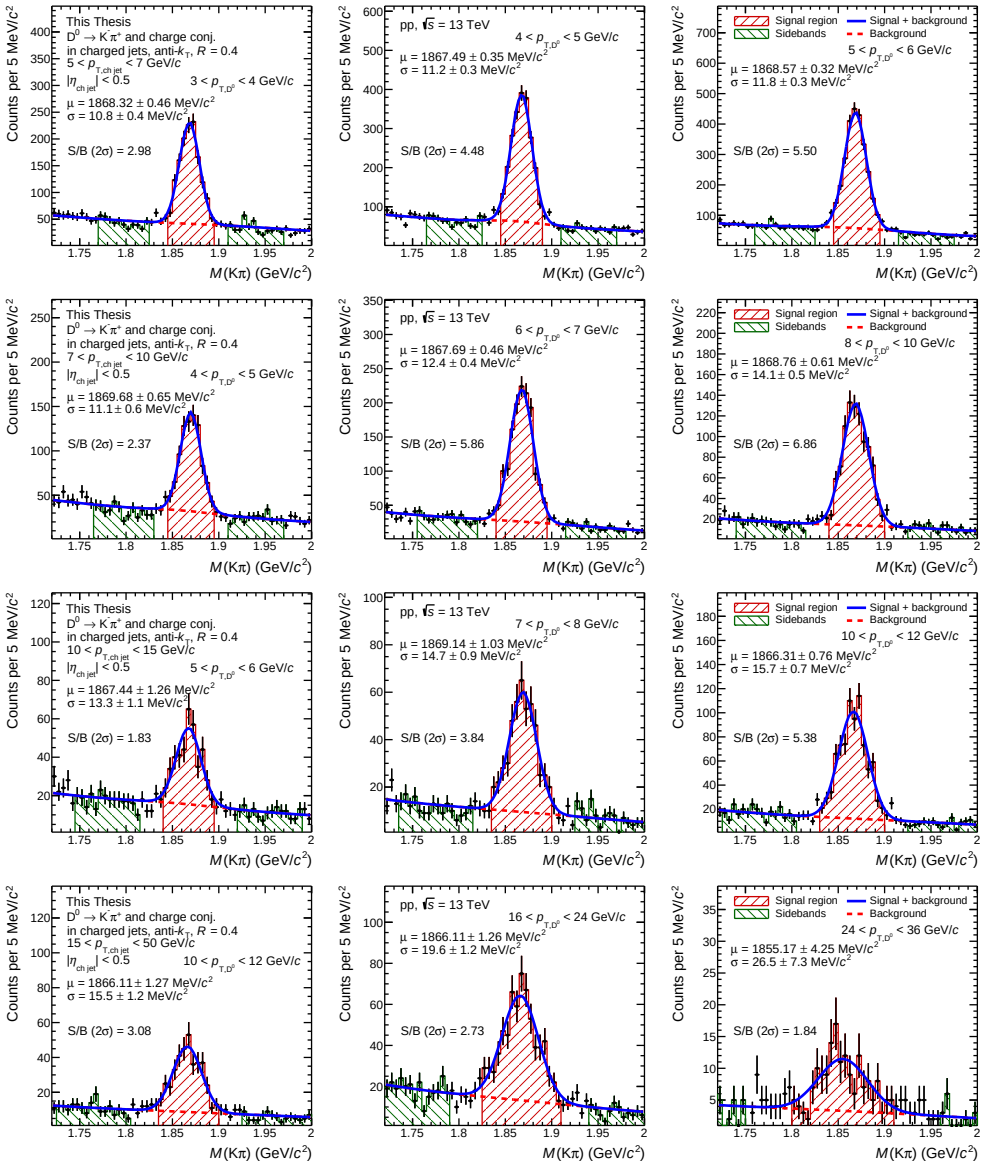

Figure 4.41: An example of invariant mass fits for selected $p_{\mathrm{T,D}}$ intervals of D^0-tagged jets for every $p_{\mathrm{T,ch\,jet}}$ momentum region in $R = 0.4$ jets in pp collisions at $\sqrt{s} = 13$ TeV. The background fit contains both exponential combinatorial background and double-Gaussian reflection function. The signal region is defined as $(-2\sigma_{\mathrm{S}}, 2\sigma_{\mathrm{S}})$ (red) and the side-band regions as $(-9\sigma_{\mathrm{S}}, -4\sigma_{\mathrm{S}})$ and $(4\sigma_{\mathrm{S}}, 9\sigma_{\mathrm{S}})$ (green).

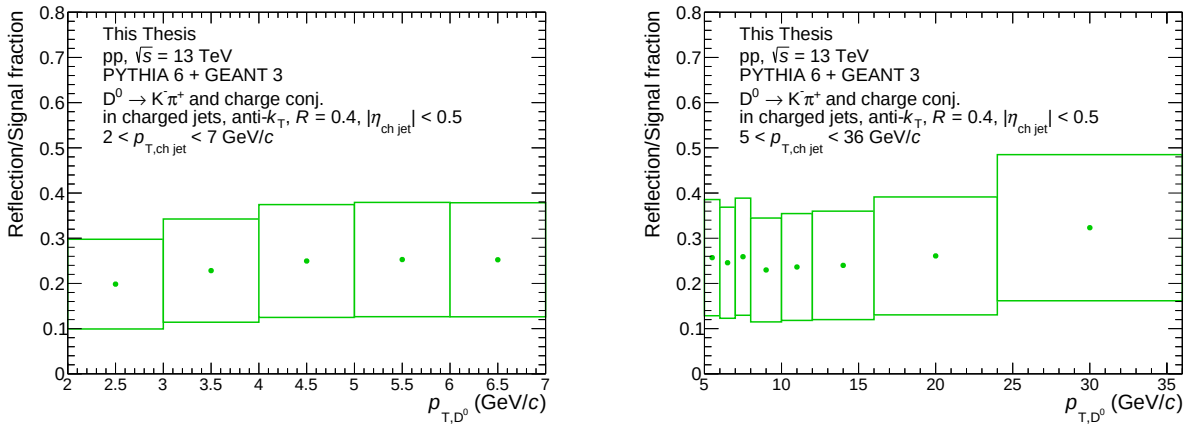

Figure 4.42: The reflection over signal f_{R} fraction as a function of the $p_{\mathrm{T,D}}$ of the D^0 meson in pp collisions at $\sqrt{s}$ = 13 TeV estimated using PYTHIA 6 + GEANT 3 with an uncertainty given by a $\pm 50\%$ variation of the function f_{R}.

background (B), reflection (R), and signal (S) contribution as depicted in Figure 4.16. The signal extraction equation (4.16) is extended into

$$N^{\mathrm{S}}_{i,j,z} = \left(N^{\mathrm{P}}_{i,j,z} - \frac{Y^{\mathrm{B,P}}_{i,j}}{Y^{\mathrm{B,SB}}_{i,j}} N^{\mathrm{SB}}_{i,j,z} \right) \left(\frac{Y^{\mathrm{S}}_{i,j}}{Y^{\mathrm{S}}_{i,j} + Y^{\mathrm{R,P}}_{i,j} - \frac{Y^{\mathrm{B,P}}_{i,j}}{Y^{\mathrm{B,SB}}_{i,j}} Y^{\mathrm{R,SB}}_{i,j}} \right), \tag{4.41}$$

where the peak yield $N^{\mathrm{P}}_{i,j,z}$ is extracted from the $(-2\sigma_{\mathrm{S}}, 2\sigma_{\mathrm{S}})$ region of D^0 mass and the side-band $N^{\mathrm{SB}}_{i,j,z}$ is extracted from the $(-9\sigma_{\mathrm{S}}, -4\sigma_{\mathrm{S}})$ and $(4\sigma_{\mathrm{S}}, 9\sigma_{\mathrm{S}})$ mass regions. The peak width σ_{S} and the scaling yields $Y_{i,j}$ are extracted from $z^{\mathrm{ch}}_{||}$ integrated invariant mass distributions. The $z^{\mathrm{ch}}_{||}$ yields for D^0-tagged jets with $R = 0.4$ in pp collisions at $\sqrt{s}$ = 13 TeV for the selected $p_{\mathrm{T,D}}$ in the reported $p_{\mathrm{T,ch\,jet}}$ bins are shown in Figure 4.43, where the peak region $N^{\mathrm{P}}_{i,j,z}$, normalised side-band $\frac{Y^{\mathrm{B,P}}_{i,j}}{Y^{\mathrm{B,SB}}_{i,j}} N^{\mathrm{SB}}_{i,j,z}$, and the background subtracted, reflection corrected $N^{\mathrm{raw}}_{i,j,z}$ are shown.

Finally, the histograms are summed per $p_{\mathrm{T,D}}$ intervals to obtain the raw $z^{\mathrm{ch}}_{||}$ yield $N^{\mathrm{raw}}_{z,j}$ for each $p_{\mathrm{T,ch\,jet}}$ interval as

$$N^{\mathrm{raw}}_{z,j} = \frac{1}{0.9545} \sum_{i \in p_{\mathrm{T,D}}} N^{\mathrm{S}}_{i,j,z}, \tag{4.42}$$

the scaling factor 1/0.9545 is there as the signal was extracted from the $2\sigma_{\mathrm{S}}$ range only.

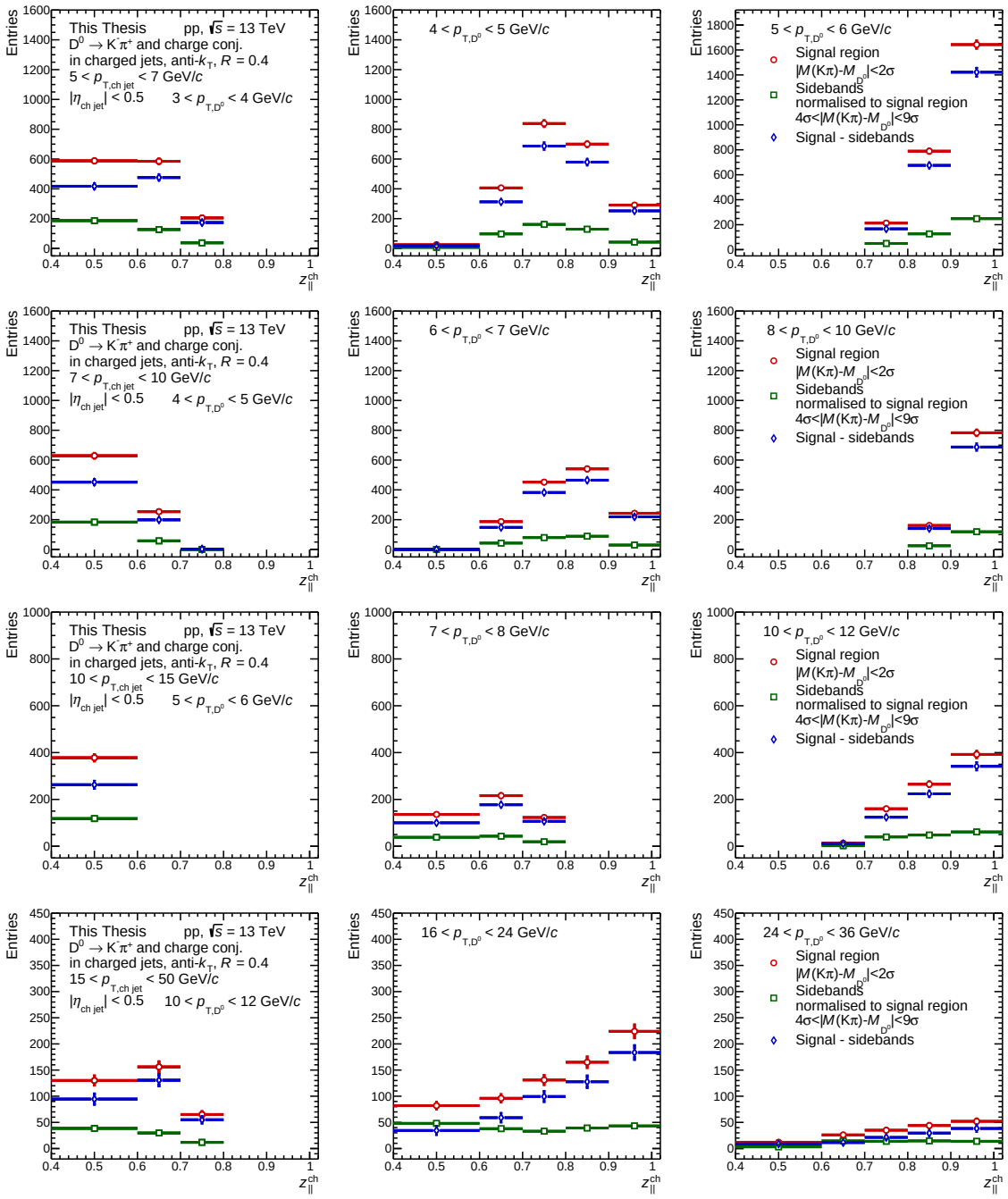

Figure 4.43: An example of the $z_{||}^{\mathrm{ch}}$ distribution for D^0-tagged jets with $R = 0.4$ in pp collisions at $\sqrt{s} = 13$ TeV for selected $p_{\mathrm{T,D}}$ bins in each $p_{\mathrm{T,ch\,jet}}$ bins with the signal ($N_{z,j}^{\mathrm{P}}$), normalised side-bands ($\frac{Y_{i,j}^{\mathrm{B,P}}}{Y_{i,j}^{\mathrm{B,SB}}} N_{z,j}^{\mathrm{SB}}$), and background subtracted reflection corrected ($N_{i,j,z}^{\mathrm{raw}}$) contribution.

4.7.2 Corrections

The correction procedure consists of the following steps

- correct raw yield for the D^0 tag reconstruction efficiency and acceptance in $p_{T,D}$ and $p_{T,ch\,jet}$ variables,
- subtract b-quark decay feed-down from raw D-tagged jet yields,
- unfold the spectra for detector-related effects in $z_{||}^{ch}$ and $p_{T,ch\,jet}$ variables.

4.7.2.1 Reconstruction efficiency

Even though the efficiency has a negligible dependence in $p_{T,ch\,jet}$ above 5 GeV/c, it was extracted for each $p_{T,ch\,jet}$ bin separately. The main reason is, that the $p_{T,ch\,jet}$ in the interval $2-5$ GeV/c, could have unwanted bias on the results due to the folding and unfolding procedure and due to the fact the $z_{||}^{ch}$ is defined with both $p_{T,D}$ and $p_{T,ch\,jet}$. The efficiency was calculated using PYTHIA 6 + GEANT 3 and is defined as a ratio of number of D^0 found in the detector, d, over the generated number of D^0, g, as a function of generated D^0 momentum, $p_{D^0}^{gen}$, and jet momentum, $p_{T,ch\,jet}^{gen}$,

$$\epsilon_{i,j} = \frac{d\left(p_{T,D^0}^{gen}, p_{T,ch\,jet}^{gen}\right)}{g\left(p_{T,D^0}^{gen}, p_{T,ch\,jet}^{gen}\right)}. \tag{4.43}$$

The $p_{T,D}$ and $p_{T,ch\,jet}$ dependent efficiencies are extracted for both prompt D^0 mesons $\epsilon_{i,j}^{c}$ originating from the charm quark hard scattering and decays of D^0 excited states, and for non-prompt D^0 originating from beauty decays $\epsilon_{i,j}^{b}$. Efficiencies for D^0-tagged jets with $R = 0.4$ with $p_{T,ch\,jet} = 5-7,\ 7-10,\ 10-15$, and $15-50$ GeV/c in pp collisions at $\sqrt{s} = 13$ TeV are shown in Figure 4.44.

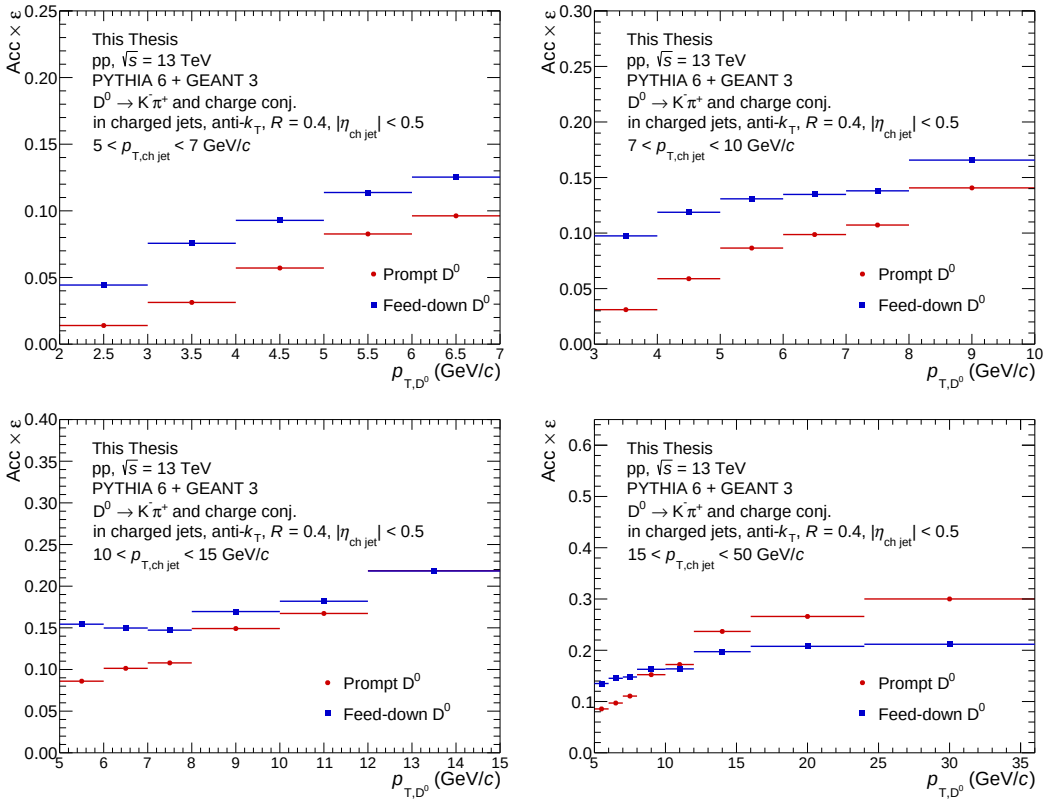

Figure 4.44: The prompt ϵ_i^{c} and non-prompt ϵ_i^{b} reconstruction efficiencies for D^0-tagged jets with $R = 0.4$ with $p_{\mathrm{T,ch\,jet}} = 5-7,\ 7-10,\ 10-15$, and $15-50$ GeV/c in pp collisions at $\sqrt{s}\ =\ 13$ TeV.

The prompt efficiency is then applied to the $z_{||}^{\mathrm{ch}}$ spectra in each $p_{\mathrm{T,D}}$ bin modifying (4.42) into

$$N_{z,j}^{\mathrm{eff.corr.}} = \frac{1}{0.9545} \sum_{i \in p_{\mathrm{T,D}}} N_{i,j,z}^{\mathrm{raw}} \frac{1}{\epsilon_{i,j}^{\mathrm{c}}}. \tag{4.44}$$

4.7.2.2 Beauty Feed-Down Subtraction

The feed-down in $p_{\mathrm{T,ch\,jet}}$ and $z_{||}^{\mathrm{ch}}$ variables has been generated using POWHEG-hvq with $\mathrm{b\bar{b}}$ process coupled with the PYTHIA 6 event generator and CT10 NLO PDF with LHAPDF 6 interpolator. The equation (4.27) is generalised by adding another variable, $z_{||}^{\mathrm{ch}}$. The feed-down

is estimated as

$$N_{z,j}^{\mathrm{b}\to\mathrm{D}^0} = \frac{1}{\epsilon_{z,j}^{\mathrm{b,\ det}}} \sum_{y\in z_{||}^{\mathrm{gen}}} \sum_{m\in p_{\mathrm{T,ch\,jet}}^{\mathrm{gen}}} \mathcal{R}_{z,j,y,m}^{*,\mathrm{b}} \epsilon_{y,m}^{\mathrm{b,\ gen}} N_{y,m}^{\prime\mathrm{sim,\ b}\to\mathrm{D}^0}, \tag{4.45}$$

where $N_{y,m}^{\prime\mathrm{sim,\ b}\to\mathrm{D}^0}$ is the simulated yield in $z_{||}^{\mathrm{ch}}$ and $p_{\mathrm{T,ch\,jet}}$ scaled by the non-prompt-to-prompt D^0 efficiency fraction in $p_{\mathrm{T,D}}$, data-to-MC luminosity fraction, D^0 branching ratio, and summed over $p_{\mathrm{T,D}}$ intervals. The $\mathcal{R}_{z,j,y,m}^{*,\mathrm{b}}$ is the non-prompt D^0 response matrix, weighted by the prompt D^0 efficiency, and normalised in $z_{||}^{\mathrm{det}}$ and $p_{\mathrm{T,ch\,jet}}^{\mathrm{det}}$. Finally, the $\epsilon_{z,j}^{\mathrm{b,\ det}}$ and $\epsilon_{y,m}^{\mathrm{b,\ gen}}$ are the corrections to address limited ranges of the response matrix in $z_{||}^{\mathrm{gen}}$, $z_{||}^{\mathrm{det}}$, $p_{\mathrm{T,ch\,jet}}^{\mathrm{gen}}$, and $p_{\mathrm{T,ch\,jet}}^{\mathrm{det}}$. The feed-down response matrix for D^0-tagged jets with $R = 0.4$ in pp collisions at $\sqrt{s}$ = 13 TeV is shown in Figure 4.45 (left). The feed-down fraction $N_{z,j}^{\mathrm{b}\to\mathrm{D}^0}/N_{z,j}^{\mathrm{eff.corr.}}$ for D^0-tagged jets in $p_{\mathrm{T,ch\,jet}} = 5-7$ GeV/c and $p_{\mathrm{T,ch\,jet}} = 15-50$ GeV/c with $R = 0.4$ in pp collisions at $\sqrt{s}$ = 13 TeV is shown in Figure 4.45 (right). The c quarks from feed-down tends to have lower $z_{||}^{\mathrm{ch}}$ as they originate from the additional decay of the b-quark.

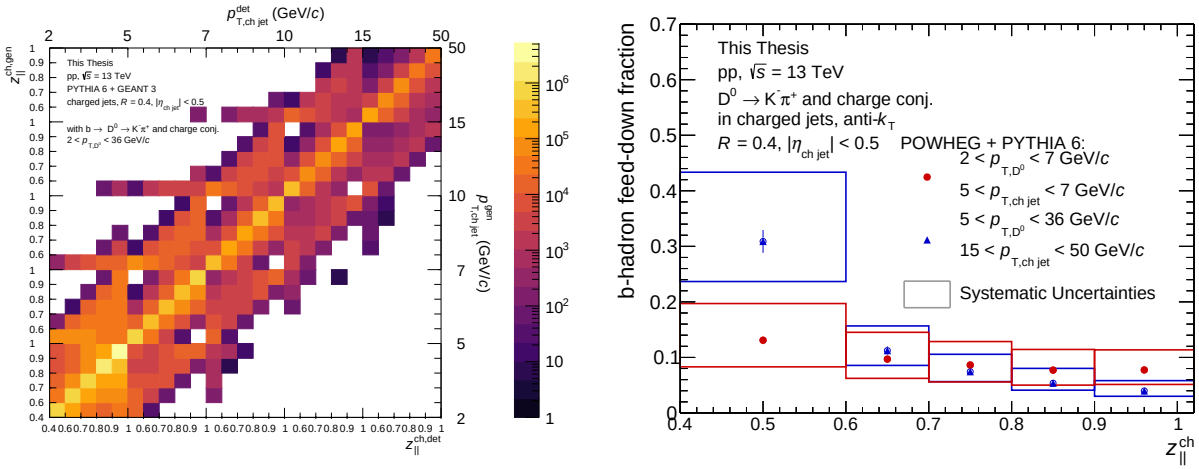

Figure 4.45: Left: A response matrix of fully-matched entries $\mathcal{R}^{+,\mathrm{b}}$ for D^0-tagged jets with $R = 0.4$ in pp collisions at $\sqrt{s}$ = 13 TeV. Right: The feed-down fraction $N_{z,j}^{\mathrm{b}\to\mathrm{D}^0}/N_{z,j}^{\mathrm{eff.corr.}}$ for D^0-tagged jets in $p_{\mathrm{T,ch\,jet}} = 5-7$ GeV/c and $p_{\mathrm{T,ch\,jet}} = 15-50$ GeV/c with $R = 0.4$ in pp collisions at $\sqrt{s}$ = 13 TeV.

The feed-down contribution is subtracted from the measured sample as

$$N_{z,j}^{\mathrm{c}\to\mathrm{D}^0} = N_{z,j}^{\mathrm{eff.corr.}} - N_{z,j}^{\mathrm{b}\to\mathrm{D}^0}. \tag{4.46}$$

The measured $N_{z,j}^{\mathrm{eff.corr.}}$, feed-down subtracted $N_{z,j}^{\mathrm{c}\to\mathrm{D}^0}$ $p_{\mathrm{T,ch\,jet}}$ spectra, and a feed-down contribution $N_{z,j}^{\mathrm{b}\to\mathrm{D}^0}$ for D^0-tagged jets in $p_{\mathrm{T,ch\,jet}} = 5-7$ GeV/c and in $p_{\mathrm{T,ch\,jet}} = 15-50$ GeV/c with $R = 0.4$ in pp collisions at $\sqrt{s}$ = 13 TeV are shown in Figure 4.46.

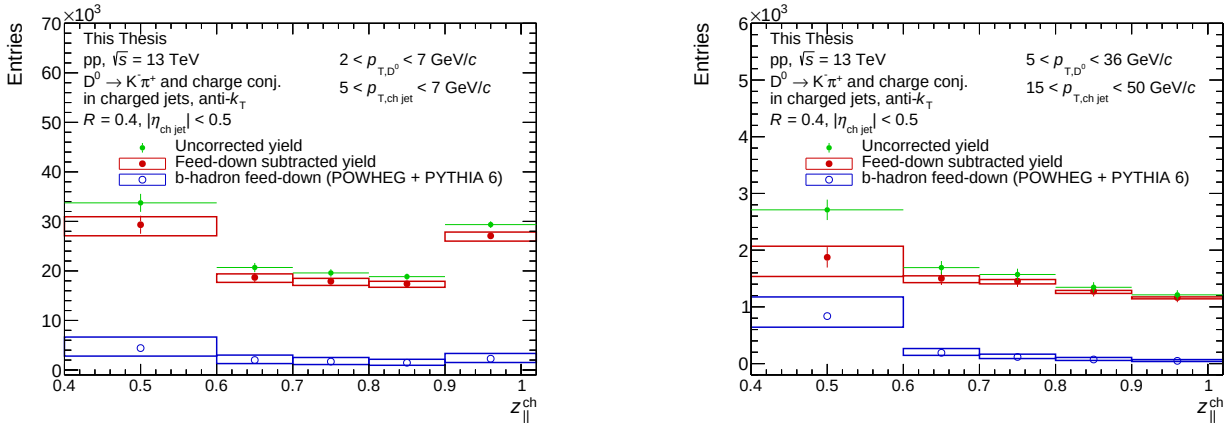

Figure 4.46: A measured, unfolded, and refolded spectra of D^0-tagged jets with $R = 0.4$ in $p_{\mathrm{T,ch\,jet}} = 5-7$ GeV/c (left) and $p_{\mathrm{T,ch\,jet}} = 15-50$ GeV/c (right) in pp collisions at $\sqrt{s}$ = 13 TeV.

4.7.2.3 Unfolding

The last step consists of unfolding the measured prompt distribution by a prompt response matrix in two dimensions $z_{||}^{\mathrm{ch}}$ and $p_{\mathrm{T,ch\,jet}}$. The response matrix is defined as

$$\mathcal{R}_{z,j,y,m}^{*,\mathrm{c}} = \frac{\mathcal{R}_{z,j,y,m}^{+,\mathrm{c}}}{\sum_{z\in z_{||}^{\mathrm{det}}}\sum_{j\in p_{\mathrm{T,ch\,jet}}^{\mathrm{det}}}\mathcal{R}_{z,j,y,m}^{+,\mathrm{c}}}, \tag{4.47}$$

where $\mathcal{R}_{z,j,y,m}^{+,\mathrm{c}}$ is the normalised prompt response matrix, weighted by the prompt efficiency. A response matrix $\mathcal{R}^{+,\mathrm{c}}$ for D^0-tagged jets with $R = 0.4$ in pp collisions at $\sqrt{s}$ = 13 TeV is shown in Figure 4.47 (left). The relative $z_{||}^{\mathrm{ch}}$ resolution, defined as $\Delta z_{||} = \left(z_{||}^{\mathrm{det}} - z_{||}^{\mathrm{gen}}\right)/z_{||}^{\mathrm{gen}}$, is shown in Figure 4.47 (right). Before unfolding, the spectra have been corrected to address

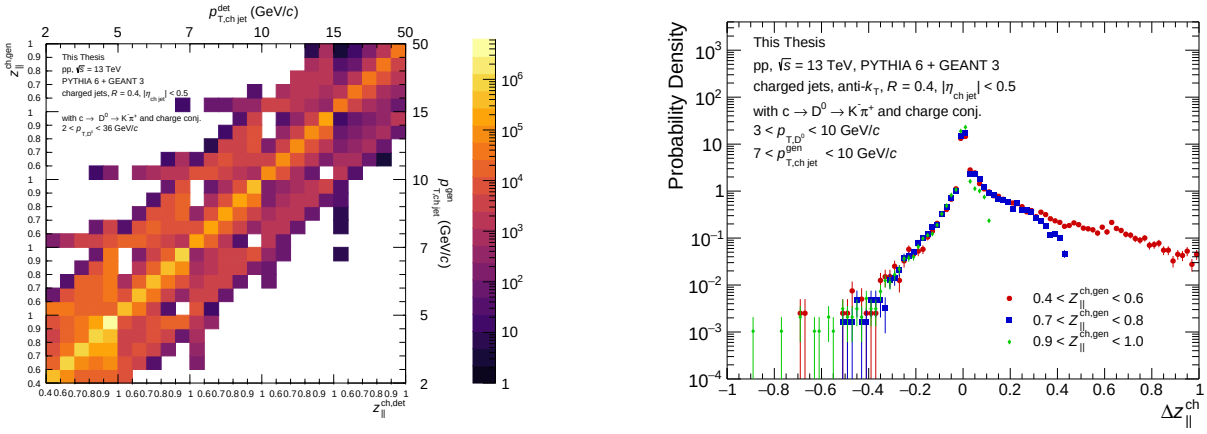

Figure 4.47: Left: A response matrix of fully-matched entries $\mathcal{R}^{+,\mathrm{c}}$ for D^0-tagged jets with $R = 0.4$ in pp collisions at $\sqrt{s} = 13$ TeV. Right: The $z_{||}^{\mathrm{ch}}$ relative resolution $\Delta z_{||} = \left(z_{||}^{\mathrm{det}} - z_{||}^{\mathrm{gen}}\right)/z_{||}^{\mathrm{gen}}$ for D^0-tagged jets with $R = 0.4$ in pp collisions at $\sqrt{s} = 13$ TeV.

missing entries from the response matrix due to limited ranges as

$$N^{*}_{z,j} = N^{\mathrm{c}\to\mathrm{D}^0}_{z,j}\epsilon^{\mathrm{c,\ det}}_{z,j}. \tag{4.48}$$

A Bayesian unfolding as defined in RooUnfold is performed, the k-th iteration is

$$N^{k}_{y,m} = \sum_{z\in z_{||}^{\mathrm{det}}}\sum_{j\in p_{\mathrm{T,ch\ jet}}^{\mathrm{det}}}\left[\frac{\mathcal{R}^{*,\mathrm{c}}_{z,j,y,m}P^{k-1}_{y,m}}{\epsilon_{y,m}\sum_{o\in z_{||}^{\mathrm{gen}}}\sum_{l\in p_{\mathrm{T,ch\ jet}}^{\mathrm{gen}}}\left(\mathcal{R}^{*,\mathrm{c}}_{z,j,o,l}P^{k-1}_{o,l}\right)}N^{*}_{z,j}\right], \tag{4.49}$$

where the priors are

$$P^{k}_{y,m}\begin{cases}\dfrac{N^{k}_{y,m}}{\sum_{y\in z_{||}^{\mathrm{gen}}}\sum_{m\in p_{\mathrm{T,ch\ jet}}^{\mathrm{gen}}}N^{k}_{y,m}} & (k>0)\\[2ex] \dfrac{n_{y,m}}{\sum_{y\in z_{||}^{\mathrm{gen}}}\sum_{m\in p_{\mathrm{T,ch\ jet}}^{\mathrm{gen}}}n_{y,m}} & (k=0)\end{cases} \tag{4.50}$$

the efficiency $\epsilon_{y,m} = \sum_{o\in z_{||}^{\mathrm{det}}}\sum_{l\in p_{\mathrm{T,ch\ jet}}^{\mathrm{det}}}\mathcal{R}^{*,\mathrm{c}}_{z,j,y,m}$ is equal to one for every index y and m as the response matrix contains only entries that were reconstructed and is self-normalised per measured bins, and $n_{y,m} = \sum_{z\in z_{||}^{\mathrm{det}}}\sum_{j\in p_{\mathrm{T,ch\ jet}}^{\mathrm{det}}}\mathcal{R}^{+,\mathrm{c}}_{z,j,y,m}$ is the total number of generated jets in the y-th and m-th bin. Finally, the second correction of finite ranges of response matrix is applied on the fifth iteration chosen for the regularisation as

$$N^{\mathrm{unfolded}}_{y,m} = N^{5}_{y,m}\frac{1}{\epsilon^{\mathrm{c,\ gen}}_{y,m}}. \tag{4.51}$$

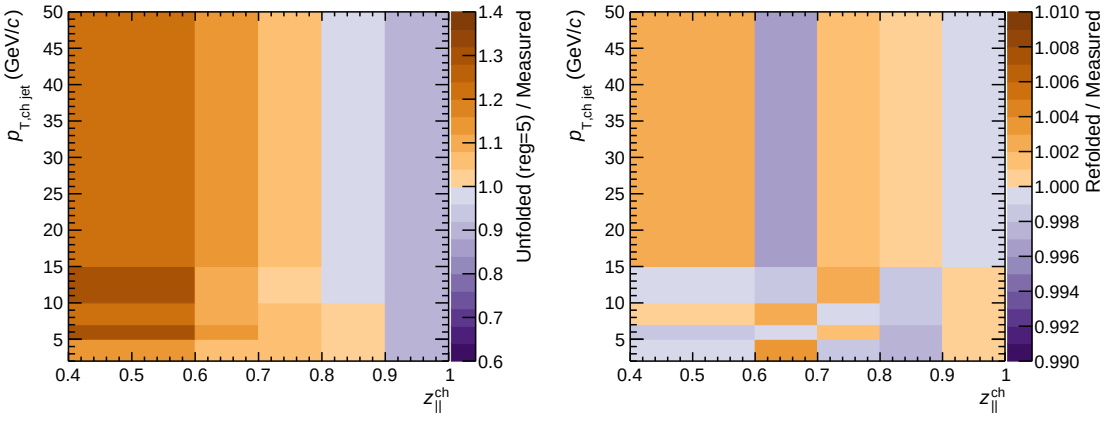

Figure 4.48: Ratio of unfolded to measured spectra (left) and refolded to measured spectra (right) for 5-th iteration of D^0-tagged jets with $R = 0.4$ in pp collisions at $\sqrt{s}$ = 13 TeV.

4.7.3 Systematic uncertainties

The systematic uncertainty has been estimated by the same method as described in $p_{\mathrm{T,ch\,jet}}$ Section 4.6.3. The systematic uncertainties from each source, the total systematic uncertainties, and the statistical uncertainties for $z_{||}^{\mathrm{ch}}$ of D^0-tagged jets in $R = 0.2, 0.4, 0.6$ in pp collisions at $\sqrt{s}$ = 13 TeV are shown in Table 4.5, 4.6 and 4.7, respectively. The $z_{||}^{\mathrm{ch}}$ probability densities are normalised per jet, thus the tracking efficiency (D meson), luminosity, and D^0 branching ratio uncertainties are not applicable. Similarly to section 4.6.3.9, the dominant uncertainty is the beauty feed-down contribution, this uncertainty is the biggest for low $z_{||}^{\mathrm{ch}}$ values as the feed-down contribution is largest for low $z_{||}^{\mathrm{ch}}$. Next dominant sources are the topological selection variables and the jet energy scale, which are large for low $z_{||}^{\mathrm{ch}}$ bins. The low $z_{||}^{\mathrm{ch}}$ bins are usually those with lower statistics and thus some of the statistical fluctuations might propagate in the systematical studies. In comparison to $p_{\mathrm{T,ch\,jet}}$ cross-section, the uncertainties on the $z_{||}^{\mathrm{ch}}$ are relatively small.

Table 4.5: Systematic uncertainties as a function of $z_{||}^{\mathrm{ch}}$ and $p_{\mathrm{T,ch\,jet}}$ for $R = 0.2$ D^0-tagged jets in pp collisions at $\sqrt{s} = 13$ TeV.

Source (%)	$z_{||}^{\mathrm{ch}}$ / $p_{\mathrm{T,ch\,jet}}$ (GeV/c)	0.4 – 0.6	0.6 – 0.7	0.7 – 0.8	0.8 – 0.9	0.9 – 1.0
Raw Yield Extraction	5–7	4.5	2.4	3.0	3.7	4.5
	7–10	4.8	3.3	3.4	2.6	2.2
	10–15	5.0	4.2	4.8	2.6	2.4
	15–50	6.5	3.2	3.3	4.0	4.1
Topological Selection	5–7	11.7	6.5	3.4	2.6	0.7
	7–10	13.7	3.0	2.9	4.2	1.3
	10–15	15.3	2.0	3.8	4.0	1.7
	15–50	21.6	6.5	3.6	3.3	7.4
B Feed-Down	5–7	+8.6	+7.0	+4.6	+3.6	+3.1
		-11.8	-10.3	-6.8	-5.1	-4.3
	7–10	+16.6	+5.6	+4.0	+2.9	+2.5
		-24.2	-8.1	-6.2	-4.5	-3.7
	10–15	+20.9	+5.4	+2.7	+2.3	+2.0
		-29.7	-8.7	-4.5	-3.8	-3.5
	15–50	+9.9	+3.5	+1.6	+1.5	+1.4
		-16.1	-6.0	-2.9	-3.3	-3.1
Unfolding	5–7	1.8	3.0	0.5	1.4	1.3
	7–10	11.1	1.9	1.3	3.8	0.9
	10–15	0.5	1.4	1.2	0.2	0.9
	15–50	11.5	4.6	1.2	2.0	2.8
Tracking Eff. (Jet Energy Scale)	5–7	6.8	6.2	4.7	3.9	1.6
	7–10	13.4	5.2	4.8	4.6	1.7
	10–15	11.8	5.2	4.5	2.8	2.0
	15–50	14.8	6.1	3.8	2.0	2.8
Total	5–7	+16.8	+12.0	+8.1	+7.1	+5.8
		-18.7	-14.2	-9.5	-8.0	-6.6
	7–10	+28.1	+9.1	+7.8	+8.2	+4.0
		-33.2	-10.8	-9.1	-8.9	-4.9
	10–15	+28.9	+9.0	+8.2	+6.0	+4.2
		-35.7	-11.3	-8.9	-6.8	-5.1
	15–50	+30.9	+11.1	+6.4	+6.1	+9.0
		-33.5	-12.1	-6.9	-6.8	-9.5
Statistical Uncertainty	5–7	13.1	11.0	7.4	5.4	1.9
	7–10	20.8	9.4	7.3	5.6	2.3
	10–15	19.0	11.7	8.5	7.3	3.4
	15–50	19.0	14.2	8.9	8.7	5.5

Table 4.6: Systematic uncertainties as a function of $z_{||}^{ch}$ and $p_{T,ch\,jet}$ for $R = 0.4$ D^0-tagged jets in pp collisions at $\sqrt{s} = 13$ TeV.

Source (%)	$z_{||}^{ch}$ / $p_{T,ch\,jet}$ (GeV/c)	0.4 – 0.6	0.6 – 0.7	0.7 – 0.8	0.8 – 0.9	0.9 – 1.0
Raw Yield Extraction	5–7	2.4	3.5	3.2	3.9	4.3
	7–10	3.6	5.8	4.3	3.6	2.4
	10–15	4.4	3.1	3.4	2.0	2.4
	15–50	3.6	3.7	4.3	4.5	5.4
Topological Selection	5–7	10.3	2.8	4.5	6.4	1.7
	7–10	2.9	3.6	1.6	2.0	1.1
	10–15	1.7	4.2	1.5	1.7	3.8
	15–50	4.2	3.7	6.1	2.1	4.0
B Feed-Down	5–7	+5.5	+3.4	+3.1	+2.8	+2.8
		-7.6	-4.8	-4.3	-3.8	-3.8
	7–10	+8.4	+3.4	+2.6	+2.4	+2.2
		-12.1	-4.9	-3.7	-3.4	-3.3
	10–15	+7.9	+2.5	+2.1	+1.7	+1.6
		-11.5	-4.1	-3.2	-3.6	-3.0
	15–50	+11.0	+2.0	+1.7	+1.2	+0.9
		-19.0	-3.3	-2.9	-2.7	-1.7
Unfolding	5–7	3.0	0.7	0.1	2.2	0.2
	7–10	0.6	1.6	0.0	0.8	1.4
	10–15	2.9	2.0	1.4	1.5	0.4
	15–50	0.1	0.4	0.2	0.3	2.2
Tracking Eff. (Jet Energy Scale)	5–7	6.2	3.2	1.9	0.6	4.9
	7–10	8.0	3.2	2.2	0.5	4.9
	10–15	9.6	3.3	3.2	0.4	5.3
	15–50	8.2	4.7	1.2	0.3	6.1
Total	5–7	+13.8	+6.6	+6.7	+8.3	+7.3
		-14.8	-7.4	-7.3	-8.7	-7.8
	7–10	+12.5	+8.4	+5.8	+4.9	+6.1
		-15.3	-9.1	-6.3	-5.4	-6.6
	10–15	+13.6	+7.0	+5.5	+3.5	+7.1
		-15.9	-7.7	-6.0	-4.8	-7.5
	15–50	+14.8	+7.3	+7.7	+5.1	+9.4
		-21.4	-7.8	-8.1	-5.6	-9.5
Statistical Uncertainty	5–7	6.9	6.2	5.4	4.6	3.1
	7–10	6.7	6.6	5.4	5.1	3.8
	10–15	7.5	7.6	7.1	6.5	5.4
	15–50	10.4	9.4	9.0	9.1	8.6

Table 4.7: Systematic uncertainties as a function of $z_{||}^{\mathrm{ch}}$ and $p_{\mathrm{T,ch\,jet}}$ for $R = 0.6$ D^0-tagged jets in pp collisions at $\sqrt{s} = 13$ TeV.

Source (%)	$z_{||}^{\mathrm{ch}}$ / $p_{\mathrm{T,ch\,jet}}$ (GeV/c)	0.4 – 0.6	0.6 – 0.7	0.7 – 0.8	0.8 – 0.9	0.9 – 1.0
Raw Yield Extraction	5–7	3.7	2.8	2.6	2.3	2.6
	7–10	3.5	5.3	4.7	2.7	1.9
	10–15	4.1	3.7	4.1	3.7	4.3
	15–50	4.2	3.1	3.9	4.5	4.7
Topological Selection	5–7	10.1	7.2	4.9	7.3	2.5
	7–10	0.9	3.9	1.7	3.3	2.9
	10–15	1.6	1.6	6.5	1.6	5.8
	15–50	1.5	4.0	4.3	4.9	5.3
B Feed-Down	5–7	+4.1 / -5.5	+2.9 / -4.0	+2.3 / -3.1	+2.3 / -3.1	+2.4 / -3.1
	7–10	+5.0 / -6.9	+2.6 / -3.4	+2.0 / -2.9	+2.2 / -3.6	+2.3 / -3.1
	10–15	+4.7 / -6.9	+2.3 / -3.2	+1.8 / -3.2	+1.5 / -3.1	+1.4 / -2.1
	15–50	+6.5 / -11.2	+2.0 / -3.1	+1.2 / -2.5	+1.0 / -2.0	+0.6 / -0.7
Unfolding	5–7	2.5	0.7	0.1	0.0	1.1
	7–10	3.0	0.8	1.7	3.6	3.2
	10–15	3.6	1.0	1.0	2.0	2.3
	15–50	3.0	0.8	0.0	3.8	3.2
Tracking Eff. (Jet Energy Scale)	5–7	5.2	0.9	0.3	3.3	8.3
	7–10	6.3	0.2	0.4	3.5	9.2
	10–15	8.4	0.7	1.0	2.7	8.5
	15–50	7.6	3.6	1.1	3.7	7.4
Total	5–7	+12.8 / -13.3	+8.3 / -8.8	+6.0 / -6.4	+8.7 / -8.9	+9.5 / -9.7
	7–10	+9.3 / -10.5	+7.0 / -7.4	+5.6 / -6.0	+6.9 / -7.5	+10.6 / -10.8
	10–15	+11.2 / -12.3	+4.8 / -5.3	+8.0 / -8.4	+5.5 / -6.1	+11.5 / -11.6
	15–50	+11.3 / -14.6	+6.6 / -7.0	+6.0 / -6.4	+8.6 / -8.8	+10.8 / -10.8
Statistical Uncertainty	5–7	6.7	7.8	6.5	6.5	6.1
	7–10	5.2	7.0	6.3	7.5	8.4
	10–15	5.9	8.3	8.8	9.1	11.0
	15–50	8.1	11.0	9.6	12.6	14.5

4.7.4 Results

This section contains the final results of the unfolded yield $N_{y,m}^{\text{unfolded}}$ and a discussion of the comparison with models. The $z_{||}^{\text{ch}}$ probability density functions for each $p_{\text{T,ch jet}}$ interval are calculated using the following formula

$$\frac{1}{N}\frac{\mathrm{d}N}{\mathrm{d}z_{||}^{\text{ch}}}|_{p_{\text{T,ch jet}}} = \frac{1}{N_m}\frac{N_{y,m}^{\text{unfolded}}}{\Delta z_{||}^{\text{ch}}}, \tag{4.52}$$

where $N_{y,m}^{\text{unfolded}}$ is the unfolded measured yield in bin $y = z_{||}^{\text{ch}}$ and $m = p_{\text{T,ch jet}}$, it is normalised using the total number of jets in the studied $p_{\text{T,ch jet}}$ interval, $N_m = \sum_{y \in z_{||}^{\text{ch}}} N_{y,m}^{\text{unfolded}}$. The probability density distributions for D^0-tagged jets with $R = 0.2, 0.4, 0.6$ in pp collisions at $\sqrt{s}$ = 13 TeV are shown in Figure 4.49. Due to the limited statistics, a different minimum D^0 $p_{\text{T,D}}$ has been applied for different $p_{\text{T,ch jet}}$ and R as shown in Table 4.2. The same kinematic conditions were applied on the models. There is a visible peak at $z_{||}^{\text{ch}} \approx 1$ for $R = 0.2$ probability density distributions. The peak contains jets whose only constituent is the D^0 itself and disappears for higher R. For a given $p_{\text{T,ch jet}}$ interval there is significant softening of the fragmentation with increased jet radii R. Moreover, the fragmentation is getting softer with increasing jet momentum $p_{\text{T,ch jet}}$.

The $z_{||}^{\text{ch}}$ distributions were compared to the same models as the $p_{\text{T,ch jet}}$ cross-section. Both PYTHIA tunes provide a good description of the data for $p_{\text{T,ch jet}} = 7 - 50$ GeV/c. A softer fragmentation is observed in data in $p_{\text{T,ch jet}} = 5 - 7$ GeV/c interval, this is particularly visible for $R = 0.4$ jets. There is small difference between the two PYTHIA tunes, however, the Monash tune predicts slightly harder fragmentation in the lowest $p_{\text{T,ch jet}}$ interval. The POWHEG + PYTHIA 8 describes data within uncertainties above $p_{\text{T,ch jet}} > 10$ GeV/c, while it predicts harder fragmentation for $p_{\text{T,ch jet}} = 5 - 10$ GeV/c. The discrepancy in lower bins is larger then predicted by the pure PYTHIA models, and is particularly visible for $R = 0.4$ and $R = 0.6$ jets.

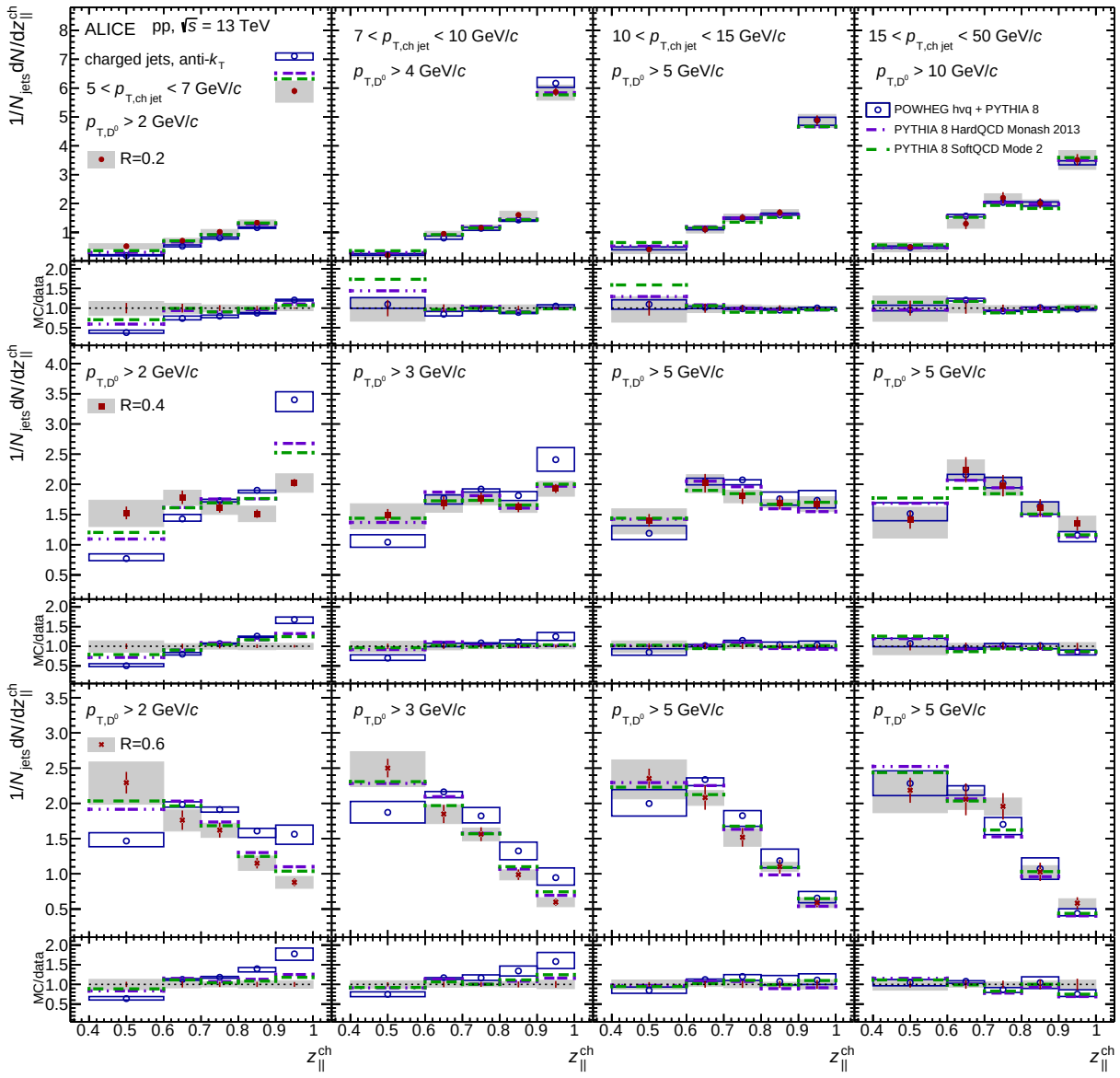

Figure 4.49: The $z_{||}^{\mathrm{ch}}$-differential distribution normalised per number of jets in a given $p_{\mathrm{T,ch\,jet}}$ interval for $R = 0.2$, 0.4 and 0.6 charm jets tagged with D^0 mesons in pp collisions at $\sqrt{s} = 13$ TeV compared to PYTHIA 8 HardQCD Monash tune (dash-dotted lines), PYTHIA 8 SoftQCD Mode 2 (dashed line) and POWHEG-hvq + PYTHIA 8 (open circles) predictions. The vertical lines represent the statistical uncertainty and the shaded bands indicate the systematic uncertainty.

4.8 Conclusion and Outlook

In this thesis, a measurement of charm jets tagged with fully reconstructed D^0 mesons in pp collisions at $\sqrt{s} = 13$ TeV, measured by ALICE at the CERN LHC, has been presented. The $p_{\mathrm{T,ch\,jet}}$-differential cross-section and $z_{||}^{\mathrm{ch}}$ probability density distributions for $R = 0.2$, 0.4 and 0.6 charged-particle jets have been reported and compared to theoretical predictions using leading-order Pythia 8 HardQCD Monash, Pythia Mode 2 with inelastic non-difractive processes, and POWHEG-hvq + Pythia 8 Monash tunes.

The $p_{\mathrm{T,ch\,jet}}$-differential cross-section is best described by the Pythia 8 SoftQCD Mode 2 tune. The POWHEG-hvq + Pythia 8 model describes the measurement within experimental and theoretical uncertainties. Studying different jet radii can constrain pQCD, hadronisation and UE effects in models, as smaller radii are more sensitive to hadronisation models and large radii to UE effects. The cross-section ratios $\sigma(R - 0.2)/\sigma(R = 0.X)$ fall sharply and reach a plateau for $p_{\mathrm{T,ch\,jet}} > 10$ GeV/c. They are well described by both Pythia modes, but systematically overpredicted by POWHEG-hvq + Pythia 8 in the low $p_{\mathrm{T,ch\,jet}}$ region.

For the $z_{||}^{\mathrm{ch}}$ probability density distributions there is a good agreement between data and models for $p_{\mathrm{T,ch\,jet}} > 10$ GeV/c. In the lower momentum regions the models predict a much harder fragmentation than seen in data. The disagreement with data is larger with POWHEG-hvq + Pythia 8 than with Pythia tunes in $p_{\mathrm{T,ch\,jet}} < 10$ GeV/c. The two Pythia tunes provide similar results, with Mode 2 tune generating slightly softer fragmentation. The study of $z_{||}^{\mathrm{ch}}$ is an important input for global fits of gluon-to-hadron fragmentation functions and ALICE provides data in the low $p_{\mathrm{T,ch\,jet}}$ regions where a hint of a bigger disagreement with models is found.

The measurement in this thesis provides better precision and a more differential study

in $p_{\mathrm{T,ch\,jet}}$ and jet R for the intermediate $p_{\mathrm{T,ch\,jet}}$ region than previously published measurements by ALICE. In particular the increased data sample allowed to split the $p_{\mathrm{T,ch\,jet}} = 5-50$ GeV/c region into four momentum bins which allows to test the models more differentially in $p_{\mathrm{T,ch\,jet}}$. In addition, the measurement is done differentially in the jet radius R to study different aspects of the MC generators. The higher precision of the measurement required implementation of new methods and corrections related to the folding and unfolding procedures. The improved systematic error calculations are done to avoid unnecessary overestimation of the uncertainties. The good agreement with models in the higher momentum regions implies that the MC generators describe charm production, fragmentation, hadronisation, and the UE sufficiently well. The most challenging parts, both experimentally and theoretically, are the low $p_{\mathrm{T,D}}$ regions which lie on the edge of perturbative calculability and thus are important in understanding the interplay between perturbative and non-perturbative effects. This measurement can be used as a baseline to study QGP effects in Pb–Pb collisions.

Substantial upgrades to the ALICE detector in Run 3, including upgrades to the tracking capabilities, will result in major improvement of detector performance and in a substantial decrease of the systematic uncertainties. In particular the new ITS will allow topologically distinguish primary and secondary vertices, and so reduce the contribution of the model-based estimation of the beauty feed-down. Significant reduction of the measurement uncertainties will tighten the constraints on theoretical predictions.

Appendix One

Introduction to HEP variables

A.1 Kinematic variables

In high energy physics, particle position and momentum are described in terms of four-vectors (see chapter 1.2 in [132]). The space–time position of a particle is represented by

$$\mathbf{x} = (ct, x, y, z)\,, \tag{A.1}$$

where c is the speed of light, t is the time, and x, y and z are spatial coordinates of a particle in a given frame. The four-momentum is written as

$$\mathbf{p} = (E/c, p_x, p_y, p_z)\,, \tag{A.2}$$

where E is the particle energy, c is the speed of light, and p_x, p_y, p_z are momentum components for a given coordinate. The four-momentum squared $\mathbf{p}^2 = m^2c^2$ is equal to associated particle mass m.

A unit of eV $= 1.602 \cdot 10^{-19}$ J is defined as the amount of energy gained by a single electron that is accelerated in a 1 V potential. To simplify the notation, a natural units are often used, where speed of light, reduced Planck constant and Boltzmann constants are

normalized to unity as $c = \hbar = k_b = 1$. This allows a redefinition of units, where the energy, momentum, temperature, and mass are in units of [eV] and time and length in [eV^{-1}].

By aligning the p_z in collider accelerators along the beam direction a transverse momentum, p_{T} is defined as

$$p_{\mathrm{T}} = \sqrt{p_x^2 + p_y^2}, \tag{A.3}$$

the four-momentum can be rewritten as $\mathbf{p} = (E, \vec{p_{\mathrm{T}}}, p_z)$. The strong feature of the p_{T} notation is an invariance under Lorentz transformation along the z-axis (beam direction)

$$\begin{aligned} E' &= \gamma \left(E - \beta p_z\right), \\ p'_{\mathrm{T}} &= p_{\mathrm{T}} \\ p'_z &= \gamma \left(p_z - \beta E\right), \end{aligned} \tag{A.4}$$

where primed variables are Lorentz transformed, $\beta = v_z/c$ is the velocity and $\gamma = \frac{1}{\sqrt{1-\beta^2}}$ is the Lorentz gamma factor.

Another useful Lorentz invariant variable is the transverse mass defined as

$$m_T^2 = E^2 - p_z^2 = p_{\mathrm{T}}^2 + m^2, \tag{A.5}$$

where m is the associated particle mass.

A.1.1 Rapidity

Rapidity (see chapter 1.2 in [132]) is used to describe particle trajectory in a frame parallel to the beam axis defined as

$$y = \frac{1}{2} \ln \left(\frac{E + p_z}{E - p_z} \right), \tag{A.6}$$

where E is the particle energy and p_z its momentum along the beam axis. Under the Lorentz transformation, rapidity changes only by an additive constant. Thus, describing particle momentum in the form $\mathbf{p} = (m_T \cosh y, p_{\mathrm{T}}, m_T \sinh y)$ is appropriate.

A.1.2 Pseudorapidity

Even though the rapidity is a good variable while describing a theory, it is hard to determine experimentally. Thus a different variable, pseudorapidity - η (see chapter 1.2 in [132]), is defined and can be derived from the rapidity as

$$\begin{aligned} y &= \frac{1}{2}\ln\left(\frac{E+p_z}{E-p_z}\right) = \frac{1}{2}\ln\left(\frac{\sqrt{m^2+p^2}+p\cos\theta}{\sqrt{m^2+p^2}-p\cos\theta}\right) \overset{p\gg m}{\approx} \\ &= \frac{1}{2}\ln\left(\frac{p+p\cos\theta}{p-p\cos\theta}\right) = -\ln\tan\frac{\theta}{2} \equiv \eta, \end{aligned} \tag{A.7}$$

where p is the particle momentum and θ is the momentum angle from the perpendicular plane to the beam axis. The equality in this form only holds when the particle momentum is so high, that the mass can be neglected: $p \gg m$. There is only one measurable quantity, angle, which is independent of any particle identification – mass, momentum and collision energy, and thus is very convenient to use.

A.1.3 Collisional energy

The Lorentz transformation invariant centre-of-mass energy, $\sqrt{s}$ (see chapter 1.3 in [132]) is used to describe collisional energy within accelerator defined as

$$\sqrt{s} = \sqrt{(\mathbf{p}_1+\mathbf{p}_2)^2}, \tag{A.8}$$

where p_1 and p_2 are four-momenta of the first and second beam. In high energetic beams, the mass is negligible and thus the energy of the first beam $E_1 = p_z$ and of the second $E_1 = -p_z$. Moreover, the energies of both beams are the same $E_1 = E_2$, this leads to $\sqrt{s} = 2E$, where E is the energy of one beam. At LHC the energy of a single proton in one beam is 6.5 TeV and thus the $\sqrt{s}$ = 13 TeV.

In case of ion-ion collisions, the energy of ion is scaled by a number of nucleons, N, to calculate per nucleon normalised centre-of-mass energy, $\sqrt{s_{\mathrm{NN}}}$. Since the accelerator can

accelerate only charged particles, the neutrons only contribute with their mass. In case the electric and magnetic properties of the machine are the same as in case of proton beams

$$\sqrt{s_{\mathrm{NN}}} = \frac{Z}{N}\sqrt{s}, \tag{A.9}$$

where the Z is the atomic number. At the LHC by having a lead-lead beams one reach a maximum energy of around $\sqrt{s_{\mathrm{NN}}} = \frac{87}{207} \cdot 13$ TeV $= 5.46$ TeV, which is close to the measured $\sqrt{s_{\mathrm{NN}}} = 5.02$ TeV and $\sqrt{s_{\mathrm{NN}}} = 5.44$ TeV.

A.1.4 Luminosity

The luminosity [133] is a measure of the beam intensity product in the collision region for a colliding beam accelerator. In a storage type accelerator (particles moving on two circular trajectories colliding at intersection points) it is defined [133] as

$$\mathscr{L} = fn\frac{N_1 N_2}{A}, \tag{A.10}$$

where f is the revolution frequency, n number of bunches (clusters of particles), N_1 and N_2 number of particles in each bunch and A is bunch cross-sectional area. Luminosity is an important concept allowing to connect measured rapidity normalized particle production per event $\frac{\mathrm{d}N}{\mathrm{d}y}$ with a cross-section as

$$\frac{\mathrm{d}\sigma}{\mathrm{d}y} = \frac{1}{\mathscr{L}}\frac{\mathrm{d}N}{\mathrm{d}y}. \tag{A.11}$$

A.1.5 Centrality

Heavy-ion collisions can be divided into centrality classes [133], corresponding to collisions with different overlapping volumes of two colliding nuclei, based on the impact parameter. The impact parameter, b, is a distance between centres of interacting nuclei in the transverse

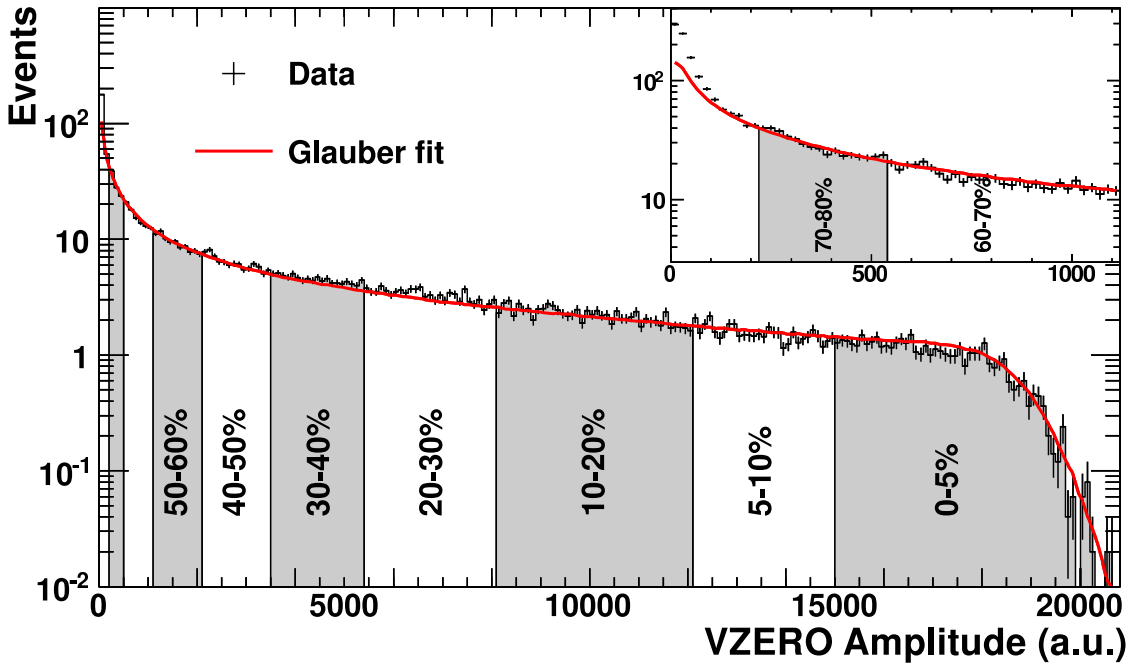

Figure A.1: Distribution of the sum of amplitudes in the V0 scintillators. The line shows the fit of the Glauber calculation to the measurement [135].

plane. Collisions with $b \approx 0$ are called most central, while collisions with $b > R_1 + R_2$, where R_1 and R_2 are participating nuclei radii, are called ultra-peripheral. As it is not possible to measure the impact parameter directly, a following assumption is made: The charged-particle multiplicity is a monotonic function of the impact parameter b.

Multiplicity is the number of charged tracks per event measured by experiment. It can be described by a Glauber Model [134]. The distribution of amplitudes in the V0 scintillators measured by ALICE, with Glauber model parametrization and centrality class definition, is shown in Figure A.1, where the amplitude is proportional to the multiplicity. The top 5% events with most tracks (highest multiplicity) is called centrality range 0-5% which, under above-stated assumptions, corresponds to events with lowest b.

Appendix Two

Additional plots for the Quality Assurance

As in the section 4.4 the main focus was towards flawed data and MC, this appendix is dedicated to typical QA distributions having the correct appearance. The φ distributions for inclusive jets in different $p_{\mathrm{T,ch\,jet}}$ intervals for data and MC for period `LHC18e` are shown in Figure B.1. The jet area, number of tracks in a jet, jet and its tracks φ and η distributions for inclusive jets from period `LHC18e` anchored to MC are shown in Figure B.2. The η distributions for D^0-tagged jets in different $p_{\mathrm{T,ch\,jet}}$ intervals of MC sets anchored to 2017 data periods, normalised to number of events, is shown in Figure B.3. The jet area, number of tracks in a jet, jet and its tracks φ and η distributions for D^0-tagged jets of MC sets anchored to 2017 data, normalised to number of events, are shown in Figure B.4.

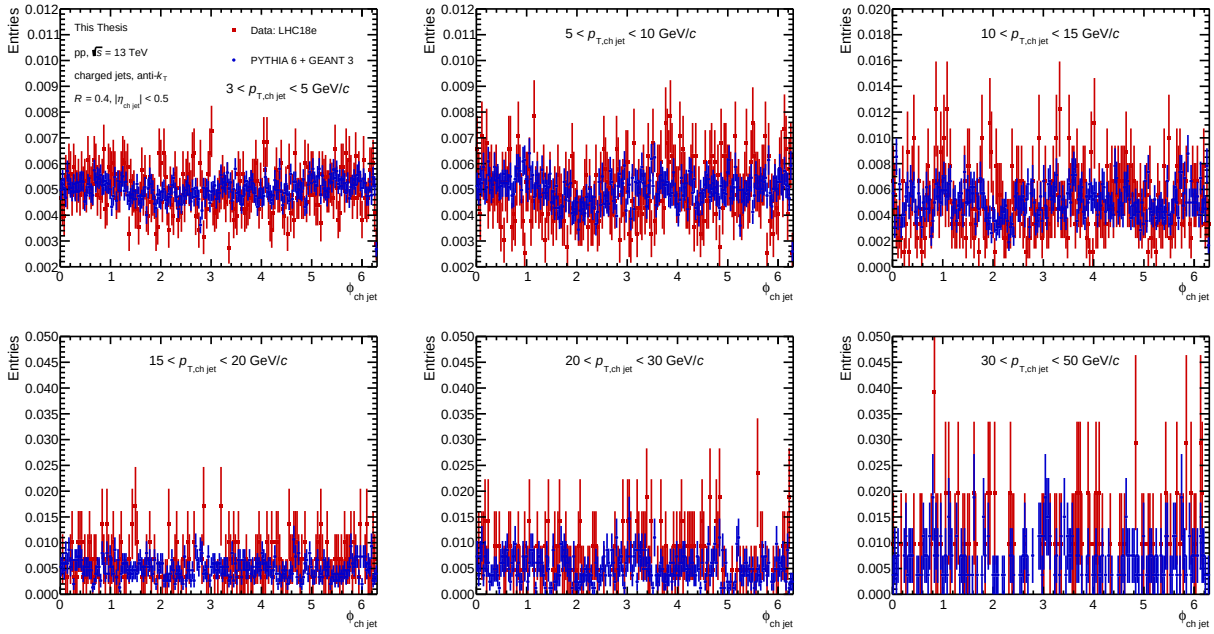

Figure B.1: The φ distributions for inclusive jets in different $p_{\mathrm{T,ch\,jet}}$ intervals for data from period `LHC18e` anchored to MC.

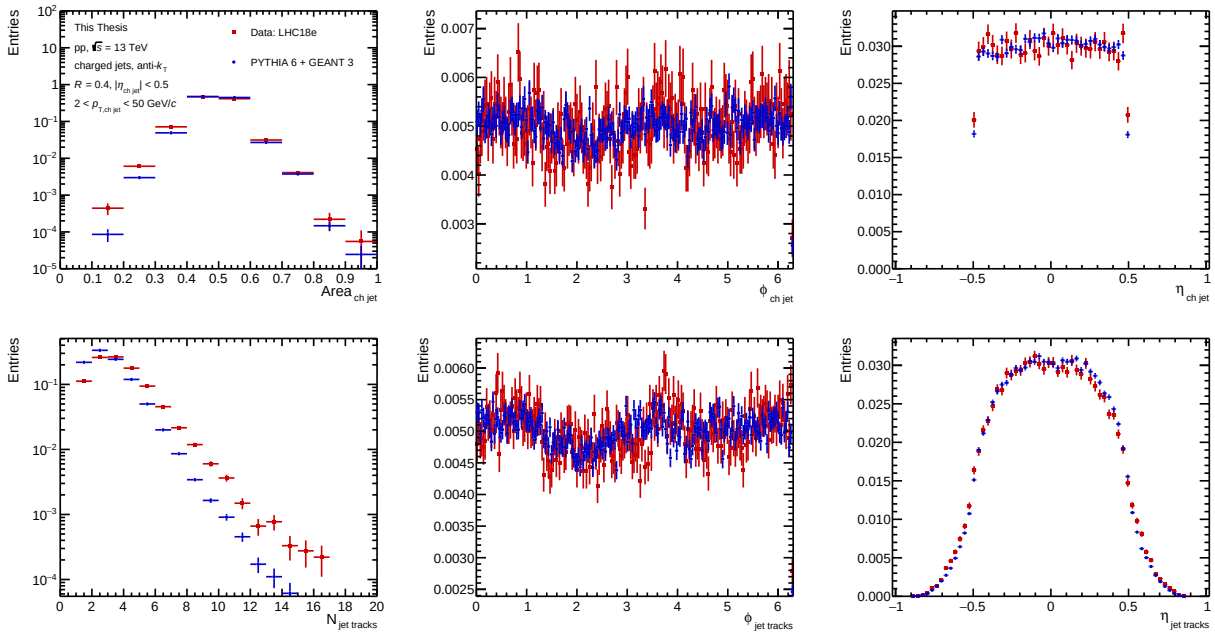

Figure B.2: The jet area, number of tracks in a jet, jet and its tracks φ and η distributions for inclusive jets from period `LHC18e` anchored to MC.

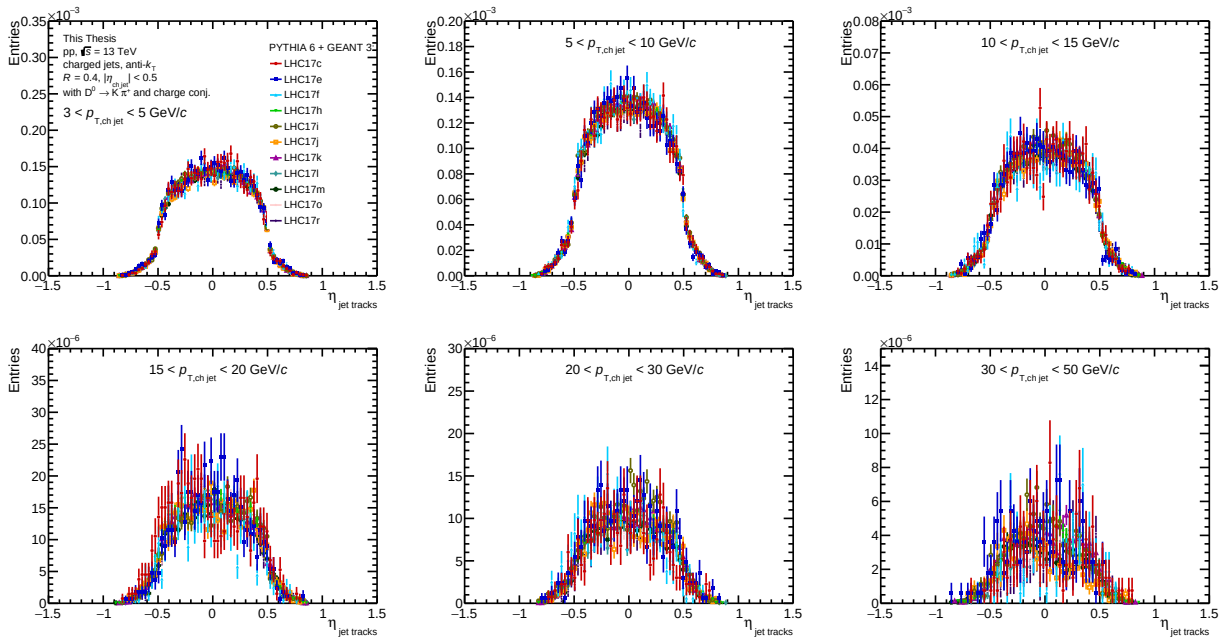

Figure B.3: The η distributions for D^0-tagged jets in different $p_{T,ch\,jet}$ intervals of MC sets anchored to 2017 data periods and normalised per number of events.

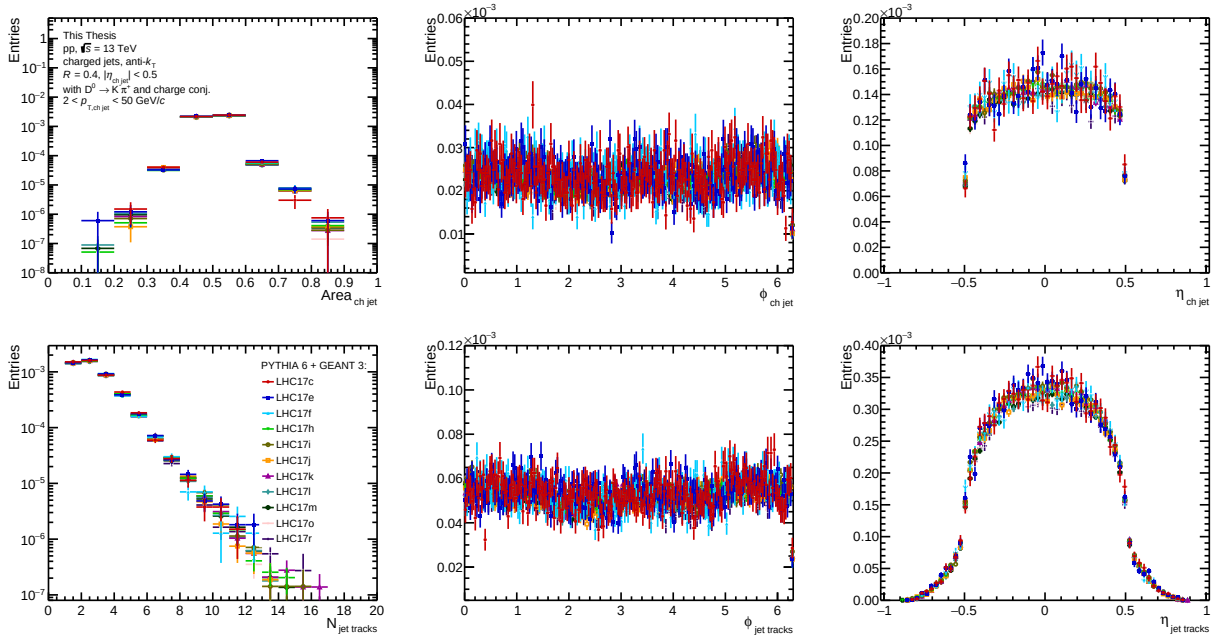

Figure B.4: The jet area, number of tracks in a jet, jet and its tracks φ and η distributions for D^0-tagged jets jets of MC sets anchored to 2017 data periods and normalised per number of events.

Appendix Three

Publications

arXiv:2106.08353v2 [physics.ins-det] 30 Jun 2021

ALICE Central Trigger System for LHC Run 3

Jakub Kvapil[1,*], *Anju* Bhasin[2,4], *Marek* Bombara[3], *David* Evans[1], *Anton* Jusko[1], *Alexander* Kluge[4], *Marian* Krivda[1], *Ivan* Kralik[5], *Roman* Lietava[1], *Sanket Kumar* Nayak[1], *Simone* Ragoni[1], and *Orlando* Villalobos Baillie[1]

[1]University of Birmingham, Birmingham, UK
[2]Physics Department, University of Jammu, India
[3]Pavol Jozef Safarik University, Kosice, Slovakia
[4]European Organization for Nuclear Research (CERN), Switzerland
[5]Slovak Academy of Science, Kosice, Slovakia

Abstract. A major upgrade of the ALICE experiment is in progress and will result in high-rate data taking during LHC Run 3 (2022-2024). The LHC interaction rate at Point 2 where the ALICE experiment is located will be increased to 50 kHz in Pb–Pb collisions and 1 MHz in pp collisions. The ALICE experiment will be able to read out data at these interaction rates leading to an increase of the collected luminosity by a factor of up to about 100 with respect to LHC Runs 1 and 2. To satisfy these requirements, a new readout system has been developed for most of the ALICE detectors, allowing the full readout of the data at the required interaction rates without the need for a hardware trigger selection. A novel trigger and timing distribution system will be implemented, based on Passive Optical Network (PON) and GigaBit Transceiver (GBT) technology. To assure backward compatibility a triggered mode based on RD12 Trigger-Timing-Control (TTC) technology, as used in the previous LHC runs, will be maintained and re-implemented under the new Central Trigger System (CTS). A new universal ALICE Trigger Board (ATB) based on the Xilinx Kintex Ultrascale FPGA has been designed to function as a Central Trigger Processor (CTP), Local Trigger Unit (LTU), and monitoring interfaces.
In this paper, this new hybrid multilevel system with continuous readout will be described, together with the triggering mechanism and algorithms. An overview of the CTS, the design of the ATB and the different communication protocols will be presented.

1 Introduction

A Large Ion Collider Experiment (ALICE) [1] at the Large Hadron Collider (LHC) [2] started its operation in 2008 and has produced important results in both heavy-ion and proton-proton collisions. The ALICE Central Trigger Processor (CTP) [3] used in LHC Run 2 operated with four trigger latencies LM (650 ns), L0 (900 ns), L1 (6.5 μs), and L2 (88 μs). The LM level was sent only to the Transition Radiation Detector (TRD), which therefore received all four levels, while all other detectors received L0 as their first trigger signal. The LM board design was used as an alpha version of the future ALICE Trigger Board (ATB). The CTP consisted

*e-mail: jakub.kvapil@cern.ch

of 6 different 6U Versa Module Europa (VME) boards, with in addition a Local Trigger Unit (LTU) board for each detector. Communication between boards was done via a customised back-plane. The communication between LTUs and detector front-end electronics (FEE) was done using the Trigger-Timing-Control (TTC) protocol developed by the RD12 collaboration [4]. The designed interaction rate was 8 kHz for Pb–Pb and 100 kHz for pp collisions. The maximum readout rate was around 1 kHz due to the space-charge and bandwidth limitations of the Time Projection Chamber detector.

For LHC Run 3, ALICE will upgrade the readout system to implement continuous detector readout. The ALICE detectors will be self-triggered, constantly pushing the data stream, and the CTP will provide time-stamps to synchronise data from different detectors. The original idea of the triggered event will no longer be valid, as there are no discrete events but rather a continuous stream. The interaction rate will be 50 kHz for Pb–Pb, 500 kHz for p–Pb, and 1 MHz for pp collisions and every event will be read out. To incorporate these changes a new CTP and LTUs were developed for timing distribution alongside the new Common Readout Unit (CRU) [5] for the readout. However, since some detectors are not upgrading their hardware, a trigger distribution and the RD12 TTC protocol must also be available.

2 Overview of Central Trigger System

The layout of the new Central Trigger System (CTS) is similar to the old one. One CTP board distributes the clock and triggers to 18 LTU boards, one for each ALICE detector, one in test setup and two spare boards. During normal (global) data-taking operations the CTP controls the LTUs, which act as a communication interface with the detector CRUs. Due to the two-tier system, a single LTU can also be decoupled from the CTP and the other LTUs and operated in the so-called standalone mode to perform independent tests without influencing the data-taking of the other detectors. In standalone mode the LTU can emulate the presence of the CTP. This feature is particularly important for the commissioning phase.

An overview of the ALICE CTS is shown in Figure 1. There are several hardware protocols used for CTS communication with detectors. Detectors that are fully upgrading their FEE, namely the Fast Interaction Trigger (FIT), which is composed of the 3 sub-detectors FT0, FV0 and FDD, Muon Chambers (MCH), Muon Identifier (MID), Time-of-Flight (TOF), Time Projection Chamber (TPC), Inner Tracking System (ITS), Muon Forward Tracker (MFT) and Zero Degree Calorimeter (ZDC), all use the Common Readout Unit card for readout. The link between LTU and CRU uses the bidirectional TTC Passive Optical Network (PON) [6] technology and the communication between CRU and detector FEE uses the GigaBit Transceiver (GBT) [7] technology. In addition to these connections, the ITS and MFT require a direct GBT link between LTU and FEE. The Electromagnetic Calorimeter (EMC), Photon Spectrometer (PHS), and High Momentum Particle Identification (HMP) are not upgrading their electronics and will continue using the RD12 TTC protocol for downstream communication. The Transition Radiation Detector (TRD) uses the TTC-PON system but requires triggers over RD12 TTC optical lines. The Charged Particle Veto (CPV) receives clock and trigger signals over GBT links. The EMC, PHS, HMP, TRD and CPV cannot read out data at the required rate and each of them will generate a BUSY signal to inform the CTP when additional triggers cannot be received.

3 The Time and Trigger distribution in ALICE

Starting from the LHC Run 3, the ALICE default operation mode will be in continuous readout at a rate of 50 kHz in Pb–Pb collisions and 1 MHz in pp collisions. A subsequent data

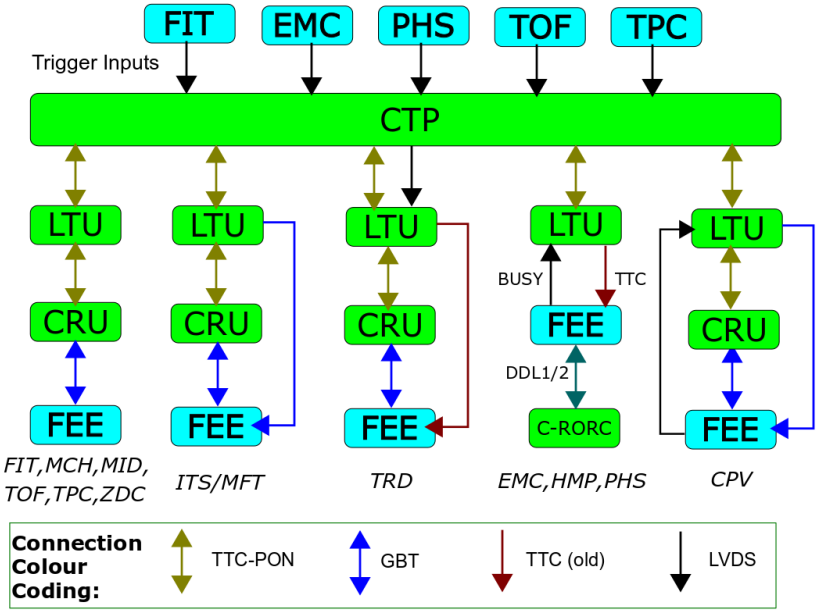

Figure 1. Central Trigger System overview showing trigger inputs to the CTP and the connection types between the CTP and the detector FEE.

selection is done using software filters. The detectors using CRUs must also be able to operate in triggered mode, which is especially important during the commissioning phase. Detectors not using CRU and GBT links are operated in triggered mode, with the CTP providing triggers distributed via the RD12 TTC protocol as explained above. Detectors using the RD12 TTC protocol and the CPV are triggered using a two-level scheme with the possibility to operate using trigger signals on three different latencies (LM, L0, L1). The two-level system is particularly important for detectors using the RD12 TTC protocol due to the limited readout bandwidth.

The trigger input detectors listed in Table 1 provide a total of 39 trigger inputs to the CTP on different latencies. In addition, the LHC Beam Pick-up Timing system (BPTX) will contribute with 2 inputs on L0 latency. Some detectors can provide multiple inputs corresponding to different trigger conditions. These inputs are only important for detectors requiring triggers.

Table 1. CTP trigger inputs with their latency and contributing trigger level.

Detector	Lat./Level	N of inputs	Latency [ns]
FT0	LM	5	425
FV0	LM	5	425
FDD	L0	5	-
TOF	L0	4	862
EMC	L0	2	843
	L1	8	6100
PHS	L0	2	843
	L1	5	6100
BPTX	L0	2	-
TPC	L0	1	900

The ALICE data are divided into so-called HeartBeat frames (HBf) and 128 (programmable value) of them will compose a Time Frame (TF). A HBf is set to have the same length as an LHC orbit ($\approx 88.92\ \mu s$), which is approximately the time required to fully read out the hits from the TPC detector. The CTP sends a HeartBeat (HB) signal and a HeartBeat reject (HBr) flag at the beginning of each HBf. The CRU either accepts or rejects data in the upcoming HBf according to the HBr flag. In response, the CRU sends back a HeartBeat acknowledge message (HBam), containing a HeartBeat acknowledge (HBack) flag for whenever an HBf was successfully transferred to the First Level Processor (FLP) [5]. Since the HBfs are buffered, successful transmission can happen up to 8 HBf after it was collected. The HBam also carries the status of the CRU buffers (Buffers Status (BS)). The HBr allows control over CRU throttling and is used in three ways. In the first case, the CTP does not issue any HBr and every CRU runs in autonomous mode. In the second case, the HBr is used to downscale the data rate by generating a certain number of HBr signals in a TF. Lastly, the CTP evaluates the CRU buffer statuses every HBf and decides whether to generate a HBr or not - this is called the collective mode.

The CTP collects the HBack flags from all 441 CRUs and builds a so-called Global HeartBeat Map (GHBmap). The HeartBeat decision (HBd) is calculated using a HB function f. Since it is not possible to implement a general function of $N = 441$ bits, the problem is simplified in the following way. A HeartBeat Mask (HBmask) corresponding to a certain subset of CRUs is introduced and the function f is defined as

$$HBd = f(GHBmap \wedge HBmask), \tag{1}$$

where $\wedge$ represents a logical "and" and the function f is a simple logical function of the "and" result. The HBd is then asynchronously transmitted via CRUs to FLP to notify them whether to save or discard a particular HBf. There will be a HB function for each detector to be universal in the creation of detector groups (clusters). For example, if the function is the same for each detector, ALICE behaves as one detector for readout, whereas if a different function is used for each detector, then each detector works independently of the others. A schematic diagram of the HB logic flow can be seen in Figure 2.

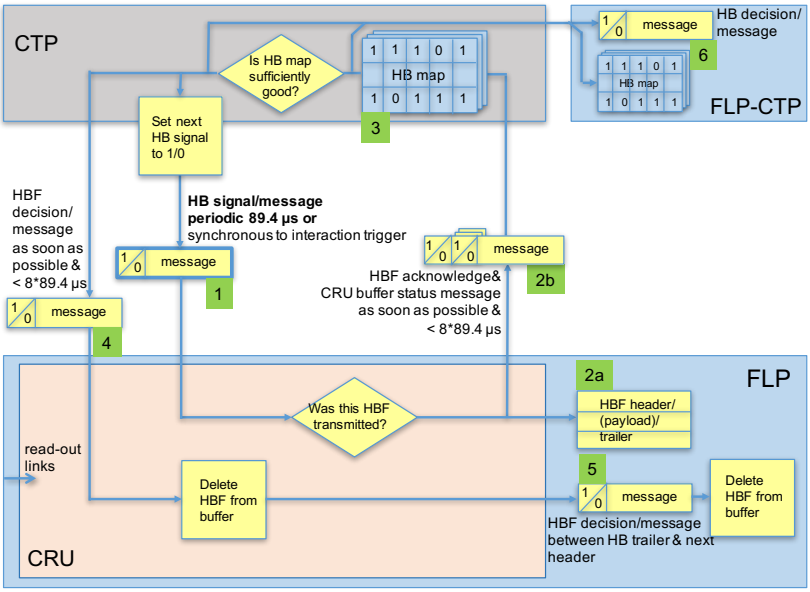

Figure 2. A logical flow of HeartBeat signals between CTP, CRU and FLP.

For the detectors that can run only in triggered mode, a design of trigger classes, similar to Run 2, is used. A trigger class is defined as a set consisting of trigger conditions, cluster, and vetoes. A trigger condition contains a logical function of trigger inputs and a Bunch Crossing (BC) mask (which specifies which BC slots correspond to physical bunch crossings). A trigger cluster is a group of detectors to be read out together. The trigger veto consists of the logical "or" of a cluster's detector busy and down-scaling veto. There can be up to 64 classes and 18 clusters in Run 3. Since triggered detectors usually need to be read out together with detectors in continuous mode, a HBr of those detectors will act as another busy veto, so the CTP does not send triggers during HBr windows. Moreover, triggered detectors do not contribute to the HBd evaluation as the HBd is evaluated long after the triggered detectors store data. This design allows independent operation of continuous readout detectors and a partial correlation with triggered detectors.

4 Implementation of the CTS

4.1 Trigger Protocols and Transceivers

The CTP generates a timing and trigger message which is transmitted to the FEE to synchronise all ALICE detectors. The trigger message consists of 80 bits arranged as follows: trigger type (32 bits), BC counter (12 bits), trigger level (4 bits), Orbit counter (32 bits). The bunch crossing number and orbit counters make up the event identification used to time stamp the data. The trigger time carries information about start/end of run, HeartBeat, physics, orbits, calibration etc.

The Passive Optical Network (PON) is an off-the-shelf technology using the Optical Line Terminal (OLT) acting mainly as a transmitter, and the Optical Network Unit (ONU), acting mainly as a receiver. It allows up to 9.6 Gbps data flow. Both units can transmit and receive, however, the opposite transceiver has limited bandwidth and speed. Each network link can send 30 8-bit words per bunch crossing (24.95 ns), of which five are for PON internal use, leaving 200 user-defined bits. The first 15 words are used for trigger messages together with additional monitoring. The last 10 bytes are used to transmit the HeartBeat Decision Record (HBDR) of a particular TF as described in Section 3.

The GBT protocol allows bidirectional transmission directly to the detector FEE. An LTU sends 120 bits per bunch crossing; the first 80 bits are the trigger message, identical to the PON message. The remaining bits are reserved for GBT internal use.

The RD12 TTC consists of 2 channels allowing transmission of only one bit per bunch crossing per channel. The TTC-A channel is used to transmit a synchronous trigger for two levels (1-bit for LL0 and 2-bit for LL1) and TTC-B is for asynchronous trigger messages. Each channel is Manchester-encoded with the clock and they are multiplexed into a 160.316 MHz optical line by the TTCex and sent to the detector FEE. One TTC-B word is a 42 bits long Hamming-encoded message, where 16 bits are available for the user, of which 4 bits are reserved for the word header, effectively leaving 12 data bits. The 76 bits of trigger message (excluding the trigger level which is sent over TTC-A) is split between 7 TTC-B words limiting the maximum trigger rate to about 130 kHz, sufficient for TTC detectors. In addition, each LHC orbit and any calibration requests, both used for synchronisation, are sent synchronously in TTC-B as a short broadcast (16 bits - 6 for user) command. To allow synchronous transmission in a channel that is by default asynchronous, a re-synchronisation is done for the duration of the broadcast transmission. Since the busy is treated on the CTP/LTU side, an internal busy is raised to prevent new trigger generation for the duration of L0-L1 to address detector busy propagation time towards the CTP/LTU. Lastly, since the transmitter

bandwidth is limited, a derandomisation is implemented, and once the buffers are full, a busy is raised to prevent acceptance of new triggers.

4.2 ALICE Trigger Board

A general ALICE Trigger Board (ATB) was designed to act as CTP, LTU, LTU-GBTit (GBT interface test) and LTU-TTCit (TTC interface test) with small modifications. The board can be seen in Figure 3. The board can be powered either through the 6U VME crate using +5V/10A ±12V/1A or using a standalone crate which provides the required voltages and cooling. The standalone box version has proved to be particularly useful when distributing LTU boards to detector groups for standalone test runs. From the power supply, the DC-DC converter generates 12 different power domains required for the board operation. To monitor the domains two UCD90120A Power Management Bus (PMBus) chips are present on the board with a connector on the front panel for monitoring using the I^2C protocol. Two Si5345 Phase-Locked Loops (PLL) are used to generate a very precise clock with a random jitter of 1 ps which can be locked to the LHC main clock using the TTC machine interface (TTCmi). The most strict requirement is from the ALICE TOF detector, requiring 12 ps jitter at worst. The main three clock domains are 240.474 MHz, which serves as the central board clock, 40.079 MHz as the LHC bunch-crossing frequency, and 31.25 MHz for ethernet communication. Two 1 GB MT40A512M16HA-083E Double Data Rate 4 Synchronous Dynamic Random Access Memory (DDR4 SDRAM) are used to store signals used for monitoring and debugging. One DDR4 is used to monitor the inputs and the other for the outputs of the board. The LTU board is equipped with a Xilinx Kintex Ultrascale FPGA (XCKU040-2FFVA1156E) and flash memory (MT25QU128ABA1EW7) to store the FPGA logic. The CTP board is equipped with a more powerful FPGA (XCKU060-2FFVA1156E) and a bigger flash memory (MT25QU256ABA1EW7) to accommodate the larger CTP requirements for logic. The flash memory can be programmed using a microUSB-JTAG connection from the front panel. A two-fold Small form-factor pluggable transceiver (SFP+) cage is used to plug in high-speed link optical modules and a single-fold SFP+ case for a plug-in ethernet module. The FPGA Mezzanine Card (FMC) port can be utilised to change the purpose of the general trigger board. The CTP FMC card will be used on the CTP board to utilise up to 64 LVDS trigger inputs/outputs. The FMC FM-S18 rev. E can be used as another SFP+ two-fold cage to increase the number of available optical links on LTU boards. Furthermore, by using FMC GBTx, the board can be converted into a LTU-GBTit board to monitor the machine interface clock and data on GBT links. Finally, by using the TTCrx FMC card the board will be converted into the LTU-TTCit board to monitor data on TTC links. On the front panel, there are 8 ECL LEMO 00B connectors for RD12 TTC, scope, clock, and orbit signals, 6 LVDS LEMO B connectors for triggers and busy and an SMA connector which is directly connected to PLL and provides the clock.

The general LTU board has one ONU to receive data from the CTP, nine OLT for connecting detector, one downstream GBT for CPV (so general firmware can be used) and 1 bidirectional GBT, in case each LTU is connected with the FLP via CRU for monitoring. The ITS and MFT detectors require more GBT links thus their board will be equipped with one ONU, one OLT, one bidirectional GBT, and 13 downstream GBT (of which 4 are located on the FMC). A summary of the detector operation latencies/trigger levels and optical and electrical connections between LTU, CRU and FEE is given in Table 2.

The CTP board is equipped with 9 OLT to control the 18 LTU, and 3 bidirectional GBT to send the interaction record, trigger class record, and monitoring to the CRU-FLP. Using the GBT protocol for the connection to CRU-FLP, an LTU and CTP behave as an additional detector for the readout system.

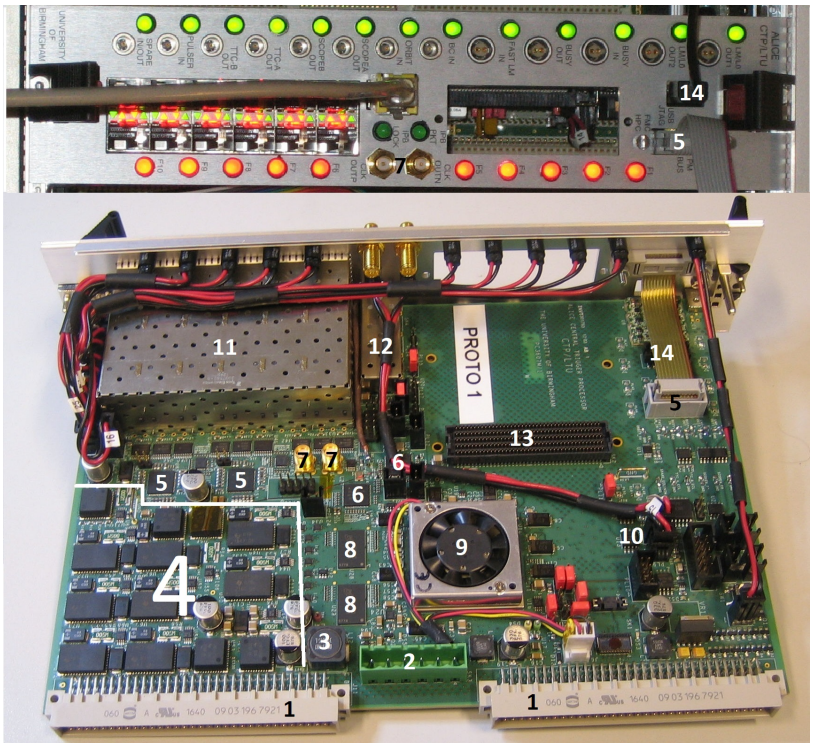

Figure 3. Front and side view of ALICE Trigger Board (ATB). The following components are visible (see in the text for details).
1: VME 6U power supply connector
2: ELMAbox power supply connector
3: power decoupling - inductance
4: DC-DC converter
5: PMbus
6: PLL
7: Clock from PLL
8: DDR4
9: FPGA
10: Flash memory
11: two six-fold SFP+
12: single-fold SFP+
13: FMC
14: JTAG-microUSB

Table 2. A summary of operating levels, number of OLT links with optical attenuation and splitter, number of GBT and TTC links, LVDS with the level it operates on, and how the busy is propagated back to CTP for various ALICE detectors.

Detectors	Lat./Level	OLT	opt. att	opt. split.	GBT	TTC	LVDS	BUSY
MID	LM	1	10 dB	1:4	-	-	-	-
TOF	LM	1	10 dB	1:4	-	-	-	-
FT0	LM	1	15 dB	none	-	-	-	-
FV0	LM	1	15 dB	none	-	-	-	-
FDD	LM	1	15 dB	none	-	-	-	-
ZDC	LM	1	15 dB	none	-	-	-	-
MCH	LM	1	none	1:32	-	-	-	-
TPC	LM	6	none	6x 1:64	-	-	-	-
ITS	LM	1	none	1:32	6/12	-	-	-
MFT	LM	1	none	1:32	6	-	-	-
TRD	LM - L0	9	10 dB	9x 1:4	-	20	-	TTC-PON
CPV	L0 - L1	1	15 dB	none	1	-	LO	LVDS
HMP	LM - L1	-	-	-	-	2	LM	LVDS
PHS	L0 - L1	-	-	-	-	2	-	LVDS
EMC	L0 - L1	-	-	-	-	3	-	LVDS

Both CTP and LTU firmware contain some common elements, namely ONU, OLT, GBT transceivers, IPbus [8] and drivers for DDR4 memories and peripherals. The IPbus is used for control and monitoring using Reverse Address Resolution Protocol (RARP) to get an IP address after power up. The CTP board can receive trigger inputs either from detectors or external emulator Trigger Input/Clock Generator (TICG), moreover, it can also emulate triggers from stored patterns in DDR4 memory functioning as Trigger Data Generator (TDG). A so-called Interaction Record (IR) containing Trigger Inputs is sent over GBT towards CRU

for bookkeeping. The LTU board contains a CTP emulator that can be used to substitute CTP during standalone runs. A preliminary block diagram of CTP FPGA can be seen in Figure 4.

,

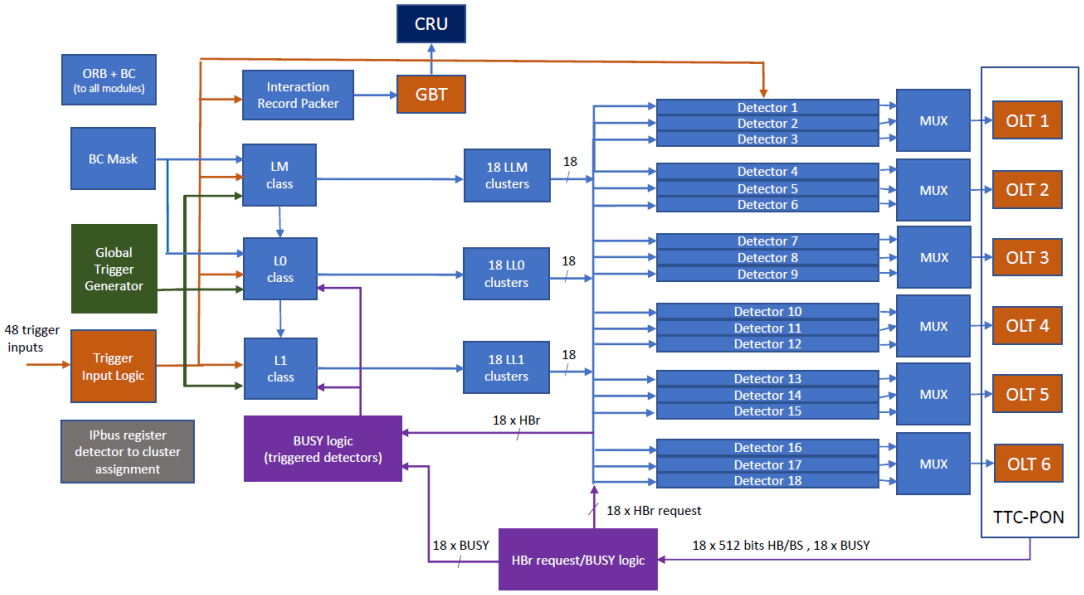

Figure 4. Main elements on the CTP FPGA firmware.

For the control and configuration software, two independent systems have been developed, one for trigger experts and the other for detector experts. The ATB board is controlled in both systems through the IPbus suite [8]. The first system, written in Python, is used as a development and debugging tool for new firmware releases and user control, e.g. arranging particular triggers in board's CTP emulator. This tool is mainly used by trigger experts and only terminal control is supported and can be seen in Figure 5 (1). The second system offers selected parts of the control and a Graphical Interface based on C++ and Qt. This interface is mainly used by detector experts to configure and set trigger generation on the LTU and can be seen in Figure 5 (2-5). Lastly, during the global runs the CTP will be configured over the Experiment Control System (ECS) using the google Remote Procedure Calls (gRPC) protocol.

Four monitoring systems have been developed. A Detector Control System (DCS) project based on WinCC software [9] monitors the boards' and crates' temperature, voltages and currents using PMbus. A Quality Control (QC) system is used to monitor interaction and trigger rates and CTP data quality. To make sure the TTC-PON connection is working correctly, a Link Health Monitor (LHMon) has been implemented, in which the CRU sends a link counter that increases by 1 in each upstream transmission, and the receiving side verifies consistent increments. Lastly, a CTP-LTU monitoring system verifies the consistency of the CTP and LTU boards.

4.3 Installation at LHC Point 2

The system was installed at LHC Point 2 at the end of September 2020. The CTP racks are as close as possible to the ALICE detectors and are located under the dipole magnet. The layout of the VME crates can be seen in Figure 6 (left). C25B contains interfaces with the

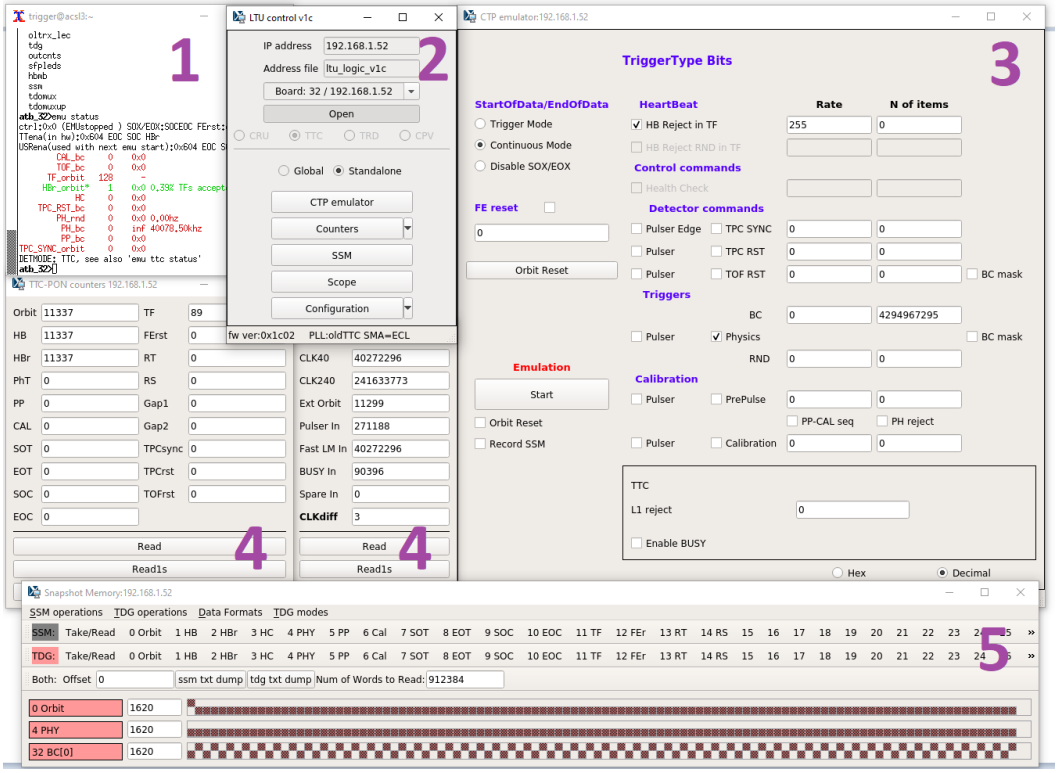

Figure 5. Overview of the possible control panels for both versions of the control and configuration software: Terminal provided from the Python-based system (1) Qt-based Graphical Interface with panels for configuration (2), trigger settings (3), counters (4) and DDR4 memory dump (5).

LHC mainly to receive LHC clock and orbit signals. The CTP and the FIT detector LTU are located in C25T (since the FIT provides a trigger input at LM latency it is as close as possible to CTP). Detectors using RD12 TTC protocol are located in C25T, where each LTU has a TTCex placed next to it. The CRU detectors are located in C24T and C24B. To monitor data on RD12 TTC optical links, an optical splitter is placed on top of C26 with a TTC interface test board in C26B. In case the ethernet connection cannot be used to reboot and update firmware and a hard reload using JTAG is required, a Network USB Hub - AnywhereUSB, placed on top of C24 and C26, is connected to each board through microUSB-JTAG. The final installation can be seen in Figure 6 (right).

5 Conclusions

This paper describes the time and trigger distribution in ALICE for LHC Run 3. The design and implementation of the new ALICE CTS and connections and protocols are also discussed. At the time of writing, all CTP and LTU boards have been produced and tested. The LTUs have been distributed to the ALICE detector groups and a full system has been installed at LHC Point 2. The ATB LTU firmware is nearly finished for downstream data generation in standalone mode or for passing the data received from the CTP. Development for the upstream data processing and passing it from detectors to the CTP has yet to be implemented. A first version of the CTP firmware, allowing global data taking in continuous mode is available. Development of the global continuous mode is the top priority. Software development is always subsequent to firmware implementation. However, further development work is still required for the ECS interface and continuous monitoring of the CTS.

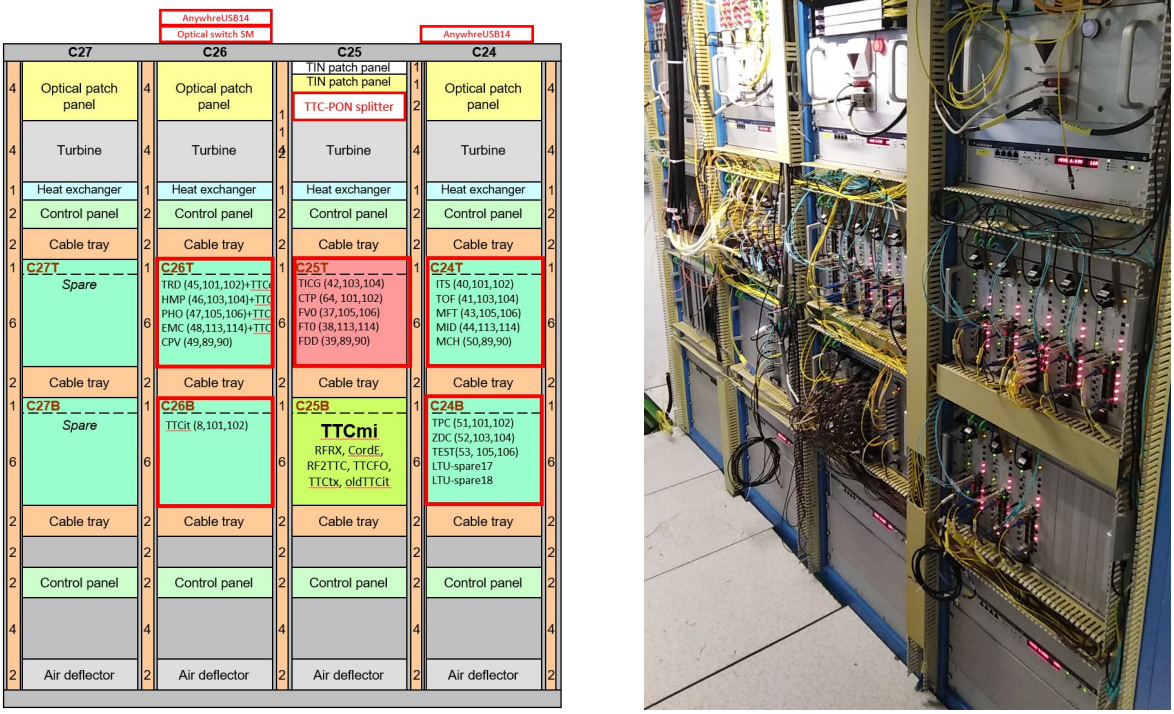

Figure 6. Central Trigger System overview with layout (left) and installation at point 2 (right).

References

[1] K. Aamodt, et al. (ALICE Collaboration), Journal of Instrumentation **3**, S08002 (2008)

[2] O.S. Brüning, P. Collier, P. Lebrun, S. Myers, R. Ostojic, J. Poole, P. Proudlock, CERN Yellow Reports: Monographs (CERN, Geneva, 2004), `https://cds.cern.ch/record/782076`

[3] C.W. Fabjan, L. Jirdén, V. Lindestruth, L. Riccati, D. Rorich, P. Van de Vyvre, O. Villalobos Baillie, H. de Groot (ALICE Collaboration), Technical design report. ALICE (CERN, Geneva, 2004), `https://cds.cern.ch/record/684651`

[4] M. Ashton, et al. (RD12 Collaboration), Tech. rep., CERN, Geneva (2000), `https://cds.cern.ch/record/421208`

[5] J. Mitra, S. Khan, S. Mukherjee, R. Paul, *Common Readout Unit (CRU) - A new readout architecture for the ALICE experiment*, Vol. 11 (2016)

[6] E.B.S. Mendes, S. Baron, D.M. Kolotouros, C. Soos, F. Vasey, *The 10G TTC-PON: challenges, solutions and performance*, Vol. 12 (2017), `http://cds.cern.ch/record/2275139`

[7] P. Moreira, R. Ballabriga, S. Baron, S. Bonacini, O. Cobanoglu, F. Faccio, T. Fedorov, , et al., *The GBT Project* (2009), `https://cds.cern.ch/record/1235836`

[8] T.S. Williams (CMS Collaboration), *IPbus A flexible Ethernet-based control system for xTCA hardware* (Geneva, 2014), `https://cds.cern.ch/record/2020872`

[9] P. Chochula, A. Augustinus, P. Bond, A. Kurepin, M. Lechman, O. Pinazza, *The Evolution of the ALICE Detector Control System* (2015), `https://cds.cern.ch/record/2213517`

Bibliography

[1] **Particle Data Group** Collaboration, P. Zyla *et al.*, "Review of Particle Physics", *PTEP* **2020** no. 8, (2020) 083C01.

[2] M. Gell-Mann, "A Schematic Model of Baryons and Mesons", *Phys. Lett.* **8** (1964) 214–215.

[3] G. Zweig, "An SU(3) model for strong interaction symmetry and its breaking. Version 2", *Developments in the Quark Theory of Hadron* (2, 1964) 22–101.

[4] V. E. Barnes *et al.*, "Observation of a Hyperon with Strangeness Minus Three", *Phys. Rev. Lett.* **12** (1964) 204–206.

[5] O. W. Greenberg, "Spin and Unitary Spin Independence in a Paraquark Model of Baryons and Mesons", *Phys. Rev. Lett.* **13** (1964) 598–602.

[6] **TASSO** Collaboration, R. Brandelik *et al.*, "Evidence for Planar Events in e^+e^- Annihilation at High-Energies", *Phys. Lett. B* **86** (1979) 243–249.

[7] **UA1** Collaboration, G. Arnison *et al.*, "Experimental Observation of Isolated Large Transverse Energy Electrons with Associated Missing Energy at $\sqrt{s} = 540$ GeV", *Phys. Lett. B* **122** (1983) 103–116.

[8] **UA2** Collaboration, M. Banner *et al.*, "Observation of Single Isolated Electrons of

High Transverse Momentum in Events with Missing Transverse Energy at the CERN $\bar{p}p$ Collider", *Phys. Lett. B* **122** (1983) 476–485.

[9] F. J. Hasert, H. Faissner, W. Krenz, J. Von Krogh, and D. Lanske, "Search for elastic muon neutrino electron scattering", *Phys. Lett. B* **46** (1973) 121–124. http://cds.cern.ch/record/243640.

[10] **Gargamelle Neutrino** Collaboration, F. J. Hasert *et al.*, "Observation of Neutrino Like Interactions without Muon or Electron in the Gargamelle Neutrino Experiment", *Nucl. Phys. B* **73** (1974) 1–22.

[11] **ATLAS** Collaboration, G. Aad *et al.*, "Observation of a new particle in the search for the Standard Model Higgs boson with the ATLAS detector at the LHC", *Phys. Lett. B* **716** (2012) 1–29, arXiv:1207.7214 [hep-ex].

[12] **CMS** Collaboration, S. Chatrchyan *et al.*, "Observation of a New Boson at a Mass of 125 GeV with the CMS Experiment at the LHC", *Phys. Lett. B* **716** (2012) 30–61, arXiv:1207.7235 [hep-ex].

[13] F. Halzen and A. D. Martin, "Quarks and Leptons: An introductory course in modern particle physics", *New York, Usa: Wiley (1984) 396p* (1984) 1–396.

[14] G. 't Hooft, "Dimensional regularization and the renormalization group", *Nucl. Phys. B* **61** (1973) 455–468.

[15] S. Weinberg, "New approach to the renormalization group", *Phys. Rev. D* **8** (Nov., 1973) 3497–3509. https://link.aps.org/doi/10.1103/PhysRevD.8.3497.

[16] **Particle Data Group** Collaboration, K. O. et al., "Review of Particle Physics", *Chin. Phys. C* **38** (2014) 090001.

[17] D. J. Gross and F. Wilczek, "Ultraviolet behavior of non-abelian gauge theories", *Phys. Rev. Lett.* **30** (June, 1973) 1343–1346. https://link.aps.org/doi/10.1103/PhysRevLett.30.1343.

[18] H. D. Politzer, "Reliable perturbative results for strong interactions?", *Phys. Rev. Lett.* **30** (June, 1973) 1346–1349. https://link.aps.org/doi/10.1103/PhysRevLett.30.1346.

[19] J. J. Aubert, U. Becker, P. J. Biggs, *et al.*, "Experimental observation of a heavy particle J", *Phys. Rev. Lett.* **33** (Dec., 1974) 1404–1406. https://link.aps.org/doi/10.1103/PhysRevLett.33.1404.

[20] J. E. Augustin, A. M. Boyarski, M. Breidenbach, *et al.*, "Discovery of a narrow resonance in e^+e^- annihilation", *Phys. Rev. Lett.* **33** (Dec., 1974) 1406–1408. https://link.aps.org/doi/10.1103/PhysRevLett.33.1406.

[21] D. H. Perkins, *Introduction to high energy physics; 4th ed.* Cambridge Univ. Press, Cambridge, 2000. https://cds.cern.ch/record/396126.

[22] J. C. Collins, D. E. Soper, and G. F. Sterman, "Factorization of Hard Processes in QCD", *Adv. Ser. Direct. High Energy Phys.* **5** (1989) 1–91, arXiv:hep-ph/0409313.

[23] V. N. Gribov and L. N. Lipatov, "Deep inelastic e p scattering in perturbation theory", *Sov. J. Nucl. Phys.* **15** (1972) 438–450.

[24] L. N. Lipatov, "The parton model and perturbation theory", *Yad. Fiz.* **20** (1974) 181–198.

[25] G. Altarelli and G. Parisi, "Asymptotic Freedom in Parton Language", *Nucl. Phys. B* **126** (1977) 298–318.

[26] Y. L. Dokshitzer, "Calculation of the Structure Functions for Deep Inelastic Scattering and e^+e^- Annihilation by Perturbation Theory in Quantum Chromodynamics.", *Sov. Phys. JETP* **46** (1977) 641–653.

[27] M. Cacciari, G. P. Salam, and G. Soyez, "FastJet User Manual", *Eur. Phys. J. C* **72** (2012) 1896, arXiv:1111.6097 [hep-ph].

[28] M. Cacciari, G. P. Salam, and G. Soyez, "The anti-k_t jet clustering algorithm", *JHEP* **04** (2008) 063, arXiv:0802.1189 [hep-ph].

[29] C. Matteo, "Jets, lecture 1: jet algorithms." MadGraph School Shanghai, 2015.

[30] Y. L. Dokshitzer, G. D. Leder, S. Moretti, and B. R. Webber, "Better jet clustering algorithms", *JHEP* **08** (1997) 001, arXiv:hep-ph/9707323.

[31] M. Wobisch and T. Wengler, "Hadronization corrections to jet cross-sections in deep inelastic scattering", in *Workshop on Monte Carlo Generators for HERA Physics (Plenary Starting Meeting)*. 4, 1998. arXiv:hep-ph/9907280.

[32] M. Cacciari and G. P. Salam, "Dispelling the N^3 myth for the k_t jet-finder", *Phys. Lett. B* **641** (2006) 57–61, arXiv:hep-ph/0512210.

[33] S. Marzani, G. Soyez, and M. Spannowsky, *Looking inside jets: an introduction to jet substructure and boosted-object phenomenology*, vol. 958. Springer, 2019. arXiv:1901.10342 [hep-ph].

[34] M. Bahr *et al.*, "Herwig++ Physics and Manual", *Eur. Phys. J. C* **58** (2008) 639–707, arXiv:0803.0883 [hep-ph].

[35] J. Bellm *et al.*, "Herwig 7.0/Herwig++ 3.0 release note", *Eur. Phys. J. C* **76** no. 4, (2016) 196, arXiv:1512.01178 [hep-ph].

[36] T. Sjostrand, S. Mrenna, and P. Z. Skands, "PYTHIA 6.4 Physics and Manual", *JHEP* **05** (2006) 026, arXiv:hep-ph/0603175.

[37] T. Sjöstrand, S. Ask, J. R. Christiansen, R. Corke, N. Desai, P. Ilten, S. Mrenna, S. Prestel, C. O. Rasmussen, and P. Z. Skands, "An introduction to PYTHIA 8.2", *Comput. Phys. Commun.* **191** (2015) 159–177, arXiv:1410.3012 [hep-ph].

[38] **Sherpa** Collaboration, E. Bothmann *et al.*, "Event Generation with Sherpa 2.2", *SciPost Phys.* **7** no. 3, (2019) 034, arXiv:1905.09127 [hep-ph].

[39] V. V. Sudakov, "Vertex parts at very high-energies in quantum electrodynamics", *Sov. Phys. JETP* **3** (1956) 65–71.

[40] A. Buckley, J. Ferrando, S. Lloyd, K. Nordström, B. Page, M. Rüfenacht, M. Schönherr, and G. Watt, "LHAPDF6: parton density access in the LHC precision era", *Eur. Phys. J. C* **75** (2015) 132, arXiv:1412.7420 [hep-ph].

[41] H.-L. Lai, M. Guzzi, J. Huston, Z. Li, P. M. Nadolsky, J. Pumplin, and C. P. Yuan, "New parton distributions for collider physics", *Phys. Rev. D* **82** (2010) 074024, arXiv:1007.2241 [hep-ph].

[42] "Ct10 nlo and nnlo parton distribution functions." https://ct.hepforge.org/PDFs/ct10.html.

[43] P. Nason, "A New method for combining NLO QCD with shower Monte Carlo algorithms", *JHEP* **11** (2004) 040, arXiv:hep-ph/0409146.

[44] S. Frixione, P. Nason, and C. Oleari, "Matching NLO QCD computations with Parton Shower simulations: the POWHEG method", *JHEP* **11** (2007) 070, arXiv:0709.2092 [hep-ph].

[45] S. Frixione, F. Stoeckli, P. Torrielli, B. R. Webber, and C. D. White, "The MCaNLO 4.0 Event Generator", arXiv:1010.0819 [hep-ph].

[46] S. Alioli, P. Nason, C. Oleari, and E. Re, "A general framework for implementing NLO calculations in shower Monte Carlo programs: the POWHEG BOX", *JHEP* **06** (2010) 043, arXiv:1002.2581 [hep-ph].

[47] J. Alwall *et al.*, "A Standard format for Les Houches event files", *Comput. Phys. Commun.* **176** (2007) 300–304, arXiv:hep-ph/0609017.

[48] S. Frixione, P. Nason, and G. Ridolfi, "A Positive-weight next-to-leading-order Monte Carlo for heavy flavour hadroproduction", *JHEP* **09** (2007) 126, arXiv:0707.3088 [hep-ph].

[49] S. Alioli, K. Hamilton, P. Nason, C. Oleari, and E. Re, "Jet pair production in POWHEG", *JHEP* **04** (2011) 081, arXiv:1012.3380 [hep-ph].

[50] A. Ryd, D. Lange, N. Kuznetsova, S. Versille, M. Rotondo, D. P. Kirkby, F. K. Wuerthwein, and A. Ishikawa, "EvtGen: A Monte Carlo Generator for B-Physics",.

[51] J. R. Christiansen and P. Z. Skands, "String Formation Beyond Leading Colour", *JHEP* **08** (2015) 003, arXiv:1505.01681 [hep-ph].

[52] S. Hands, "The phase diagram of qcd", *Contemporary Physics* **42** no. 4, (July, 2001) 209–225. http://dx.doi.org/10.1080/00107510110063843.

[53] H. Satz, "Colour deconfinement and quarkonium binding", *Journal of Physics G: Nuclear and Particle Physics* **32** no. 3, (Feb., 2006) R25–R69. http://dx.doi.org/10.1088/0954-3899/32/3/R01.

[54] X. Luo and N. Xu, "Search for the QCD Critical Point with Fluctuations of Conserved Quantities in Relativistic Heavy-Ion Collisions at RHIC : An Overview", *Nucl. Sci. Tech.* **28** no. 8, (2017) 112, arXiv:1701.02105 [nucl-ex].

[55] W. Busza, K. Rajagopal, and W. van der Schee, "Heavy ion collisions: The big picture and the big questions", *Annual Review of Nuclear and Particle Science* **68** no. 1, (Oct., 2018) 339–376. http://dx.doi.org/10.1146/annurev-nucl-101917-020852.

[56] S. Sarkar, H. Satz, and B. Sinha, *The physics of the quark-gluon plasma: introductory lectures*, vol. 785. Springer, 2009.

[57] D. d'Enterria and B. Betz, *High-p_{T} Hadron Suppression and Jet Quenching*, vol. 785, pp. 285–339. Springer, 11, 2009.

[58] T. Matsui and H. Satz, "J/ψ suppression by quark-gluon plasma formation", *Phys. Lett. B* **178** (June, 1986) 416–422. 17 p. http://cds.cern.ch/record/169304.

[59] D. d'Enterria, "Jet quenching", *Landolt-Bornstein* **23** (2010) 471, arXiv:0902.2011 [nucl-ex].

[60] S. Peigne and A. Peshier, "Collisional energy loss of a fast heavy quark in a quark-gluon plasma", *Phys. Rev. D* **77** (2008) 114017, arXiv:0802.4364 [hep-ph].

[61] Y. L. Dokshitzer, V. A. Khoze, and S. I. Troian, "On specific QCD properties of heavy quark fragmentation ('dead cone')", *J. Phys. G* **17** (1991) 1602–1604.

[62] **ALICE** Collaboration, S. Acharya *et al.*, "Direct observation of the dead-cone effect in QCD", arXiv:2106.05713 [nucl-ex].

[63] **ALICE** Collaboration, K. Aamodt *et al.*, "Suppression of Charged Particle Production at Large Transverse Momentum in Central Pb-Pb Collisions at $\sqrt{s_{NN}} =$ 2.76 TeV", *Phys. Lett. B* **696** (2011) 30–39, arXiv:1012.1004 [nucl-ex].

[64] I. Vitev and M. Gyulassy, "High-p_T tomography of $d+$Au and Au + Au at sps, rhic, and lhc", *Phys. Rev. Lett.* **89** (Dec, 2002) 252301. https://link.aps.org/doi/10.1103/PhysRevLett.89.252301.

[65] **CMS** Collaboration, A. M. Sirunyan *et al.*, "Nuclear modification factor of D^0 mesons in PbPb collisions at $\sqrt{s_{NN}} = 5.02$ TeV", *Phys. Lett. B* **782** (2018) 474–496, arXiv:1708.04962 [nucl-ex].

[66] **ALICE** Collaboration, B. B. Abelev *et al.*, "Centrality, rapidity and transverse momentum dependence of J/ψ suppression in Pb-Pb collisions at $\sqrt{s_{NN}}$=2.76 TeV", *Phys. Lett. B* **734** (2014) 314–327, arXiv:1311.0214 [nucl-ex].

[67] **ALICE** Collaboration, R. Arnaldi, "J/ψ and $\psi(2S)$ production in Pb-Pb collisions with the ALICE Muon Spectrometer at the LHC", *Nucl. Phys. A* **904-905** (2013) 595c–598c, arXiv:1211.2578 [nucl-ex].

[68] **CMS** Collaboration, V. Khachatryan *et al.*, "Suppression of $\Upsilon(1S)$, $\Upsilon(2S)$ and $\Upsilon(3S)$ production in PbPb collisions at $\sqrt{s_{NN}} = 2.76$ TeV", *Phys. Lett. B* **770** (2017) 357–379, arXiv:1611.01510 [nucl-ex].

[69] **ALICE** Collaboration, K. Aamodt *et al.*, "Particle-yield modification in jet-like azimuthal di-hadron correlations in Pb-Pb collisions at $\sqrt{s_{NN}} = 2.76$ TeV", *Phys. Rev. Lett.* **108** (2012) 092301, arXiv:1110.0121 [nucl-ex].

[70] **ATLAS** Collaboration, G. Aad *et al.*, "Observation of a Centrality-Dependent Dijet Asymmetry in Pb-Pb Collisions at $\sqrt{s_{NN}} = 2.77$ TeV with the ATLAS Detector at the LHC", *Phys. Rev. Lett.* **105** (2010) 252303, arXiv:1011.6182 [hep-ex].

[71] **ATLAS** Collaboration, M. Aaboud *et al.*, "Measurement of jet fragmentation in Pb+Pb and pp collisions at $\sqrt{s_{NN}} = 5.02$ TeV with the ATLAS detector", *Phys. Rev. C* **98** no. 2, (2018) 024908, arXiv:1805.05424 [nucl-ex].

[72] CERN, "About cern", 2018. https://home.cern/about, accessed 2018-04-17.

[73] J. Haffner, "The CERN accelerator complex.",. https://cds.cern.ch/record/1621894. General Photo.

[74] D. Dominguez, "Distribution of protons delivered by the accelerator chain to the different installations", 2021. https://home.cern/news/news/accelerators/accelerating-particles-not-just-lhc, accessed 2021-03-26.

[75] L. Evans and P. Bryant, "LHC machine", *Journal of Instrumentation* **3** no. 08, (Aug, 2008) S08001–S08001. https://doi.org/10.1088/1748-0221/3/08/s08001.

[76] D. Boussard and T. P. R. Linnecar, "The LHC Superconducting RF System", Tech. Rep. LHC-Project-Report-316. CERN-LHC-Project-Report-316, CERN, Geneva, 12, 1999. https://cds.cern.ch/record/410377.

[77] CERN, "About alice", 2021. http://alice.cern, accessed 2021-03-26.

[78] **ALICE** Collaboration, K. Aamodt *et al.*, "The ALICE experiment at the CERN LHC", *JINST* **3** (2008) S08002.

[79] A. Maire and D. Dobrigkeit Chinellato, "ALICE sub-detectors highlighted (LHC runs 1+2 // runs 3+4)." General Photo, 5, 2017.

[80] **ALICE** Collaboration, C. Lippmann, "Upgrade of the ALICE Time Projection Chamber",.

[81] G. Contin, "Performance of the present ALICE Inner Tracking System and studies for the upgrade", *JINST* **7** (2012) C06007.

[82] C. Lippmann, "Performance of the alice time projection chamber", *Physics Procedia* **37** (12, 2012) 434–441.

[83] A. Akindinov, A. Alici, and A. Zichichi, "Performance of the alice time-of-flight detector at the lhc", *The European Physical Journal Plus* **128** no. 4, (4, 2013) 44.

[84] **ALICE** Collaboration, F. Carnesecchi, "Performance of the ALICE Time-Of-Flight detector at the LHC", *JINST* **14** no. 06, (2019) C06023, arXiv:1806.03825 [physics.ins-det].

[85] **ALICE** Collaboration, M. Krzewicki and V. Lindenstruth, "ALICE HLT Run 2 performance overview", *J. Phys.: Conf. Ser.* **898** (2017) 032056. 7 p. https://cds.cern.ch/record/2297461.

[86] "The grid: A system of tiers." https://home.cern/science/computing/grid-system-tiers.

[87] B. Jones, G. McCance, C. Cordeiro, D. Giordano, S. Traylen, and D. Moreno García, "Future approach to tier-0 extension", *J. Phys. Conf. Ser.* **898** no. 8, (2017) 082040.

[88] J. Kvapil *et al.*, "ALICE Central Trigger System for LHC Run 3", *EPJ Web Conf.* **251** (2021) 04022, arXiv:2106.08353 [physics.ins-det].

[89] P. Moreira, R. Ballabriga, S. Baron, S. Bonacini, O. Cobanoglu, F. Faccio, T. Fedorov, , and et al., "The GBT Project",. https://cds.cern.ch/record/1235836.

[90] E. B. S. Mendes, S. Baron, D. M. Kolotouros, C. Soos, and F. Vasey, "The 10G TTC-PON: challenges, solutions and performance", *JINST* **12** (2017) C02041. 12 p. http://cds.cern.ch/record/2275139.

[91] **RD12 Collaboration** Collaboration, M. Ashton and et al., "Status report on the RD12 project: timing, trigger and control systems for LHC detectors",. https://cds.cern.ch/record/421208.

[92] B. Taylor, "Ttc laser transmitter (ttcex, ttctx, ttcmx) user manual",.

[93] B. Taylor, "Ttc distribution for lhc detectors", *IEEE Transactions on Nuclear Science* **45** no. 3, (1998) 821–828.

[94] **RD12 Collaboration** Collaboration, J. Christiansen, A. Marchioro, P. Moreira, and T. T, "TTCrx Reference Manual: A Timing, Trigger and Control Receiver ASIC for LHC Detectors",. http://ttc.web.cern.ch/TTCrx_manual3.12.pdf.

[95] **CMS Collaboration** Collaboration, T. S. Williams, "IPbus A flexible Ethernet-based control system for xTCA hardware",. https://cds.cern.ch/record/2020872.

[96] M. Cacciari, P. Nason, and R. Vogt, "QCD predictions for charm and bottom production at RHIC", *Phys. Rev. Lett.* **95** (2005) 122001, arXiv:hep-ph/0502203 [hep-ph].

[97] B. A. Kniehl, G. Kramer, I. Schienbein, and H. Spiesberger, "Inclusive Charmed-Meson Production at the CERN LHC", *Eur. Phys. J.* **C72** (2012) 2082, arXiv:1202.0439 [hep-ph].

[98] R. Maciula and A. Szczurek, "Open charm production at the LHC - k_t-factorization approach", *Phys. Rev.* **D87** no. 9, (2013) 094022, arXiv:1301.3033 [hep-ph].

[99] **CDF** Collaboration, D. Acosta *et al.*, "Measurement of prompt charm meson production cross sections in $p\bar{p}$ collisions at $\sqrt{s} = 1.96$ TeV", *Phys. Rev. Lett.* **91** (2003) 241804, arXiv:hep-ex/0307080 [hep-ex].

[100] **STAR** Collaboration, L. Adamczyk *et al.*, "Measurements of D^0 and D^* Production in $p + p$ Collisions at $\sqrt{s} = 200$ GeV", *Phys. Rev.* **D86** (2012) 072013, arXiv:1204.4244 [nucl-ex].

[101] **ATLAS** Collaboration, G. Aad *et al.*, "Measurement of the differential cross-section of B^+ meson production in pp collisions at $\sqrt{s} = 7$ TeV at ATLAS", *JHEP* **10** (2013) 042, arXiv:1307.0126 [hep-ex].

[102] **LHCb** Collaboration, R. Aaij *et al.*, "Measurements of prompt charm production cross-sections in pp collisions at $\sqrt{s} = 13$ TeV", *JHEP* **03** (2016) 159, arXiv:1510.01707 [hep-ex]. [Erratum: JHEP09,013(2016); Erratum: JHEP05,074(2017)].

[103] **ALICE** Collaboration, S. Acharya *et al.*, "Measurement of D-meson production at mid-rapidity in pp collisions at $\sqrt{s} = 7$ TeV", *Eur. Phys. J.* **C77** no. 8, (2017) 550, arXiv:1702.00766 [hep-ex].

[104] M. Cacciari, M. Greco, and P. Nason, "The p_{T} spectrum in heavy flavor hadroproduction", *JHEP* **05** (1998) 007, arXiv:hep-ph/9803400.

[105] M. Cacciari, S. Frixione, and P. Nason, "The p_{T} spectrum in heavy flavor photoproduction", *JHEP* **03** (2001) 006, arXiv:hep-ph/0102134.

[106] **CMS** Collaboration, A. M. Sirunyan *et al.*, "Measurements of the charm jet cross section and nuclear modification factor in pPb collisions at $\sqrt{s_{NN}} = 5.02$ TeV", *Phys. Lett. B* **772** (2017) 306–329, arXiv:1612.08972 [nucl-ex].

[107] R. Field, "Min-Bias and the Underlying Event at the LHC", *Acta Phys. Polon. B* **42** (2011) 2631–2656, arXiv:1110.5530 [hep-ph].

[108] **ALICE** Collaboration, S. Acharya *et al.*, "Measurement of the production of charm jets tagged with D^0 mesons in pp collisions at $\sqrt{\mathrm{s}} = 7$ TeV", *JHEP* **08** (2019) 133, arXiv:1905.02510 [nucl-ex].

[109] A. Beraudo *et al.*, "Extraction of Heavy-Flavor Transport Coefficients in QCD Matter", *Nucl. Phys. A* **979** (2018) 21–86, arXiv:1803.03824 [nucl-th].

[110] X. Dong, Y.-J. Lee, and R. Rapp, "Open Heavy-Flavor Production in Heavy-Ion Collisions", *Ann. Rev. Nucl. Part. Sci.* **69** (2019) 417–445, arXiv:1903.07709 [nucl-ex].

[111] H. T. Li and I. Vitev, "Inclusive heavy flavor jet production with semi-inclusive jet functions: from proton to heavy-ion collisions", *JHEP* **07** (2019) 148, arXiv:1811.07905 [hep-ph].

[112] **CMS** Collaboration, A. M. Sirunyan *et al.*, "Studies of charm quark diffusion inside jets using PbPb and pp collisions at $\sqrt{s_{\mathrm{NN}}} = 5.02$ TeV", *Phys. Rev. Lett.* **125** no. 10, (2020) 102001, arXiv:1911.01461 [hep-ex].

[113] **STAR** Collaboration, B. I. Abelev *et al.*, "Measurement of D* Mesons in Jets from p+p Collisions at $\sqrt{s}$ = 200-GeV", *Phys. Rev. D* **79** (2009) 112006, arXiv:0901.0740 [hep-ex].

[114] **ATLAS** Collaboration, G. Aad *et al.*, "Measurement of $D^{*+/-}$ meson production in jets from pp collisions at $\sqrt{s}$ = 7 TeV with the ATLAS detector", *Phys. Rev. D* **85** (2012) 052005, arXiv:1112.4432 [hep-ex].

[115] F. Abe, D. Amidei, and Apollinari, "Measurement of d^* production in jets from $p\overline{p}$ collisions at $\sqrt{s}$=1.8 tev", *Phys. Rev. Lett.* **64** (Jan, 1990) 348–352. https://link.aps.org/doi/10.1103/PhysRevLett.64.348.

[116] C. Albajar, M. Albrow, and O. Allkofer, "A study of the d^* content of jets at the cern pp collider", *Physics Letters B* **244** no. 3, (1990) 566–572. https://www.sciencedirect.com/science/article/pii/037026939090363B.

[117] Y.-T. Chien, Z.-B. Kang, F. Ringer, I. Vitev, and H. Xing, "Jet fragmentation functions in proton-proton collisions using soft-collinear effective theory", *JHEP* **05** (2016) 125, arXiv:1512.06851 [hep-ph].

[118] **ZEUS** Collaboration, S. Chekanov *et al.*, "Measurement of the charm fragmentation function in D* photoproduction at HERA", *JHEP* **04** (2009) 082, arXiv:0901.1210 [hep-ex].

[119] **Belle** Collaboration, R. Seuster *et al.*, "Charm hadrons from fragmentation and B decays in e^+e^- annihilation at $\sqrt{s}$ = 10.6-GeV", *Phys. Rev. D* **73** (2006) 032002, arXiv:hep-ex/0506068.

[120] D. P. Anderle, T. Kaufmann, M. Stratmann, F. Ringer, and I. Vitev, "Using hadron-in-jet data in a global analysis of D^* fragmentation functions", *Phys. Rev. D* **96** no. 3, (2017) 034028, arXiv:1706.09857 [hep-ph].

[121] S. van der Meer, "Calibration of the effective beam height in the ISR", tech. rep., CERN, Geneva, 1968. https://cds.cern.ch/record/296752.

[122] **ALICE** Collaboration, S. Acharya *et al.*, "ALICE 2016-2017-2018 luminosity determination for pp collisions at $\sqrt{s}$ = 13 TeV", ALICE-PUBLIC-2021-005. https://cds.cern.ch/record/2776672.

[123] **ALICE** Collaboration, S. Acharya *et al.*, "Azimuthal correlations of prompt D mesons with charged particles in pp and p–Pb collisions at $\sqrt{s_{NN}}$ = 5.02 TeV", *Eur. Phys. J. C* **80** no. 10, (2020) 979, arXiv:1910.14403 [nucl-ex].

[124] P. Z. Skands, "Tuning Monte Carlo Generators: The Perugia Tunes", *Phys. Rev. D* **82** (2010) 074018, arXiv:1005.3457 [hep-ph].

[125] R. Brun, R. Hagelberg, M. Hansroul, and J. C. Lassalle, *Simulation program for particle physics experiments, GEANT: user guide and reference manual.* CERN, Geneva, 1978. https://cds.cern.ch/record/118715.

[126] B. A. et al and, "Technical design report for the upgrade of the ALICE inner tracking system", *Journal of Physics G: Nuclear and Particle Physics* **41** no. 8, (July, 2014) 087002. https://doi.org/10.1088/0954-3899/41/8/087002.

[127] **ALICE** Collaboration, S. Acharya *et al.*, "Measurement of D-meson production at

mid-rapidity in pp collisions at $\sqrt{s} = 7$ TeV", *Eur. Phys. J. C* **77** no. 8, (2017) 550, arXiv:1702.00766 [hep-ex].

[128] **ALICE** Collaboration, S. Acharya *et al.*, "Measurement of prompt D^0, D^+, D^{*+}, and D_S^+ production in p–Pb collisions at $\sqrt{s_{NN}} = 5.02$ TeV", *JHEP* **12** (2019) 092, arXiv:1906.03425 [nucl-ex].

[129] T. Adye, "Unfolding algorithms and tests using RooUnfold", in *PHYSTAT 2011*, pp. 313–318. CERN, Geneva, 2011. arXiv:1105.1160 [physics.data-an].

[130] S. Schmitt, "Data Unfolding Methods in High Energy Physics", *EPJ Web Conf.* **137** (2017) 11008, arXiv:1611.01927 [physics.data-an].

[131] P. Skands, S. Carrazza, and J. Rojo, "Tuning PYTHIA 8.1: the Monash 2013 Tune", *Eur. Phys. J. C* **74** no. 8, (2014) 3024, arXiv:1404.5630 [hep-ph].

[132] R. Vogt, *Ultrarelativistic Heavy-Ion Collisions*. Elsevier Science B.V., Amsterdam, 2007.

[133] M. Kliemant, R. Sahoo, T. Schuster, and R. Stock, "Global Properties of Nucleus-Nucleus Collisions", *Lect. Notes Phys.* **785** (2010) 23–103, arXiv:0809.2482 [nucl-ex].

[134] M. L. Miller, K. Reygers, S. J. Sanders, and P. Steinberg, "Glauber modeling in high energy nuclear collisions", *Ann. Rev. Nucl. Part. Sci.* **57** (2007) 205–243, arXiv:nucl-ex/0701025.

[135] **ALICE** Collaboration, K. Aamodt *et al.*, "Centrality dependence of the charged-particle multiplicity density at mid-rapidity in Pb-Pb collisions at $\sqrt{s_{NN}} = 2.76$ TeV", *Phys. Rev. Lett.* **106** (2011) 032301, arXiv:1012.1657 [nucl-ex].